



Functionalized carbon nanomaterials

Edited by Anke Krueger

Imprint

Beilstein Journal of Organic Chemistry

www.bjoc.org

ISSN 1860-5397

Email: journals-support@beilstein-institut.de

The *Beilstein Journal of Organic Chemistry* is published by the Beilstein-Institut zur Förderung der Chemischen Wissenschaften.

Beilstein-Institut zur Förderung der Chemischen Wissenschaften
Trakehner Straße 7–9
60487 Frankfurt am Main
Germany
www.beilstein-institut.de

The copyright to this document as a whole, which is published in the *Beilstein Journal of Organic Chemistry*, is held by the Beilstein-Institut zur Förderung der Chemischen Wissenschaften. The copyright to the individual articles in this document is held by the respective authors, subject to a Creative Commons Attribution license.



Carbon nanomaterials

Anke Krueger^{1,2}

Editorial

Open Access

Address:

¹Institute for Organic Chemistry, Julius Maximilians University Würzburg, Am Hubland, 97074 Würzburg, Germany and ²Wilhelm Conrad Röntgen Research Center for Complex Material Systems (RCCM), Julius Maximilians University Würzburg, Sanderring 2, 97070 Würzburg, Germany

Email:

Anke Krueger - anke.krueger@uni-wuerzburg.de

Keywords:

carbon allotropes; carbon nanomaterials; carbon-rich molecules

Beilstein J. Org. Chem. **2014**, *10*, 1785–1786.

doi:10.3762/bjoc.10.186

Received: 23 June 2014

Accepted: 30 June 2014

Published: 05 August 2014

This article is part of the Thematic Series "Carbon nanomaterials".

Guest Editor: A. Krueger

© 2014 Krueger; licensee Beilstein-Institut.

License and terms: see end of document.

The era of carbon nanomaterials has started with the first reports on fullerenes and related compounds in the mid-eighties, and a tremendous increase of the research activity in the field has been observed ever since. New classes of carbon materials have entered the scene such as carbon nanotubes, carbon onions, nanoscale diamond and diamondoids. A major turning point was the appearance of graphene as a material available for in-depth investigations – spurred by the development of reliable production methods. The progress in terms of understanding the properties and chemistry of carbon nanomaterials has opened a whole new world of applications for nanomaterials in general.

The reliable production of a material represents a necessary requirement for the development of a research field. By now, all types of carbon nanomaterials and many carbon-rich organic materials are available to the scientific community in excellent quality and suitable amounts for the investigation of fundamental properties and prospective applications. This has led to the emergence of a new community of scientists working in an interdisciplinary area involving materials science, organic chemistry and physics.

Synthetic organic chemistry is a major part of carbon materials chemistry as the rational synthesis of carbon allotropes such as

fullerenes and nanotubes and related molecular compounds with and without heteroatoms remains a challenging task. The contribution does not end here but continues with the development of suitable reactions for the controlled functionalization of molecular as well as nanoscale allotropes such as fullerenes, diamondoids, carbon onions, carbynes or nanodiamonds. The interplay with knowledge gained by materials scientists and physicists on the electronic or optic properties of materials enables the fine-tuning of materials properties and the conjugation of functional moieties with the carbon nanomaterial. This interdisciplinary approach opened the door to a broad range of applications including energy conversion and storage, catalysis, electronic and optoelectronic as well as biomedical applications.

The present Thematic Series attempts to showcase the diversity in the field of carbon nanomaterials and carbon-rich compounds and to emphasize the links between the different classes of materials. Contributions from synthetic organic chemistry dealing with the formation and functionalization of carbon-rich molecules and from the area of functional nanomaterials illustrate the plethora of research activities. Obviously, such an issue will fail to present the field in its entirety. The sheer number of publications appearing globally every year attests to this. However, a topical collection enables a focused view on some of the novel developments.

I would like to thank all authors for their excellent contributions to this Thematic Series. The publication of the manuscripts would not have been possible without the contribution of detailed and timely reports by reviewers from all fields of carbon chemistry. Furthermore, I would like to thank the editorial team at the Beilstein-Institut for their support and hard work. The open access policy of the Beilstein Journal of Organic Chemistry facilitates the availability of the articles of this Thematic Series to researchers and interested people all over the world, thus enabling a broad discussion of the topics.

Anke Krueger

Würzburg, June 2014

License and Terms

This is an Open Access article under the terms of the Creative Commons Attribution License (<http://creativecommons.org/licenses/by/2.0>), which permits unrestricted use, distribution, and reproduction in any medium, provided the original work is properly cited.

The license is subject to the *Beilstein Journal of Organic Chemistry* terms and conditions:
(<http://www.beilstein-journals.org/bjoc>)

The definitive version of this article is the electronic one which can be found at:
doi:10.3762/bjoc.10.186



Tuning the interactions between electron spins in fullerene-based triad systems

Maria A. Lebedeva¹, Thomas W. Chamberlain¹, E. Stephen Davies¹,
Bradley E. Thomas¹, Martin Schröder¹ and Andrei N. Khlobystov^{*1,2}

Full Research Paper

Open Access

Address:

¹School of Chemistry, University of Nottingham, Nottingham, NG7 2RD, UK and ²Nottingham Nanoscience & Nanotechnology Centre, University of Nottingham, University Park, Nottingham, NG7 2RD, UK

Email:

Andrei N. Khlobystov^{*} - andrei.khlobystov@nottingham.ac.uk

* Corresponding author

Keywords:

carbon nanomaterials; electrochemistry; EPR; fullerene dimers; fullerene triads; spin–spin interactions

Beilstein J. Org. Chem. **2014**, *10*, 332–343.

doi:10.3762/bjoc.10.31

Received: 25 September 2013

Accepted: 06 January 2014

Published: 05 February 2014

This article is part of the Thematic Series "Functionalized carbon-nanomaterials".

Guest Editor: A. Krueger

© 2014 Lebedeva et al; licensee Beilstein-Institut.

License and terms: see end of document.

Abstract

A series of six fullerene–linker–fullerene triads have been prepared by the stepwise addition of the fullerene cages to bridging moieties thus allowing the systematic variation of fullerene cage (C_{60} or C_{70}) and linker (oxalate, acetate or terephthalate) and enabling precise control over the inter-fullerene separation. The fullerene triads exhibit good solubility in common organic solvents, have linear geometries and are diastereomerically pure. Cyclic voltammetric measurements demonstrate the excellent electron accepting capacity of all triads, with up to 6 electrons taken up per molecule in the potential range between -2.3 and 0.2 V (vs Fe^{+}/Fe). No significant electronic interactions between fullerene cages are observed in the ground state indicating that the individual properties of each C_{60} or C_{70} cage are retained within the triads. The electron–electron interactions in the electrochemically generated dianions of these triads, with one electron per fullerene cage were studied by EPR spectroscopy. The nature of electron–electron coupling observed at 77 K can be described as an equilibrium between doublet and triplet state biradicals which depends on the inter-fullerene spacing. The shorter oxalate-bridged triads exhibit stronger spin–spin coupling with triplet character, while in the longer terephthalate-bridged triads the intramolecular spin–spin coupling is significantly reduced.

Introduction

Fabricating molecular systems that are capable of storing one or more unpaired electrons is essential for the development of molecular spintronics and electron-spin-based quantum computing. Endohedral fullerenes are compounds that contain a heteroatom trapped inside the fullerene cage and are able to

support the formation of stable radical materials [1]. They can also show interesting properties such as magnetism, and photoactivity and are thermally and chemically stable. Their ability to form well-ordered 1D arrays makes them leading candidate materials for the study of polyfunctional materials.

For example, significant effort has been directed into incorporating $\text{N}@\text{C}_{60}$ molecules into quantum computing devices [2]. Incorporating a second radical centre into these molecules, in addition to the endohedral atom, introduces a mechanism to control the magnetic properties of the resulting materials. This is essential for the recording, storing and read-out processes performed in spin-based quantum information processing using nanoscale molecular architectures [3]. This has been achieved recently within a copper porphyrin– $\text{N}@\text{C}_{60}$ dyad [4] and several types of $\text{N}@\text{C}_{60}$ – $\text{N}@\text{C}_{60}$ molecules [5–7]. However the application of these systems is limited due to a number of synthetic challenges associated with the preparation and purification of endohedral fullerenes [8]. This notwithstanding, fullerene cages are excellent electron acceptors and can support up to six electrons per fullerene cage to form species containing one or more unpaired electrons, in which overall charge and the spin state can be controlled precisely by applied potential [9]. In addition, combining two fullerene cages within the same molecule increases the total spin-carrying capacity and introduces a mechanism of spin-tuning while retaining the intrinsic properties of each of the fullerene cages [10]. The synthesis of such fullerene–bridge–fullerene triads, though not straightforward, has been reported [11], the simplest involving species where the fullerene cages are connected directly by a C–C bond [12], a bridging O-atom [13], or by a transition metal atom [14]. A variety of more complex triads have since evolved in which the fullerene molecules are connected using optically or electrochemically active spacers [15]. The choice of linker in triad systems is crucial as it has a significant impact on the properties of the resulting arrays [16]. As the strength of dipolar coupling between unpaired electrons decreases as a function of r^{-3} , where r is the average distance between unpaired electrons, the strength of any electron–electron interactions in fullerene triads rapidly decreases with increasing distance between fullerene cages [17]. Thus, the ability to control the interfullerene separation is crucial in fabricating systems in which specific interactions between multiple unpaired electrons are targeted.

The shape of the fullerene containing molecule is also very important. 1D and 2D ordering is a critical factor in the design of molecular electronics. For example, linear molecules can be ordered readily into 1D arrays using carbon nanotubes as templates [18] and are therefore advantageous compared to non-linear or branched molecules for which 1D packing arrangements are inhibited. In addition, solubility can also be a significant issue as fullerene triads tend to show poor solubility [19]. The majority of fullerene triads reported to date are either synthesised via complicated non-scalable synthetic procedures, which makes controlling the fullerene–fullerene distance difficult, or incorporate bulky spacers and solubilising groups

resulting in cumbersome non-linear structures and hence are not ideal for potential applications in molecular electronics and spintronics devices. We recently reported a new general synthetic methodology for the formation of fullerene triads which allows the introduction of fullerene cages in a stepwise fashion and thus allows the length of the spacer to be adjusted [20]. We report herein the preparation of six different fullerene–linker–fullerene triads in which both the length of the linker and the nature of the fullerene cage are systematically varied, and we explore their spin-carrying and spin-tuning capacity in reduced states using electrochemical techniques and electron paramagnetic resonance (EPR) spectroscopy.

Results and Discussion

Synthesis of the fullerene triads

This study aimed to vary the fullerene–fullerene separation and the nature of the fullerene cages resulting in the preparation of six fullerene–linker–fullerene (triad) compounds (Figure 1). The fullerenes were functionalised via Prato reaction chemistry forming a pyrrolidine ring across the [6.6] bond of the cage [21]. The resulting pyrrolidine functionalised fullerenes are known to be electrochemically stable and can be readily linked together via the N atom to form linear and diastereomerically pure triads. The choice of linker was determined by the target fullerene–fullerene separation in the product, and terephthalate and oxalate bridges were chosen as they possess similar chemical properties but differ significantly in size. The distance between the centres of the corresponding fullerene cages in the terephthalate bridged triads (compounds **1–3**) was estimated to be 16–20 Å depending on the conformation of the molecule (see Figure S4, Supporting Information File 1), whereas the oxalate (compounds **4** and **6**) or acetate (compound **5**) bridged triads have significantly shorter separations (12–15 Å). Functionalised fullerenes **7** and **8**, which are precursors in the synthesis of triads **1–3**, were utilised as control compounds in the electrochemical studies and to aid the assignment of redox processes in the triad species.

The triads **1–3** were synthesised in five steps by functionalisation of each fullerene cage using the Prato reaction, addition of the terephthalate spacer to the fulleropyrrolidine unit and subsequent coupling of two fullerene moieties [20]. The oxalate or acetate bridged triads **4–6** were prepared using a similar strategy. To link the two C_{60} or two C_{70} fullerene cages with the oxalate spacer (compounds **4** and **6**) a one-step procedure was used in which the corresponding fulleropyrrolidine was treated with an excess of oxalyl chloride in the presence of 4-dimethylaminopyridine (DMAP) and pyridine (Scheme 1).

Oxalate bridged triads **4** and **6** were obtained in moderate yields and displayed physical and spectroscopic properties very

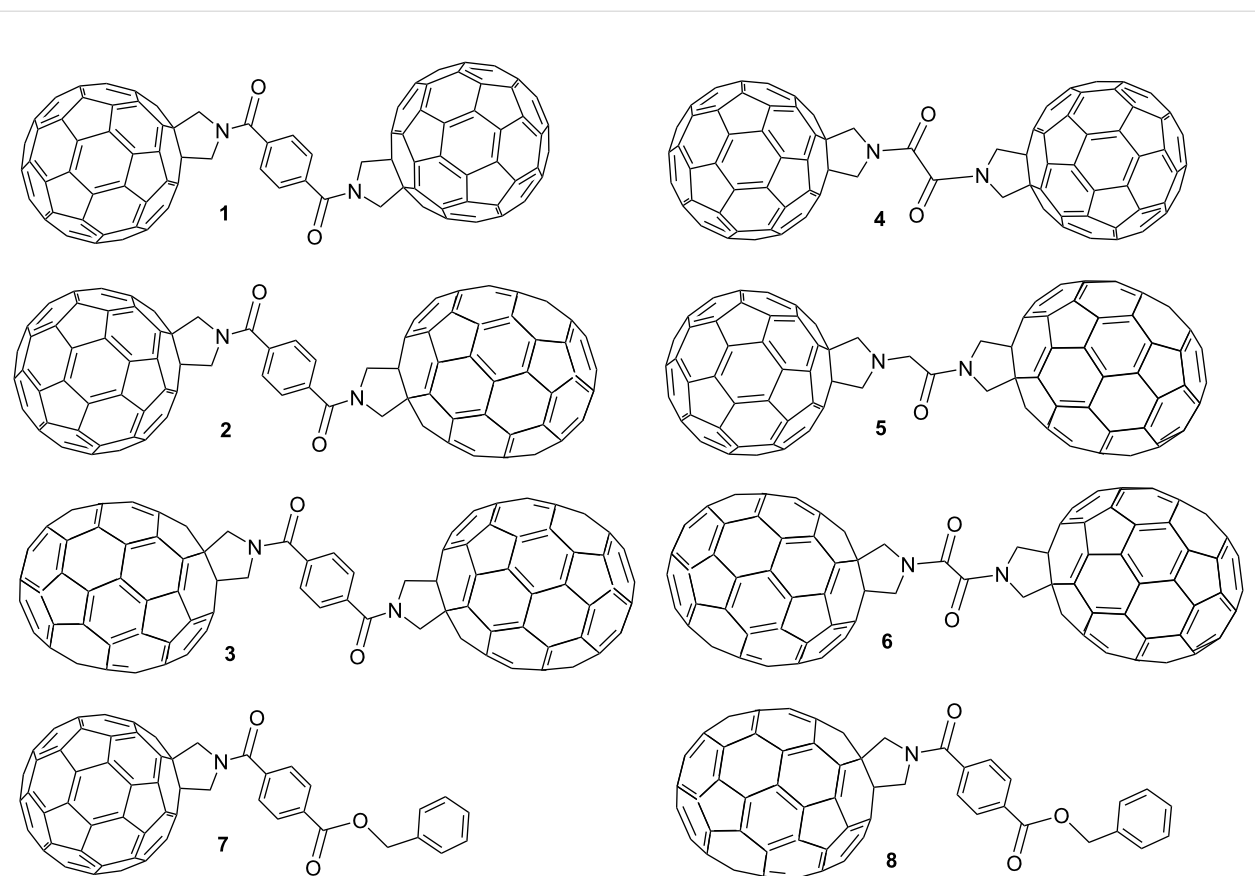
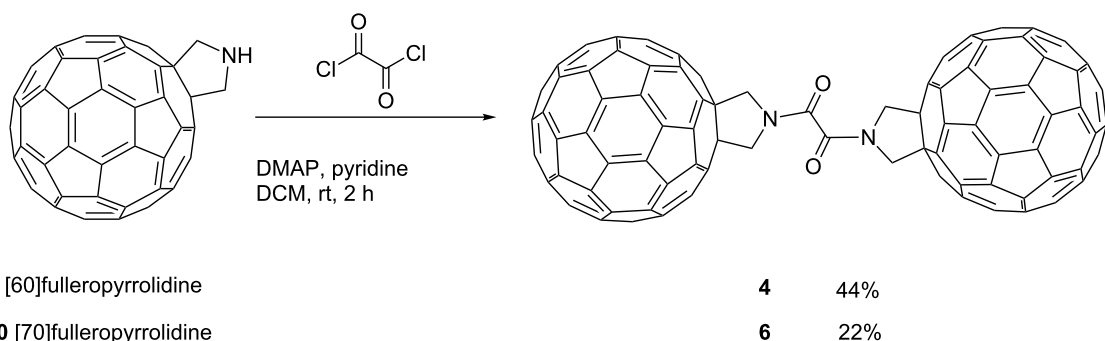


Figure 1: Structures of triads **1–6** and precursor molecules **7–8** used for the synthesis of the asymmetric systems. For the C₇₀ containing compounds only the major (8,25) regioisomer is shown for clarity.

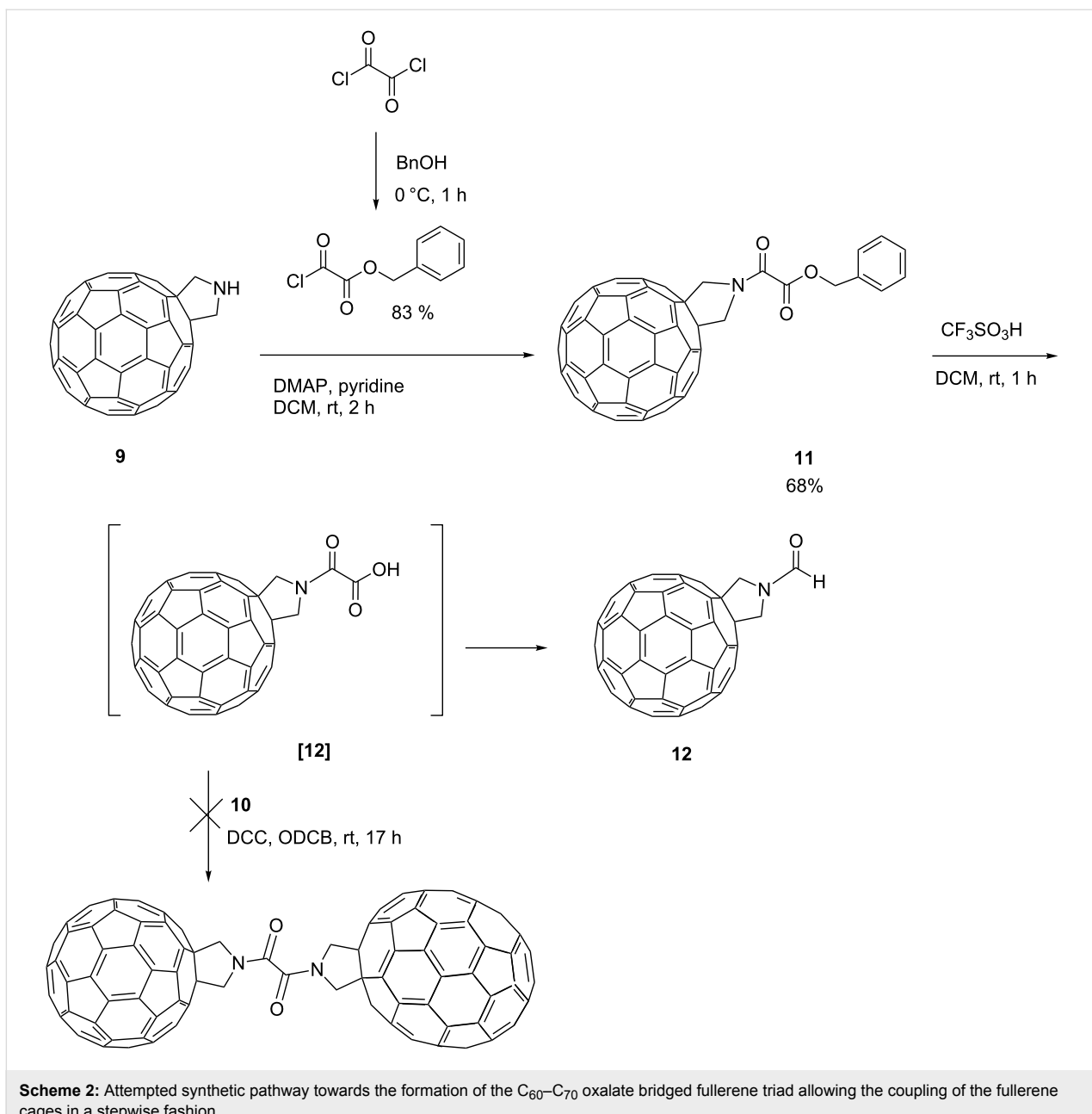


Scheme 1: The one-step synthetic procedure towards the oxalate-bridged fullerene triads **4** and **6**.

similar to those of terephthalate bridged triads **1–3**, including good solubility in organic solvents such as CS₂ and *o*-dichlorobenzene (ODCB).

To link the C₆₀ and C₇₀ fulleropyrrolidines within asymmetric triads with an oxalate spacer we attempted a similar stepwise approach as reported for compounds **1–3** (Scheme 2).

Oxalic acid monobenzyl ester monochloride was prepared by equimolar reaction of oxalyl chloride and benzyl alcohol [22] and was reacted with [60]fulleropyrrolidine **9** to give the benzyl ester protected compound **11** in 68% yield. Subsequent deprotection of **11** by CF₃SO₃H yielded the insoluble product **12** that precluded characterisation by solution based methods. However, MALDI-MS of **12** showed a molecular ion peak with

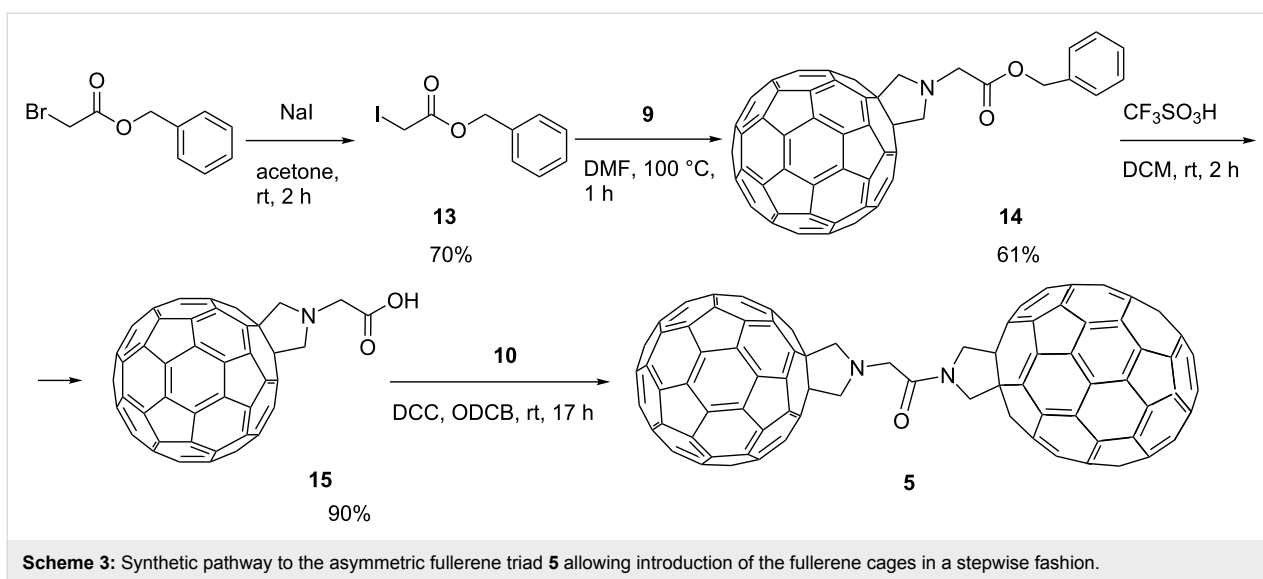


m/z 791 and the solid state IR spectrum as a pressed disc in KBr indicated only one signal in the carbonyl region characteristic of the amide group (1653 cm^{-1}) and no signal related to the carboxylic group stretch. The desired carboxylic acid compound **[12]** seems to be unstable under acidic conditions and undergoes decarboxylation to form an insoluble amide compound **12**. This reaction under acidic conditions is characteristic of carboxylic acids that contain an electron withdrawing substituent in the α -position [23].

To prevent decarboxylation processes we modified the linker to exclude the electron withdrawing amide group from the α -pos-

ition of the carboxylate functionality, while maintaining an identical inter-fullerene separation in the asymmetric triad when compared with the symmetric analogue (Scheme 3).

The key step in this procedure is the formation of intermediate compound **14** via the nucleophilic substitution of the iodide centre in benzyl 2-iodoacetate [24] (**13**) with $[60]$ fulleropyrrolidine **9** (Scheme 3). Compound **14** is a benzyl ester of an α -amino acid which is stable under acidic conditions. Indeed, deprotection of **14** yielded the desired carboxylic acid **15**. Compound **15** also shows limited solubility, but MALDI-MS (m/z 821) and IR spectroscopy (carbonyl stretch at 1733 cm^{-1})



Scheme 3: Synthetic pathway to the asymmetric fullerene triad **5** allowing introduction of the fullerene cages in a stepwise fashion.

confirm the assigned structure. The dicyclohexylcarbodiimide (DCC) assisted acid–amine coupling reaction between **15** and [70]fulleropyrrolidine **10** resulted in the formation of the desired asymmetric triad **5**, which displayed physical properties similar to those of **1–4** and **6**.

Electrochemical characterisation of fullerene triads **1–6**

Compounds **1–6** were studied by cyclic voltammetry (CV) as solutions in *o*-dichlorobenzene in order to investigate the sequence of electron additions and possible electronic interactions in these triads.

The cyclic voltammograms recorded for the fullerene triads **1–6** are very similar to those of their monomeric precursors **7** and **8** and do not appear to show interactions between the individual

fullerene cages. This observation is consistent with the lack of an effective electronic communication pathway through the linker groups within the triads (Table 1 and Figure 2).

Each triad molecule **1–6** exhibits a series of reduction processes in a potential range between -0.3 and -2.3 V (vs Fc^+/Fc), some of which are overlapping or appear as shoulders to the main peaks. By comparison with the cyclic voltammetry of the precursor compounds **7** and **8** (Figure S5, Supporting Information File 1), we suggest that this series of reductions corresponds to the addition of up to 3 electrons per fullerene cage (in total 6 electrons per molecule). No oxidation processes were found in the range up to 1.5 V (vs Fc^+/Fc). For triads **1** and **4**, containing C_{60} only, these potentials are similar to those of their precursor **7**. A similar correlation was noted for the C_{70} containing triads **3** and **6** and their precursor **8**. Comparison of **1**

Table 1: Electrochemical data^a for fullerene based compounds **1–8**.

Compound	$E_{1/2}$ red ₁ , V	$E_{1/2}$ red ₂ , V	$E_{1/2}$ red ₃ , V	ΔE , Fc^+/Fc
1	-1.09 (0.16)	-1.47 (0.16)	-2.01 (0.16)	0.17
2	-1.12 (0.10)	-1.48 (0.08)	-1.89 (0.05) -2.02 (0.06)	0.20
3	-1.12 (0.06)	-1.50 (0.08)	-1.89 (0.06)	0.10
4	-1.09 (0.16)	-1.47 (0.16)	-2.01 (0.18)	0.16
5	-1.13 (0.10)	-1.49 (0.10)	-1.89 (0.11) -2.05 (0.10)	0.10
6	-1.10 (0.11)	-1.47 (0.10)	-1.89 (0.11)	0.12
7	-1.11 (0.09)	-1.49 (0.09)	-2.02 (0.08)	0.15
8	-1.15 (0.06)	-1.52 (0.06)	-1.94 (0.06)	0.09

^aPotentials ($E_{1/2} = (E_p^a + E_p^c)/2$) in volt are quoted to the nearest 0.01 V. All potentials are reported against the Fc^+/Fc couple for 0.5 mM solutions in *o*-dichlorobenzene containing 0.2 M [*n*-Bu₄N][BF₄] as the supporting electrolyte. The anodic/cathodic peak separation ($\Delta E = E_p^a - E_p^c$) is given in brackets where applicable. ΔE for the Fc^+/Fc couple was used as the internal standard.

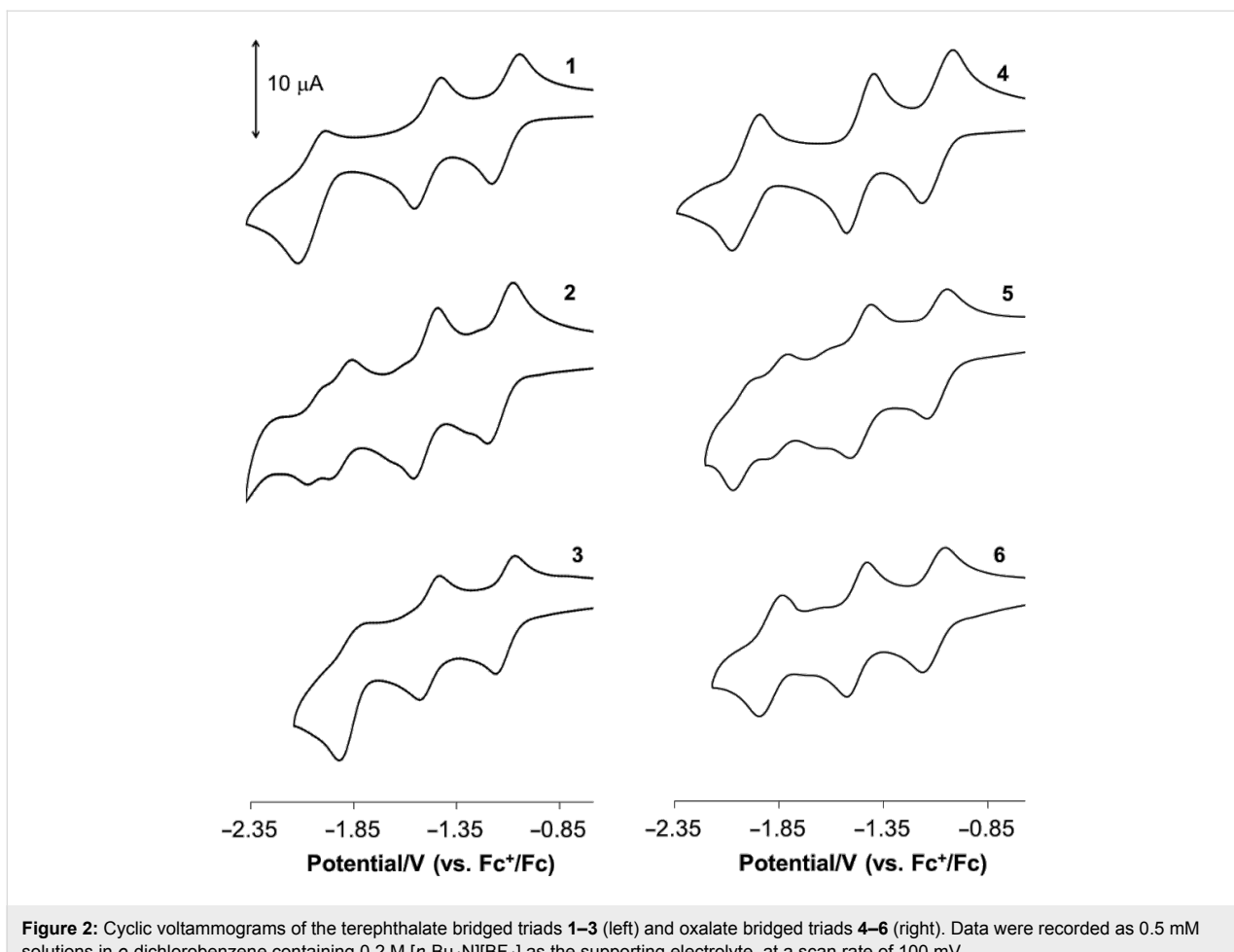


Figure 2: Cyclic voltammograms of the terephthalate bridged triads **1–3** (left) and oxalate bridged triads **4–6** (right). Data were recorded as 0.5 mM solutions in *o*-dichlorobenzene containing 0.2 M $[n\text{-Bu}_4\text{N}][\text{BF}_4]$ as the supporting electrolyte, at a scan rate of 100 mV.

with **3**, **4** with **6** and **7** with **8** shows that the first and second reductions of C_{60} , in general, occur at slightly more anodic potentials than those of C_{70} cages. However beyond the second reduction, C_{70} is more readily reduced. For **2** and **5**, each containing a mixture of C_{60} and C_{70} fullerenes, two well defined reduction couples are observed at $E_{1/2}$ ca. -1.12 and -1.49 V, which we assigned to an overlap of $\text{C}_{60}/\text{C}_{70}$ -based reductions. These processes are separated by an additional process that appears as a shoulder on the first reduction in **2** and **5** (Figure 2 and Figure S6, Supporting Information File 1). A similar feature is noted to cathodic potential of the second reduction process. For **2** and **5** we associate these features with the generation of a reduced C_{70} cage in a triad molecule, noting a similar, although less pronounced effect in **3** and **6**, each containing two equivalent C_{70} cages (see Supporting Information File 1) and an absence of these features in C_{60} triads, **1** and **4**, and in the C_{70} containing dyad, **8**. The origin of these effects is unclear and may result from the nature of interaction of the reduced triad with the electrode surface. We note that the first and second reductions on C_{70} are expected to be slightly more cathodic than those for C_{60} but comparing

potentials for **7** and **8**, we suggest that this difference alone is too small to explain the position of these features. We note also that **2** and **5** are mixtures of two regioisomers of the pyrrolidine functionalised C_{70} [19], in a ratio of 6:4 as determined by ^1H NMR spectroscopy (see Experimental section). It is possible that these isomers may interact with the electrode differently.

Based on these results we can confirm that for C_{60} – C_{60} triad molecules changing the nature and the size of the bridging group has little effect on the nature and potentials of the redox processes. Thus, we conclude that the two C_{60} -fullerene cages in the triads behave independently in the ground state. These results are consistent with other fullerene triad systems in which intramolecular fullerene–fullerene interactions are only observed where fullerene cages are bonded directly [25] or bridged by a transition metal atom [26,27]. For triads containing C_{70} the results are less clear where additional electrode processes are observed. However we do not attribute these features to intramolecular fullerene–fullerene interactions.

EPR spectroscopic characterisation of the fullerene triads in the reduced state

The electron spin–spin interactions that are crucial for the application of fullerene triads were investigated by EPR spectroscopy as fluid and frozen solutions at room temperature and 77 K, respectively, following electrochemical reduction. Whilst these triads are capable of accepting multiple electrons into each of the fullerene groups, we restrict our discussion to dianionic species in compounds where the electrochemistry is well defined; under these conditions each fullerene cage is reduced by a single electron. We have evaluated the effects of varying the inter-fullerene separation (oxalate bridge vs terephthalate bridge) and the nature of the fullerene (C_{60} vs C_{70}) on the nature of the spin–spin coupling obtained.

The two electron reduced species of **1** and **4** (1^{2-} and 4^{2-}) and the corresponding mono reduced species of their monomeric precursor **7** (7^{1-}) (i.e. one electron per fullerene cage for all species) were obtained by electrochemical reduction at -1.4 V of 0.5 mM solutions of compound in *o*-dichlorobenzene containing $[n\text{-Bu}_4\text{N}][\text{BF}_4]$ as the supporting electrolyte.

Fluid solution EPR spectra of 1^{2-} , 4^{2-} and 7^{1-} (Figure 3) are similar in *g* value (2.0002, 2.0001 and 2.0000, respectively) but

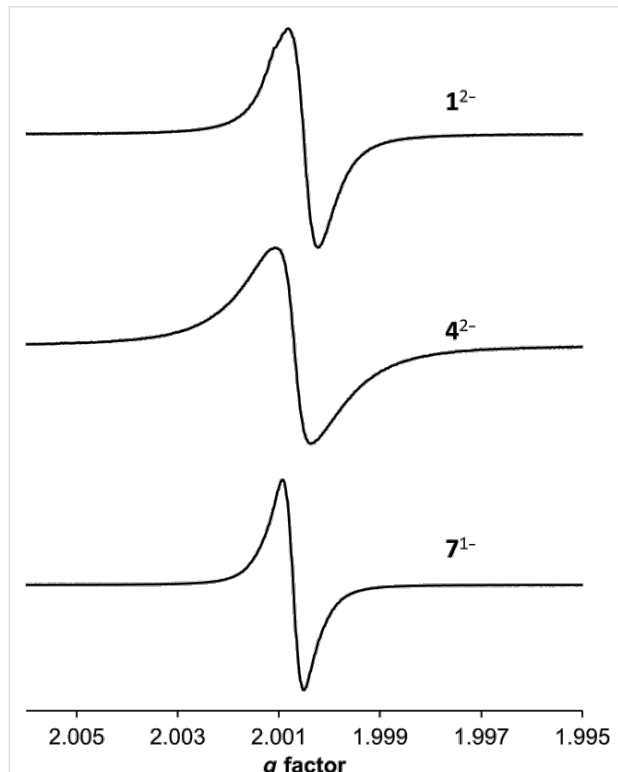


Figure 3: Fluid solution EPR spectra recorded at 297 K for the two electron reduced species of compounds **1** and **4** and the one electron reduced species of **7**.

differ in linewidth ($\Delta H_{\text{p-p}}$ 1.1, 1.3 and 0.8 G, respectively) and are typical of C_{60} based radical anions [28], confirming that the electrochemically introduced electrons are localised on the fullerene cages.

The EPR spectrum of 4^{2-} in frozen solution recorded at 77 K shows an intense central feature at $g = 2.0001$ (Figure 4a) indicating that the majority of the molecules exist as two independent doublet ($S = 1/2$) radicals and suggesting a small singlet-triplet energy gap [29]. The intramolecular triplet biradical ($S = 1$) of 4^{2-} is also present with a zero-field splitting parameter (D) of 27.8 G (Figure 4a,b). This value is in the same range (26–29 G) as that observed for other triplet biradicals of pyrrolidine-functionalised C_{60} derivatives in C_{60} –bridge– C_{60} triads [15,28] and gives an average distance of 10 Å between the unpaired electrons [16], a distance well within the range predicted by models of **4** (Figure S4b, Supporting Information File 1). The half-field signal corresponding to the triplet state is not observed which is also consistent with previous reports for fulleride based triplets [30]. The presence of an intramolecular triplet would indicate that the distance between the two fulleropyrrolidine units is short enough to allow through-space interaction despite the lack of electronic conjugation between the interacting units. In addition to the intramolecular triplet, a set of inner features is tentatively assigned to an intermolecular (or “powder”) triplet ($D = 7.9$ G) that may result from the aggregation of 4^{2-} molecules in the frozen solution however we do not exclude other possible assignments [31].

The frozen solution EPR spectrum of 1^{2-} displays a central feature at $g = 2.0003$, consistent with that of a doublet biradical (Figure 4c) that is flanked on each side by broad “wings” that we assign to the presence of an intermolecular triplet and give a maximum D value of 9 G which is similar to that observed in the spectrum of 4^{2-} . The same “wings” around the central feature ($g = 2.0000$) have been observed in the EPR spectra of the one electron reduced species of the monomer **7** (Figure S7, Supporting Information File 1) and hence may be explained by intermolecular interactions. Also present are small baseline features (Figure 4d) that may represent the outer features of either an intramolecular or intermolecular triplet. We note similar small baseline features in the spectrum of 7^{1-} ; in this case their assignment to an intramolecular triplet must be excluded. Hence, by changing the linker from oxalate in 4^{2-} to terephthalate in 1^{2-} we have either reduced the interaction of the spin centres or significantly perturbed the formation of an intramolecular triplet biradical.

The EPR spectra of the C_{70} containing compounds **6** $^{2-}$ and **8** $^{1-}$ (Figure S8, Supporting Information File 1) in fluid solution recorded at room temperature (Figure S8a, Supporting Informa-

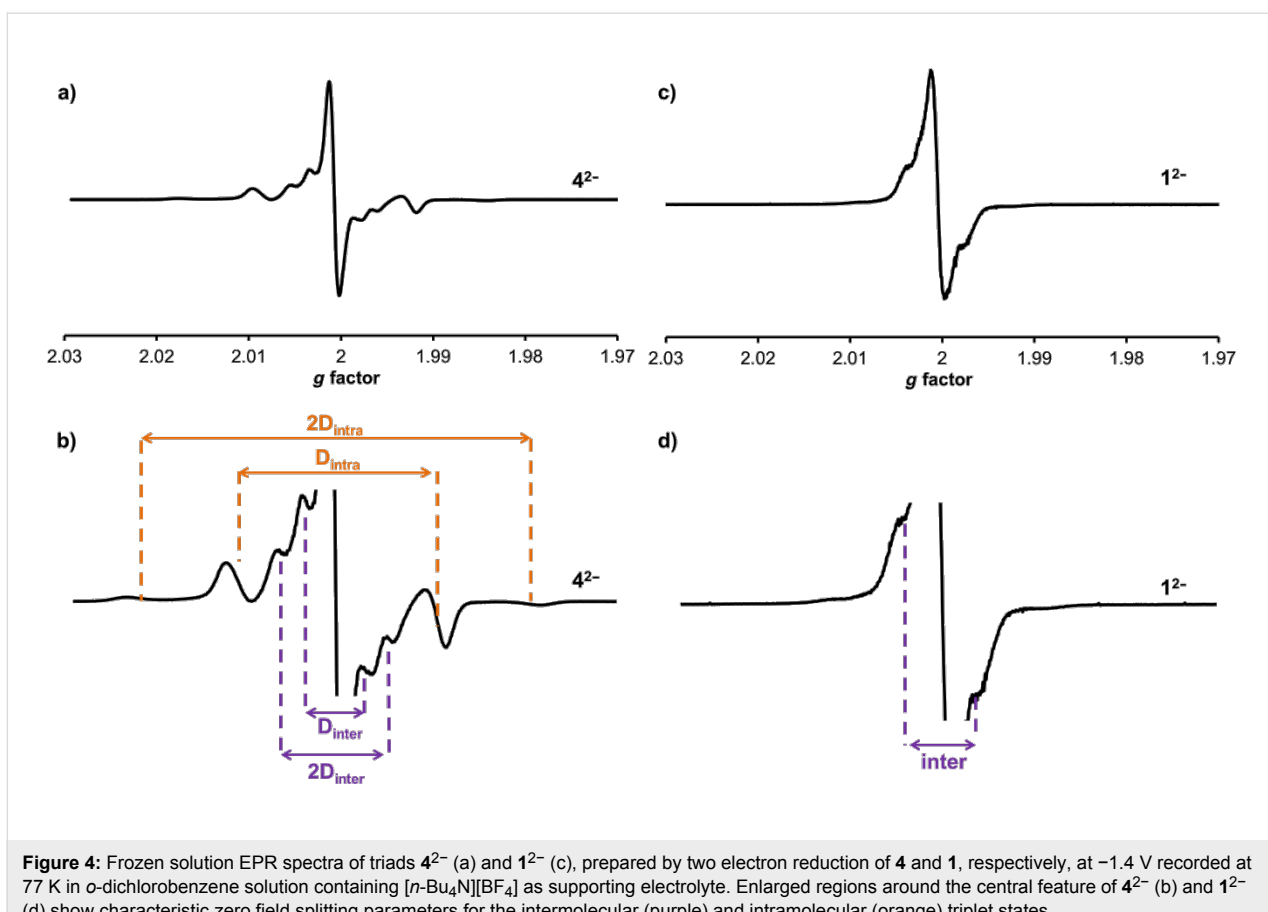


Figure 4: Frozen solution EPR spectra of triads 4^{2-} (a) and 1^{2-} (c), prepared by two electron reduction of **4** and **1**, respectively, at -1.4 V recorded at 77 K in *o*-dichlorobenzene solution containing $[n\text{-Bu}_4\text{N}][\text{BF}_4]$ as supporting electrolyte. Enlarged regions around the central feature of 4^{2-} (b) and 1^{2-} (d) show characteristic zero field splitting parameters for the intermolecular (purple) and intramolecular (orange) triplet states.

tion File 1) and particularly in frozen solution recorded at 77 K (Figure S8b, Supporting Information File 1) are significantly different from those observed for the reduced C_{60} containing compounds. The difference is due to the lower symmetry of the C_{70} (D_{5h} compared to I_h of the C_{60}) which results in an anisotropic spectrum [30]. In addition, due to this asymmetry the spectra are significantly broader which means that any features corresponding to the triplet biradicals will overlap with the main central features and hence are not resolved. This complicates the assignment of the spin states in the C_{70} containing compounds and hence they were not investigated further in this study.

Conclusion

We have developed a synthetic methodology for a range of linear, soluble fullerene triads where the nature of the fullerene cage and the length of the bridge between the cages can be controlled. Cyclic voltammetry measurements demonstrate the high electron accepting capacity of these molecules, which can accept up to six electrons reversibly, but indicate no interactions between the fullerene cages in the ground state of the triads, regardless of the nature of the fullerene (C_{60} or C_{70}) or the length of the bridge (oxalate or terephthalate). The first and

second reduction potentials of C_{60} and C_{70} in the asymmetric triads appear to be indistinguishable, whilst the third reduction of the two fullerene cages is observed as two separate one-electron processes with the reduction potential being slightly less cathodic for the C_{70} cage. EPR spectroscopy measurements of the two electron reduced triads reveal that the nature of the intramolecular electron spin–spin interactions is dependent on the length of the bridge. Specifically, the two electron reduced oxalate bridged triad, where the fullerene cages are separated by a minimum distance of 12 Å, can exhibit strong intramolecular spin coupling with a D value of 27.8 G. Under the same conditions the triad with the terephthalate bridge, where fullerene cages are separated by a minimum distance of over 16 Å, does not show similar strong intramolecular spin coupling and may exist mainly as an independent doublet biradical. Our methodology enables precise control of the inter-fullerene separation thus providing a mechanism for controlling the spin properties of fullerene triads which is important for the future development of molecular electronic and spintronic devices.

Experimental

C_{60} (99.5%) and C_{70} (95%) were purchased from SES Research and MER corporation respectively. CH_2Cl_2 was freshly distilled

over CaH_2 before use. All other reagents and solvents were purchased from Aldrich and used without further purification. Compounds **1–3** and **7–10** were synthesised according to previously reported procedure [20]. Infra-red spectra were measured as KBr discs using a Nicolet Avatar 380 FTIR spectrometer over the range 400–4000 cm^{-1} . ^1H and ^{13}C NMR spectra were obtained using Bruker DPX 300, Bruker DPX 400, Bruker AV(III) 400 or Bruker AV(III) 500 spectrometers. Mass spectrometry was carried out using a Bruker microTOF spectrometer and a Bruker ultraFlexIII MALDI–TOF spectrometer using trans-2-[3-(4-*tert*-butylphenyl)-2-methyl-2-propenylidene]malononitrile (DCTB) as supporting matrix. UV–vis spectra were measured using a Lambda 25 Perkin Elmer Spectrometer. EPR spectra were obtained on a Bruker EMX EPR spectrometer.

Cyclic voltammetry

Cyclic voltammetric studies were carried out using an Autolab PGSTAT20 potentiostat, using a three-electrode arrangement in a single compartment cell. A glassy carbon working electrode, a Pt wire secondary electrode and a saturated calomel reference electrode (chemically isolated from the test solution via a bridge tube containing electrolyte solution and fitted with a porous Vycor frit) were used in the cell. Experiments were performed under an atmosphere of argon and in anhydrous solvents. Sample solutions were prepared under an atmosphere of argon using Schlenk line techniques and consisted of a 0.2 M $[\text{n-Bu}_4\text{N}][\text{BF}_4]$ solution as the supporting electrolyte and a 0.5 mM solution of the test compound. Redox potentials were referenced vs the Fc^+/Fc couple, which was used as an internal standard. Compensation for internal resistance was not applied.

Bulk electrolysis

Bulk electrolysis experiments at a controlled potential were carried out using a two-compartment cell. A Pt/Rh gauze basket working electrode was separated from a wound Pt/Rh gauze secondary electrode by a glass frit. A saturated calomel electrode was bridged to the test solution through a Vycor frit that was orientated at the centre of the working electrode. The working electrode compartment was fitted with a magnetic stirrer bar and the test solution was stirred rapidly during electrolysis. Each solution contained $[\text{n-Bu}_4\text{N}][\text{BF}_4]$ (0.2 M) as the supporting electrolyte and the compound under investigation (5 mL, 0.5 mM) and were prepared using Schlenk line techniques.

Synthesis of the fullerene triads **4–6**

Synthesis of **4**

[60]Fulleropyrrolidine **9** (35 mg, 0.045 mmol) was suspended in freshly distilled CH_2Cl_2 (35 mL) with 4-dimethylaminopyridine (17 mg, 0.139 mmol) and pyridine (0.35 mL), and the reaction

mixture was stirred for 10 min. Oxalyl chloride (0.1 mL, 1.16 mmol) was then added, and the reaction mixture stirred at room temperature for 2 h. On removal of solvent, the resulting residue was dissolved in CS_2 (40 mL) by sonication, and any undissolved material removed by filtration. The filtrate was concentrated and purified by column chromatography (silica gel, *o*-dichlorobenzene/isopropyl alcohol 99.5:0.5) to give the product which was washed with MeOH (30 mL), petroleum ether 40–60 (30 mL) and diethyl ether (30 mL). The resultant solid was dried under vacuum to give the product (16 mg, 44%) as a brown solid. ^1H NMR (400 MHz, 297 K, $\text{CS}_2/\text{CDCl}_3$, δ , ppm) 5.79 (s, 4H, CH_2), 5.69 (s, 4H, CH_2); ^{13}C NMR (125 MHz, 297 K, $\text{CS}_2/\text{CDCl}_3$, δ , ppm) 160.97 (CO), 153.09, 152.74, 147.47, 146.46, 146.44, 146.26, 146.24, 145.80, 145.72, 145.46, 145.43, 145.40, 145.38, 144.59, 144.46, 143.21, 142.83, 142.80, 142.30, 142.23, 142.21, 142.16, 142.07, 142.05, 140.50, 140.40, 135.97, 135.76, 133.02, 130.61, 128.44, 127.69 (sp^2 carbons, 31 environments), 70.85, 69.31, 60.22, 57.07 (sp^3 carbons, 4 environments); MALDI–TOF MS (DCTB/MeCN, *m/z*): 1580.2 (M^-); IR (KBr, ν , cm^{-1}): 2960 (w), 2922 (w), 1645 (s), 1453 (w), 1328 (m), 1186 (m), 746 (m), 526 (s); UV–vis (CS_2): λ_{max} ($\epsilon \times 10^{-3}/\text{dm}^3 \text{ mol}^{-1} \text{ cm}^{-1}$): 703 (0.750), 433 (8.526).

Synthesis of **6**

[70]Fulleropyrrolidine **10** (20 mg, 0.023 mmol) was suspended in CH_2Cl_2 (18 mL), and DMAP (8.7 mg, 0.071 mmol) and pyridine (0.2 mL) were added. The reaction mixture was stirred for 10 min and oxalyl chloride (0.055 mL, 0.64 mmol) was added. The reaction mixture was stirred at room temperature for 2 h, and the solvent was then removed. The resulting residue dissolved in CS_2 (40 mL) by sonication, and the undissolved material removed by filtration. The filtrate was concentrated and purified by column chromatography (silica gel, *o*-dichlorobenzene/isopropyl alcohol 99.5:0.5) to give the product which was washed with MeOH (30 mL) and petroleum ether 40–60 (30 mL). The resultant material was dried under vacuum to give the product (9 mg, 22%) as a brown solid. ^1H NMR (400 MHz, 297 K, $\text{CS}_2/\text{CDCl}_3$, δ , ppm) 5.25–4.36 (m, 8H, CH_2); ^{13}C NMR (125 MHz, 297 K, $\text{CS}_2/\text{CDCl}_3$, δ , ppm) 168.90 (C=O), 167.43 (C=O), 156.55, 156.13, 155.02, 154.96, 154.11, 152.17, 151.56, 151.42, 151.35, 151.07, 151.01, 151.00, 150.96, 150.94, 150.78, 150.71, 150.41, 150.37, 149.93, 149.89, 149.85, 149.79, 149.47, 149.40, 149.36, 149.31, 149.26, 149.11, 149.07, 149.03, 148.79, 148.45, 148.10, 148.06, 147.88, 147.46, 147.21, 147.10, 147.08, 147.05, 147.00, 146.96, 146.93, 146.64, 146.62, 146.57, 145.84, 145.71, 145.53, 145.41, 145.00, 144.90, 144.84, 144.50, 144.48, 144.23, 144.20, 144.16, 144.12, 144.08, 143.48, 143.43, 143.32, 143.26, 143.18, 143.10, 141.43, 140.32, 140.30, 140.27, 137.28, 133.76, 133.72, 133.68, 132.41, 132.13, 131.38, 131.28, 131.25, 128.40 (sp^2 carbons, 80 environments), 71.84, 69.68, 68.74, 64.10, 62.67, 62.63 (sp^3 carbons, 6 environments).

ronments); MALDI–TOF MS (DCTB/MeCN, *m/z*): 1820.5; IR (KBr, ν , cm^{-1}): 2932 (m), 2363 (s), 1663 (s, C=O), 1435 (m), 669 (s); UV–vis (CS₂): λ_{max} ($\epsilon \times 10^{-3}/\text{dm}^3 \text{ mol}^{-1} \text{ cm}^{-1}$): 693 (3.74), 556 (20.32), 476 (39.28), 462 (39.60), 411 (48.49).

Synthesis of 5

Compound **15** (16 mg, 0.018 mmol), [70]fulleropyrrolidine **10** (16 mg, 0.019 mmol) and dicyclohexylcarbodiimide (3.9 mg, 0.019 mmol) were suspended in anhydrous *o*-dichlorobenzene (2.7 mL) and stirred at room temperature under an Ar atmosphere for 17 h. The reaction mixture was purified by column chromatography (silica gel, *o*-dichlorobenzene) to afford the product which was washed with MeOH (30 mL) and petroleum ether (30 mL) to give the product (9 mg, 27%) as a dark brown solid. Isomer **a** (see Supporting Information File 1): ¹H NMR (400 MHz, 297 K, CS₂/CDCl₃, δ , ppm) 5.47 (s, 4H, CH₂), 5.28 (m, 2H, CH₂), 4.77 (s, 2H, CH₂), 4.66 (s, 2H, CH₂); Isomer **b** (see Supporting Information File 1): ¹H NMR (400 MHz, 297 K, CS₂/CDCl₃, δ , ppm) 5.63 (s, 1H), 4.97 (m, 1H), 4.88 (s, 1H), 4.61 (m, 2H), 4.27 (s, 2H), 4.16 (s, 1H), 4.11 (m, 2H); ¹³C NMR (125 MHz, 297 K, CS₂/CDCl₃, δ , ppm) 165.69 (C=O), 155.45, 155.16, 155.07, 154.23, 153.30, 153.19, 151.74, 151.38, 151.21, 151.19, 150.92, 150.79, 150.74, 150.66, 149.91, 149.89, 149.81, 149.36, 149.35, 149.32, 149.24, 149.09, 148.78, 148.44, 148.13, 147.61, 147.41, 147.21, 146.94, 146.36, 146.18, 146.15, 145.94, 145.89, 145.57, 145.40, 145.31, 144.64, 144.60, 143.45, 143.22, 143.07, 142.78, 142.18, 142.03, 140.60, 140.38, 139.15, 137.17, 134.25, 133.75, 132.92 (sp² carbons, 52 environments), 74.22, 73.26, 70.50, 68.18, 68.14, 64.51, 63.11 (sp³ carbons, 7 environments); MALDI–TOF MS (DCTB/MeCN, *m/z*): 1686.3; IR (KBr, ν , cm^{-1}): 2926 (s), 2365 (s), 1674 (s, C=O), 1433 (m), 1250 (m), 1182 (m), 1119 (m), 671 (w), 527 (m); UV–vis (CS₂): λ_{max} ($\epsilon \times 10^{-3}/\text{dm}^3 \text{ mol}^{-1} \text{ cm}^{-1}$): 693 (2.51), 556 (11.83), 479 (22.00), 456 (22.91), 430 (22.48), 410 (30.38).

Oxalic acid monobenzyl ester monochloride [22]

Oxalyl chloride (1 mL) was cooled to 0 °C, and anhydrous benzyl alcohol (1.4 mL) added dropwise over 15 min. After the addition of the alcohol was completed, the reaction mixture was warmed up to room temperature and stirred for 1.5 h. The resulting mixture was analysed by ¹H and ¹³C NMR spectroscopy and found to be a mixture of the oxalic acid monobenzyl ester monochloride and the dibenzyl oxalate in a 5:1 molar ratio. The mixture was used in the next step immediately without further purification. ¹H NMR (300 MHz, 297 K, CDCl₃, δ , ppm) 7.47–7.42 (m, 5H), 7.42–7.38 (m, 1.75 H), 5.38 (s, 2H), 5.32 (s, 0.72 H); ¹³C NMR (75 MHz, 297 K, CDCl₃, δ , ppm) 160.95, 157.57, 155.53, 134.18, 133.33, 129.35, 128.91, 128.78, 128.74, 70.38, 68.63.

[60]Fulleropyrrolidine oxalate benzyl ester **11**

[60]Fulleropyrrolidine **9** (70 mg, 0.092 mmol) was suspended in freshly distilled CH₂Cl₂ and DMAP (50 mg, 0.41 mmol) and pyridine (0.3 mL) added. The mixture was stirred for 10 min at room temperature, and oxalyl acid monobenzyl ester monochloride (100 mg, 0.50 mmol) was added, and the mixture left to stir at room temperature for 2 h. The solvent was removed, the resulting residue dissolved in CS₂ (10 mL) and filtered to remove insoluble materials. The filtrate was then concentrated and purified by column chromatography (silica gel, toluene) to afford the product which was washed with MeOH (40 mL) and petroleum ether (40 mL) and dried in vacuum to give compound **11** as black powder (58 mg, 68%). ¹H NMR (400 MHz, 297 K, CDCl₃/CS₂, δ , ppm) 7.47 (d, J = 6.3 Hz, 2H), 7.35 (m, 3H), 5.51 (s, 2H), 5.45 (s, 4H); ¹³C NMR (125 MHz, 297 K, CDCl₃/CS₂, δ , ppm) 160.85 (C=O), 157.49 (C=O), 153.01, 152.57, 147.50, 147.44, 146.49, 146.44, 146.26, 146.24, 145.80, 145.76, 145.61, 145.46, 145.45, 145.43, 145.31, 144.62, 144.51, 143.22, 142.83, 142.82, 142.25, 142.18, 142.10, 142.03, 140.46, 140.32, 137.51, 136.25, 135.94, 134.60, 129.15, 128.99, 128.96, 128.66, 128.44, 128.42, 125.53 (sp² carbons, 37 environments), 70.67, 69.09, 67.99, 59.35, 57.16 (sp³ carbons, 5 environments); MALDI–TOF MS (DCTB/MeCN, *m/z*): 924.1 (M⁺); IR (KBr, ν , cm^{-1}): 2924 (m), 2362 (m), 1718 (s, C=O), 1671 (s, C=O), 1438 (m), 1125 (s), 527 (s).

Synthesis of 12

Compound **11** (5 mg) was dissolved in freshly distilled CH₂Cl₂ (5 mL), and CF₃SO₃H (0.05 mL) added. The resulting mixture was stirred for 1 h at room temperature after which the solvent was removed under vacuum and the resultant brown solid was suspended in diethyl ether (10 mL). The precipitate was separated by centrifugation, the ether removed by decantation, and this procedure was repeated three times. The resultant brown solid was dried under vacuum to give the product, **12** (4 mg, 95%) as a brown solid. MALDI–TOF MS (DCTB/MeCN, *m/z*): 791.2 (M⁺); IR (KBr, ν , cm^{-1}): 3446 (s, NH), 2964 (m), 2360 (m), 1636 (s, C=O), 1507 (m), 1384 (s), 1216 (m), 527 (m).

Synthesis of 13 [24]

NaI (5.3 g, 34 mmol) was suspended in acetone (15 mL) and heated under reflux for 5 min. The mixture was cooled to room temperature, and benzyl bromoacetate (1 mL, 6.3 mmol) added. The reaction mixture was stirred at room temperature for 2 h and the solvent removed under vacuum. The resulting mixture was partitioned between water (20 mL) and ethyl acetate (10 mL). The organic fraction was separated, washed with a saturated solution of Na₂S₂O₃ (2 × 10 mL) followed by brine (10 mL) and dried over Na₂SO₄. The solvent was removed to give the product (1.57 g, 90%) as a yellow oil; ¹H NMR

(300 MHz, 297 K, CDCl_3 , δ , ppm) 7.40 (s, 5H), 5.20 (s, 2H), 3.76 (s, 2H); ^{13}C NMR (75 MHz, 297 K, CDCl_3 , δ , ppm) 168.60 (C=O), 135.14, 128.65, 128.54, 128.33, 67.81 (-CH₂-O-), -5.51 (-CH₂I); ESIMS (MeOH, m/z): 298.95 (M + Na)⁺.

Synthesis of 14

To a solution of [60]fulleropyrrolidine **9** (110 mg, 0.144 mmol) in dry DMF (30 mL) benzyliodoacetate (150 mg) was added, and the resulting mixture heated to 100 °C for 1 h. The solvent was then removed under vacuum, and the resulting solid purified by column chromatography (silica gel, eluted with CS₂, followed by CS₂/toluene 1:1 v/v). The product was washed with MeOH (40 mL) and the resultant solid was dried in vacuum to give compound **14** as a black powder (80 mg, 61%). ^1H NMR (400 MHz, 297 K, $\text{CDCl}_3/\text{CS}_2$, δ , ppm) 7.49 (d, J = 6.8 Hz, 2H), 7.42 (m, 3H), 5.37 (s, 2H), 4.68 (s, 2H), 4.09 (s, 2H); ^{13}C NMR (125 MHz, 297 K, $\text{CDCl}_3/\text{CS}_2$, δ , ppm) 169.31 (C=O), 154.61, 147.37, 146.33, 146.14, 146.03, 145.74, 145.56, 145.36, 144.62, 143.18, 142.72, 142.28, 142.16, 141.98, 140.26, 136.39, 135.64, 135.22, 128.81, 128.62, 128.53, 128.37 (sp^2 carbons, 22 environments), 70.58, 67.05, 66.78, 54.84 (sp^3 carbons, 4 environments); MALDI-TOF MS (DCTB/MeCN m/z): 911.5 (M⁺); IR (KBr, ν , cm⁻¹): 2962 (w), 2359 (w), 1736 (s, C=O), 1393 (m), 1344 (m), 1095 (s), 737 (m), 527 (s).

Synthesis of 15

To a solution of **14** (5 mg, 0.0055 mmol) in dry CH_2Cl_2 (5 mL) $\text{CF}_3\text{SO}_3\text{H}$ (0.05 mL) was added and the mixture was stirred for 2 h at room temperature. The solvent was removed under vacuum and the resultant brown solid suspended in diethyl ether (10 mL). The precipitate was separated by centrifugation, the ether removed, and this procedure was repeated three times. The resultant brown solid was dried in vacuum to give the product, **15** (4.2 mg, 90%); MALDI-TOF MS (DCTB/MeCN, m/z): 821.2 (M⁺); IR (KBr, ν , cm⁻¹): 3446 (s, OH), 2957 (w), 2361 (w), 1732 (m, C=O), 1483 (m), 1170 (m), 746 (m), 527 (s).

Supporting Information

Supporting Information File 1

Additional spectra.

[<http://www.beilstein-journals.org/bjoc/content/supplementary/1860-5397-10-31-S1.pdf>]

Acknowledgements

We thank the European Research Council, the EPSRC, the Royal Society and the University of Nottingham for financial support of this work.

References

- Popov, A.; Yang, S.; Dunsch, L. *Chem. Rev.* **2013**, *113*, 5989–6113. doi:10.1021/cr300297r
- Harneit, W. *Phys. Rev. A* **2002**, *65*, 032322. doi:10.1103/PhysRevA.65.032322
- Ardavan, A.; Blundell, S. J. *J. Mater. Chem.* **2009**, *19*, 1754–1760. doi:10.1039/b809525f
- Liu, G.; Khlobystov, A. N.; Charalambidis, G.; Coutsolelos, A. G.; Briggs, G. A. D.; Porfyrakis, K. *J. Am. Chem. Soc.* **2012**, *134*, 1938–1941. doi:10.1021/ja209763u
- Farrington, B. J.; Jevric, M.; Rance, G. A.; Ardavan, A.; Khlobystov, A. N.; Briggs, G. A. D.; Porfyrakis, K. *Angew. Chem., Int. Ed.* **2012**, *51*, 3587–3590. doi:10.1002/anie.201107490
- Hörmann, F.; Hirsch, A.; Porfyrakis, K.; Briggs, G. A. D. *Eur. J. Org. Chem.* **2011**, 117–121. doi:10.1002/ejoc.201000867
- Plant, S. R.; Jevric, M.; Morton, J. J. L.; Ardavan, A.; Khlobystov, A. N.; Briggs, G. A. D.; Porfyrakis, K. *Chem. Sci.* **2013**, *4*, 2971–2975. doi:10.1039/c3sc50395j
- Kanai, M.; Porfyrakis, K.; Briggs, G. A. D.; Dennis, T. J. S. *Chem. Commun.* **2004**, 210–211. doi:10.1039/b310979h
- Echegoyen, L.; Echegoyen, L. E. *Acc. Chem. Res.* **1998**, *31*, 593–601. doi:10.1021/ar970138v
- Chamberlain, T. W.; Davies, E. S.; Khlobystov, A. N.; Champness, N. R. *Chem.–Eur. J.* **2011**, *17*, 3759–3767. doi:10.1002/chem.201003092
- Segura, J. L.; Martín, N. *Chem. Soc. Rev.* **2000**, *29*, 13–25. doi:10.1039/a903716k
- Komatsu, K.; Wang, G.-W.; Murata, Y.; Tanaka, T.; Fujiwara, K.; Yamamoto, K.; Saunders, M. *J. Org. Chem.* **1998**, *63*, 9358–9366. doi:10.1021/jo981319t
- Lebedkin, S.; Ballenweg, S.; Gross, J.; Taylor, R.; Krätschmer, W. *Tetrahedron Lett.* **1995**, *36*, 4971–4974. doi:10.1016/0040-4039(95)00784-A
- Jin, X.; Xie, X.; Tang, K. *Chem. Commun.* **2002**, 750–751. doi:10.1039/b200793b
- Sánchez, L.; Herranz, M. Á.; Martín, N. *J. Mater. Chem.* **2005**, *15*, 1409–1421. doi:10.1039/b417580h
- Sastre-Santos, A.; Parejo, C.; Martín-Gomis, L.; Ohkubo, K.; Fernández-Lázaro, F.; Fukuzumi, S. *J. Mater. Chem.* **2011**, *21*, 1509–1515. doi:10.1039/c0jm02635b
- Gerson, F.; Huber, W. *Electron Spin Resonance Spectroscopy of Organic Radicals*; Wiley-VCH: Weinheim, 2003. doi:10.1002/3527601627
- Chamberlain, T. W.; Pfeiffer, R.; Peterlik, H.; Kuzmany, H.; Zerbetto, F.; Melle-Franco, M.; Staddon, L.; Champness, N. R.; Briggs, G. A. D.; Khlobystov, A. N. *Small* **2008**, *4*, 2262–2270. doi:10.1002/smll.200800552
- de Lucas, A. I.; Martín, N.; Sánchez, L.; Seoane, C. *Tetrahedron Lett.* **1996**, *37*, 9391–9394. doi:10.1016/S0040-4039(97)82972-3
- Lebedeva, M. A.; Chamberlain, T. W.; Schröder, M.; Khlobystov, A. N. *Tetrahedron* **2012**, *68*, 4976–4985. doi:10.1016/j.tet.2012.04.061
- Maggini, M.; Scorrano, G.; Prato, M. *J. Am. Chem. Soc.* **1993**, *115*, 9798–9799. doi:10.1021/ja00074a056
- Duan, H.-F.; Xie, J.-H.; Qiao, X.-C.; Wang, L.-X.; Zhou, Q.-L. *Angew. Chem., Int. Ed.* **2008**, *47*, 4351–4353. doi:10.1002/anie.200800423
- Wallach, L.; Lehmann, F. *Justus Liebigs Ann. Chem.* **1887**, *237*, 236–260. doi:10.1002/jlac.18872370205

24. Wagner, R.; Rhoades, T. A.; Or, Y. S.; Lane, B. C.; Hsieh, G.; Mollison, K. W.; Luly, J. R. *J. Med. Chem.* **1998**, *41*, 1764–1776. doi:10.1021/jm960066y
25. Balch, A. L.; Costa, D. A.; Fawcett, W. R.; Winkler, K. *J. Phys. Chem.* **1996**, *100*, 4823–4827. doi:10.1021/jp953144m
26. Lee, K.; Song, H.; Kim, B.; Park, J. T.; Park, S.; Choi, M.-G. *J. Am. Chem. Soc.* **2002**, *124*, 2872–2873. doi:10.1021/ja017496k
27. Zanello, P.; de Biani, F. F.; Cinquantini, A.; Grigiotti, E. *C. R. Chim.* **2005**, *8*, 1655–1659. doi:10.1016/j.crci.2005.03.011
28. Brustolon, M.; Zoleo, A.; Agostini, G.; Maggini, M. *J. Phys. Chem. A* **1998**, *102*, 6331–6339. doi:10.1021/jp981385z
29. Sun, Y.; Drovetskaya, T.; Bolskar, R. D.; Bau, R.; Boyd, P. D. W.; Reed, C. A. *J. Org. Chem.* **1997**, *62*, 3642–3649. doi:10.1021/jo970357u
30. Dubois, D.; Jones, M. T.; Kadish, K. M. *J. Am. Chem. Soc.* **1992**, *114*, 6446–6451. doi:10.1021/ja00042a023
31. Mori, N.; Fukui, K.; Nakazawa, S.; Takekuma, S.; Takekuma, H.; Yoshida, Z.; Sato, K.; Shiomi, D.; Takui, T. *Synth. Met.* **2003**, *137*, 1315–1316. doi:10.1016/S0379-6779(02)01003-2

License and Terms

This is an Open Access article under the terms of the Creative Commons Attribution License (<http://creativecommons.org/licenses/by/2.0>), which permits unrestricted use, distribution, and reproduction in any medium, provided the original work is properly cited.

The license is subject to the *Beilstein Journal of Organic Chemistry* terms and conditions: (<http://www.beilstein-journals.org/bjoc>)

The definitive version of this article is the electronic one which can be found at:
doi:10.3762/bjoc.10.31



Polyglycerol-functionalized nanodiamond as a platform for gene delivery: Derivatization, characterization, and hybridization with DNA

Li Zhao¹, Yuki Nakae², Hongmei Qin¹, Tadamasa Ito³, Takahide Kimura¹,
Hideto Kojima², Lawrence Chan⁴ and Naoki Komatsu^{*1,§}

Full Research Paper

Open Access

Address:

¹Department of Chemistry, Shiga University of Medical Science, Seta, Otsu 520-2192, Japan, ²Department of Stem Cell Biology and Regenerative Medicine, Shiga University of Medical Science, Seta, Otsu 520-2192, Japan, ³Department of Materials Science and Engineering, Faculty of Science and Technology, Meijo University, Tempaku, Nagoya 468-8502, Japan and ⁴Departments of Medicine, and Molecular and Cellular Biology, Baylor College of Medicine, Houston, Texas 77030, USA

Email:

Naoki Komatsu^{*} - nkomatsu@belle.shiga-med.ac.jp

* Corresponding author

§ Telephone number: +81-77-548-2102; Fax number: +81-77-548-2405

Keywords:

carbon-nanomaterials; click chemistry; DNA; gene delivery; nanodiamond; polyglycerol; polypeptides

Beilstein J. Org. Chem. **2014**, *10*, 707–713.

doi:10.3762/bjoc.10.64

Received: 12 October 2013

Accepted: 04 March 2014

Published: 24 March 2014

This article is part of the Thematic Series "Functionalized carbon-nanomaterials".

Guest Editor: A. Krueger

© 2014 Zhao et al; licensee Beilstein-Institut.

License and terms: see end of document.

Abstract

A gene vector consisting of nanodiamond, polyglycerol, and basic polypeptide (ND-PG-BPP) has been designed, synthesized, and characterized. The ND-PG-BPP was synthesized by PG functionalization of ND through ring-opening polymerization of glycidol on the ND surface, multistep organic transformations ($-\text{OH} \rightarrow -\text{OTs}$ (tosylate) $\rightarrow -\text{N}_3$) in the PG layer, and click conjugation of the basic polypeptides (Arg₈, Lys₈ or His₈) terminated with propargyl glycine. The ND-PG-BPP exhibited good dispersibility in water (>1.0 mg/mL) and positive zeta potential ranging from +14.2 mV to +44.1 mV at neutral pH in Milli-Q water. It was confirmed by gel retardation assay that ND-PG-Arg₈ and ND-PG-Lys₈ with higher zeta potential hybridized with plasmid DNA (pDNA) through electrostatic attraction, making them promising as nonviral vectors for gene delivery.

Introduction

A variety of nanoparticles have been investigated as nonviral vectors in drug and gene delivery systems [1,2]. Among these nanoparticles, nanodiamond (ND) has attracted a great deal of

attention due to its high chemical stability, low toxicity, and large specific surface area [3–6]. In addition, various functions can be added to ND through organic reactions on the ND

surface [4,5,7-11]. In this sense, ND has an advantage over non-carbonaceous nanomaterials, because the methodology in synthetic organic chemistry can be applied to the ND surface, which is covered with organic functional groups [12]. Quite recently, we found that ring-opening polymerization of glycidol is initiated at the oxygen-containing functionalities, hydroxy and carboxy groups, on the ND surface to give polyglycerol (PG) grafted ND with 30 nm size (ND30-PG) [13]. The resulting ND30-PG exhibited very good dispersibility not only in water (>20 mg/mL), but also in phosphate buffered saline (PBS) (>16 mg/mL), making the *in vivo* use of ND more promising in biomedical applications. In addition, the good dispersibility and a large number of hydroxy groups of ND-PG enable further surface functionalization to add more functions to ND [14].

As for gene delivery, on the other hand, DNA was immobilized on the surface of nanoparticles mostly by electrostatic attraction between the negative charge of DNA and the positive charge on the surface of the nanoparticle [15]. In the case of ND, for example, basic polypeptides [16], polyamine polymer [17], primary and tertiary amines [17,18], and quaternary ammonium salts [19] were employed to coat ND covalently or noncovalently as positively charged ligands for DNA immobilization. Although the functionalized ND is proven to immobilize DNA, more functions such as enough dispersibility

and targeting efficacy are required to use ND *in vivo* as a gene vector. Therefore, a more reliable and general process is desired to add sufficient functions for ND-based gene vectors. Herein a conjugation of ND-PG with basic polypeptides (Arg₈, Lys₈ and His₈) through click chemistry followed by hybridization with plasmid DNA (pDNA) and its characterization by electrophoresis is reported.

Results and Discussion

Preparation and characterization of ND50-PG

In view of actual cancer therapy utilizing the enhanced permeation and retention (EPR) effect, ND with 50 nm size was chosen for this study. The ND50 was covalently functionalized with hyperbranched PG through ring-opening polymerization of glycidol according to the procedure we reported previously [13]. The resulting ND50-PG was characterized qualitatively by FTIR and ¹H NMR, and quantitatively by TGA. The IR (Figure 1a) and NMR spectra (Figure 2a) of ND50-PG are almost the same as those of ND30-PG [13], proving the PG grafting on the ND50. In addition, PG:ND weight ratio of ND50-PG (37:63) is almost the same as that of ND30-PG (40:60) in TGA (Figure 3), though ND50 has a smaller specific surface area than ND30. Accordingly, the dispersibility (>20 mg/mL) of ND50-PG in water is almost the same as that of ND30-PG [13]. However, ND5-PG showed an opposite weight ratio (PG:ND = 78:22), though IR and NMR spectra

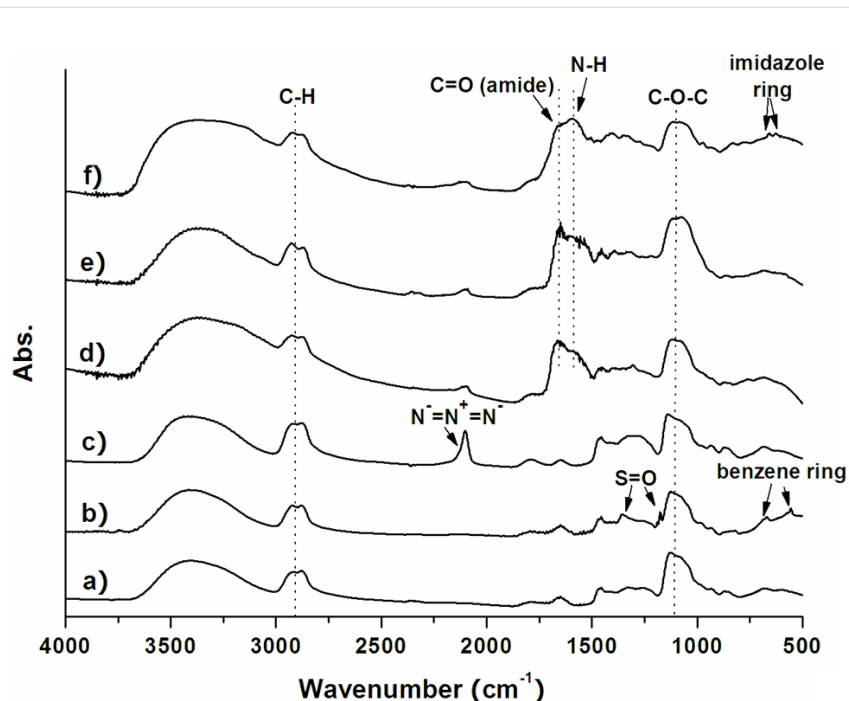


Figure 1: FTIR spectra of a) ND50-PG, b) ND-PG-OTs, c) ND-PG-N₃, d) ND-PG-Arg₈, e) ND-PG-Lys₈, and f) ND-PG-His₈. Arrows indicate new absorption bands in each step.

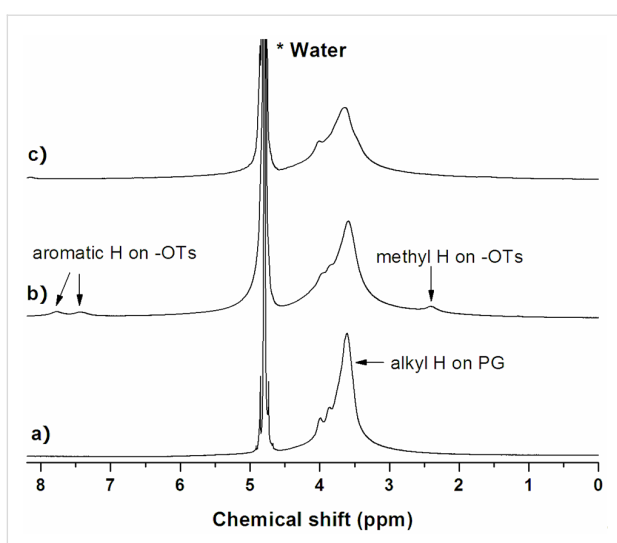


Figure 2: ^1H NMR spectra of a) ND50-PG, b) ND-PG-OTs and c) ND-PG- N_3 in D_2O .

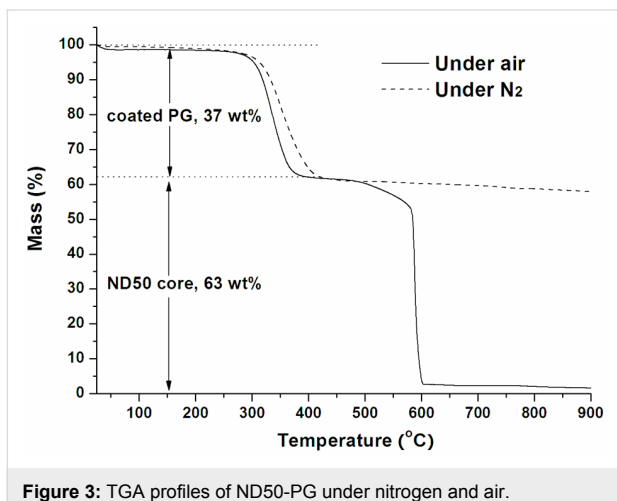


Figure 3: TGA profiles of ND50-PG under nitrogen and air.

were almost the same as those of ND30-PG and ND50-PG [20]. The much larger weight ratio of the PG layer improved the dispersibility of ND5-PG significantly (>80 mg/mL in PBS), implying that the dispersibility of ND-PG is proportional to the weight ratio of PG to the ND core.

The particle size of ND50 and ND50-PG was measured by STEM and DLS. In contrast to bare ND50 particles that are prone to aggregate (Figure 4a), ND50-PG is individually dispersed as shown in Figure 4b. Moreover, 5–10 nm blank space between the ND particles in the STEM image (Figure 4b) may be attributed to the PG layer on the ND surfaces. The average core diameter and the mean hydrodynamic diameter of ND50-PG were determined to be 52.2 ± 14.4 nm by STEM (Figure 4b) and 66.9 ± 14.8 nm by DLS (Table 1), respectively. Based on the difference of the core and hydrodynamic diameters, the thickness of the PG layer on the ND50-PG was estimated to be ca. 7 nm, which is in agreement with the interparticle distance in the STEM image (Figure 4b) as mentioned above.

Table 1: Hydrodynamic diameter and zeta potential of nanoparticles in Milli-Q water.

Nanoparticle	Hydrodynamic diameter ^a (nm)	Zeta potential (mV)
ND50	52.8 ± 20.3	-46.7 ± 3.5
ND50-PG	66.9 ± 14.8	-36.8 ± 1.7
ND-PG-Arg ₈	372 ± 105	$+44.1 \pm 1.9$
ND-PG-Lys ₈	176 ± 44	$+38.7 \pm 1.4$
ND-PG-His ₈	195 ± 64	$+14.2 \pm 0.5$

^aMean diameter \pm SD was determined by DLS on the basis of number distribution.

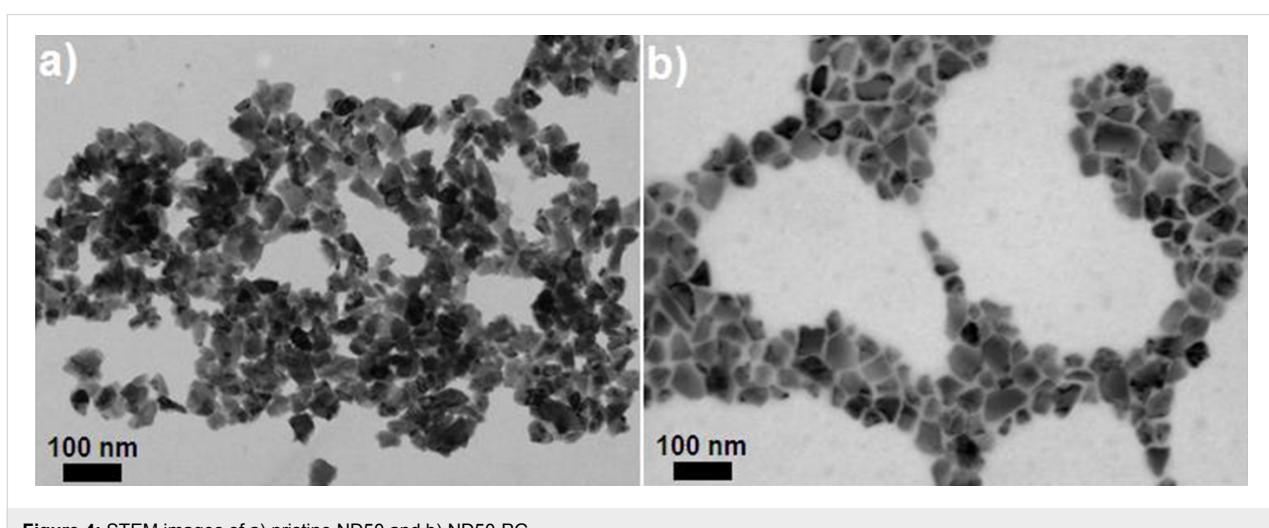


Figure 4: STEM images of a) pristine ND50 and b) ND50-PG.

Immobilization of basic polypeptides through click chemistry

The PG layer including a large number of hydroxy groups endows ND50-PG not only with very high hydrophilicity (Figure 5), but also with a versatile platform for further surface engineering. The synthetic route from ND50-PG to ND-PG-BPP is shown in Scheme 1. Some of the hydroxy groups of ND50-PG were reacted with tosyl chloride (TsCl) in pyridine and the resulting tosylates (ND-PG-OTs) were substituted by azide (ND-PG- N_3). The azido groups reacted with the alkyne group at the end of the polypeptides (click chemistry) to produce ND-PG-BPP [12,21,22].

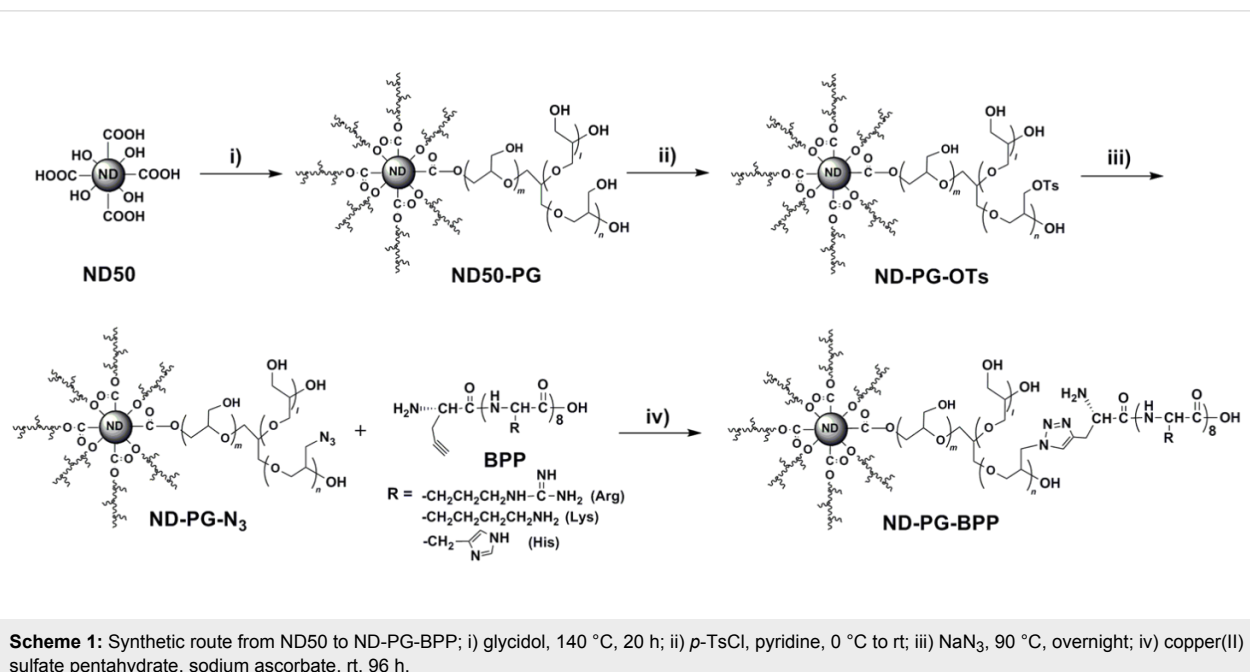
A series of reactions from ND-PG to ND-PG-BPP were monitored by FTIR (Figure 1) [20]. The absorption bands at 1350 cm^{-1} and 1176 cm^{-1} are attributed to asymmetric and symmetric stretchings of $\text{S}\rightarrow\text{O}$ bonds of the tosyl group in ND-PG-OTs, respectively. Another two new absorption bands at 556 and 669 cm^{-1} are assigned to the bending vibrations of aromatic C–H (Figure 1b). The ND-PG- N_3 clearly shows a characteristic strong absorption band at 2100 cm^{-1} corresponding to the azido group (Figure 1c). The azido absorption band disappeared after the click conjugation of the BPP (Figure 1d–f), indicating the complete consumption of azido groups. The immobilization of polypeptides was verified by the absorption bands at 1650 and 1590 cm^{-1} , which correspond to the $\text{C}=\text{O}$ stretching and N–H bending of amide bonds in the polypeptide. In the case of ND-PG-His₈, absorption peaks at 624 and 657 cm^{-1} are attributed to C–H bending of the imidazole rings in the polyhistidine (Figure 1f).

Taking advantage of the good dispersibility of the ND50-PG and their derivatives, they are characterized by solution-phase ^1H NMR (Figure 2). As shown in Figure 2b, the peaks at 7.7 and 7.4 ppm are assigned to the aromatic hydrogens of the tosyl group, and the methyl hydrogens are found at 2.3 ppm . These three peaks of the ND-PG-OTs in Figure 2b disappeared in Figure 2c after the reaction with sodium azide, indicating the complete substitution of the tosyl group.

The hydrodynamic diameter of ND-PG-BPP in water largely increased to more than 150 nm (Table 1), indicating that aggregation occurred in the dispersions. Since ND-PG-BPP has positive charge as will be discussed below, the charges may be connected by some anions to assemble the particles. However, ND-PG-BPP still has dispersibility of $>1.0\text{ mg/mL}$ with less stability (Figure 5).

Zeta potential characterization and pDNA complexation

To analyze the surface charge of the nanoparticles, we measured the zeta potential of ND50, ND50-PG and ND-PG-BPP at neutral pH in Milli-Q water. The results are summarized in Table 1. ND50 showed a relatively high negative zeta potential of $-46.7 \pm 3.5\text{ mV}$ because of a large number of carboxylic groups on the surface. The zeta potential changed to $-36.8 \pm 1.7\text{ mV}$ by PG coating of ND50, probably because some of the carboxylic groups (protic functional groups) are converted to ester (aprotic ones) by initiation of the ring-opening polymerization of glycidol. The immobilization of polypeptides turned the zeta potentials into plus ($-36.8\text{ mV} \rightarrow$



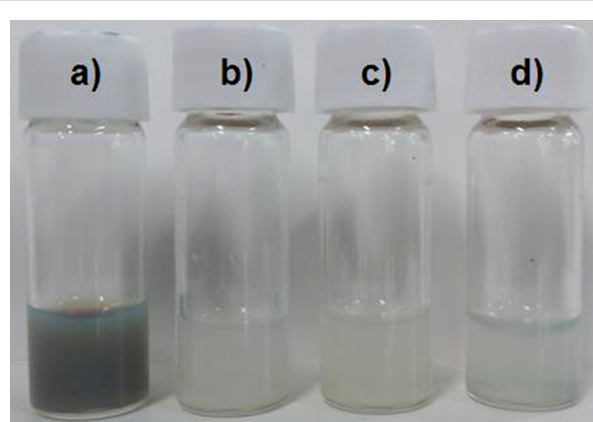


Figure 5: Picture of the dispersions of a) ND50-PG (20 mg/mL), b) ND-PG-Arg₈, c) ND-PG-Lys₈ and d) ND-PG-His₈ (b–d, 1.0 mg/mL) in water.

+14.2 to +44.1 mV) due to the protonation to the basic groups in the peptides; imidazole, amine, and guanidine. These zeta potentials of the ND-PG-BPP are roughly proportional to the pKa values of the side chains in these basic amino acids; His (6.0), Lys (10.5), and Arg (12.5).

The positive surface charge of nanoparticles enables complexation with negatively charged DNA through electrostatic interaction. To analyze the DNA complexation capability of the ND-PG-BPP, we performed an agarose gel retardation assay. The result of the electrophoresis is shown in Figure 6. ND-PG-Arg₈ and ND-PG-Lys₈ with higher positive zeta potential formed complexes with the pDNA, which can be seen as becoming light of density of the pDNA bands. In particular, ND-PG-Arg₈ with the highest positive zeta potential completely retarded the pDNA at a low NP:pDNA weight ratio (30:1). In contrast, ND50-PG and ND-PG-His₈ were not able to form a complex with the pDNA even at the highest NP:pDNA weight ratio (50:1).

Conclusion

We have prepared ND-PG-BPP through multistep organic transformations including click chemistry. The PG layer on ND gave good aqueous dispersibility, enabling derivatization and characterization in the solution phase. The ND-PG-Arg₈ and ND-PG-Lys₈ possessing relatively high positive zeta potential immobilized the pDNA, demonstrating their potential of ND-PG-BPP as vectors for gene delivery.

Experimental

Materials and instruments

All the reagents and solvents used for the synthesis were employed as received. ND with 50 nm median diameter (ND50), prepared from high-pressure-high-temperature (HPHT)

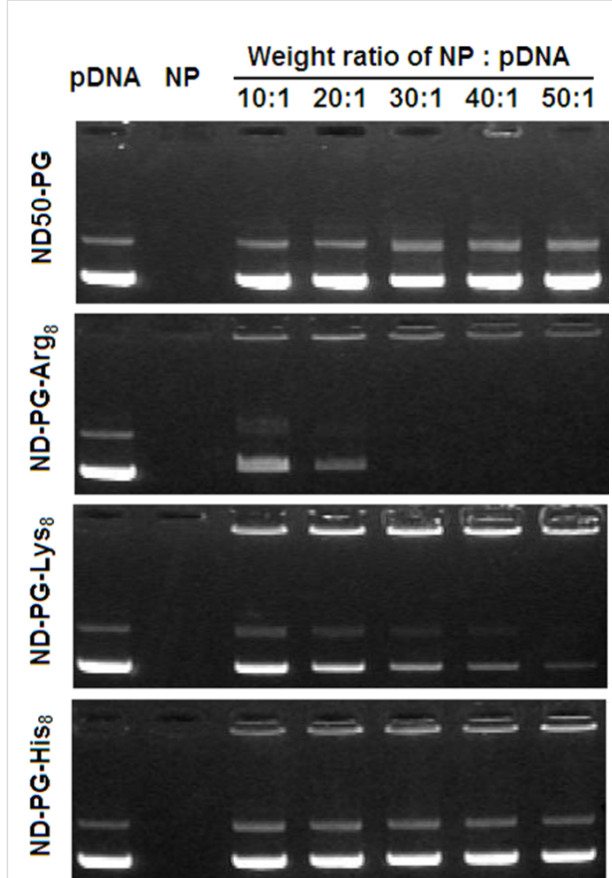


Figure 6: Electrophoretic migration of pDNA, NP (ND50-PG or ND-PG-BPP), and NP/pDNA mixtures at various weight ratios.

bulk diamond, was kindly provided by Tomei Diamond Co., Ltd. (Lot. No. 66093). Glycidol was purchased from Kanto Chemical Co., Ltd. *p*-Toluenesulfonyl chloride and sodium azide were purchased from Nacalai Tesque, Co. Basic polypeptides binding propargyl glycine (G*) at an N terminal (G*BPP) were obtained from two sources; G*Lys₈ and G*His₈ were synthesized by the central research laboratory of Shiga University of Medical Science and G*Arg₈ was purchased from GL Biochem Ltd. in Shanghai, China. The pBluescript II KS (Agilent Technologies, Inc., Tokyo, Japan) was used as a test pDNA for the hybridization with ND-PG-BPP. Dialysis was carried out by use of Spectra/Pro® dialysis membrane, MWCO: 12–14 kDa.

FTIR spectral measurements were conducted using IR Prestige-21 (Shimadzu Co.). Samples were prepared by drop-coating of suspension to form a thin film on a stainless alloy plate, and then dried at 70 °C. Hydrodynamic diameters in solution were determined by dynamic light scattering (DLS) using a Nanotrac UPA-UT151 system (Microtrac, Inc.). ¹H NMR spectra (270 MHz) were recorded on a JEOL Model JNM-EX270 spec-

trometer. Scanning transmission electron microscopy (STEM) was performed on a JEOL JSM-7500F field emission scanning electron microscope at 25 kV accelerating voltage for the TEM model. All samples for electron microscopy were prepared by evaporating one drop (~50 μ L) of samples on ultrathin carbon-coated copper grids. Thermogravimetric analyses (TGA) were carried out by a Q-50 analyzer (TA instruments) with a heating rate of 20 $^{\circ}$ C/min under a nitrogen or an air flow (60 mL/min). Zeta potential measurement was conducted in water solutions using an Otsuka ELSZ-1 zeta-potential analyzer.

Synthesis and characterization

ND50-PG

ND50-PG was prepared according to our reported method [13] using ND50 as a starting material, and characterized by FTIR (Figure 1a) and solution-phase 1 H NMR (Figure 2a).

ND-PG-OTs

ND50-PG (100 mg) was dissolved in pyridine (4.0 mL) by bath sonication and then cooled down to 0 $^{\circ}$ C in an ice/water bath. *p*-Toluenesulfonyl chloride (200 mg, 1.05 mmol) was dissolved in pyridine (2.0 mL) and added dropwise into the mixture under rapid stirring. The solution was stirred at 0–5 $^{\circ}$ C for 3 h and at room temperature overnight. The resulting solid was collected by centrifugation (Beckman Coulter Avanti[®] J-E centrifuge) at 50400 g and purified in DMF by repeated redispersion/centrifugation cycles. It was characterized by FTIR (Figure 1b) and solution-phase 1 H NMR (Figure 2b).

ND-PG-N₃

In a similar manner to our reported method [20], sodium azide (100 mg, 1.54 mmol) in water (2.0 mL) was added into ND-PG-OTs (80 mg) in DMF (6.0 mL) and stirred at 90 $^{\circ}$ C overnight. After cooling down, the product was collected by centrifugation and purified in water by repeated redispersion/centrifugation cycles. It was characterized by FTIR (Figure 1c) and solution-phase 1 H NMR (Figure 2c).

ND-PG-BPP

The click reaction of ND-PG-N₃ and G*BPP was conducted in a similar manner to our reported procedure [22]. G*BPP (8.0 mg) was added to a solution of ND-PG-N₃ (10 mg) in water (2.0 mL). Copper(II) sulfate pentahydrate (8.0 mg) in water (0.5 mL) and sodium ascorbate (10 mg) in water (0.5 mL) were added into the mixture with vigorous stirring. The resulting brown suspension was bath-sonicated for 10 min and then stirred at room temperature for 96 h. Diluted ammonia was dropped into the suspension to dissolve insoluble copper salts, giving a blue-gray suspension. The solid was collected by centrifugation and washed with 1% ammonia repeatedly. The washed sample was dialyzed against Milli-Q water to thor-

oughly remove ammonia. The resulting ND-PG-BPP were characterized by FTIR (Figure 1d–f). Decent NMR spectra of the ND-PG-BPP were not obtained because of lower dispersibility of the ND-PG-BPP than the above ND-PG derivatives.

Gel retardation assay

The hybridization of ND-PG-BPP with DNA was studied by means of an agarose gel retardation assay. The agarose gel was prepared by dissolving 1% (w/v) agarose in tris-acetate-EDTA (TAE) buffer containing ethidium bromide (0.1 mg/mL). The ND-PG-BPP was mixed with 0.2 μ g of pDNA in 10 μ L double-distilled water at designated NP (ND-PG-BPP):pDNA weight ratios (Figure 6). The mixture together with ND-PG-BPP and pDNA were loaded into the slots of the gel and subjected to electrophoresis at a voltage of 100 V for 20 min. The pDNA in the gel was visualized and photographed on a FAS-IV ultraviolet transilluminator (Nippon Genetics Co. Ltd).

Acknowledgements

This work was financially supported by the Science and Technology Incubation Program in Advanced Region (JST), Industrial Technology Research Grant Program (NEDO), Grant-in-Aid for Challenging Exploratory Research (JSPS), and Hoansha Fundation (to H. K.). The authors thank Dr. Nobuhiro Ogawa (Shiga University of Medical Science) and Tomei Diamond Co., Ltd. for providing us with pDNA and ND50, respectively. We are also grateful to Prof. Masaki Ozawa (Meijo University) for zeta potential measurements.

References

1. Mintzer, M. A.; Simanek, E. E. *Chem. Rev.* **2009**, *109*, 259–302. doi:10.1021/cr800409e
2. Guo, X.; Huang, L. *Acc. Chem. Res.* **2012**, *45*, 971–979. doi:10.1021/ar200151m
3. Mochalin, V. N.; Shenderova, O.; Ho, D.; Gogotsi, Y. *Nat. Nanotechnol.* **2012**, *7*, 11–23. doi:10.1038/nnano.2011.209
4. Krueger, A. *Chem.–Eur. J.* **2008**, *14*, 1382–1390. doi:10.1002/chem.200700987
5. Krueger, A. *Adv. Mater.* **2008**, *20*, 2445–2449. doi:10.1002/adma.200701856
6. Krueger, A. J. *Mater. Chem.* **2011**, *21*, 12571–12578. doi:10.1039/c1jm11674f
7. Krueger, A.; Ozawa, M.; Jarre, G.; Liang, Y.; Stegk, J.; Lu, L. *Phys. Status Solidi A* **2007**, *204*, 2881–2887. doi:10.1002/pssa.200776330
8. Krüger, A.; Liang, Y.; Jarre, G.; Stegk, J. *J. Mater. Chem.* **2006**, *16*, 2322–2328. doi:10.1039/b601325b
9. Hartmann, M.; Betz, P.; Sun, Y.; Gorb, S. N.; Lindhorst, T. K.; Krueger, A. *Chem.–Eur. J.* **2012**, *18*, 6485–6492. doi:10.1002/chem.201104069
10. Takimoto, T.; Chano, T.; Shimizu, S.; Okabe, H.; Ito, M.; Morita, M.; Kimura, T.; Inubushi, T.; Komatsu, N. *Chem. Mater.* **2010**, *22*, 3462–3471. doi:10.1021/cm100566v

11. Nakamura, T.; Ohana, T.; Yabuno, H.; Kasai, R.; Suzuki, T.; Hasebe, T. *Appl. Phys. Express* **2013**, *6*, 015001. doi:10.7567/APEX.6.015001
12. Krueger, A.; Lang, D. *Adv. Funct. Mater.* **2012**, *22*, 890–906. doi:10.1002/adfm.201102670
13. Zhao, L.; Takimoto, T.; Ito, M.; Kitagawa, N.; Kimura, T.; Komatsu, N. *Angew. Chem., Int. Ed.* **2011**, *50*, 1388–1392. doi:10.1002/anie.201006310
14. Calderón, M.; Quadir, M. A.; Sharma, S. K.; Haag, R. *Adv. Mater.* **2010**, *22*, 190–218. doi:10.1002/adma.200902144
15. Maeda-Mamiya, R.; Noiri, E.; Isobe, H.; Nakanishi, W.; Okamoto, K.; Doi, K.; Sugaya, T.; Izumi, T.; Homma, T.; Nakamura, E. *Proc. Natl. Acad. Sci. U. S. A.* **2010**, *107*, 5339–5344. doi:10.1073/pnas.0909223107
16. Kong, X.; Huang, L. C. L.; Liao, S.-C. V.; Han, C.-C.; Chang, H.-C. *Anal. Chem.* **2005**, *77*, 4273–4277. doi:10.1021/ac050213c
17. Zhang, X.-Q.; Chen, M.; Lam, R.; Xu, X.; Osawa, E.; Ho, D. *ACS Nano* **2009**, *3*, 2609–2616. doi:10.1021/nn900865g
18. Zhang, P.; Yang, J.; Li, W.; Wang, W.; Liu, C.; Griffith, M.; Liu, W. *J. Mater. Chem.* **2011**, *21*, 7755–7764. doi:10.1039/c1jm10813a
19. Martín, R.; Álvaro, M.; Herance, J. R.; García, H. *ACS Nano* **2010**, *4*, 65–74. doi:10.1021/nn901616c
20. Zhao, L.; Shiino, A.; Qin, H.; Kimura, T.; Komatsu, N. *J. Nanosci. Nanotechnol.*, in press.
21. Meinhardt, T.; Lang, D.; Dill, H.; Krueger, A. *Adv. Funct. Mater.* **2011**, *21*, 494–500. doi:10.1002/adfm.201001219
22. Zhao, L.; Chano, T.; Morikawa, S.; Saito, Y.; Shiino, A.; Shimizu, S.; Maeda, T.; Irie, T.; Aonuma, S.; Okabe, H.; Kimura, T.; Inubushi, T.; Komatsu, N. *Adv. Funct. Mater.* **2012**, *22*, 5107–5117. doi:10.1002/adfm.201201060

License and Terms

This is an Open Access article under the terms of the Creative Commons Attribution License (<http://creativecommons.org/licenses/by/2.0>), which permits unrestricted use, distribution, and reproduction in any medium, provided the original work is properly cited.

The license is subject to the *Beilstein Journal of Organic Chemistry* terms and conditions: (<http://www.beilstein-journals.org/bjoc>)

The definitive version of this article is the electronic one which can be found at:
doi:10.3762/bjoc.10.64

Thermodynamically stable [4 + 2] cycloadducts of lanthanum-encapsulated endohedral metallofullerenes

Yuta Takano¹, Yuki Nagashima², M. Ángeles Herranz³, Nazario Martín^{*3,4}
and Takeshi Akasaka^{*2,5,6}

Full Research Paper

Open Access

Address:

¹Institute for Integrated Cell-Material Sciences (WPI-iCeMS), Kyoto University, Sakyo-ku, Kyoto 606-8501, Japan, ²Life Science Center of Tsukuba Advanced Research Alliance, University of Tsukuba, Tsukuba, Ibaraki 305-8577, Japan, ³Departamento de Química Orgánica I, Facultad de Química, Universidad Complutense, E-28040 Madrid, Spain, ⁴IMDEA-Nanoscience, Campus de Cantoblanco, Madrid E-28049, Spain, ⁵Foundation for Advancement of International Science, Tsukuba, Ibaraki 305-0821, Japan and ⁶State Key Laboratory of Materials Processing and Die & Mould Technology, School of Materials Science and Technology, Huazhong University of Science and Technology, Wuhan 430074, China and Department of Chemistry, Tokyo Gakugei University, Tokyo 184-8501, Japan

Email:

Nazario Martín^{*} - nazmar@quim.ucm.es; Takeshi Akasaka^{*} - akasaka@tara.tsukuba.ac.jp

* Corresponding author

Keywords:

carbon nanomaterials; dynamic NMR; endofullerenes; La₂@C₈₀; La@C₈₂; sultine

Beilstein J. Org. Chem. **2014**, *10*, 714–721.

doi:10.3762/bjoc.10.65

Received: 17 September 2013

Accepted: 04 March 2014

Published: 25 March 2014

This article is part of the Thematic Series "Functionalized carbon-nanomaterials".

Guest Editor: A. Krueger

© 2014 Takano et al; licensee Beilstein-Institut.

License and terms: see end of document.

Abstract

The [4 + 2] cycloaddition of *o*-quinodimethanes, generated *in situ* from the sultine 4,5-benzo-3,6-dihydro-1,2-oxathiin 2-oxide and its derivative, to La metal-encapsulated fullerenes, La₂@C₈₀ or La@C₈₂, afforded the novel derivatives of endohedral metallofullerenes (**3a,b**, **4a,b** and **5b**). Molecular structures of the resulting compounds were elucidated using spectroscopic methods such as MALDI-TOF mass, optical absorption, and NMR spectroscopy. The [4 + 2] adducts of La₂@C₈₀ (**3a,b**, and **4a,b**) and La@C₈₂ (**5b**), respectively, retain diamagnetic and paramagnetic properties, as confirmed by EPR spectroscopy. Dynamic NMR measurements of **4a** at various temperatures demonstrated the boat-to-boat inversions of the addend. In addition, **5b** revealed remarkable thermal stability in comparison with the reported [4 + 2] cycloadduct of pentamethylcyclopentadiene and La@C₈₂ (**6**). These findings demonstrate the utility of sultines to afford thermodynamically stable endohedral metallofullerene derivatives for the use in material science.

Introduction

Endohedral metallofullerenes (EMFs) are a family of nanocarbons, which encapsulated one or more metal atoms inside a hollow carbon cage [1–4]. The encapsulation results in the electron transfer from metal atoms to the fullerene cage, which leads to unique electronic, magnetic, and chemical properties for EMFs that cannot be expected for empty fullerenes. Due to the numerous electronic properties EMFs are anticipated as promising materials in various fields such as chemistry, biology, and material science.

Among various kinds of EMFs, those encapsulating La atoms are especially attractive molecules because of their electronic and magnetic characteristics. As a result of the three electron transfer per La atom to the fullerene cage, the fullerenes simultaneously possess a low ionizing potential and a high electron affinity [1,2]. For mono-La endohedral fullerenes such as $\text{La}@\text{C}_{82}$, the electron transfer results in paramagnetism of the fullerene cage [5]. The di-La endohedral fullerenes such as $\text{La}_2@\text{C}_{80}$ show diamagnetism [6]. This feature leads to remarkable differences in chemical and electronic properties between these two classes of EMFs.

Chemical functionalization of fullerenes enhances molecular properties and possible applications of fullerenes [1,4]. The [4 + 2] cycloaddition reaction is a useful chemical modification method because it enables to introduce a variety of addends and/or the combination of different functionalities on the fullerene [7]. Regarding the [4 + 2] cycloaddition of EMFs, however, no report is available for endohedral di-metallocfullerenes, with the exception of azafullerene [8]. A limited number of reports describe other EMFs [4,9,10]. Moreover, the only precedent of [4 + 2] cycloadducts of the fullerenes which have an open-shell electronic structure of the cage, e.g., $\text{La}@\text{C}_{82}$, are thermodynamically unstable and show retro-cycloaddition reactions [10,11]. In addition, boat-to-boat inver-

sion of the addend of the cycloadducts of EMFs has not been well-studied to date; the investigation of this interconversion serves to demonstrate the existence of a dynamic process in the molecules and is regarded as one index of the bonding energy of the addition position of the fullerene and the addend.

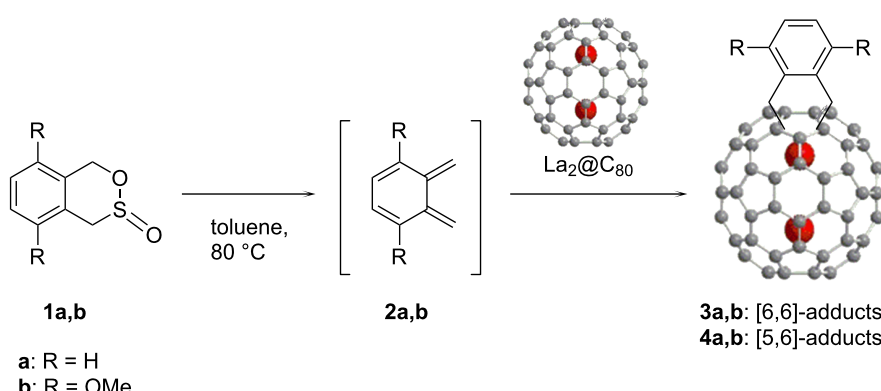
Among various precursors to afford [4 + 2] cycloadducts of fullerenes, the sultine 4,5-benzo-3,6-dihydro-1,2-oxathiin 2-oxide and its derivatives are useful to afford thermodynamically stable compounds because thermolysis of sultine affords highly reactive *o*-quinodimethanes by extrusion of sulfur dioxide without production of any organic or inorganic byproduct [12,13].

Here, we present the first chemical derivatization of $\text{La}_2@\text{C}_{80}$ and $\text{La}@\text{C}_{82}$ by [4 + 2] cycloaddition using sultines **1a,b**. The resulting products **3a,b**, **4a,b** and **5b** were characterized and their thermodynamic properties were investigated.

Results and Discussion

Synthesis and characterization of $\text{La}_2@\text{C}_{80}$ cycloadducts

o-Quinodimethanes **2a** and **2b** were generated in situ by thermolysis of the corresponding sultines **1a** and **1b** in toluene at 80 °C (Scheme 1). The highly reactive intermediates are trapped efficiently by $\text{La}_2@\text{C}_{80}$, which acts as a dienophile to form the cycloadducts (**3a,b** and **4a,b**). The reactions were traced using HPLC analyses (Figure 1), and formation of the resulting [4 + 2] adducts was confirmed by matrix-assisted laser desorption ionization (MALDI) TOF mass spectrometry (Figure 2), which shows the molecular ion peaks for the corresponding compounds. Isolation of **3b** and **4b** were achieved by one-step HPLC separation using a Buckyprep column, although this purification method was not applicable for **3a** and **4a** (vide infra).



Scheme 1: Synthesis of [4 + 2] adducts of $\text{La}_2@\text{C}_{80}$.

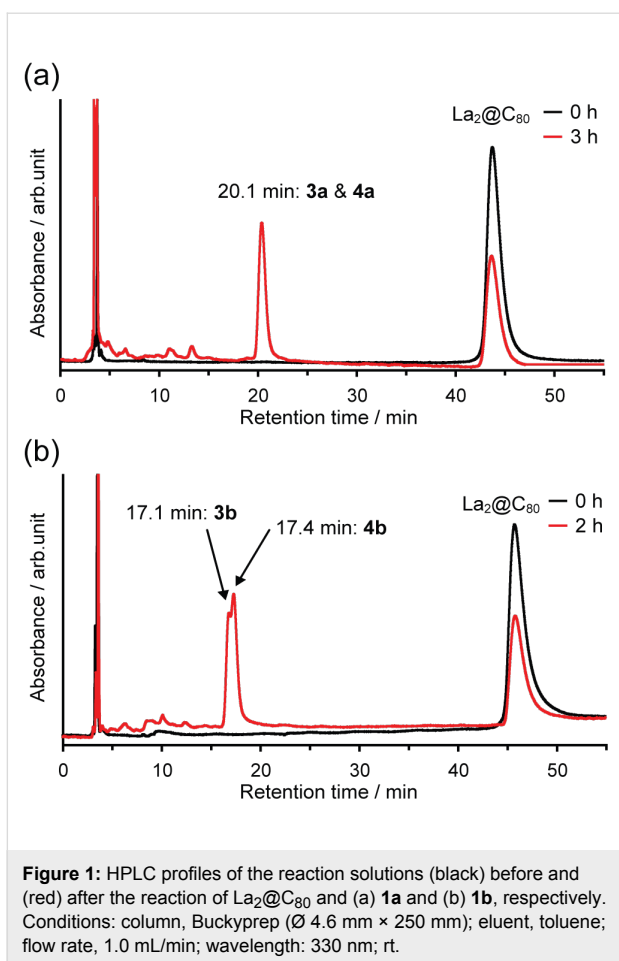


Figure 1: HPLC profiles of the reaction solutions (black) before and (red) after the reaction of $\text{La}_2@\text{C}_{80}$ and (a) **1a** and (b) **1b**, respectively. Conditions: column, Buckyprep (\varnothing 4.6 mm \times 250 mm); eluent, toluene; flow rate, 1.0 mL/min; wavelength: 330 nm; rt.

Because only two types of $\text{C}=\text{C}$ bonds are available in $\text{La}_2@\text{C}_{80}$, which has I_h symmetry, only two site-isomers namely [6,6]- and [5,6]-isomers, are allowed to be formed by cycloaddition reactions. (Please note that “site-isomer” refers to an isomer of the adducts which has the same fullerene and addend but different addition position – a classification proposed recently for fullerene’s chemistry by Martin et al. [14]). Therefore, **3b** and **4b** are concluded to be the site-isomers which were afforded by the reaction as a result of using highly reactive *o*-quinodimethane.

The UV–vis spectra of **3b** and **4b** partially provide information related to their molecular structures. The spectra were firstly recorded using a diode-array detector of the HPLC apparatus (Figure 3). The spectrum of **3b** shows the specific absorption band around 700 nm, which strongly suggests the electric nature of a [6,6]-closed adduct of the $\text{La}_2@\text{C}_{80}$ derivatives [15], because the absorption spectra of fullerenes and their derivatives are mainly attributable to $\pi-\pi^*$ transitions, which reflects the distinctive fingerprints of the π -electron system topology of the fullerene cage. Similarly, the characteristic spectrum of **4b** suggests its [5,6]-closed structure.

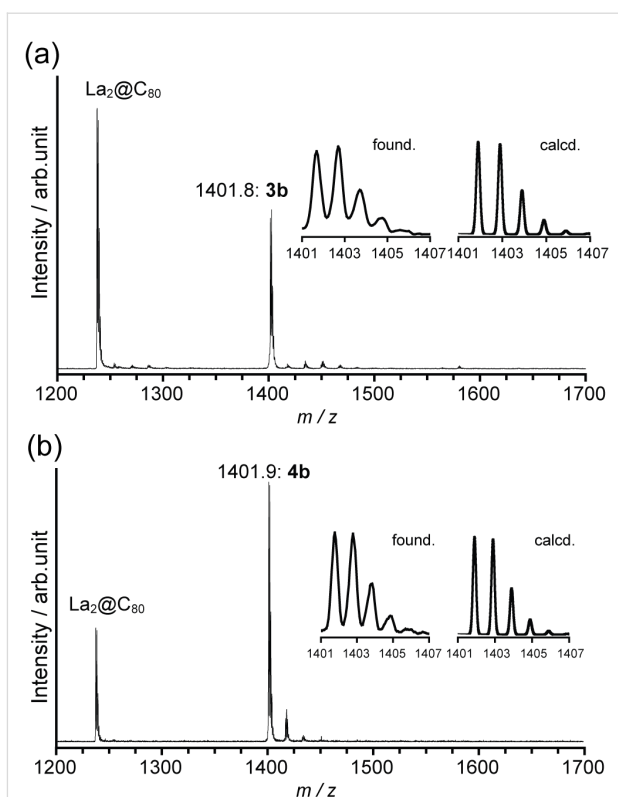


Figure 2: MALDI-TOF mass (negative mode) spectra of (a) **3b** and (b) **4b**, using 1,1,4,4-tetraphenyl-1,3-butadiene as matrix.

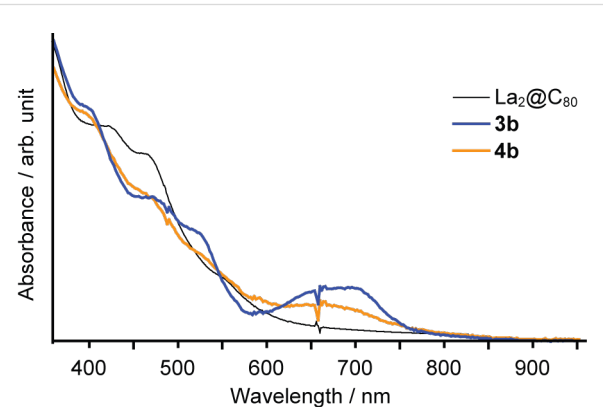


Figure 3: UV–vis/near-IR absorption spectra of **3b** and **4b** recorded by the diode array detector of the HPLC apparatus.

A different approach was taken to purify **3a** and **4a** because of the similar retention time of these compounds in HPLC. The mixture of **3a** and **4a** was first separated from the unreacted starting materials and byproducts through one-step HPLC separation. The MALDI-TOF mass spectra of **3a** and **4a** showed single peaks attributed to the molecular ion peak of the target molecule, $\text{La}_2@\text{C}_{80}\text{C}_2\text{H}_4\text{C}_6\text{H}_4$, at $1342\text{ }m/z$ (Figure 4). The existence of both [6,6]- and [5,6]-isomers in the mixture was

indicated by the ^1H NMR spectrum recorded at 248 K (Figure 5b), which cannot be expected from a single regioisomer. The [6,6]-adduct should show only two sets of AB quartets. The [5,6]-adduct should demonstrate one or two AB quartets based on its C_s molecular symmetry. Consequently, the spectrum containing more than two AB quartets indicates the existence of the both site-isomers.

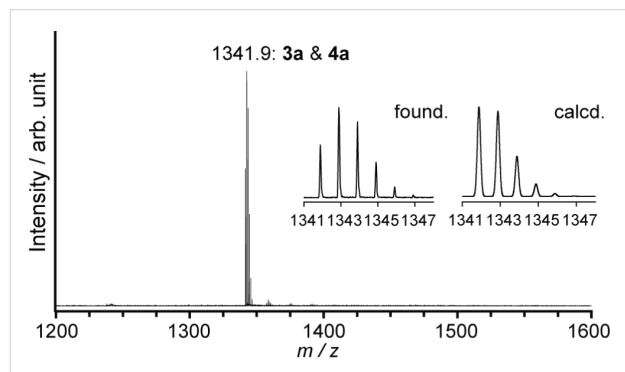


Figure 4: MALDI-TOF mass spectrum (negative mode) of the reaction mixture from $\text{La}_2@\text{C}_{80}$ and **1a**, using 1,1,4,4-tetraphenyl-1,3-butadiene as matrix.

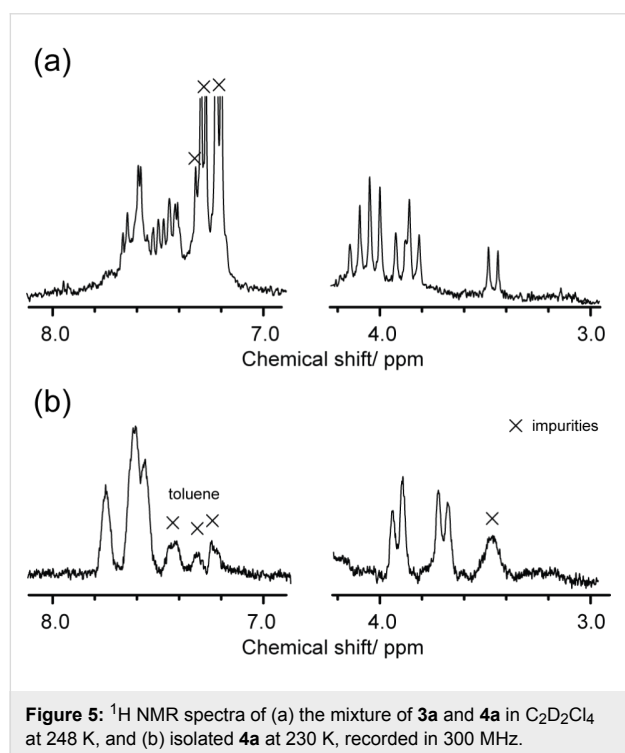


Figure 5: ^1H NMR spectra of (a) the mixture of **3a** and **4a** in $\text{C}_2\text{D}_2\text{Cl}_4$ at 248 K, and (b) isolated **4a** at 230 K, recorded in 300 MHz.

Further isolation of **4a** and **3b** was respectively accomplished using a combination of heating and HPLC separation. When the powdery mixture of **3a** and **4a** was heated to a temperature of 250 °C, selective decomposition of **3a** was observed (Figure 6). Since the peak of pristine $\text{La}@\text{C}_{82}$ at ca. 30 min is observed

after heating (see Figure 6b), most probably the detachment of the addend is taking place and a thermal isomerization thereafter. After HPLC purification of the crude reaction mixture, the number of the ^1H NMR signals attributed to the methylene protons was reduced (Figure 5b). Furthermore, the ^1H NMR spectrum of **4a** at 230 K unambiguously shows the existence of a single regioisomer, a [5,6]-adduct, which has C_s symmetry showing one AB quartet of the one set of equivalent methylene protons. The existence of the [6,6]-adduct is excluded because the adduct must show at least two AB quartets based on its molecular symmetry.

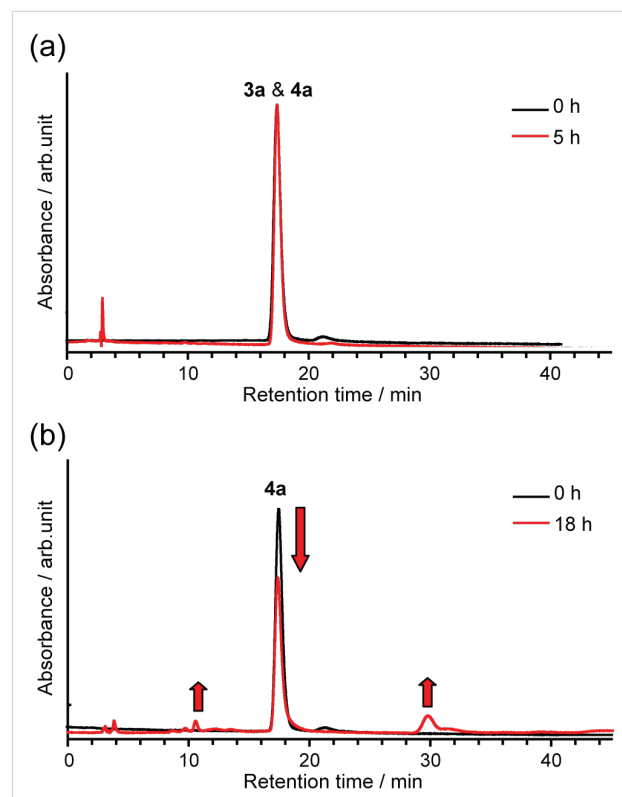
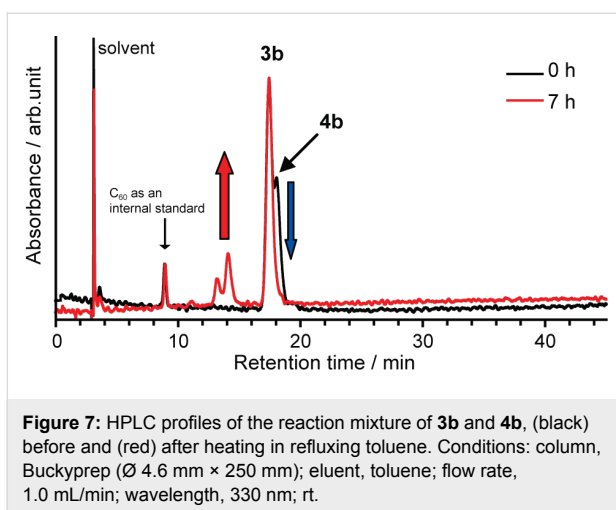
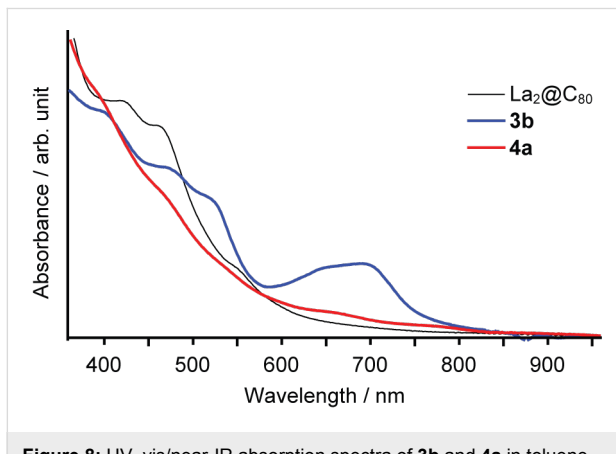


Figure 6: HPLC profiles of the mixture of **3a** and **4a**, (a) after heating in refluxing 1,2-dichlorobenzene and (b) after heating at 250 °C. Conditions: column, Buckyprep (\varnothing 4.6 mm \times 250 mm); eluent, toluene; flow rate, 1.0 mL/min; wavelength, 330 nm; rt.

In the case of purifying **3b**, selective decomposition of **4b** was observed at much lower temperature than that of **3a** and **4a**, after refluxing the mixture of **3b** and **4b** in toluene (Figure 7). This phenomenon is rationalized by the decomposition of the addend itself, because no pristine $\text{La}@\text{C}_{82}$ was detected after the heating in contrast to the case of **3a** and **4a** (vide supra). Therefore, it is concluded that the addend of **4b** containing methoxy groups is thermally less stable than the addend of **3a** and **4a**. The following HPLC purification afforded isolated **3b**. This result suggests that **3b** is more stable against heating than **4b**.



The UV-vis spectra of purified **4a** and **3b** were recorded using a spectrophotometer (UV-3150; Shimadzu Corp.) instead of the HPLC apparatus (Figure 8). The spectra reveal that **4a** shows no clear absorption peaks in the measuring range, and demonstrates a similar spectrum to those of [5,6]-adducts of $\text{La}_2@\text{C}_{80}$ [15]. This result shows good agreement with the ^1H NMR spectrum, which indicates that **4a** is a [5,6]-adduct. However, **3b** shows a specific absorption band around 700 nm as in the spectrum recorded by the HPLC system shown in Figure 3, indicating its [6,6]-structure.



Temperature-dependent dynamics of the [4 + 2] adducts of endohedral metallofullerenes were studied for **4a** by dynamic ^1H NMR measurements. Although **4a** did not show clear peaks at 290 K, distinct peaks were observed when the temperature was sufficiently lower or high enough distant from the coalescence temperature (T_c) (Figure 9). This fact suggests that the boat-to-boat inversions of **4a** between the pentagon side and the hexagon side are sufficiently slow or fast to allow their observation in an NMR time scale. The signals from the AB-quartet of

4a coalesce at 290 K (= T_c) indicate a dynamic process, which is attributed to the boat-to-boat interconversion of the cyclohexane ring of the addend similarly to the related carbocyclic analogues of C_{60} adducts [12].

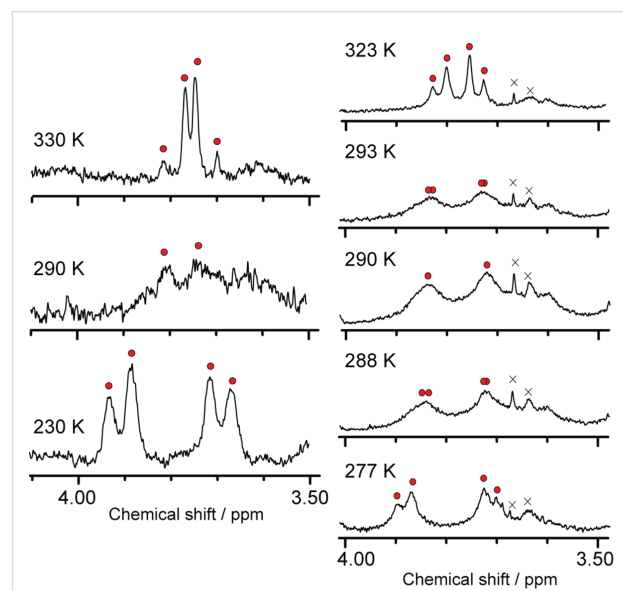


Figure 9: Temperature-dependent ^1H NMR spectra of **4a** in $\text{C}_2\text{D}_2\text{Cl}_4$ (left) at 300 MHz, and (right) at 500 MHz for precise analysis.

Synthesis and characterization of $\text{La}@\text{C}_{82}$ cycloadducts

Thermal reactions of **1b** and $\text{La}@\text{C}_{82}$ afforded the [4 + 2] adduct **5b** (Scheme 2). **5b** was separated from the unreacted starting materials and byproducts through a one-step HPLC procedure (Figure 10). The MALDI-TOF mass spectrum of **5b** shows the peak attributed to the molecular ion peak (Figure 11).

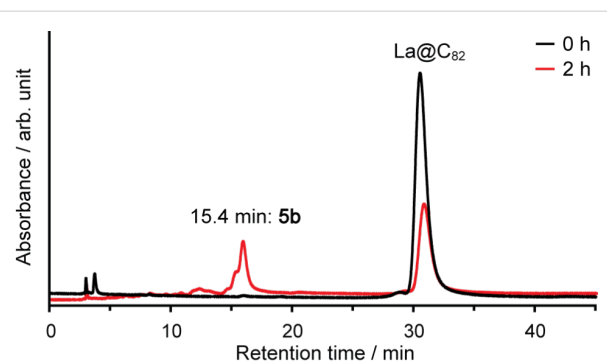
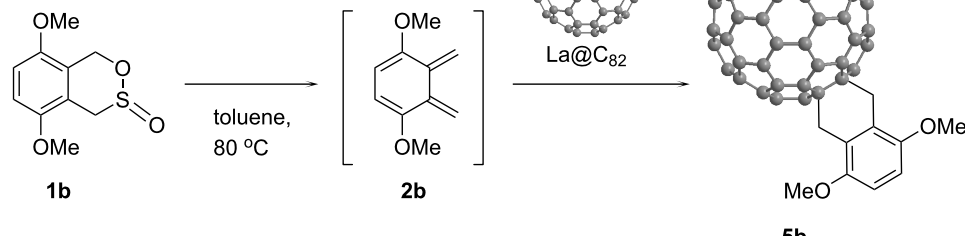


Figure 10: HPLC profiles of the reaction mixture for **5b**. Conditions: column, Buckyprep (\varnothing 4.6 mm \times 250 mm); eluent, toluene; flow rate, 1.0 mL/min; wavelength: 330 nm; 40 °C.

The electron spin resonance (ESR) spectrum of **5b** showed a unique octet signal (see Supporting Information File 1), indi-



Scheme 2: Synthesis of [4 + 2] adducts of La@C₈₂.

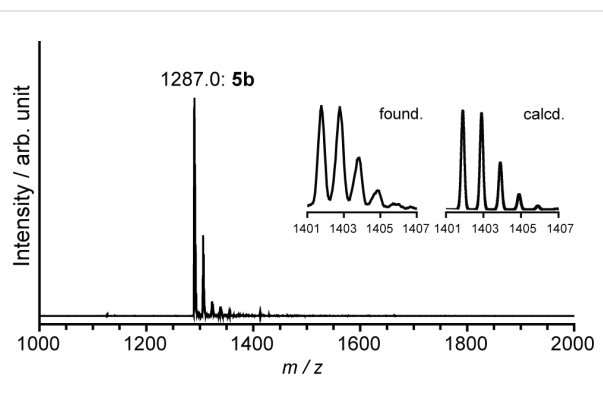


Figure 11: MALDI-TOF mass spectra (negative mode) of **5b**, using 1,1,4,4-tetraphenyl-1,3-butadiene as matrix.

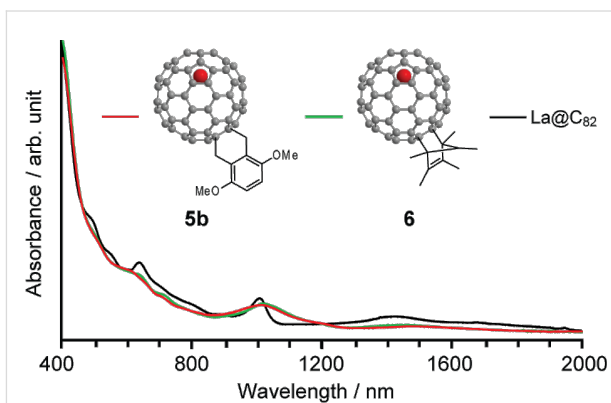


Figure 12: Vis–near-IR spectra of **5b**, **6** and La@C₈₂ in CS₂.

cating the paramagnetic property of **5b** as well as pristine La@C₈₂. This result also indicates that the cycloaddition of the *o*-quinodimethane does not lead to a remarkable change in the electronic properties of the fullerene. This fact is supported by the vis–NIR absorption spectrum of **5b**, which retains the specific absorption bands of the pristine La@C₈₂ (Figure 12). Broadening of the absorption bands is also observed, which is expected to be caused by the reduction of the molecular symmetry from *C*_{2v} to *C*₁ (vide infra).

Further characterization of the molecular structure was performed using NMR measurements. Because **5b** has an open-shell electronic structure as well as pristine La@C₈₂, **5b** was reduced electrochemically by one electron using bulk potential electrolysis for the NMR measurements. ¹H NMR spectrum of the resulting anionic **5b** ($[\mathbf{5b}]^-$) clearly illustrates the characteristic signals from the addend (Figure 13). Signals of the methylene protons appear as a sharp AB system at 4.55, 4.30, 2.94, and 2.82 ppm. The ¹³C NMR spectrum demonstrates the total sum of 82 signals from the carbon cage (Figure 14), indicating *C*₁ molecular symmetry for $[\mathbf{5b}]^-$. Signals at 58.2 and 56.0 ppm are attributed to the *sp*³ carbons of the addition position of the addend.

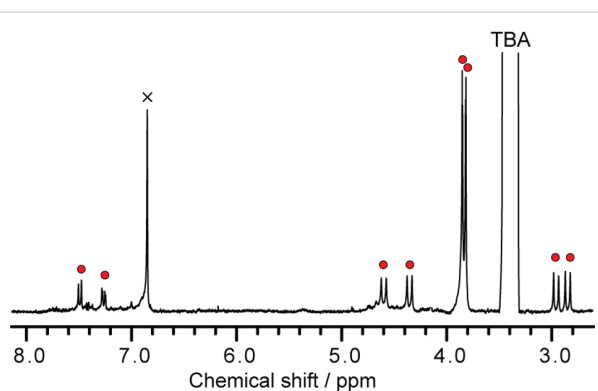


Figure 13: ¹H NMR spectrum of $[\mathbf{5b}]^-$ in acetone-*d*₆/CS₂ (3/1 = v/v) at 223 K.

The vis–NIR absorption spectra provide information related to the molecular structure of **5b** (Figure 12). The resemblance between the spectra of **5b** and that of the previously reported [4 + 2] cycloadduct of La@C₈₂ (**6**: La@C₈₂Cp*) [11] in the vis–NIR region imply the isostructural characteristics of the respective compounds, which show the same addition pattern of the substituents. Although the structure of **5b** was not elucidated using X-ray crystallographic analysis, synthetic prece-

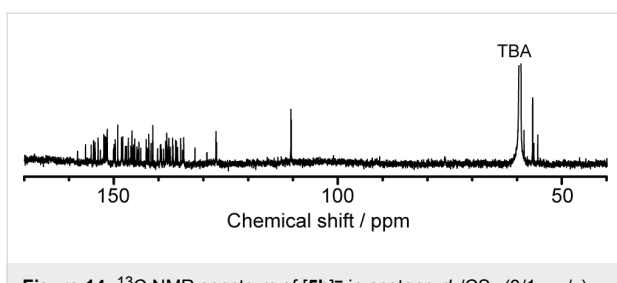


Figure 14: ^{13}C NMR spectrum of $[\mathbf{5b}]^-$ in acetone- d_6 /CS₂ (3/1 = v/v).

dents with absorption spectral data and theoretical calculations [16] strongly suggest that the most feasible addition site of the addend is that indicated in Scheme 2.

The thermodynamic stability of **5b** was evaluated by thermal heating. When a toluene solution of **5b** was let to stand at 30 °C, no decomposition was observed, whereas **6** showed decomposition and generation of pristine La@C₈₂ (Figure 15). This result shows that using sultines, which generate reactive *o*-quinodimethanes and which afford cycloadducts, is an effective means to afford thermodynamically stable [4 + 2] adducts of La@C₈₂.

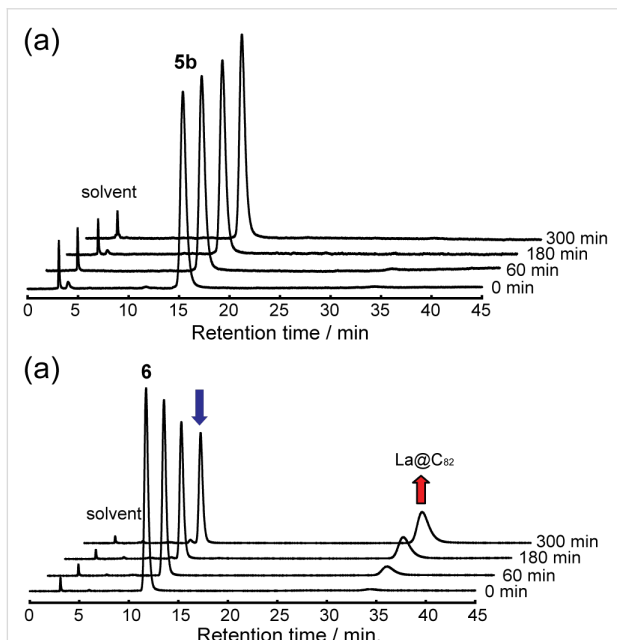


Figure 15: HPLC profiles for comparison of the thermal stabilities of (a) **5b** and (b) **6** at 30 °C. Conditions: column, Buckyprep (\varnothing 4.6 mm × 250 mm); temperature, 40 °C.

Conclusion

In summary, novel cycloadducts of La₂@C₈₀ and La@C₈₂ were synthesized efficiently by a [4 + 2] cycloaddition reaction using sultines as a precursor of reactive *o*-quinodimethanes. Isolation of **3b** and **4a**, respectively, was achieved by the selective

thermal decomposition of unstable isomers. The thermal stability of **5b** was also evaluated in comparison with **6**, and **5b** shows remarkable thermal stability. The molecular structures of the resulting compounds were characterized by spectroscopic analyses. Dynamic ^1H NMR spectroscopic investigations of **4a** reveal temperature-dependent changes related to the conformational changes in the cyclohexane moiety generated upon reaction. The use of sultines for chemical modification of endohedral metallofullerenes has proved to be of general scope, being particularly useful to prepare thermally stable [4 + 2] cycloadducts.

Supporting Information

Supporting information features detailed experimental procedures and spectral data for the compounds.

Supporting Information File 1

Descriptions on the synthesis and analyses of the compounds.

[<http://www.beilstein-journals.org/bjoc/content/supplementary/1860-5397-10-65-S1.pdf>]

Acknowledgements

This work is supported by a Grant-in-Aid for Scientific Research on Innovative Areas (20108001, "pi-Space"), a Grant-in-Aid for Scientific Research (A) (202455006), (B) (24350019) and Young Scientists (B) (25810098) from the Ministry of Education, Culture, Sports, Science, and Technology of Japan, The Strategic Japanese-Spanish Cooperative Program funded by JST and MINECO (Projects PLE-2009-0039 and PIB2010JP-00196), and by the European Research Council ERC-2012-ADG_20120216 (Chirallcarbon). The iCEMS is supported by the World Premier International Research Center Initiative (WPI), MEXT, Japan. N. M. thanks to Alexander van Humboldt Foundation.

References

1. Akasaka, T.; Wudl, F.; Nagase, S., Eds. *Chemistry of Nanocarbons*; Wiley: Chichester, 2010.
2. Chaur, M. N.; Melin, F.; Ortiz, A. L.; Echegoyen, L. *Angew. Chem., Int. Ed.* **2009**, *48*, 7514–7538. doi:10.1002/anie.200901746
3. Rudolf, M.; Wolfrum, S.; Guldi, D. M.; Feng, L.; Tsuchiya, T.; Akasaka, T.; Echegoyen, L. *Chem.–Eur. J.* **2012**, *18*, 5136–5148. doi:10.1002/chem.201102844
4. Popov, A. A.; Yang, S.; Dunsch, L. *Chem. Rev.* **2013**, *113*, 5989–6113. doi:10.1021/cr300297r
5. Nagase, S.; Kobayashi, K. *J. Chem. Soc., Chem. Commun.* **1994**, 1837–1838. doi:10.1039/c39940001837
6. Kobayashi, K.; Nagase, S.; Akasaka, T. *Chem. Phys. Lett.* **1996**, *261*, 502–506. doi:10.1016/0009-2614(96)01026-3

7. Hirsch, A.; Bettereich, M. *Fullerenes, Chemistry and Reaction*; Wiley-VCH: Weinheim, Germany, 2005.
8. Fu, W.; Zhang, J.; Fuhrer, T.; Champion, H.; Furukawa, K.; Kato, T.; Mahaney, J. E.; Burke, B. G.; Williams, K. A.; Walker, K.; Dixon, C.; Ge, J.; Shu, C.; Harich, K.; Dorn, H. C. *J. Am. Chem. Soc.* **2011**, *133*, 9741–9750. doi:10.1021/ja202011u
9. Lee, H. M.; Olmstead, M. M.; Iezzi, E.; Duchamp, J. C.; Dorn, H. C.; Balch, A. L. *J. Am. Chem. Soc.* **2002**, *124*, 3494–3495. doi:10.1021/ja020065x
10. Maeda, Y.; Miyashita, J.; Hasagawa, T.; Wakahara, T.; Tsuchiya, T.; Nakahodo, T.; Akasaka, T.; Mizorogi, N.; Kobayashi, K.; Nagase, S.; Kato, T.; Ban, N.; Nakajima, H.; Watanabe, Y. *J. Am. Chem. Soc.* **2005**, *127*, 12190–12191. doi:10.1021/ja053983e
11. Maeda, Y.; Sato, S.; Inada, K.; Nikawa, H.; Yamada, M.; Mizorogi, N.; Hasegawa, T.; Tsuchiya, T.; Akasaka, T.; Kato, T.; Slanina, Z.; Nagase, S. *Chem.-Eur. J.* **2010**, *16*, 2193–2197. doi:10.1002/chem.200902512
12. Illescas, B. M.; Martín, N.; Seoane, C.; Ortí, E.; Viruela, P. M.; Viruela, R.; de la Hoz, A. *J. Org. Chem.* **1997**, *62*, 7585–7591. doi:10.1021/jo9706436
13. Segura, J. L.; Martín, N. *Chem. Rev.* **1999**, *99*, 3199–3246. doi:10.1021/cr990011e
14. Maroto, E. E.; de Cázar, A.; Filippone, S.; Martín-Domenech, A.; Suárez, M.; Cossío, F. P.; Martín, N. *Angew. Chem., Int. Ed.* **2011**, *50*, 6060–6064. doi:10.1002/anie.201101246
15. Yamada, M.; Wakahara, T.; Nakahodo, T.; Tsuchiya, T.; Maeda, Y.; Akasaka, T.; Yoza, K.; Horn, E.; Mizorogi, N.; Nagase, S. *J. Am. Chem. Soc.* **2006**, *128*, 1402–1403. doi:10.1021/ja056560l
16. Takano, Y.; Obuchi, S.; Mizorogi, N.; García, R.; Herranz, M. Á.; Rudolf, M.; Wolfrum, S.; Guldi, D. M.; Martín, N.; Nagase, S.; Akasaka, T. *J. Am. Chem. Soc.* **2012**, *134*, 16103–16106. doi:10.1021/ja3055386

License and Terms

This is an Open Access article under the terms of the Creative Commons Attribution License (<http://creativecommons.org/licenses/by/2.0>), which permits unrestricted use, distribution, and reproduction in any medium, provided the original work is properly cited.

The license is subject to the *Beilstein Journal of Organic Chemistry* terms and conditions: (<http://www.beilstein-journals.org/bjoc>)

The definitive version of this article is the electronic one which can be found at:
doi:10.3762/bjoc.10.65

Columnar/herringbone dual crystal packing of pyrenylsumanene and its photophysical properties

Binod Babu Shrestha¹, Shuhei Higashibayashi^{*1,2,3} and Hidehiro Sakurai^{*1,2}

Full Research Paper

Open Access

Address:

¹Department of Functional Molecular Science, School of Physical Sciences, The Graduate University for Advanced Studies, Myodaiji, Okazaki, Aichi 444-8787, Japan, ²Research Center of Integrative Molecular Systems, Institute for Molecular Science, Myodaiji, Okazaki, Aichi 444-8787, Japan, and ³Japan Science and Technology Agency, ACT-C, 4-1-8 Honcho, Kawaguchi, Saitama 332-0012, Japan

Email:

Shuhei Higashibayashi^{*} - higashi@ims.ac.jp; Hidehiro Sakurai^{*} - hsakurai@ims.ac.jp

* Corresponding author

Keywords:

carbon nanomaterials; columnar crystal packing; fluorescence; herringbone; pyrenylsumanene

Beilstein J. Org. Chem. **2014**, *10*, 841–847.

doi:10.3762/bjoc.10.80

Received: 16 December 2013

Accepted: 21 March 2014

Published: 11 April 2014

This article is part of the Thematic Series "Functionalized carbon-nanomaterials".

Guest Editor: A. Krueger

© 2014 Shrestha et al; licensee Beilstein-Institut.

License and terms: see end of document.

Abstract

A single crystal of pyrenylsumanene was found to exhibit both columnar and herringbone crystal packing. The sumanene moieties form unidirectional columnar structures based on π – π stacking while the pyrene moieties generate herringbone structures due to CH– π interactions. The absorption and emission maxima of pyrenylsumanene were both red-shifted relative to those of sumanene and pyrene, owing to the extension of π -conjugation. Monomer emission with high quantum yield (0.82) was observed for pyrenylsumanene in solution, while excimer-type red-shifted emission was evident in the crystalline phase.

Introduction

Buckybowls – bowl-shaped aromatic hydrocarbons – possess unique physical properties due to their curved π -conjugated systems [1–5]. One of these characteristic features is a columnar packing structure in the crystal state. Many buckybowls, including sumanene [2], exhibit columnar packing in which the bowl-shaped molecules are stacked in a convex-to-concave fashion, since this particular pattern results in more highly favored intermolecular π – π interactions [1–13]. The columnar packing structures of buckybowls typically occur in two forms

which are differentiated by the stacking of the columns: unidirectional (Figure 1a) and opposite (Figure 1b). These columnar structures allow buckybowls to exhibit specific solid-state properties, including high electron conductivity and solid-state emission [14–18]. In contrast, planar π -conjugated aromatic compounds tend to favour a herringbone packing structure (Figure 1c) due to π – π and CH– π interactions [19,20]. To date, buckybowl derivatives with planar aromatic substituents have not been well studied and thus we wished to examine the crystal

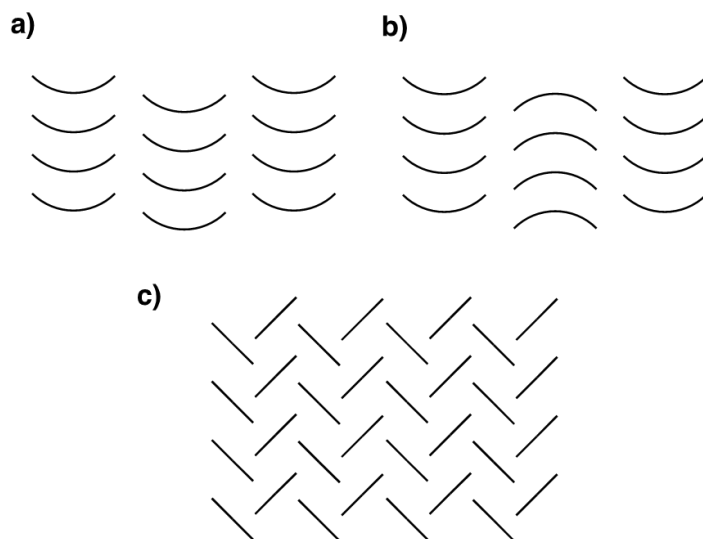


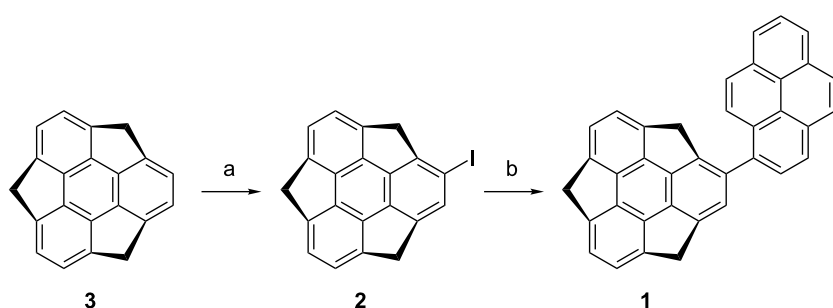
Figure 1: Columnar packing structures of buckybowls showing (a) unidirectional and (b) opposite structures, in addition to (c) the herringbone packing structure typical of planar π -conjugated compounds.

packing modes and solid-state properties of dual-nature compounds incorporating both bowl and planar structures. Pyrene was selected as the planar substituent when studying solid-state photophysical properties [21,22] and herein we report the columnar/herringbone dual crystal packing of pyrenylsumanene (**1**) in addition to its photophysical properties.

Results and Discussion

Pyrenylsumanene (**1**) was prepared from iodosumanene [8] and pyreneboronic acid in 84% yield through a Suzuki–Miyaura cross-coupling reaction (Scheme 1). The preparation of iodosumanene was improved by using a catalytic amount of scandium (III)triflate ($\text{Sc}(\text{OTf})_3$) with 6,6'-diido-2,2'-dimethoxy-1,1'-binaphthol (DIH) [23] compared to the previously reported system of AuCl_3 and *N*-iodosuccinimide [8], resulting in an 80% yield.

Following synthesis of **1**, a single crystal was obtained from $\text{CH}_2\text{Cl}_2/\text{MeOH}$ solution, with the crystal structure shown in Figure 2. The bowl depth of **1** from the centroid of the rim carbons to the centroid of the benzene ring is 1.09 Å (Figure 2b) and thus the bowl is slightly shallower than that of sumanene (1.11 Å) [11]. The structure resulting from DFT calculations at the $\omega\text{B97XD}/6-31\text{G}(\text{d})$ level indicates that **1** has a greater bowl depth (1.15 Å) than sumanene (1.13 Å). This difference results from the effects of intermolecular interactions in the crystal state [9]. The X-ray data indicate that the dihedral angle between the sumanene and pyrene moieties is 41.4° (Figure 2a). Most notably, **1** exhibits dual columnar and herringbone packing modes; the sumanene moiety undergoes columnar packing with convex-to-concave stacking, while the pyrene moiety shows herringbone packing with $\text{CH}-\pi$ interactions (Figures 2c,d). The columns of **1** are arranged unidirectionally,



Scheme 1: Synthesis of pyrenylsumanene (**1**): (a) $\text{Sc}(\text{OTf})_3$ (5 mol %), DIH (100 mol %), CH_2Cl_2 , rt, 2.5 h, yield 80%; (b) palladium (II) acetate (20 mol %), 1-pyreneboronic acid (150 mol %), acetone/water 4:1, 40 °C, 12 h, yield 84%.

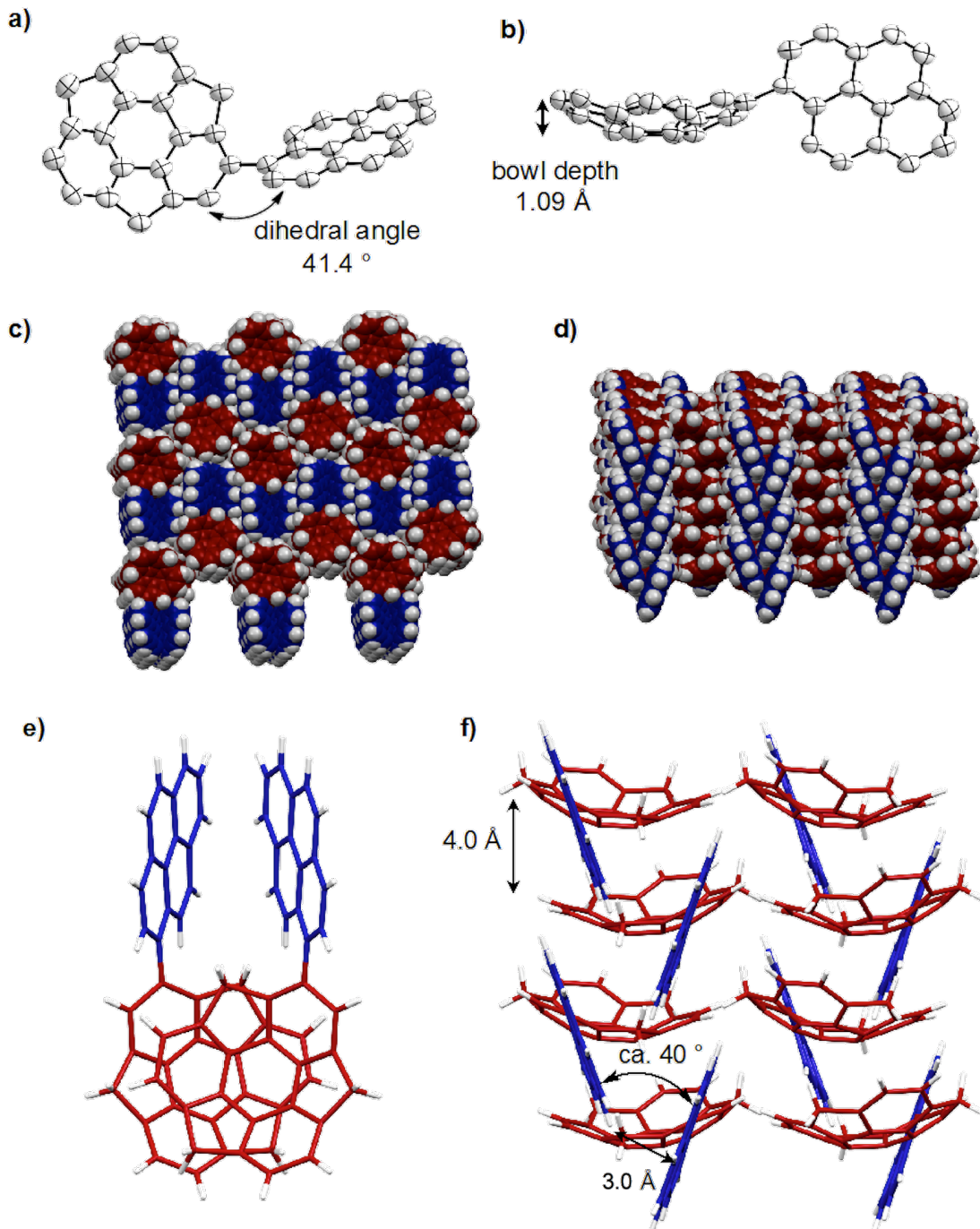


Figure 2: The X-ray crystal structure of **1**, showing: (a) top view of the ORTEP drawing with 50% probability, b) side view, c) top view of the packing structure with the sumanene bowl in red and the pyrene substituent in blue, d) side view, e) top view of column stacking of enantiomers and f) side view of columns with a herringbone packing of the pyrene moiety due to CH- π interactions.

in the same manner as observed in sumanene and hexafluorosumanene (representing the type a stacking shown in Figure 1) [7,11]. Compound **1** possesses bowl chirality [9,24,25] and the crystal represents a racemic mixture in which the two enantiomers are stacked in columns alternating at 4.0 Å

intervals with side-to-side offsets (Figures 2e,f). In the herringbone arrangement of the pyrene moieties, the CH- π interactions occur at a distance of 3.0 Å (Figure 1f). The π - π stacking of pyrene moieties, however, is not evident in the arrangement.

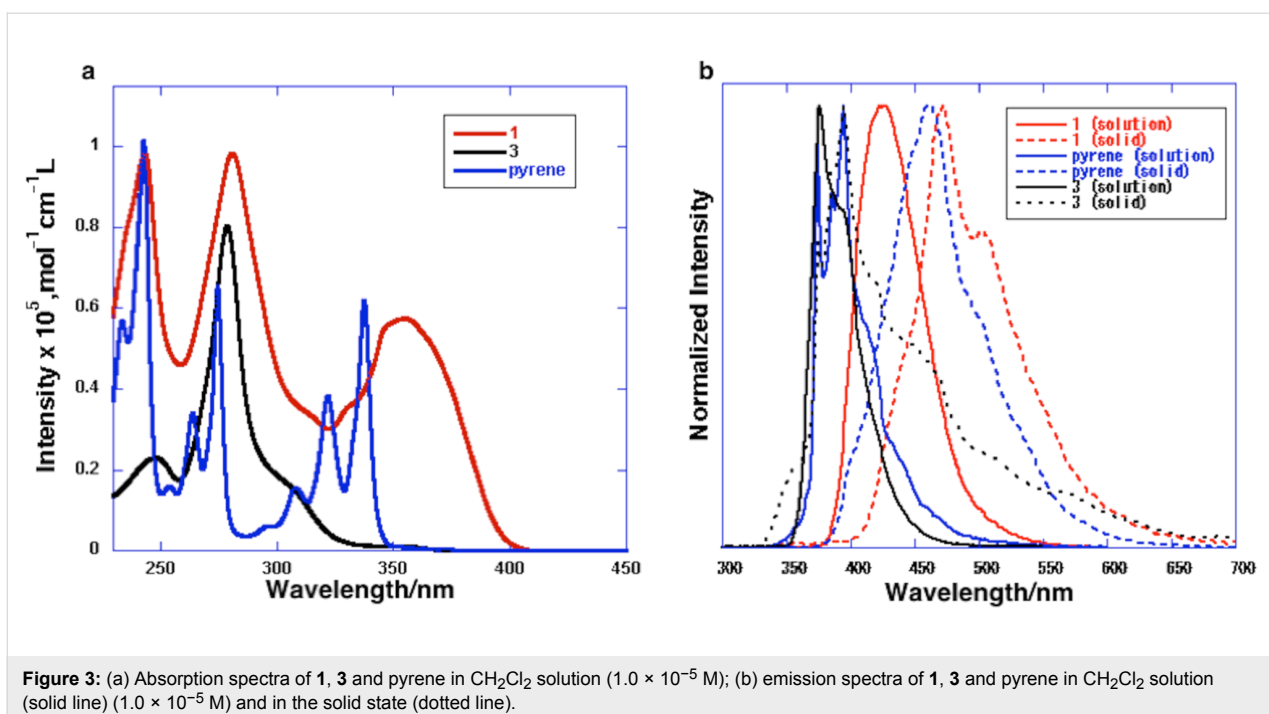


Figure 3: (a) Absorption spectra of **1**, **3** and pyrene in CH_2Cl_2 solution (1.0×10^{-5} M); (b) emission spectra of **1**, **3** and pyrene in CH_2Cl_2 solution (solid line) (1.0×10^{-5} M) and in the solid state (dotted line).

The UV-vis absorption and emission spectra and maxima as well as the quantum yields of **1**, **3** and pyrene in CH_2Cl_2 or in the solid state are summarized in Figure 3 and Table 1. The absorption maximum of **1** was evidently red-shifted relative to those of **3** and pyrene. The 355 nm absorption band of **1** was assigned to the HOMO–LUMO transition by TD-DFT calculations (ω B97XD/6-31G(d)). DFT calculations also demonstrated that the HOMO and LUMO of **1** are primarily located on the pyrene moiety (Figure 4). The dihedral angle between the sumanene and pyrene moieties resulting from calculations was 48.2° . This angle causes some extension of the π -conjugation to the sumanene moiety, resulting in a narrower HOMO–LUMO gap and the observed red shift in absorption. The emission of **1** in solution is also red-shifted relative to those of **3** and pyrene,

again owing to the π -extension. The emission of pyrene at 395 nm in solution is considered to result from the monomer form because of the low concentration, since pyrene is known to generate excimer emission at 480 nm at high concentrations ($>10^{-5}$ M) [26,27]. The emission of **1** at 422 nm is also assigned to monomer emission. Compound **1** did not generate excimer emission in solution concentrations over the range of 10^{-4} – 10^{-7} M and, due to the poor solubility of this compound, spectra at concentrations above 10^{-4} M could not be acquired. The emissions of **1** and pyrene in the solid state (at 473 and 463 nm) were red-shifted relative to those observed for these compounds in solution. The red-shifted emission of pyrene in the solid state originates from the excimer state of the crystal [26,27]. In the herringbone packing of **1**, the distance asso-

Table 1: Absorption, emission and quantum yield data for **1**, **3** and pyrene.

compound	λ_{abs} (nm) ^a ($\epsilon = 1 \times 10^5, \text{mol}^{-1} \text{cm}^{-1} \text{L}$)	λ_{em} (nm) ^b	Φ^c
1 (solution)	243 (0.98), 280 (0.98), 355 (0.57)	422	0.82
3 (solution)	278 (0.80)	375	0.02
pyrene (solution)	242 (1.01), 274 (0.64), 337 (0.61)	395	0.64 ^d
1 (solid)	–	473	0.10
3 (solid)	–	395	0.03
pyrene (solid)	–	463	0.68 ^d

^aAbsorption spectra in CH_2Cl_2 (1.0×10^{-5} M); ^bEmission spectra in CH_2Cl_2 (1.0×10^{-5} M) or in solid state. Excitation at 280 nm for **1** (solution) and **3** (solution and solid), 300 nm for **1** (solid), 270 nm for pyrene (solution and solid); ^cRelative quantum yield in cyclohexane solution (5.0×10^{-7} M) with 9,10-diphenylanthracene as a standard or absolute quantum yield in solid state; ^dReported quantum yield of pyrene in [26,27].

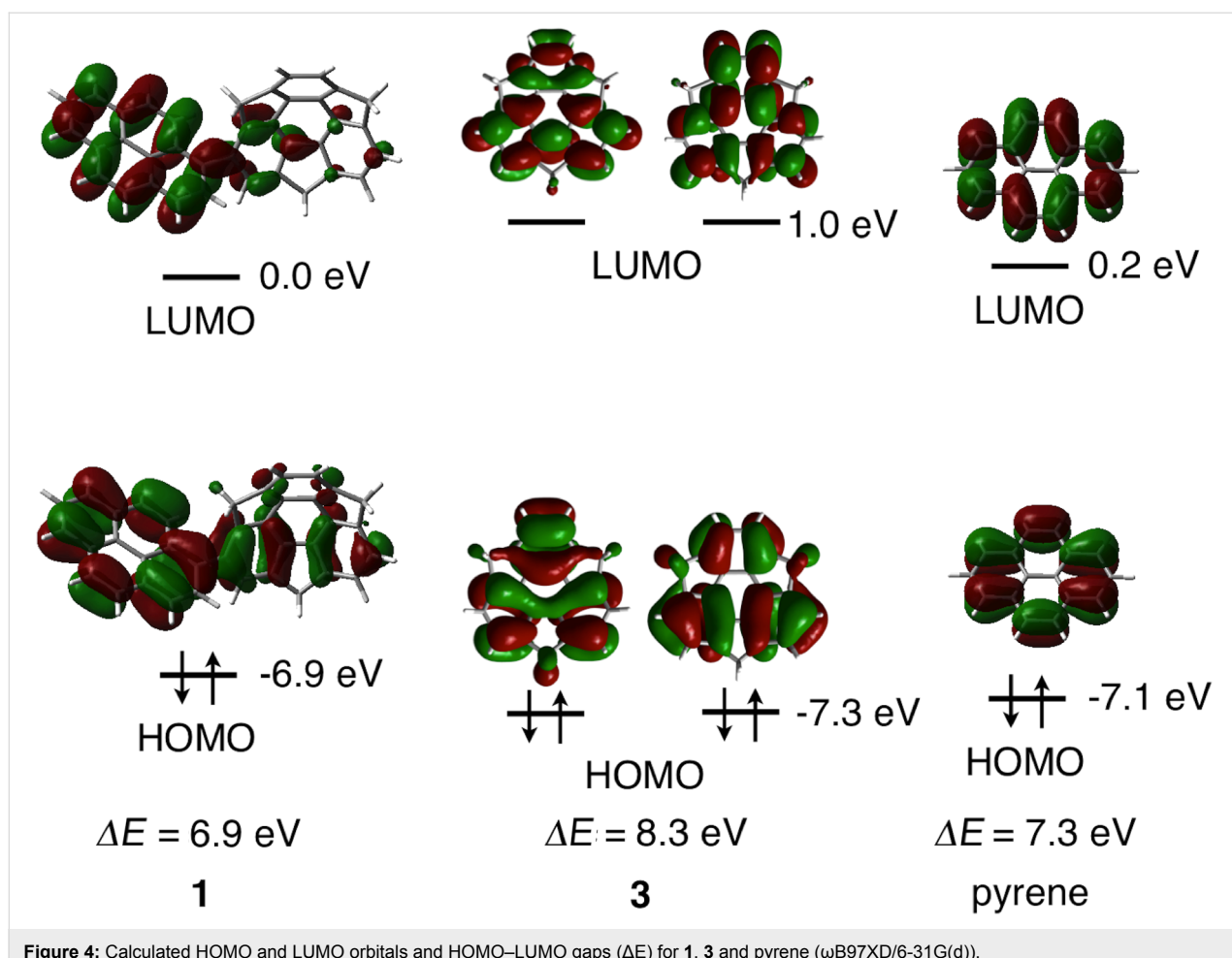


Figure 4: Calculated HOMO and LUMO orbitals and HOMO–LUMO gaps (ΔE) for **1**, **3** and pyrene (ωB97XD/6-31G(d)).

ciated with the CH– π interaction is 3.0 Å which is sufficiently close to form an excimer (Figure 2f). The angle of the pyrene moieties resulting from the CH– π interaction is approximately 40° (Figure 2f), which enables the partial π – π interactions. Judging from the crystal features of **1**, the red-shifted emission of **1** in the crystal is also assigned to the excimer state. The quantum yields of pyrene in solution and in the solid state are almost equal (0.64 and 0.68). In contrast, the quantum yield of **1** in the solid state (0.10) is decreased significantly from that in solution (0.82). This exciton quenching may be due to the effect of the sumanene moiety, since the quantum yield of **3** is low both in solution and in the solid state.

Conclusion

The ability to predict the crystal packing of organic molecules is important in the design of functional organic compounds but remains challenging. In this regard, the columnar structure of buckybowl crystals resulting from convex–concave intermolecular π – π interactions is expected to be quite predictable and to serve as a directing force to provide specific crystal structures [16,17]. The present study demonstrates the promising possi-

bility of utilizing the sumanene moiety as a directing group to obtain specific crystal structures.

Experimental General

UV-visible absorption spectra were recorded on a JASCO V-670 spectrometer. Fluorescence spectra were recorded on a JASCO FP6500 spectrometer. Melting points were determined on a Standford Research Systems MPA 100 and were uncorrected. Infrared (IR) spectra were recorded on a JASCO FT IR-4100 spectrometer. ^1H and ^{13}C NMR spectra were measured on a JEOL JNM-ECS (Delta V5.0) 400 spectrometer at 23 °C at 400 MHz and 100 MHz. CDCl_3 was used as a solvent and the residual solvent peaks were used as an internal standard (^1H NMR: CDCl_3 7.24 ppm; ^{13}C NMR: CDCl_3 77.00 ppm). Elemental analyses were measured on a J-Science Micro corder JM10. Mass spectra were measured on a JEOL JMS-777V spectrometer using electron impact mode (EI). Gel-permeation chromatography (GPC) was performed on JAIGEL 1H and 2H using a JAI Recycling Preparative HPLC LC-908W with CHCl_3 as eluent. TLC analysis was performed using Merck silica gel

60 F254. All reagents and solvents were commercially purchased from Kanto, Wako, Nacalai, and Kishida and further purified according to the standard methods, if necessary.

Synthesis of 2

Sumanene (**3**) (100 mg, 0.378 mmol), 6,6'-diiodo-2,2'-dimethoxy-1,1'-binaphthol (DIH) (144 mg, 0.378 mmol) and scandium(III) triflate (9.3 mg, 0.0189 mmol) were placed in a 50 mL dry flask under an Ar atmosphere. Dry CH_2Cl_2 (37 mL) was then added. The reaction mixture was allowed to stir for 2.5 h at rt. The completion of reaction was monitored by TLC (100% cyclohexane). The reaction was quenched by saturated aq. $\text{Na}_2\text{S}_2\text{O}_3$ and the mixture was extracted with CH_2Cl_2 (50 mL \times 3). The combined organic extracts were washed with water, brine, dried over Na_2SO_4 , filtered through Celite, and evaporated. The residue was purified by GPC to afford pure **2** (106 mg, 80%) with recovery of **3** (10.0 mg).

Synthesis of 1

Iodosumanene (**2**) (10.0 mg, 0.025 mmol), pyreneboronic acid (7.8 mg, 0.038 mmol) and palladium(II) acetate (1.2 mg, 0.0051 mmol) were placed in a 50 mL dry test-tube. Dry acetone (8 mL) and water (4 mL) was then added. The reaction mixture was allowed to stir for 12 h at 40 °C. The completion of reaction was monitored by TLC (100% cyclohexane). The reaction was diluted by CH_2Cl_2 and the mixture was extracted with CH_2Cl_2 (50 mL \times 3). The combined organic extracts were washed with water, brine, dried over Na_2SO_4 , filtered through Celite, and evaporated. The residue was purified by GPC to afford pure **1** (10.0 mg, 84%).

Characterization data

Pyrenylsumanene (**1**)

Mp: 255 °C; IR (KBr) v: 3039, 2895, 2780, 1396, 842, 788, 725, 683, 602, 488, 418 cm^{-1} ; ^1H NMR (CDCl_3) δ 8.68 (s, 1H), 8.20–7.99 (m, 7H), 7.71 (s, 1H), 7.40 (s, 1H) 7.19–6.90 (m, 4H), 4.84 (d, J = 19.6 Hz, 1H), 4.74 (d, J = 19.6 Hz, 1H), 4.53 (d, J = 19.6 Hz, 1H), 3.61 (d, J = 19.6 Hz, 1H), 3.45 (d, J = 19.6 Hz, 1H), 2.94 (d, J = 19.6 Hz, 1H) ppm; ^{13}C NMR (CDCl_3) δ 149.22, 149.21, 149.13, 149.12, 149.02, 149.10, 148.95, 148.94, 148.93, 148.73, 148.30, 148.18, 136.84, 131.62, 131.19, 130.95, 130.73, 127.71, 127.70, 127.69, 127.52, 127.51, 127.44, 126.09, 125.86, 125.77, 125.19, 125.09, 124.97, 124.67, 123.52, 123.40, 123.39, 123.25, 42.05, 41.99, 41.90 ppm; anal. calcd for $\text{C}_{37}\text{H}_{20}$: C, 95.66; H, 4.34; found: C, 95.38; H, 4.40; HRMS (EI) m/z calcd for $\text{C}_{37}\text{H}_{20}$ [M^+]: 464.1565; found: 464.1570.

Crystallographic data have been deposited with Cambridge Crystallographic Data Centre: Deposition number CCDC-986895. Copies of the data can be obtained free of charge via <http://www.ccdc.cam.ac.uk/conts/retrieving.html>.

Supporting Information

Supporting Information File 1

CIF file for the pyrenylsumanene crystal.

[<http://www.beilstein-journals.org/bjoc/content/supplementary/1860-5397-10-80-S1.cif>]

Acknowledgements

This work was supported by Ministry of Education, Culture, Sports, Science and Technology (MEXT), Japan Science and Technology (JST (ACT-C)) and Sumitomo Chemical. We thank Prof. Masaki Kawano (POSTECH) for the crystallographic analysis.

References

1. Higashibayashi, S.; Sakurai, H. *Chem. Lett.* **2011**, *40*, 122–128. doi:10.1246/cl.2011.122
2. Amaya, T.; Hirao, T. *Chem. Commun.* **2011**, *47*, 10524–10535. doi:10.1039/c1cc12532j
3. Sygula, A. *Eur. J. Org. Chem.* **2011**, 1611–1625. doi:10.1002/ejoc.201001585
4. Wu, Y. T.; Siegel, J. S. *Chem. Rev.* **2006**, *106*, 4843–4867. doi:10.1021/cr050554q
5. Tsefrikas, V. M.; Scott, L. T. *Chem. Rev.* **2006**, *106*, 4868–4884. doi:10.1021/cr050553y
6. Sakurai, H.; Daiko, T.; Hirao, T. *Science* **2003**, *301*, 1878. doi:10.1126/science.1088290
7. Schmidt, B. M.; Topolinski, B.; Higashibayashi, S.; Kojima, T.; Kawano, M.; Lentz, D.; Sakurai, H. *Chem.–Eur. J.* **2013**, *19*, 3282–3286. doi:10.1002/chem.201204622
8. Shrestha, B. B.; Karanjit, S.; Panda, G.; Higashibayashi, S.; Sakurai, H. *Chem. Lett.* **2013**, *42*, 386–389. doi:10.1246/cl.121273
9. Higashibayashi, S.; Tsuruoka, R.; Soujanaya, Y.; Purushotham, U.; Sastry, G. N.; Seki, S.; Ishikawa, T.; Toyota, S.; Sakurai, H. *Bull. Chem. Soc. Jpn.* **2012**, *85*, 450–467. doi:10.1246/bcsj.20110286
10. Mebs, S.; Weber, M.; Luger, P.; Schmidt, B. M.; Sakurai, H.; Higashibayashi, S.; Onogi, S.; Lentz, D. *Org. Biomol. Chem.* **2012**, *10*, 2218–2222. doi:10.1039/c2ob07040e
11. Sakurai, H.; Daiko, T.; Sakane, H.; Amaya, T.; Hirao, T. *J. Am. Chem. Soc.* **2005**, *127*, 11580–11581. doi:10.1021/ja0518169
12. Filatov, A. S.; Scott, L. T.; Petrukhina, M. A. *Cryst. Growth Des.* **2010**, *10*, 4607–4621. doi:10.1021/cg100898g
13. Wu, Y.-T.; Bandera, D.; Maag, R.; Linden, A.; Baldridge, K. K.; Siegel, J. S. *J. Am. Chem. Soc.* **2008**, *130*, 10729–10739. doi:10.1021/ja802334n
14. Morita, Y.; Nakao, S.; Haesuwanakij, S.; Higashibayashi, S.; Sakurai, H. *Chem. Commun.* **2012**, *48*, 9050–9052. doi:10.1039/c2cc33643j
15. Amaya, T.; Seki, S.; Moriuchi, T.; Nakamoto, K.; Nakata, T.; Sakane, H.; Saeki, A.; Tagawa, S.; Hirao, T. *J. Am. Chem. Soc.* **2009**, *131*, 408–409. doi:10.1021/ja805997v
16. Bando, Y.; Sakurai, T.; Seki, S.; Maeda, H. *Chem.–Asian J.* **2013**, *8*, 2088–2095. doi:10.1002/asia.201300635
17. Schmidt, B. M.; Seki, S.; Topolinski, B.; Ohkubo, K.; Fukuzumi, S.; Sakurai, H.; Lentz, D. *Angew. Chem., Int. Ed.* **2012**, *51*, 11385–11388. doi:10.1002/anie.201205757

18. Miyajima, D.; Tashiro, K.; Araoka, F.; Takezoe, H.; Kim, J.; Kato, K.; Takata, M.; Aida, T. *J. Am. Chem. Soc.* **2009**, *131*, 44–45. doi:10.1021/ja808396b
19. Feng, Q.; Liang, M.; Dong, B.; Xu, C.; Zhao, J.; Zhang, H. *CrystEngComm* **2013**, *15*, 3623–3629. doi:10.1039/C3CE27102A
20. Wang, C.; Dong, H.; Li, H.; Zho, H.; Meng, Q.; Hu, W. *Cryst. Growth Des.* **2010**, *10*, 4155–4160. doi:10.1021/cg100863q
21. Feng, X.; Hu, J.-Y.; Tomiyasu, H.; Seto, N.; Redshaw, C.; Elsegood, M. R. J.; Yamato, T. *Org. Biomol. Chem.* **2013**, *11*, 8366–8374. doi:10.1039/C3OB41350K
22. Winnik, F. M. *Chem. Rev.* **1993**, *93*, 587–614. doi:10.1021/cr00018a001
23. Kamei, T.; Shibaguchi, H.; Sako, M.; Toribatake, K.; Shimada, T. *Tetrahedron Lett.* **2012**, *53*, 3894–3896. doi:10.1016/j.tetlet.2012.05.063
24. Tan, Q.; Higashibayashi, S.; Karanjit, S.; Sakurai, H. *Nat. Commun.* **2012**, *3*, 891. doi:10.1038/ncomms1896
25. Higashibayashi, S.; Sakurai, H. *J. Am. Chem. Soc.* **2008**, *130*, 8592–8593. doi:10.1021/ja802822k
26. Katoh, R.; Suzuki, K.; Furube, A.; Kotani, M.; Tokumaru, K. *J. Phys. Chem. C* **2009**, *113*, 2961–2965. doi:10.1021/jp807684m
27. Crawford, A. G.; Dwyer, A. D.; Liu, Z.; Steffen, A.; Beeby, A.; Pålsson, L.-O.; Tozer, D. J.; Marder, T. B. *J. Am. Chem. Soc.* **2011**, *133*, 13349–13362. doi:10.1021/ja2006862

License and Terms

This is an Open Access article under the terms of the Creative Commons Attribution License (<http://creativecommons.org/licenses/by/2.0>), which permits unrestricted use, distribution, and reproduction in any medium, provided the original work is properly cited.

The license is subject to the *Beilstein Journal of Organic Chemistry* terms and conditions: (<http://www.beilstein-journals.org/bjoc>)

The definitive version of this article is the electronic one which can be found at:
doi:10.3762/bjoc.10.80

Site-selective covalent functionalization at interior carbon atoms and on the rim of circumtrindene, a $C_{36}H_{12}$ open geodesic polyarene

Hee Yeon Cho, Ronald B. M. Ansems and Lawrence T. Scott*

Full Research Paper

Open Access

Address:

Department of Chemistry, Merkert Chemistry Center, Boston College, Chestnut Hill, Massachusetts 02467-3860, USA

Beilstein J. Org. Chem. **2014**, *10*, 956–968.

doi:10.3762/bjoc.10.94

Email:

Lawrence T. Scott* - lawrence.scott@bc.edu

Received: 16 December 2013

Accepted: 03 April 2014

Published: 28 April 2014

* Corresponding author

This article is part of the Thematic Series "Functionalized carbon-nanomaterials".

Keywords:

Bingel–Hirsch reaction; buckybowl; carbon nanomaterials; cyclopropanation; polycyclic aromatic hydrocarbon; Prato reaction

Guest Editor: A. Krueger

© 2014 Cho et al; licensee Beilstein-Institut.

License and terms: see end of document.

Abstract

Circumtrindene (**6**, $C_{36}H_{12}$), one of the largest open geodesic polyarenes ever reported, exhibits fullerene-like reactivity at its interior carbon atoms, whereas its edge carbons react like those of planar polycyclic aromatic hydrocarbons (PAHs). The Bingel–Hirsch and Prato reactions – two traditional methods for fullerene functionalization – afford derivatives of circumtrindene with one of the interior 6:6 C=C bonds modified. On the other hand, functionalization on the rim of circumtrindene can be achieved by normal electrophilic aromatic substitution, the most common reaction of planar PAHs. This peripheral functionalization has been used to extend the π -system of the polyarene by subsequent coupling reactions and to probe the magnetic environment of the concave/convex space around the hydrocarbon bowl. For both classes of functionalization, computational results are reported to complement the experimental observations.

Introduction

Investigations into the structures and properties of geodesic polyarenes began with the synthesis of corannulene (**1**, $C_{20}H_{10}$) in 1966 [1,2] and were greatly stimulated by the discovery of buckminsterfullerene (**2**, C_{60}) in 1985 (Figure 1) [3]. Whereas fullerenes comprising complete three-dimensional polyhedra can be classified as “closed” geodesic polyarenes, curved subunits of fullerenes are regarded as “open” geodesic

polyarenes [4]. The fullerenes constitute one family of geodesic polyarenes, and bowl-shaped polycyclic aromatic hydrocarbons (PAHs) constitute another.

Both open and closed geodesic polyarenes are characterized by curved π -systems composed of pyramidalized carbon atoms (Figure 2). Pyramidalization not only imposes curvature, but it

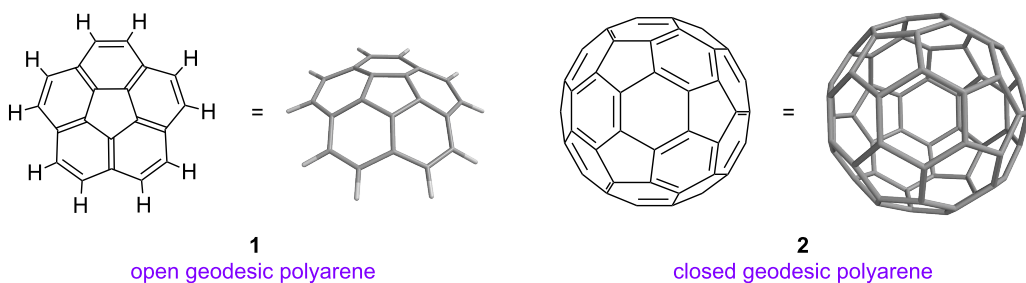
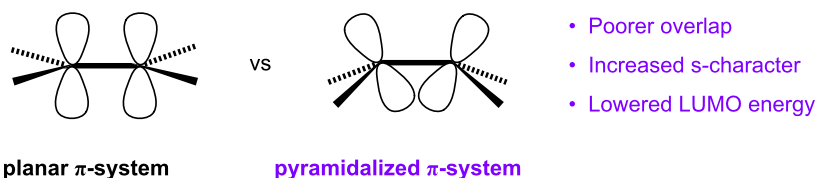


Figure 1: Prototypical open and closed geodesic polyarenes.

Figure 2: Planar vs pyramidalized π -system.

also imparts significant electronic perturbations. The less parallel the alignment of p-orbitals, for example, the poorer will be their overlap, and that will lead to weaker π -bonds. Weakening a π -bond raises the energy of the bonding π molecular orbital (MO) and lowers the energy of the antibonding π^* -MO. This is one important consequence of pyramidalization. A second consequence is the mixing of s-orbital character with the p-orbitals in the π -system. This hybridization lowers the energy of each atomic orbital in the π -system and thereby lowers the energy of all the derived π -MOs, i.e., both the HOMO (highest occupied molecular orbital) and the LUMO (lowest unoccupied molecular orbital) [5]. This lowering of the HOMO offsets the raising of the HOMO caused by poorer π overlap; however, lowering the LUMO as a consequence of orbital hybridization amplifies the lowering caused by the weaker π -bond. The major electronic consequence of π -system curvature, therefore, is a substantial lowering of the energy of the LUMO, while leaving the energy of the HOMO relatively unchanged.

Considerable effort by a number of research groups has been devoted to the preparation of fullerene fragments and to studies of their chemical and physical properties [6-9]. Several laboratories, including the authors', have been particularly successful in synthesizing geodesic polyarenes using flash vacuum pyrolysis (FVP) [6]. The FVP method involves slow sublimation of a starting material under vacuum, rapid passage of the gas-phase molecules through a hot zone, and subsequent capture of the products in a cold trap [10-12]. The high temperatures used in FVP (often up to 1100 °C) provide sufficient thermal energy to enable molecules to overcome high activation energy barriers.

The FVP approach takes advantage of the fact that the normal out-of-plane deformations of simple planar polyarenes become greatly amplified at high temperatures. FVP has been employed to prepare numerous highly-curved polyarenes, including corannulene (**1**) [[13,14], dibenzo[*a,g*]corannulene (**3**, C₂₈H₁₄) [15], a C₃-symmetric hemifullerene (**4**, C₃₀H₁₂) [16,17], the geodesic heterocycle triphenylene[1,12-*bcd*:4,5-*b'c'd'*:8,9-*b''c'd'*]trithiophene (**5**, C₁₈H₆S₃) [18], the deep buckybowl circumtrindene (**6**, C₃₆H₁₂) [19,20], and even fullerene C₆₀ (**2**) (Figure 1 and Figure 3) [21,22]. Syntheses of curved PAHs are not limited, however, to FVP; non-pyrolytic, “wet chemical” methods to access fullerene fragments have also been developed in our laboratory and elsewhere [1,2,15,23-27].

In addition to synthesis, the functionalization of geodesic polyarenes – by both covalent and noncovalent bonding – has attracted significant attention in recent years. The functionalization of fullerenes was intensively explored immediately following the discovery of methods for bulk preparation of fullerenes in 1990 [28]. Within the first few years, several covalent functionalization sequences were introduced that became widely used for the construction of multifunctional architectures with C₆₀ as an integral building unit. Representative synthetic reactions of fullerene C₆₀ (**2**) include cyclopropanation [29,30], [3 + 2] cycloaddition [31,32], [4 + 2] cycloaddition [33], nucleophilic addition [34], and radical addition reactions [35]. Two of the earliest and most widely used reactions, the Bingel–Hirsch reaction [29,30] and the Prato reaction [31,32] are illustrated in Scheme 1. The Bingel–Hirsch reaction affords a cyclopropanated fullerene **7**, and the Prato reaction gives a

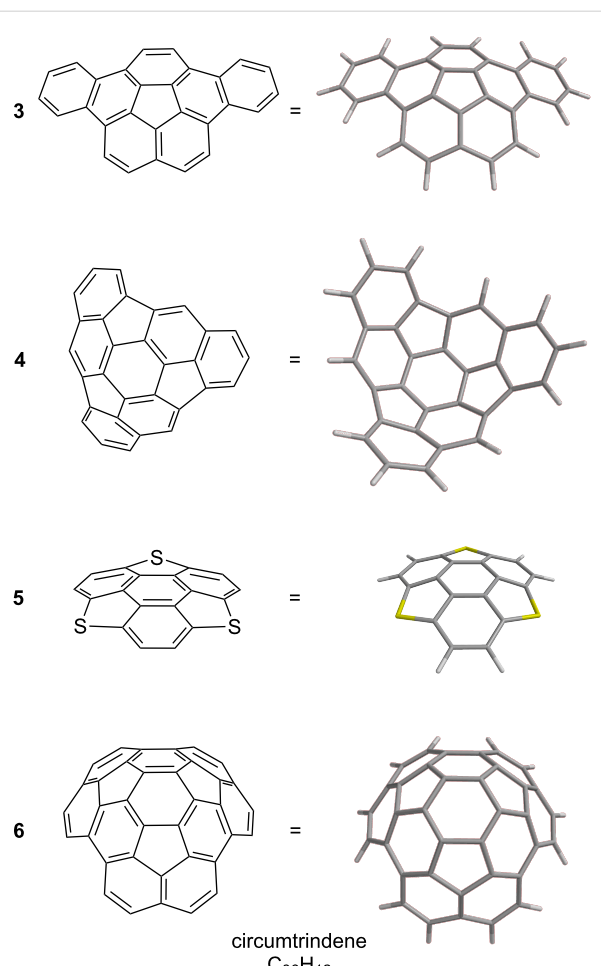
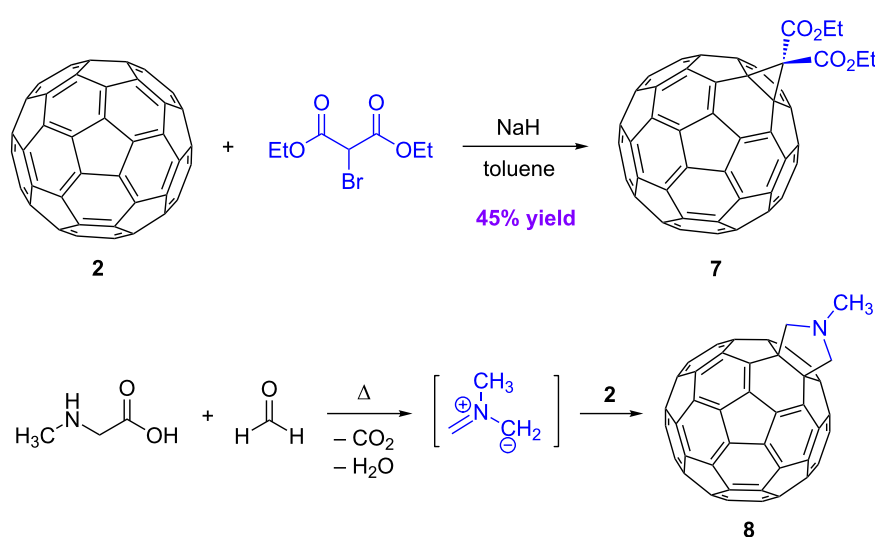


Figure 3: Selected examples of geodesic polyarenes synthesized by FVP.

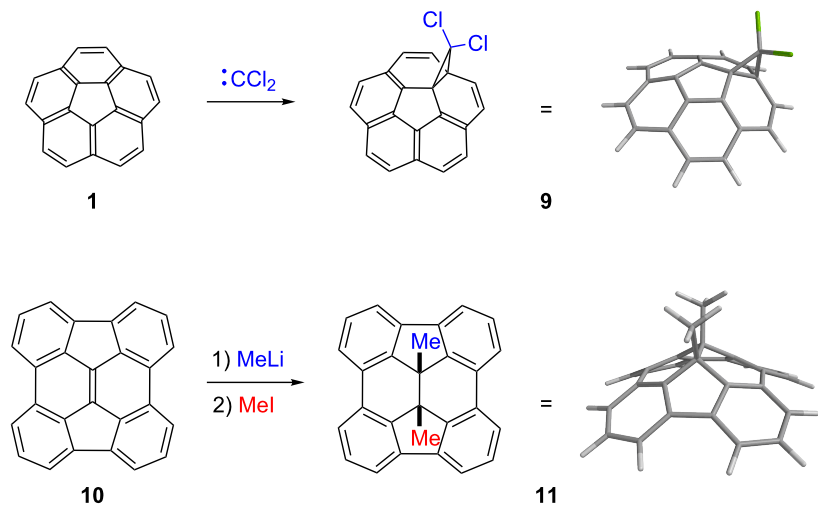
[3 + 2] cycloaddition adduct **8**. Concurrent with the development of covalent functionalization, numerous noncovalent functionalization methods were also investigated. In particular, the preparation of endohedral fullerenes, having metal atoms or other “guests” trapped inside the fullerene cage, opened yet another new branch of fullerene chemistry [36,37].

Our laboratory has been interested in the covalent functionalization of open geodesic polyarenes at their interior carbon atoms (i.e., carbon atoms that are shared by three rings) [4,38]. The curved PAHs corannulene (**1**) and diindenochrysene (**10**), for example, show fullerene-type reactivity towards carbenes and nucleophiles, respectively (Scheme 2). Dichlorocarbene adds to corannulene (**1**) to afford predominantly the cyclopropanated product **9** [39], whereas methylolithium adds to **10**, giving the 1,2-addition product **11**, after alkylation of the resulting anion by methyl iodide [40]. In contrast to these examples, no planar PAH has ever been observed to suffer direct covalent bond formation at an interior carbon atom, despite the long history of aromatic hydrocarbon chemistry [41,42].

These PAHs (**1** and **10**) are obviously nonplanar and have the same patterns of pentagons and hexagons as that found on the surface of fullerene C_{60} . The distortions of the π -systems in these molecules, however, are less severe than that in C_{60} , as indicated by their π -orbital axis vector (POAV) angles [43,44]. The POAV angles of C_{60} (**2**), corannulene (**1**), and diindenochrysene (**10**) are 11.6° ($101.6^\circ - 90^\circ = 11.6^\circ$ pyramidalization), 8.2° , and 9.0° , respectively (Figure 4) [23,24,45]. Furthermore, the barrier for bowl-to-bowl inversion in corannulene (10.2 kcal/mol at $-64^\circ C$) [46] is so low that corannulene



Scheme 1: Covalent functionalization of fullerene C_{60} by the Bingel–Hirsch reaction and the Prato reaction.



Scheme 2: Fullerene-type chemistry at interior carbon atoms of corannulene (**1**) and diindenochrysene (**10**).

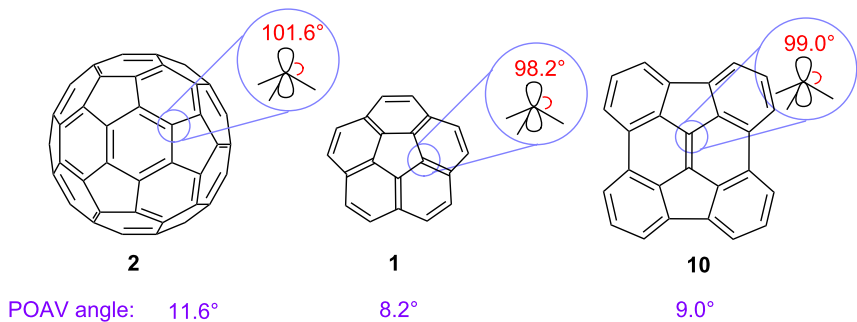


Figure 4: POAV angles of fullerene C₆₀ (**2**), corannulene (**1**), and diindenochrysene (**10**).

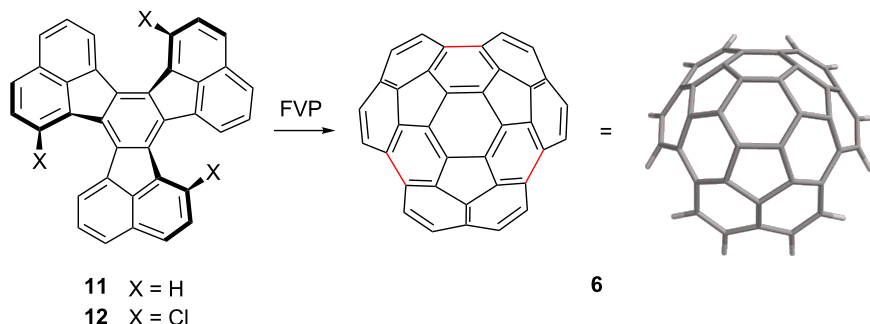
inverts rapidly even at room temperature. The inversion barrier of diindenochrysene (**10**) was calculated to be even lower (6.7 kcal/mol at ambient temperature by B3LYP/6-311G**) [47].

While there are many examples of covalent chemistry for fullerenes (i.e., closed geodesic polyarenes), covalent functionalizations of open geodesic polyarenes other than corannulene have been reported only rarely. As in fullerene chemistry, chemical derivatization of buckybowl can be expected to change the electronic, optical, magnetic, mechanical, and chemical properties of the material. For such functionalization reactions, site selectivity often becomes an issue when there is more than one site where the reaction could occur. Herein, we report methods for the site-selective covalent functionalization of circumtrindene (**6**), one of the most highly-curved fullerene fragments known, comprising 60% of the C₆₀ ball.

Results and Discussion

Synthesis and properties of circumtrindene (**6**)

In 1996, our laboratory reported that the C₃₆H₁₂ bowl circumtrindene (**6**) could be obtained by flash vacuum pyrolysis of decacyclene (**11**, Scheme 3) [19]. Extreme temperatures, in the range of 1200–1300 °C, were required, and the yield was less than 1%, but the transformation gave 60% of the C₆₀ ball in multimilligram quantities in a single step from a cheap, commercially available starting material with no reagents other than heat. Obviously, this brute-force triple-cyclodehydrogenation is not an efficient process. The yield could be improved dramatically, however, by the incorporation of substituents capable of generating aryl radicals by C–X bond homolysis in the fjord regions; the C₃₆H₁₂ bowl was produced in 26% yield from 3,9,15-trichlorodecacyclene (**12**) by FVP at 1100 °C (Scheme 3) [20].



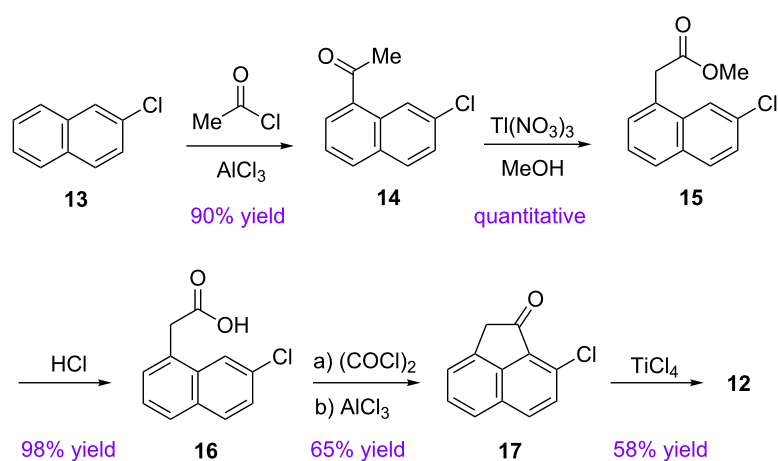
Scheme 3: Synthesis of circumtrindene (6) by FVP.

The importance of strategically functionalizing hydrocarbon precursors in a way that will generate radical centers where new bonds are to be formed by FVP is dramatically illustrated by the vastly improved efficiency of this triple cyclization reaction when starting from **12** instead of **11**. Unfortunately, the extra mass and polarity introduced by the chlorine atoms impedes sublimation of the substrate. A thin stream of nitrogen carrier gas leaked into the sample chamber largely overcomes this complication; however, even with this modification of the set-up, some 30% of starting material **12** decomposes in the sample chamber and fails to sublime.

The halogenated FVP precursor, 3,9,15-trichlorodecadacylene (**12**), was prepared in five steps from commercially available starting materials, following the same route reported in our earlier publication (Scheme 4) [20]. Cyclotrimerization of **17** to the *C*₃-symmetric trichlorodecadacylene **12** was accomplished by a triple aldol condensation of the chloro ketone **17** [48,49]. Improvements in the procedures reported previously are described in the experimental section in the Supporting Information File 1.

In agreement with DFT calculations [50] the X-ray crystal structure of circumtrindene (**6**) confirms that the carbon atoms comprising the top of the dome are distorted from planarity to an even greater degree than the carbon atoms in *C*₆₀ [51]; the pyramidalization in circumtrindene (POAV angle = 12.1° [52], Figure 5) significantly surpasses that in fullerene *C*₆₀ (POAV angle = 11.6°, Figure 4). Moreover, the X-ray structure of circumtrindene (**6**) reveals that the carbon–carbon bonds around the 6-membered ring at the top of the dome are not equivalent. The bond lengths vary depending on their location (Figure 5), as is also observed in fullerenes [53]. The carbon–carbon bond shared by two six-membered rings (so-called 6:6-bonds: 1.379 Å) are shorter than those shared by a 5-membered ring and a 6-membered ring (5:6-bonds: 1.430 Å). That is, the carbon–carbon bonds of the hexagonal ring in the center of circumtrindene are not the same as those in benzene. They look more like those of a “cyclohexatriene” than as those of a benzene ring.

The ¹H NMR spectrum of circumtrindene (**6**) consists of two doublets at δ 7.58 and 7.20 ppm. Induced diamagnetic ring



Scheme 4: Synthetic route to 3,9,15-trichlorodecadacylene (12).

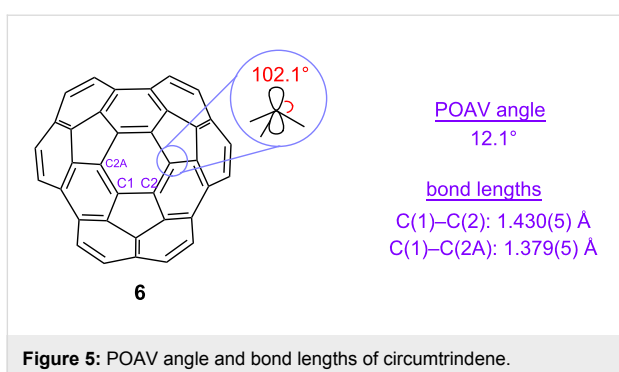


Figure 5: POAV angle and bond lengths of circumtrindene.

currents in this conjugated π -system deshield the hydrogen atoms on the rim; however, the magnitude of the effect is significantly less pronounced than that seen even in smaller PAHs that are less curved or planar [54]. Clearly, the high degree of curvature in this geodesic polyarene has a strong impact on the NMR resonances. The unequal magnitudes of the ring currents on the convex and concave faces of circumtrindene are probed and discussed in a later section.

Interior functionalization of circumtrindene

Unlike planar PAHs, circumtrindene (**6**) exhibits fullerene-like covalent chemistry at its “interior” carbon atoms. Two examples are reported below [55].

Bingel–Hirsch reaction

The Bingel–Hirsch reaction produces 3-membered rings by a reaction that begins with a nucleophilic addition to a fullerene (Scheme 1). It is considered to be one of the most valuable preparative methods for functionalizing fullerenes, since it changes both the solubility and the electrochemical behavior.

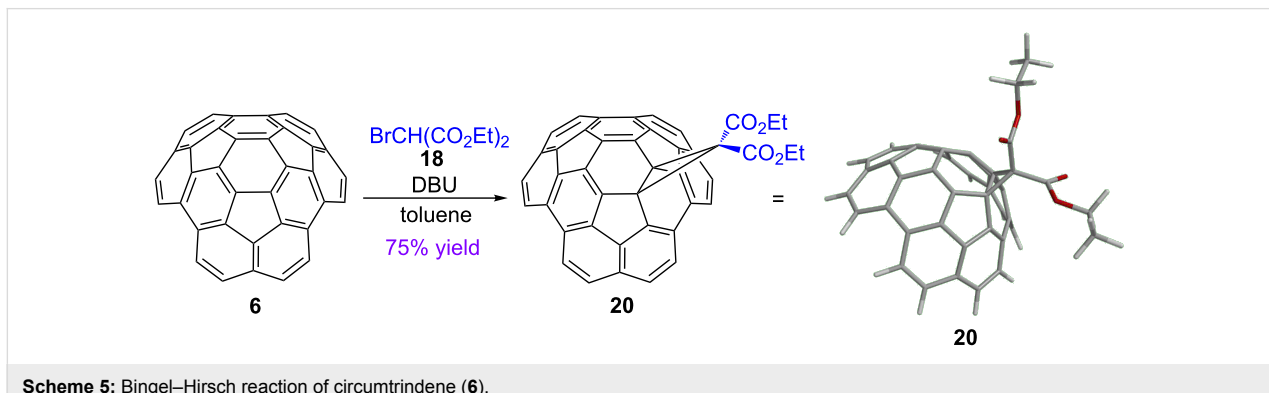
Considering the similarity between the curved π -systems of circumtrindene and fullerene C_{60} , we speculated that the Bingel–Hirsch reaction might occur with circumtrindene (**6**) in the same manner as it does with fullerene C_{60} . Gratifyingly, the cyclopropanation of circumtrindene by the Bingel–Hirsch reac-

tion proceeds smoothly to afford **20** in good yield and with complete site selectivity (Scheme 5). The reaction was performed with five equivalents of bromomalonate **18** and one equivalent of DBU (1,8-diazabicyclo[5.4.0]undec-7-ene) as a base in toluene at room temperature.

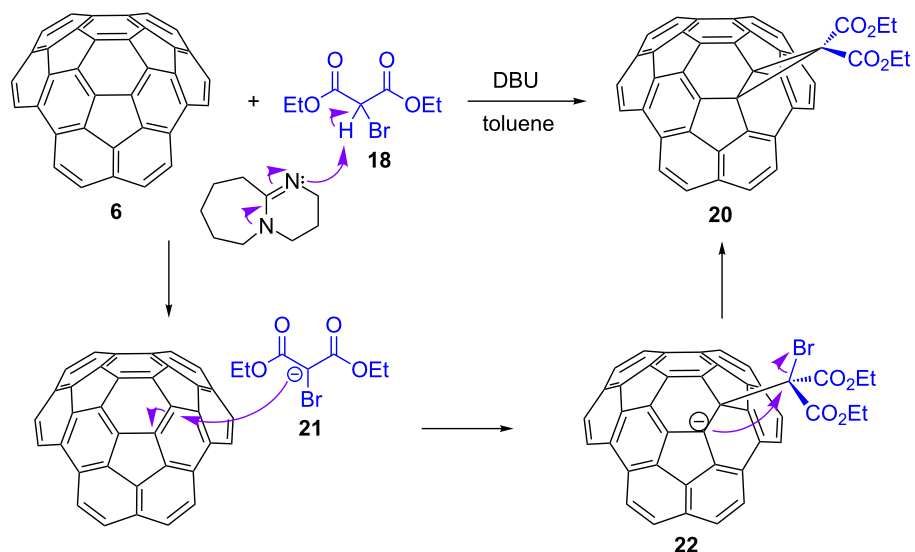
Based on mechanism studies on the corresponding reaction of fullerenes, the mechanism in Scheme 6 is proposed for the Bingel–Hirsch reaction of circumtrindene. The enolate generated by deprotonation of bromomalonate **18** with DBU functions as a nucleophile; it attacks one of the strongly pyramidalized carbon atoms of circumtrindene, and subsequent intramolecular displacement of the bromide generates the cyclopropanated circumtrindene **20**. As with fullerenes, this cyclopropanation reaction occurs exclusively at a 6:6-bond of circumtrindene.

In contrast to the highly symmetrical fullerene C_{60} , circumtrindene has three distinct sets of 6:6-bonds. Only structure **20**, however, is consistent with the ^1H and ^{13}C NMR spectra of the cyclopropanated circumtrindene obtained (C_s -symmetric with non-equivalent esters, see Supporting Information File 1). Thus, the reaction is site selective for the 6:6-bond at the point of greatest curvature on the convex surface (i.e., the carbon atoms with the greatest POAV angle, see Figure 5). Similar site selectivity for the 6:6-bond that incorporates the most pyramidalized carbon atoms has previously been observed in the functionalization of fullerene C_{70} [56].

As explained in the introductory section, curving a π -system lowers the energy of the LUMO as a consequence of both poorer π overlap and increased s-character in the atomic orbitals used for π -bonding. The unusually high reactivity of both fullerenes and circumtrindene towards nucleophiles is one manifestation of these lowered LUMO energies. In the initial nucleophilic attack (Scheme 6), the nucleophile adds to the site with the largest LUMO coefficient (see below for DFT calculations on the LUMO of circumtrindene).



Scheme 5: Bingel–Hirsch reaction of circumtrindene (**6**).



Scheme 6: Proposed mechanism for the Bingel–Hirsch reaction of circumtrindene (6).

This reaction also proceeds with excellent facial selectivity; the cyclopropane ring is formed exclusively on the convex face of circumtrindene. The different electron densities of the two faces reinforce the steric bias for addition to the convex face. As a consequence of the curved π -system, the convex face has less electron density than the concave face (see DFT calculations below), and that renders the convex side electronically more favorable for a nucleophilic attack.

Prato reaction

Cycloadditions to the π -system constitute another major family of fullerene reactions. In particular, 1,3-dipolar reagents readily add to the 6:6-bond of fullerene C₆₀, which acts as a good dipolarophile. Among such [3 + 2] cycloadditions, the reaction with azomethine ylides has found great popularity, because it leads to versatile pyrrolidine derivatives of C₆₀. The sources of the ylide can be iminium salts, aziridines, oxazolidines or silylated iminium compounds. In 1993, Prato and coworkers developed the protocol that is now used most commonly [31,32]. In the first step, an *N*-substituted amino acid (e.g., *N*-methylglycine) reacts with an aldehyde or ketone to generate an azomethine ylides in situ. Trapping of the ylide by a fullerene provides a fullerene-pyrrolidine derivative (8), as illustrated in Scheme 1.

In light of the great electrophilicity of circumtrindene in the Bingel–Hirsch reaction, it came as no surprise that circumtrindene can act as a good dipolarophile in a [3 + 2] cycloaddition reaction as well. Accordingly, the azomethine ylide 23 generated in situ from *N*-methylglycine and formaldehyde adds to circumtrindene in refluxing benzene to give the pyrrolidine derivative 24 (Scheme 7). As in the Bingel–Hirsch reaction, the

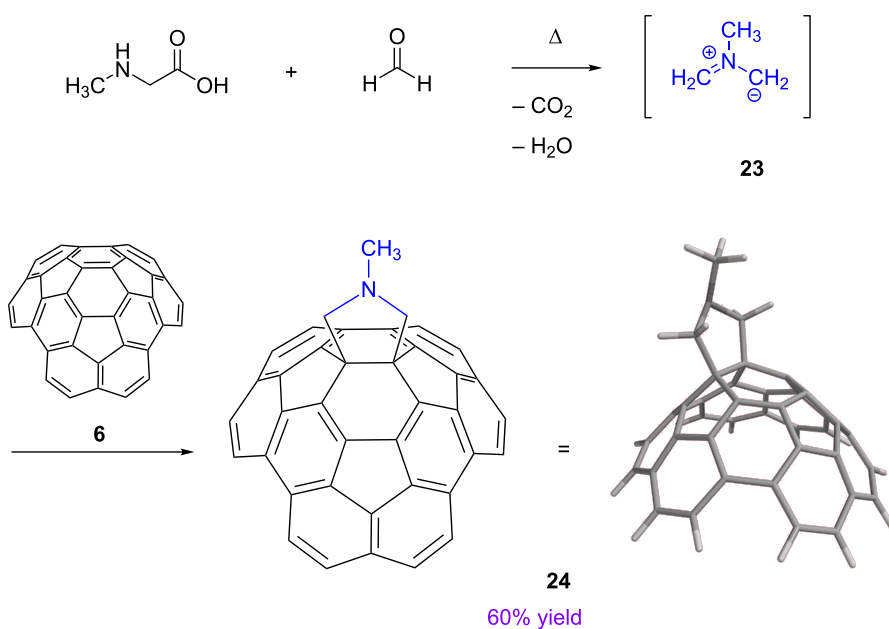
1,3-dipole reacts exclusively with the 6:6-bond in circumtrindene that contains the most pyramidalized carbon atoms in the molecule.

Considering the [3 + 2] cycloaddition processes in terms of frontier molecular orbitals, the dominant interaction should be that between the HOMO of the 1,3-dipole and the LUMO of the dipolarophile. In the Prato reaction in Scheme 7, the electron-rich ylide seeks out the carbon atoms of circumtrindene with the highest LUMO coefficient. As in the Bingel–Hirsch reaction above, the Prato reaction of circumtrindene likewise shows complete facial selectivity for the convex face.

Molecular orbitals and electrostatic potentials

Both of these fullerene-type functionalization reactions at the interior carbon atoms of circumtrindene show complete site and facial selectivity. The molecule behaves as an electrophile toward the bromoenolate (deprotonated bromomalonate) in the Bingel–Hirsch reaction and as an electrophile toward the 1,3-dipole (azomethine ylide) in the Prato reaction. Consequently, the LUMO of circumtrindene is the frontier molecular orbital that should control these interior functionalizations. As noted above, the distortion of the circumtrindene π -system imposed by its geodesic curvature is expected to lower the LUMO energy of the molecule substantially, thereby enhancing its reactivity (see Figure 2).

We have calculated the LUMO of circumtrindene at the B3LPY/6-31G* level of theory, using the curved geometry obtained by optimization at the same level of theory, and find that it is doubly degenerated. Figure 6 depicts one of these anti-



Scheme 7: Prato reaction of circumtrindene (**6**).

bonding orbitals in two different formats. As these images show, the LUMO of circumtrindene has its largest coefficients at the interior 6:6-bond composed of carbon atoms with the greatest degree of pyramidalization. This is precisely where the Bingel–Hirsch reaction and the Prato reaction of circumtrindene occur. The DFT calculations and the experimental results are therefore in complete agreement.

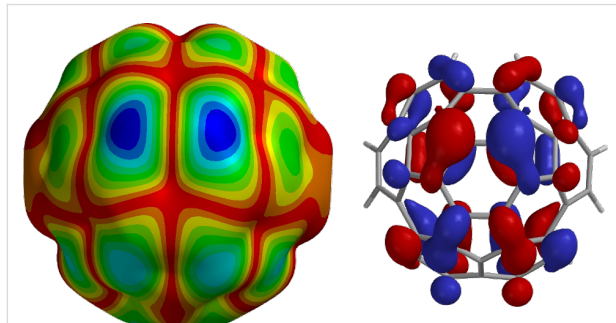


Figure 6: LUMO orbital map of circumtrindene (B3LYP/6-31G*). The darkest blue areas correspond to the regions with the largest LUMO coefficients.

As another consequence of π -system curvature, the electron densities for the two different faces of circumtrindene are expected to be unequal [57]. Density functional calculations (B3LYP/6-31G*) reveal that the outer surface of circumtrindene should be relatively electron deficient, resembling that of C₆₀, whereas the inside surface should be relatively electron rich (Figure 7). The high facial selectivity of these interior func-

tionalization reactions, giving exclusive covalent bond formation on the convex face with electron-rich reaction partners, is also consistent with the DFT calculations.

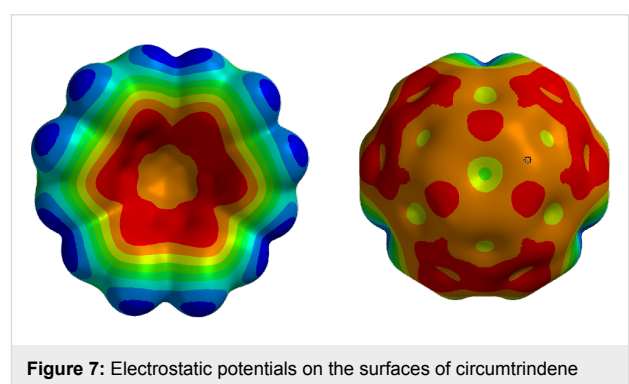


Figure 7: Electrostatic potentials on the surfaces of circumtrindene (B3LYP/6-31G*).

Peripheral functionalization of circumtrindene

Since the isolation and characterization of the first polycyclic aromatic hydrocarbons in the 1800s, a tremendous range of chemical reactions on such compounds has been developed [41,42]. Most of this chemistry involves chemical modifications on the edge carbons and has been used to functionalize the existing polyarenes and/or to extend them to larger PAHs. The most common class of reactions is the electrophilic aromatic substitution; however, free radical, nucleophilic addition, reduction, and oxidation reactions are also possible. To synthesize larger PAHs that are not available from natural sources or to make existing ones in more rational ways, functionalization

reactions can be followed by functional group interconversions and coupling reactions.

As discussed above, the synthesis of bowl-shaped geodesic polyarenes is non-trivial, owing to the great strain energy in such molecules. In this regard, it is generally easier to construct deeper bowls from already existing curved molecules, rather than to make them from planar building blocks. Circumtrindene (**6**) has a curvature comparable to C_{60} fullerene and, therefore, has much of the strain already built in that is needed to synthesize deeper bowls. Circumtrindene represents 60% of the network of sp^2 carbons that constitute C_{60} fullerene; to go to 70%, 80%, and 90% of C_{60} , the number of carbon atoms added in each step would be six, as in monoindeno-, diindeno-, and triindenocircumtrindene (**25–27**) (Figure 8). We envisioned that circumtrindene might be used as a building block from which to prepare deeper bowls by a peripheral functionalization method with standard aromatic chemistry.

Such functionalization reactions will also allow us to probe the magnetic environments of the two different faces of circumtrindene. As illustrated in Figure 8, the inside surface of circumtrindene is considerably more electron rich than the outside surface. If a suitable substituent could be placed on the rim of circumtrindene that hangs probe groups over both the concave and the convex faces without restraints, it would be possible to explore the different magnetic environments above the two surfaces experimentally.

Ring extension

To extend the bowl and π -system of circumtrindene, a reasonable first step would be functionalizing the rim of circumtrindene with a group that is suitable for subsequent coupling reactions, e.g., a bromine atom (Figure 9). Since the α -positions of the naphthalene subunits should be more reactive than the crowded β -positions, the site selectivity between the two types of rim carbon atoms was not expected to present a problem.

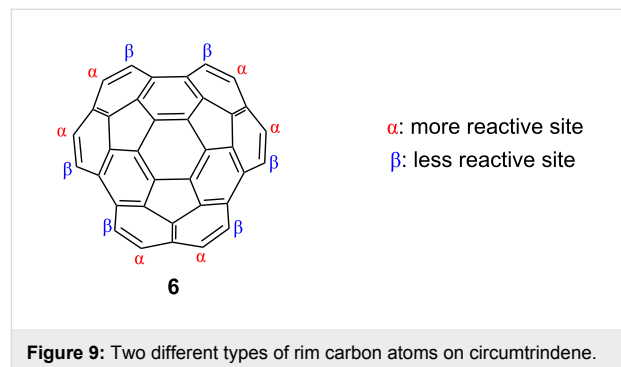


Figure 9: Two different types of rim carbon atoms on circumtrindene.

We were aware, however, that the interior carbon atoms of circumtrindene might also be brominated. Fullerenes are known to undergo bromination with elemental bromine in chlorinated solvents at room temperature [28]. To avoid the unwanted bromination at interior carbon atoms, the reaction conditions were carefully optimized (see Supporting Information File 1 for more details). In a reasonably dilute solution and with two

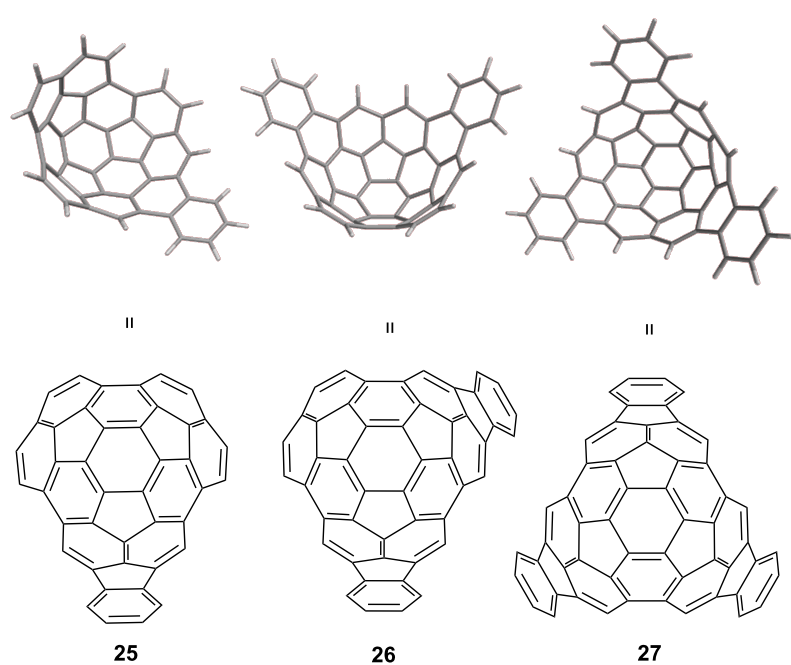
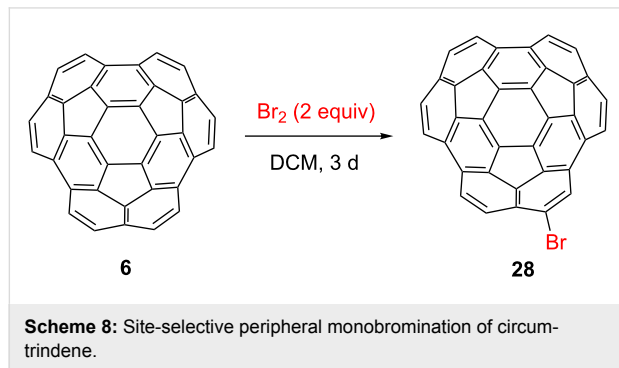


Figure 8: Monoindeno- (**25**), diindeno- (**26**), and triindenocircumtrindene (**27**).

equivalents of bromine, selective monobromination on the α -carbon of circumtrindene has been achieved with a quantitative yield (Scheme 8).



With bromocircumtrindene **28** in hand, Suzuki coupling reactions were carried out with commercially available boronic acids. The reaction proceeds smoothly with 2-bromophenylboronic acid in the presence of Pd(0) and a base to furnish **29** (Scheme 9). The Suzuki reaction proceeds reasonably well, despite the potential complication of the product undergoing a subsequent Suzuki coupling with the bromine of the phenyl group. The next step of the sequence, a ring closure to indeno-circumtrindene (**25**), was accomplished by FVP. The bromine in the *ortho*-position of the phenyl group is presumably lost by homolytic bond cleavage, and the resulting aryl radical then cyclizes [6]. Unfortunately, the reaction also generates a significant amount of circumtrindene by loss of the phenyl group during the FVP process [58].

In an effort to improve on the yield over the FVP process, solution-phase ring-closure methods were also examined. All attempts to close **29** to indeno-circumtrindene (**25**) by intramolecular arylations (Heck-type cyclization), unfortunately, were unsuccessful. Heck-type cyclizations work nicely with planar PAHs and even on moderately curved PAHs, such as corannulene [15,23,24]. Nonetheless, when applied to the indeno-circumtrindene synthesis, the reaction did not give any ring-closed

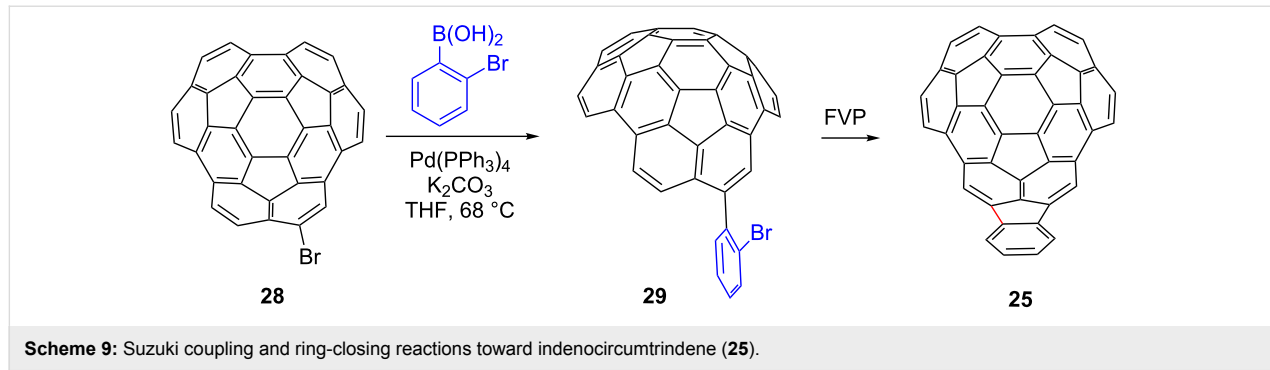
products. Oxidative addition of Pd(0) into one of the strained C–C bonds on the rim of circumtrindene might be competing with the desired cyclization [59]; however, we have not characterized any of the decomposition products from this reaction.

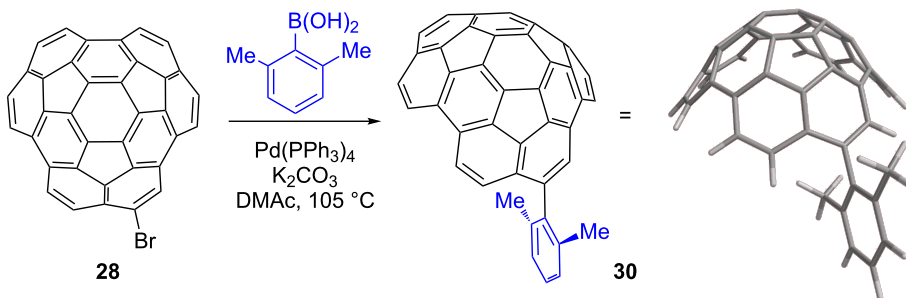
Magnetic environments

Induced diamagnetic ring currents strongly shield nuclei that are positioned over the faces of aromatic rings. In planar PAHs, the π -orbitals are perpendicular to the σ -bonds, the electrons are distributed equally on the two faces of the aromatic system, and the ring currents on the two faces are equivalent. When curvature is built into molecules, however, the electron densities of the two faces become unequal, and the shielding ability of the ring currents are no longer expected to be the same [60]. To probe the ring currents of the two faces of circumtrindene, we designed a compound with groups hanging over both the concave and the convex faces. Such a compound can be synthesized by replacing the bromo group of **28** with a 2,6-dimethyl substituted phenyl group (Scheme 10). The Suzuki coupling was again employed; compound **28** underwent the coupling reaction with 2,6-dimethylphenylboronic acid in the presence of a palladium catalyst [$\text{Pd}(\text{PPh}_3)_4$] and potassium carbonate (K_2CO_3) to furnish **30** in 60% yield.

In the ^1H NMR spectrum of **30**, the singlets for the two methyl groups appear at very different chemical shifts: 2.29 and 1.12 ppm. The difference in chemical shift between the two singlets is 1.17 ppm. On the basis of calculations described below, we conclude that the higher field resonance (1.12 ppm) corresponds to the methyl group over the concave side, whereas the lower field resonance (2.29 ppm) corresponds to the methyl group over the convex side.

Since the walls of circumtrindene consist of three naphthalene units, a 2,6-dimethylphenyl substituted naphthalene **31** was synthesized as a reference compound [61]. The naphthalene units of circumtrindene are arched, but the naphthyl group of **31** is planar; therefore, it provides a good comparison for shielding and de-shielding effects. The ^1H NMR spectrum of reference





Scheme 10: Suzuki coupling to prepare compound 30.

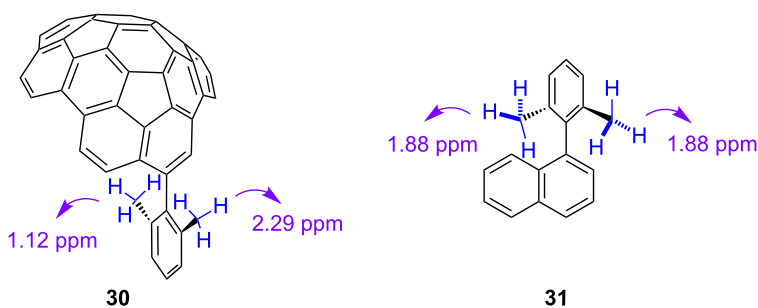
compound **31** shows that the methyl groups are magnetically equivalent, as anticipated, giving rise to a single peak at 1.88 ppm (Figure 10). A comparison between **30** and **31** reveals that the signal of the methyl group hanging over the concave side of circumtrindene is shifted upfield by 0.76 ppm, whereas that for the methyl group hanging over the convex side is shifted downfield by 0.41 ppm.

To assign the two NMR signals in the circumtrindene derivative, computational studies of the ^1H NMR chemical shifts were conducted (GIAO method at the B3LYP/6-31G** level of theory). The results of the calculation show good agreement between the experimentally obtained chemical shifts and those calculated, both for **30** and for reference compound **31** (Table 1). The data clearly indicate that the resonance of the methyl group over the concave face is the one shifted upfield by 0.76 ppm and that the signal for the methyl group over the

convex face is the one shifted downfield by 0.41 ppm. Thus, the concave face is substantially more shielding than the convex face. These data reveal a striking difference in the magnetic environments over the two different faces – convex and concave – of circumtrindene, which is a dramatic consequence of the curved π -system.

Conclusion

Bowl-shaped geodesic polyarenes can be considered the missing links between the “classic” flat PAHs and the spheroidal fullerenes. The present study has shown that open geodesic polyarenes can exhibit chemistry inherent to both classes of aromatics. The curved π -system induces unequal electron densities and unique magnetic environments on the two faces of circumtrindene, significant strain energy in the molecule, and non-identical bond lengths. The lowered LUMO energy and the interior localization of the LUMO coefficients

Figure 10: Chemical shifts of *ortho*-methyl groups in **30** and **31**.Table 1: Calculated (B3LYP/6-31G**) and experimentally obtained NMR chemical shifts of methyl groups in compounds **30** and **31**.

Compound	δ_{exp} (ppm)	δ_{calc} (ppm)
1-(2,6-dimethylphenyl)naphthalene (31)	1.88	1.94
1-(2,6-dimethylphenyl)circumtrindene (30-endo CH ₃)	1.12	1.13
1-(2,6-dimethylphenyl)circumtrindene (30-exo CH ₃)	2.29	2.32

enabled site-selective interior functionalization of circumtrindene by fullerene-type chemistry. On the other hand, the edge carbons, which are not present in fullerenes, still possess reactivity of common planar PAHs. Peripheral functionalization was conducted on those edge carbons, which allowed the π -system to be extended to make a larger bowl indenocircumtrindene (**25**), and the magnetic environments of the two different faces were probed. Computational studies not only supported the experimental data but also provided deeper insights into this curved polycyclic aromatic fullerene fragment.

Supporting Information

Supporting Information File 1

Experimental procedures and characterization data for all new compounds.

[<http://www.beilstein-journals.org/bjoc/content/supplementary/1860-5397-10-94-S1.pdf>]

Acknowledgements

This work was supported by the National Science Foundation. H.Y.C. is thankful for a Fellowship from the ACS Division of Organic Chemistry.

References

1. Barth, W. E.; Lawton, R. G. *J. Am. Chem. Soc.* **1966**, *88*, 380–381. doi:10.1021/ja00954a049
2. Lawton, R. G.; Barth, W. E. *J. Am. Chem. Soc.* **1971**, *93*, 1730–1745. doi:10.1021/ja00736a028
3. Kroto, H. W.; Heath, J. R.; O'Brien, S. C.; Curl, R. F.; Smalley, R. E. *Nature* **1985**, *318*, 162–163. doi:10.1038/318162a0
4. Scott, L. T.; Bronstein, H. E.; Preda, D. V.; Ansems, R. B. M.; Bratcher, M. S.; Hagen, S. *Pure Appl. Chem.* **1999**, *71*, 209–219. doi:10.1351/pac199971020209
5. Fleming, I. *Molecular Orbitals and Organic Chemical Reactions*; John Wiley & Sons: Chichester, 2010. doi:10.1002/9780470689493
6. Tsefrikas, V. M.; Scott, L. T. *Chem. Rev.* **2006**, *106*, 4868–4884. doi:10.1021/cr050553y
7. Wu, Y.-T.; Siegel, J. S. *Chem. Rev.* **2006**, *106*, 4843–4867. doi:10.1021/cr050554q
8. Sygula, A.; Rabideau, P. W. In *Carbon-Rich Compounds*; Haley, M. M.; Tykwiński, R. R., Eds.; Wiley-VCH: Weinheim, 2006; pp 529–565.
9. Petrukhina, M. A.; Scott, L. T., Eds. *ragments of Fullerenes and Carbon Nanotubes: Designed Synthesis, Unusual Reactions, and Coordination Chemistry*; John Wiley & Sons: Hoboken, 2011. doi:10.1002/9781118011263
10. Brown, R. F. C. *Pyrolytic Methods in Organic Chemistry: Application of Flow and Flash Vacuum Pyrolytic Techniques*; Academic Press: New York, 1980.
11. Brown, R. F. C. *Pure Appl. Chem.* **1990**, *62*, 1981–1986. doi:10.1351/pac199062101981
12. Necula, A.; Scott, L. T. *J. Anal. Appl. Pyrolysis* **2000**, *54*, 65–87. doi:10.1016/S0165-2370(99)00085-6
13. Scott, L. T.; Hashemi, M. M.; Meyer, D. T.; Warren, H. B. *J. Am. Chem. Soc.* **1991**, *113*, 7082–7084. doi:10.1021/ja00018a082
14. Scott, L. T.; Cheng, P.-C.; Hashemi, M. M.; Bratcher, M. S.; Meyer, D. T.; Warren, H. B. *J. Am. Chem. Soc.* **1997**, *119*, 10963–10968. doi:10.1021/ja972019g
15. Reisch, H. A.; Bratcher, M. S.; Scott, L. T. *Org. Lett.* **2000**, *2*, 1427–1430. doi:10.1021/o1005755p
16. Abdourazak, A. H.; Marcinow, Z.; Sygula, A.; Sygula, R.; Rabideau, P. W. *J. Am. Chem. Soc.* **1995**, *117*, 6410–6411. doi:10.1021/ja00128a052
17. Hagen, S.; Bratcher, M. S.; Erickson, M. S.; Zimmermann, G.; Scott, L. T. *Angew. Chem., Int. Ed. Engl.* **1997**, *36*, 406–408. doi:10.1002/anie.199704061
18. Imamura, K.; Takimiya, K.; Otsubo, T.; Aso, Y. *Chem. Commun.* **1999**, 1859–1860. doi:10.1039/a905860e
19. Scott, L. T.; Bratcher, M. S.; Hagen, S. *J. Am. Chem. Soc.* **1996**, *118*, 8743–8744. doi:10.1021/ja9621511
20. Ansems, R. B. M.; Scott, L. T. *J. Am. Chem. Soc.* **2000**, *122*, 2719–2724. doi:10.1021/ja993028n
21. Scott, L. T.; Boorum, M. M.; McMahon, B. J.; Hagen, S.; Mack, J.; Blank, J.; Wegner, H.; de Meijere, A. *Science* **2002**, *295*, 1500–1503. doi:10.1126/science.1068427
22. Scott, L. T. *Angew. Chem., Int. Ed.* **2004**, *43*, 4994–5007. doi:10.1002/anie.200400661
23. Jackson, E. A.; Steinberg, B. D.; Bancu, M.; Wakamiya, A.; Scott, L. T. *J. Am. Chem. Soc.* **2007**, *129*, 484–485. doi:10.1021/ja067487h
24. Steinberg, B. D.; Jackson, E. A.; Filatov, A. S.; Wakamiya, A.; Petrukhina, M. A.; Scott, L. T. *J. Am. Chem. Soc.* **2009**, *131*, 10537–10545. doi:10.1021/ja9031852
25. Sygula, A.; Xu, G.; Marcinow, Z.; Rabideau, P. W. *Tetrahedron* **2001**, *57*, 3637–3644. doi:10.1016/S0040-4020(01)00251-4
26. Sakurai, H.; Daiko, T.; Hirao, T. *Science* **2003**, *301*, 1878–1882. doi:10.1126/science.1088290
27. Butterfield, A. M.; Gilomen, B.; Siegel, J. S. *Org. Process Res. Dev.* **2012**, *16*, 664–676. doi:10.1021/op200387s
28. Hirsch, A.; Brettreich, M. *Fullerenes*; Wiley-VCH: Weinheim, 2004.
29. Bingel, C. *Chem. Ber.* **1993**, *126*, 1957–1959. doi:10.1002/cber.19931260829
30. Camps, X.; Hirsch, A. *J. Chem. Soc., Perkin Trans. 1* **1997**, 1595–1596. doi:10.1039/a702055d
31. Maggini, M.; Scorrano, G.; Prato, M. *J. Am. Chem. Soc.* **1993**, *115*, 9798–9799. doi:10.1021/ja00074a056
32. Prato, M.; Maggini, M. *Acc. Chem. Res.* **1998**, *31*, 519–526. doi:10.1021/ar970210p
33. Rubin, Y.; Khan, S.; Freedberg, D. I.; Yeretzian, C. *J. Am. Chem. Soc.* **1993**, *115*, 344–345. doi:10.1021/ja00054a049
34. Hirsch, A.; Soi, A.; Karfunkel, H. R. *Angew. Chem., Int. Ed. Engl.* **1992**, *31*, 766–768. doi:10.1002/anie.199207661
35. McEwen, C. N.; McKay, R. G.; Larsen, B. S. *J. Am. Chem. Soc.* **1992**, *114*, 4412–4414. doi:10.1021/ja00037a064
36. Murata, M.; Murata, Y.; Komatsu, K. *Chem. Commun.* **2008**, 6083–6094. doi:10.1039/b811738a
37. Murata, M.; Murata, Y.; Komatsu, K. Molecular Surgery toward Organic Synthesis of Endohedral Fullerenes. In *Chemistry of Nanocarbons*; Akasaka, T.; Wudl, F.; Nagase, S., Eds.; John Wiley & Sons: Chichester, 2010; pp 215–237. doi:10.1002/9780470660188.ch8
38. Carbon atoms on the rims of PAHs can be either methine carbons, with a hydrogen atom or a substituent attached, (belonging to only one ring) or quaternary (belonging to two rings); “interior” carbon atoms belong to three rings.

39. Preda, D. V.; Scott, L. T. *Tetrahedron Lett.* **2000**, *41*, 9633–9637. doi:10.1016/S0040-4039(00)01734-2

40. Bronstein, H. E.; Scott, L. T. *J. Org. Chem.* **2008**, *73*, 88–93. doi:10.1021/jo7018224

41. Harvey, R. G. *Polycyclic Aromatic Hydrocarbons*; Wiley-VCH: New York, N. Y., 1997.

42. Clar, E. *Polycyclic Hydrocarbons*; Academic Press: New York, 1964.

43. Haddon, R. C.; Scott, L. T. *Pure Appl. Chem.* **1986**, *58*, 137–142.

44. Haddon, R. C. *J. Am. Chem. Soc.* **1987**, *109*, 1676–1685. doi:10.1021/ja00240a013

45. Bronstein, H. E.; Choi, N.; Scott, L. T. *J. Am. Chem. Soc.* **2002**, *124*, 8870–8875. doi:10.1021/ja0123148

46. Scott, L. T.; Haschemi, M. M.; Bratcher, M. S. *J. Am. Chem. Soc.* **1992**, *114*, 1920–1921. doi:10.1021/ja00031a079

47. Eisenberg, D.; Shenhar, R.; Rabinovitz, M. Anions of Buckybowls. In *Fragments of Fullerenes and Carbon Nanotubes: Designed Synthesis, Unusual Reactions, and Coordination Chemistry*; Petrukhina, M. A.; Scott, L. T., Eds.; John Wiley & Sons: Hoboken, 2011; pp 63–93. doi:10.1002/9781118011263.ch3

48. Boorum, M. M.; Scott, L. T. The synthesis of tris-annulated benzenes by aldol trimerization of cyclic ketones. In *Modern Arene Chemistry*; Astruc, D., Ed.; Wiley-VCH: Weinheim, 2002; pp 20–31. doi:10.1002/3527601767.ch1

49. Amick, A. W.; Scott, L. T. *J. Org. Chem.* **2007**, *72*, 3412–3418. doi:10.1021/jo070080q

50. *Gaussian 09*, Revision C.01; Gaussian, Inc.: Wallingford, CT, 2010. All the calculations were performed at the B3LYP/6-31G** level of theory.

51. Forkey, D. M.; Attar, S.; Noll, B. C.; Koerner, R.; Olmstead, M. M.; Balch, A. L. *J. Am. Chem. Soc.* **1997**, *119*, 5766–5767. doi:10.1021/ja970845j

52. The POAV angle at the largest curved point of the molecule was considered.

53. Bühl, M.; Hirsch, A. *Chem. Rev.* **2001**, *101*, 1153–1184. doi:10.1021/cr990332q

See for more details on the X-ray structure of fullerene-C₆₀, which shows that the 6:6-bond of C₆₀ is 1.355 Å; the 6:5-bond is 1.467 Å.

54. The ¹H NMR spectrum of corannulene (C₂₀H₁₀) shows a single resonance at 7.8 ppm, and the ¹H NMR spectrum of coronene (C₂₄H₁₂) shows a single resonance at 8.9 ppm.

55. Ansems, R. B. M. Ph.D. Thesis, Boston College, Chestnut Hill, Massachusetts, 2004.

See for additional examples.

56. Hawkins, J. M.; Meyer, A.; Solow, M. A. *J. Am. Chem. Soc.* **1993**, *115*, 7499–7500. doi:10.1021/ja00069a058

57. Klärner, F.-G.; Panitzky, J.; Preda, D.; Scott, L. T. *J. Mol. Model.* **2000**, *6*, 318–327. doi:10.1007/PL00010733

58. Xue, X. Ph.D. Thesis, Boston College, Chestnut Hill, Massachusetts, 2008.

See for an example of an investigation of the phenyl-loss mechanism is currently on-going in the authors' laboratory. We have observed similar phenyl loss processes in other FVP reactions with phenyl substituted substrates.

59. Shaltout, R. M.; Sygula, R.; Sygula, A.; Fronczek, F. R.; Stanley, G. G.; Rabideau, P. W. *J. Am. Chem. Soc.* **1998**, *120*, 835–836. doi:10.1021/ja973454d

60. Monaco, G.; Scott, L. T.; Zanasi, R. *J. Phys. Chem. A* **2008**, *112*, 8136–8147. doi:10.1021/jp8038779

61. Lipshutz, B. H.; Siegmann, K.; Garcia, E.; Kayser, F. *J. Am. Chem. Soc.* **1993**, *115*, 9276–9282. doi:10.1021/ja00073a051

License and Terms

This is an Open Access article under the terms of the Creative Commons Attribution License (<http://creativecommons.org/licenses/by/2.0>), which permits unrestricted use, distribution, and reproduction in any medium, provided the original work is properly cited.

The license is subject to the *Beilstein Journal of Organic Chemistry* terms and conditions: (<http://www.beilstein-journals.org/bjoc>)

The definitive version of this article is the electronic one which can be found at:

[doi:10.3762/bjoc.10.94](http://10.3762/bjoc.10.94)

Homochiral BINOL-based macrocycles with π -electron-rich, electron-withdrawing or extended spacing units as receptors for C₆₀

Marco Caricato¹, Silvia Díez González¹, Idoia Arandia Ariño¹
and Dario Pasini^{*1,2}

Full Research Paper

Open Access

Address:

¹Department of Chemistry, University of Pavia, Viale Taramelli 10, 27100 Pavia, Italy and ²INSTM Research Unit, Department of Chemistry, University of Pavia, 27100 Pavia, Italy

Email:

Dario Pasini* - dario.pasini@unipv.it

* Corresponding author

Keywords:

BINOL; C₆₀; carbon nanomaterials; carbon nanostructures; chirality; macrocycles; sensors; supramolecular chemistry

Beilstein J. Org. Chem. **2014**, *10*, 1308–1316.

doi:10.3762/bjoc.10.132

Received: 09 December 2013

Accepted: 15 May 2014

Published: 06 June 2014

This article is part of the Thematic Series "Functionalized carbon-nanomaterials".

Associate Editor: S. C. Zimmerman

© 2014 Caricato et al; licensee Beilstein-Institut.

License and terms: see end of document.

Abstract

The “one-pot” synthesis of several homochiral macrocycles has been achieved by using π -electron-rich, electron-deficient or extended aromatic dicarboxylic acids in combination with an axially-chiral dibenzylidene alcohol, derived from enantiomerically-pure BINOL. Two series of cyclic adducts with average molecular D_2 and D_3 molecular symmetries, respectively, have been isolated in pure forms. Their yields and selectivities deviate substantially from statistical distributions. NMR and CD spectroscopic methods are efficient and functional in order to highlight the variability of shapes of the covalent macrocyclic frameworks. The larger D_3 cyclic adducts exhibit recognition properties towards C₆₀ in toluene solutions (up to $\log K_a = 3.2$) with variable stoichiometries and variable intensities of the charge-transfer band upon complexation.

Introduction

Shape persistent macrocycles are carbon-based nanomaterials and are more and more in demand. They enrich the molecular toolkit available to a variety of disciplines, e.g., supramolecular chemistry and materials science [1-4]. Shape persistency properties are traditionally sought after for enhancing the recognition toward suitable guests [5-10], and for the self-assembly, of stable organic nanotubes from the macrocyclic structures as molecular building blocks [11]. Cyclic peptides [12-14], phenylacetylene macrocycles [15], amide-containing macro-

cycles [16], and urea-based structures [17] have all been exploited to develop the nanotube concept.

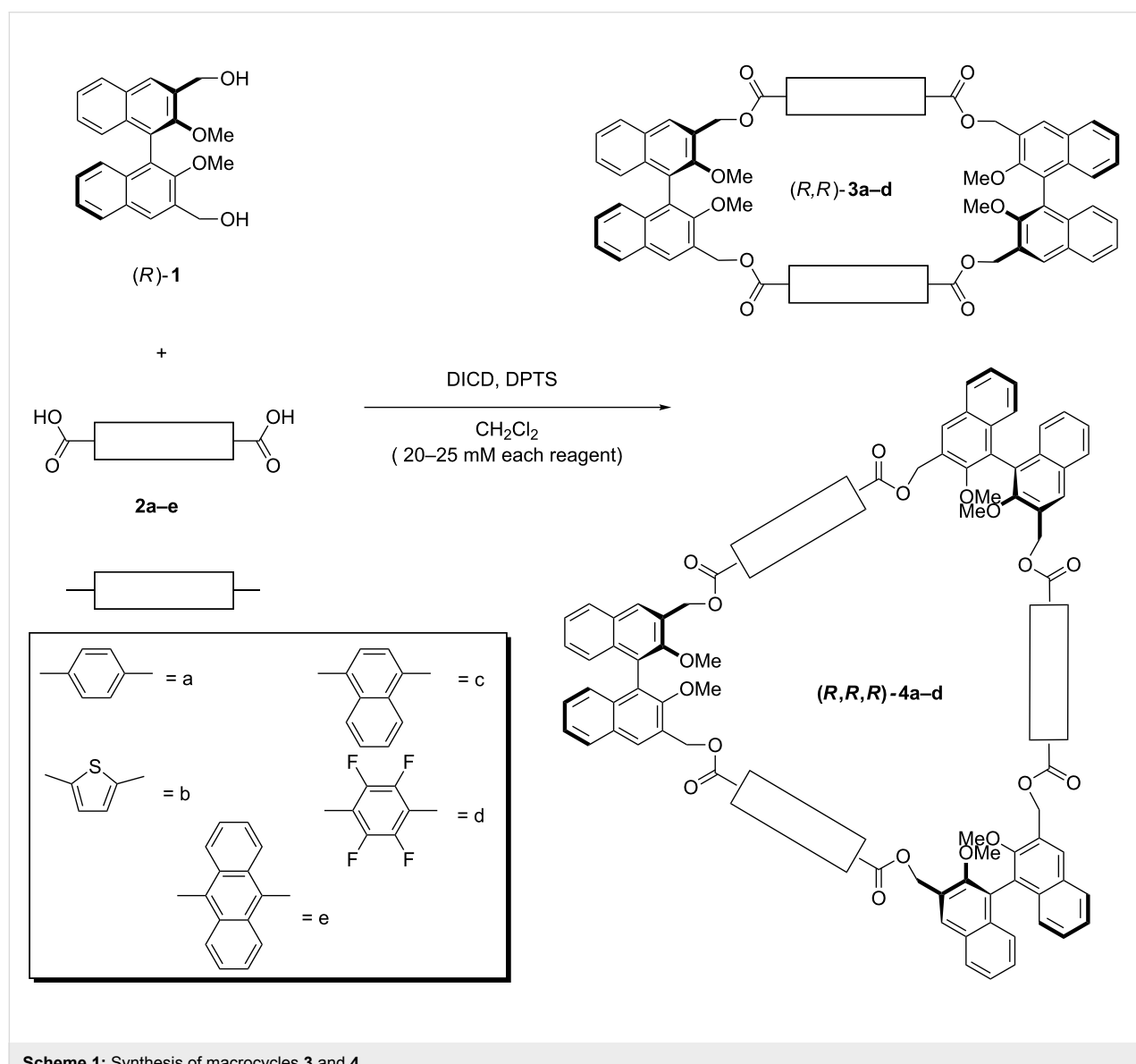
Efficient supramolecular receptors for C₆₀ and higher fullerenes have been already reported in the literature and research in this area is still very active [18,19]. Jasti and co-workers have demonstrated how cyclo-*p*-phenylenes of suitable size are able to form very stable complexes with C₆₀ [20]. Aida and co-workers have reported on π -electron rich, porphyrin-based

cyclic structures, which are able to selectively recognize C_{60} [21]. In subsequent work, similar porphyrin-based systems have been made chiral by substituting one of the nitrogen atoms, and the enantioselective complexation of chiral higher fullerenes (C_{84}) has been demonstrated [22]. Complexes of C_{60} and C_{70} with large, calix-type macrocycles formed by π -electron deficient pyridine aromatic rings bridged by a nitrogen heteroatom, have been reported and characterized in terms of thermodynamic stability by using fluorescence measurements [23]. Martin, Perez et al. have reported on a series of extended TTF units able to form strong complexes with C_{60} and C_{70} in organic solutions [24,25].

We have recently reported an efficient protocol for the preparation of several chiral macrocycles incorporating BINOL (1,1'-

bi-2-naphthol) units, through the formation of bridging ester functionalities, which ensure chemical inertness for the purposes of supramolecular sensing, recognition, or self-assembly. We have shown their application in the chiroptical sensing of organic or ionic species [26–39]. We have previously reported how some of our systems are able to sense C_{60} in toluene solutions, and how the recognition behavior is shape selective [28]. In the case of extended [2 + 2] macrocycles, induced CD activity in the characteristic UV–vis absorption bands of C_{60} showed how the chirality of the macrocyclic units could be transferred to the overall supramolecular ensemble [30].

In this paper, we extend on our previous studies by describing the synthesis of optically-active D_2 and D_3 macrocycles, whose



spacing units are systematically changed in terms of their electronic nature, and we report on the recognition behavior towards C₆₀.

Results and Discussion

Design, synthesis and spectroscopic characterization

In our design approach, rigid, aromatic dicarboxylic acid spacers are combined with a BINOL derivative with masked phenol functionalities in the 2,2'-positions and benzylic alcohol functionalities in the 3,3'-positions (diol **1** in Scheme 1). The incorporation of sp³ methylene carbon atoms in the cyclic structure adds a certain degree of conformational freedom to the covalent structure. This feature balances the distortion of the planarity which is inevitably introduced by the binaphthyl units. Enantiopure (*R*)-**1** [40] was used in all cases, in order to achieve homochiral macrocycles. As previously reported in the case of terephthalic acid, both the [2 + 2] and the [3 + 3] macrocycles (compounds **3** and **4** in Scheme 1) were obtained.

The compounds have average molecular *D*₂ and *D*₃ point group symmetries, respectively. Our optimized esterification reaction protocol is carried out at intermediate dilution levels (each reagent 20–25 mM) in CH₂Cl₂. Several dicarboxylic acids with varying electronic structures and steric demands were tested. In the case of 9,10-anthracedicarboxylic acid (**2e**), no cyclic product could be obtained, and only oligomeric, baseline materials were detected. Isolated yields, after column chromatography, are reported in Table 1. The yields and selectivities of isolated products are unusual, considering that the [3 + 3] macrocycles are sometimes formed with similar synthetic efficiency as the [2 + 2] macrocycles (entries 2 and 3 in Table 1). It is very likely that those conformational preferences dominate in this context.

Table 1: Yields of isolated cyclized products.^a

Entry	Diacid precursor	Macrocyclic 3	Macrocyclic 4
1 ^b	2a	18	9
2	2b	6	4
3	2c	8	5
4	2d	18	4
5	2e	0	0

^aIsolated yield after column chromatography. For conditions, see experimental. ^bData taken from ref. [28].

The macrocycles were correctly identified by NMR spectroscopy and mass spectrometry (see Supporting Information File 1). The room temperature ¹H NMR spectra for all cyclic compounds display only one set of signals for each group of

symmetry-related proton resonances, showing that all dynamic processes are fast on the NMR timescale at this temperature (Figure 1 and Figure 2).

In the case of macrocycles **3**, significant differences in the chemical shift of the proton resonances of the methoxy groups (Table 2, from 3.27 ppm to 3.48 ppm) and of the BINOL H-4,4' proton resonances (from 8.02 ppm to 8.19 ppm) could be detected. These significant differences tend to cancel out in the case of the larger macrocycles **4**, pointing to a more flexible nature of the latter class of macrocycles. In the case of all the *D*₃ macrocycles **4**, the CH₂ benzylic proton resonances appear as collapsed AB systems at room temperature (Figure 2). They demonstrate a peculiar arrangement for the two diastereotopic methylene protons, substantially different from that of the more rigid *D*₂ symmetrical analogues **3**, in which the methylene proton resonances appear as well-defined AB systems. Small amounts (5–10%) of impurities in macrocycles **4** were difficult to remove by flash column chromatography. These byproducts were tentatively characterized as higher oligomers from their NMR pattern.

Table 2: Selected chemical shifts for compounds in CDCl₃ (25 °C).^a

Entry	Compound	Binol-H4,4' ^b	Benzylic CH ₂	OCH ₃
1 ^c	3a	8.19	5.63 ^d	3.48
2	3b	8.10	5.60 ^d	3.27
4	3c	8.02	5.72 ^d	3.34
5	3d	8.15	5.67 ^d	3.44
6 ^c	4a	8.15	5.68 ^e	3.35
7	4b	8.10	5.63 ^e	3.31
8	4c	8.13	5.79 ^e	3.35
9	4d	8.11	5.71 ^e	3.29

^aAll spectra recorded at 5–10 mM sample concentration. ^bResonances related to the singlet corresponding to the proton in the 4,4'-positions of the BINOL skeleton. ^cData taken from ref. [28]. ^dMultiplicity of the ¹H NMR signal: Quartet, AB system. ^eMultiplicity of the ¹H NMR signal: collapsed AB system.

The UV–vis absorption spectra in EtOH of a selection of macrocyclic compounds (**3b**, **3d**, **4b** and **4d** with π -electron rich and π -electron deficient spacing units, Figure S1, Supporting Information File 1) show the major absorption band centered around 230 nm, typical of the binaphthyl chromophore [41]. Circular dichroism spectroscopy of the same macrocycles show the exciton couplet typical of binaphthyl moieties (Figure 3), corresponding to the maximum absorption band in the UV–vis spectra.

Induced CD activity associated with other absorption bands in the UV–vis spectra (particularly intense in the case of **3b** and

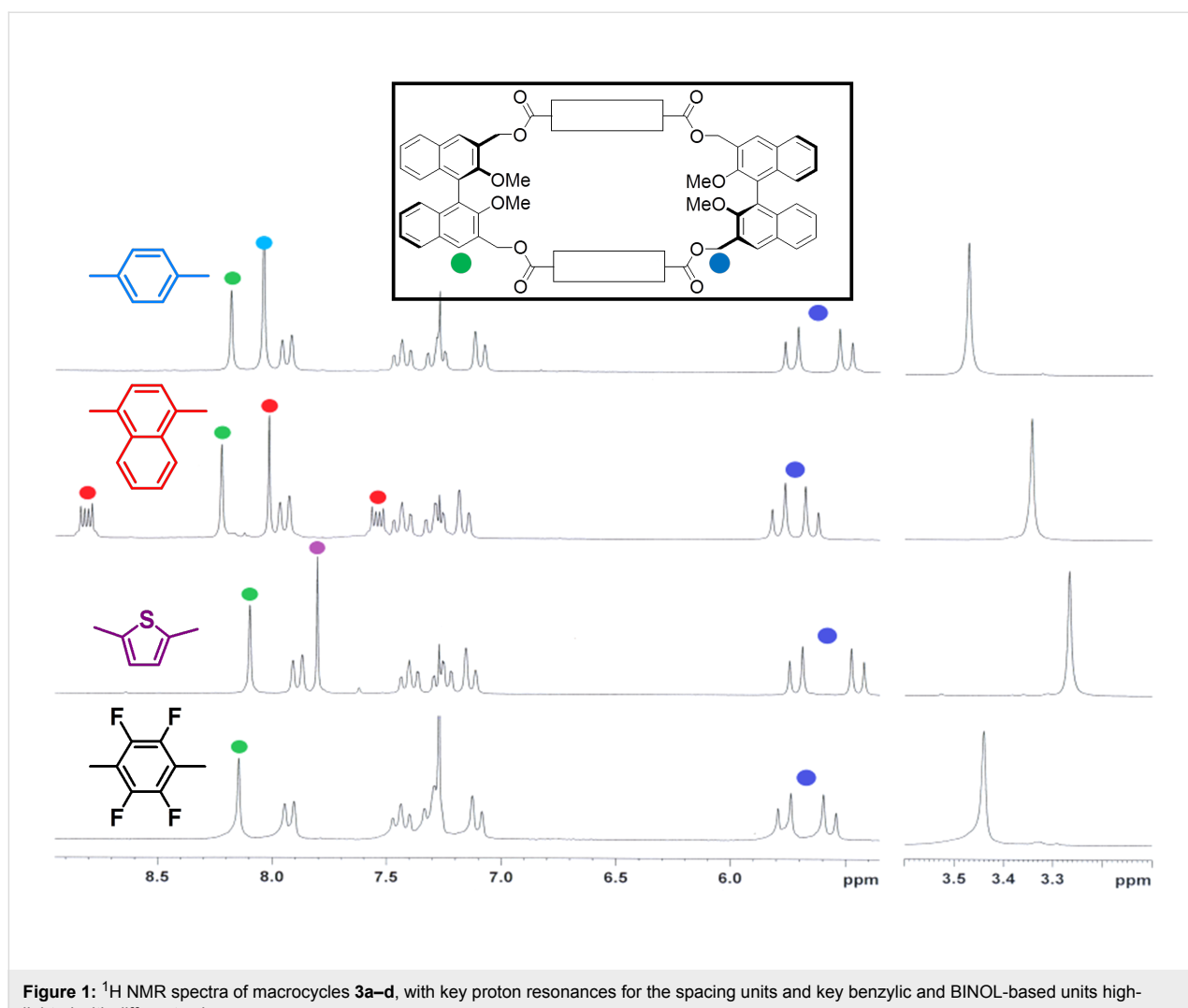


Figure 1: ^1H NMR spectra of macrocycles **3a–d**, with key proton resonances for the spacing units and key benzylic and BINOL-based units highlighted with different colors.

4b, Figure S1, Supporting Information File 1) could not be detected. The intensity of the low energy component of the triplet is significantly different in the case of the smallest macrocycles ($\Delta\epsilon$ values of -113 for **3d** and -326 for **3b**). For substituted 2,2'-binaphthol derivatives, it has been reported that the low energy component values are related to variations of the dihedral angle between the naphthyl units due to the steric hindrance of the substituents in the 2,2'-positions [41]. Since compounds **3** possess the same substituent (OMe) in the 2,2'-positions, the variability of these values and thus the variation of the dihedral angle of the binaphthyl units, must depend on the buttressing effects of the neighbouring 3,3'-benzylic ester positions. They, in turn, can derive from the differing macrocyclic structural flexibility or from an equally rigid conformation altering the coupling of the benzylic protons. These data corroborate the NMR data in highlighting that the influence of the differing geometrical shapes of the spacing units on the macrocyclic conformation is strong in the case of the more

rigid [2 + 2] macrocycles **3**, but it tends to cancel out in the case of the more flexible [3 + 3] macrocycles **4**.

Complexation studies

Titrations of a solution of C_{60} with increasing amounts of macrocycles **3b–d** in toluene solutions resulted in no detectable changes in the UV-vis spectra, similarly to what was previously described for the [2 + 2] adduct **3a**. In the case of macrocycles **4b** and **4d**, instead, an enhancement of the absorption band above 400 nm could be readily detected (Figure 4). This behavior is similar to previously reported cases in terms of band shape, involving both cyclic π -electron rich and π -electron deficient substrates [23,25].

The calculated thermodynamic binding constants are reported in Table 3. In the case of macrocycle **4d**, a 1:1 binding isotherm could be efficiently employed to fit the titration data, strongly indicating that a 1:1 binding behavior between the host and the

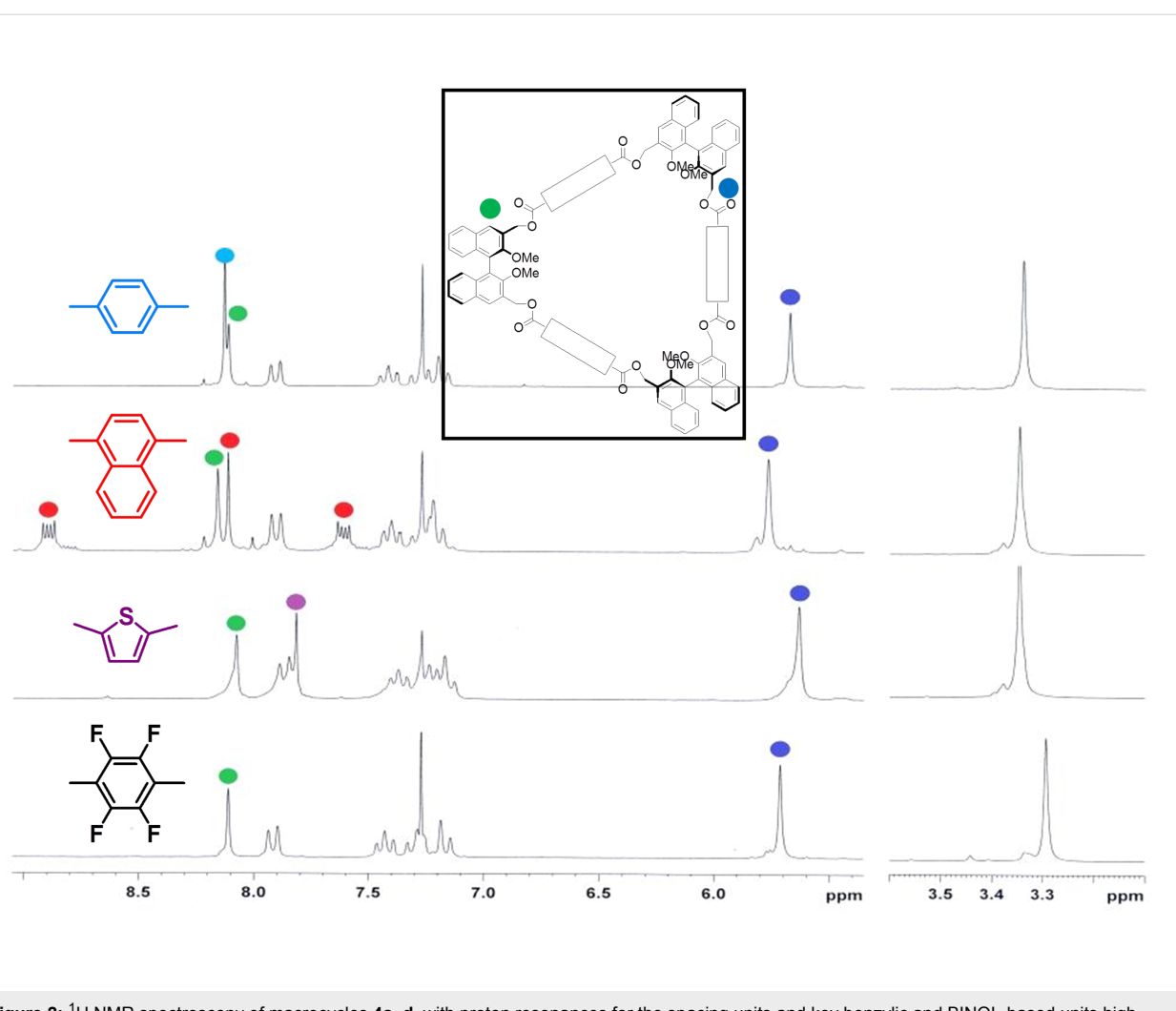


Figure 2: ^1H NMR spectroscopy of macrocycles **4a–d**, with proton resonances for the spacing units and key benzylic and BINOL-based units highlighted with color.

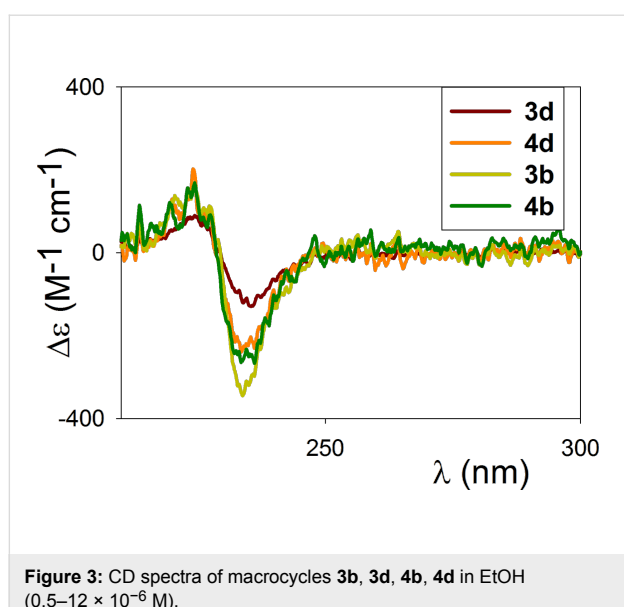


Figure 3: CD spectra of macrocycles **3b**, **3d**, **4b**, **4d** in EtOH ($0.5\text{--}12 \times 10^{-6}$ M).

C_{60} guest is predominant in solution. The insertion of the π -electron deficient tetrafluoroterephthalic moieties lowers the affinity with the electron acceptor C_{60} guest, when compared with the reference host **4a** (Table 3, entry 1 vs entry 4). This is reasonable as the C_{60} core is an acceptor of electron density, so

Table 3: Thermodynamic binding constants of the complexation of C_{60} with macrocycles **4** in toluene (25 °C).^a

Entry	Compound	k_a ^b	Hill coefficient ^c
1 ^c	4a	1100 ± 100	1
2	4b	1600 ± 200	1.5
3	4c	No binding	–
4	4d	200 ± 40	1

^a C_{60} concentration constant at 1.8×10^{-4} M in all cases. The k_a values are the average of two independent titrations. ^b M^{-1} . ^cData taken from ref. [28].

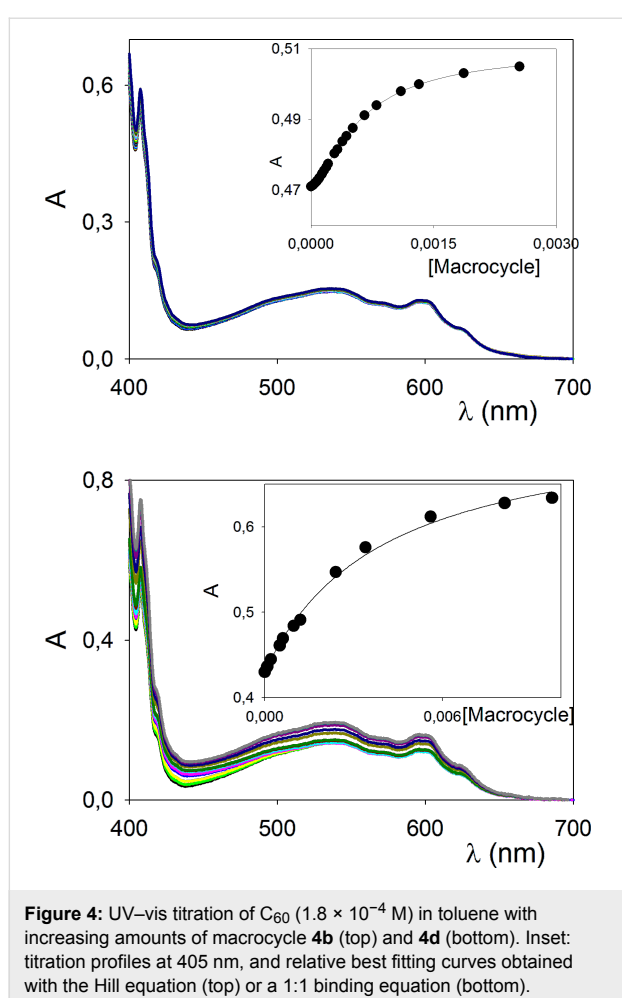


Figure 4: UV-vis titration of C_{60} (1.8×10^{-4} M) in toluene with increasing amounts of macrocycle **4b** (top) and **4d** (bottom). Inset: titration profiles at 405 nm, and relative best fitting curves obtained with the Hill equation (top) or a 1:1 binding equation (bottom).

that π -electron neutral or rich substrates are more suitable for complexation.

In the case of **4b**, an acceptable fitting with the 1:1 binding equation could not be achieved, indicating multiple binding stoichiometries in solution. Data treatment with the Hill equation [42] gave an average binding constant of 1600 M^{-1} , thus confirming a higher affinity for the π -electron rich thiophene-derived spacer units. The Hill coefficient [43,44] suggests the presence of concomitant 1:1 and 1:2 C_{60} :macrocycle complexes in solution.

Even more interestingly, the titration profiles in the insets of Figure 4 display marked differences for the calculated molar absorbivity values of the **4b**@ C_{60} and **4d**@ C_{60} complexes at saturation (2800 and $4000\text{ M}^{-1}\text{ cm}^{-1}$, respectively). In the case of **4c**, no variation in the UV-vis spectra was detected. It is likely that in this case the steric demand of the naphthalene spacing units does not allow for the optimal positioning of the C_{60} and the formation of a **4c**@ C_{60} complex of measurable stability.

Conclusion

We have reported on the synthesis and characterization of novel homochiral macrocycles, built upon resolved 1,1'-binaphthyl scaffolds, which incorporate either π -electron rich, π -electron deficient or π -extended spacing units. The cyclic adducts are obtained in an acceptable yield in a one-pot synthetic procedure, and easily purified by flash column chromatography. NMR and CD spectroscopy give an insight into the conformational properties of these cyclic structures and indicate a more rigid structure for the [2 + 2] adducts, whereas the [3 + 3] adducts are more flexible. The latter are also capable of binding C_{60} in toluene solutions. Both the thermodynamic strengths and the optical absorptivity coefficients of the complexes in solution give insights into the role of nonspecific host–guest interactions (such as π – π stacking) for the overall stabilization of the complexes. We are currently designing binaphthyl-based hosts for the enantioselective recognition and separation of higher fullerenes and chiral nanotubes. These binaphthyl-based hosts may also be utilized as chiroptical sensors for chiral carbon-based nanomaterials in functional nanochemical environments.

Experimental

General experimental. All commercially available compounds were purchased from commercial sources and used as received. Compounds (*R*)-**1** [40], **3a** [28], **4a** [28] and *p*-toluenesulfonic acid 4-dimethylaminopyridinium salt (PTSA-DMAP) [45] were prepared according to literature procedures. THF (Na, benzophenone) and CH_2Cl_2 (CaH_2) were dried before use. Analytical thin-layer chromatography was performed on silica gel, chromophore loaded, and with commercially available plates. Flash chromatography was carried out by using silica gel (pore size 60 \AA , 230–400 mesh). 1H and ^{13}C NMR spectra were recorded from solutions in $CDCl_3$ on 200 or 300 MHz spectrometer with the solvent residual proton signal or tetramethylsilane as a standard. The UV-vis spectroscopic studies were recorded by means of commercially-available spectrophotometers. Mass spectra were recorded by using an electrospray ionization instrument. Optical rotations were measured on a polarimeter with a sodium lamp ($\lambda = 589\text{ nm}$) and are reported as follows: $[\alpha]_D^{rt}$ ($c = g$ (100 mL solvent) $^{-1}$). CD spectroscopy was performed with a spectropolarimeter; spectra were recorded at $25\text{ }^\circ\text{C}$ at a scanning speed of 50 nm min^{-1} and were background corrected. The reported spectra are the instrument-averaged results of four consecutive scans.

General procedure for the preparation of macrocycles **3 and **4**.** In a manner similar to the procedure described in [28], a solution of DICD (diisopropylcarbodiimide, 3 equivalents vs diol and dicarboxylic acid) in a minimum amount of dry CH_2Cl_2 is added to a solution of the appropriate dicarboxylic acid

(20–25 mM), *(R*)-**1** (20–25 mM), PTSA-DMAP (2 equivalents) in dry CH_2Cl_2 under stirring and N_2 . The solution is stirred overnight, and then H_2O (10 mL) is added. The aqueous phase is extracted with CH_2Cl_2 (3×), the organic phase is washed with H_2O (3×) and dried (MgSO_4). The products are then purified by flash chromatography.

Macrocycles *(R,R*)-3b** and *(R,R,R*)-**4b**.** From 2,5-thiophenedi-carboxylic acid (115 mg, 0.67 mmol, 1 equiv), DICD (312 μL , 2.01 mmol, 3 equiv), *(R*)-**1** (250 mg, 0.67 mmol, 1 equiv), PTSA-DMAP (414 mg, 1.337 mmol, 2 equiv). Purified by flash column chromatography (hexanes/EtOAc 8:2 to 7:3) to yield **3b** (21 mg, 6%) and **4b** (13 mg, 4%) as white solids. *(R,R*)-**3b**. $[\alpha]_D^{25} +54$ (*c* 0.0015, CH_2Cl_2); ESIMS *m/z* (%): 1043 ([M + Na]⁺, 100); ¹H NMR (CDCl_3 , 200 MHz, 25 °C) δ 8.10 (s, 4H, binaphthyl), 7.89 (d, 4H, binaphthyl), 7.81 (s, 4H, thiophene), 7.38 (t, 4H, binaphthyl), 7.27 (m, 4H, binaphthyl), 7.16 (d, 4H, binaphthyl), 5.60 (dd, 8H, CH_2), 3.27 (s, 12H, -OCH₃); ¹³C NMR (CDCl_3 , 75 MHz, 25 °C) δ 161.3 (Cq), 155.9 (Cq), 138.2 (Cq), 134.6 (Cq), 133.5 (CH), 132.9 (CH), 130.0 (Cq), 128.3 (CH), 128.2 (Cq), 127.1 (CH), 125.5 (CH), 125.0 (CH), 124.2 (Cq), 64.2 (CH₂), 61.4 (CH₃). *(R,R,R*)-**4b**. $[\alpha]_D^{25} +43$ (*c* 0.0015, CH_2Cl_2); ESIMS *m/z* (%): 1553 ([M + Na]⁺, 100); ¹H NMR (CDCl_3 , 200 MHz, 25 °C) δ 8.10 (s, 6H, binaphthyl), 7.95–7.80 (m, 12H, binaphthyl + thiophene), 7.35 (t, 6H, binaphthyl), 7.5–7.1 (m, 12H, binaphthyl), 5.63 (s, 12H, CH_2), 3.31 (s, 18H, OCH₃); ¹³C NMR (CDCl_3 , 75 MHz, 25 °C) δ 161.2 (Cq), 154.9 (Cq), 138.7 (Cq), 134.3 (Cq), 133.3 (CH), 130.8 (CH), 130.1 (Cq), 128.5 (Cq), 128.1 (CH), 126.9 (CH), 125.5 (CH), 125.1 (CH), 124.4 (Cq), 63.6 (CH₂), 61.3 (CH₃).

Macrocycles *(R,R*)-3c** and *(R,R,R*)-**4c**.** From 1,4-naphthalenedi-carboxylic acid (144 mg, 0.67 mmol, 1 equiv), DICD (312 μL , 2.0 mmol, 3 equiv), *(R*)-**1** (250 mg, 0.67 mmol, 1 equiv), PTSA-DMAP (414 mg, 1.34 mmol, 2 equiv). Purified by flash column chromatography (hexanes/EtOAc 7:3) to yield **3c** (30 mg, 8%) and **4c** (17 mg, 5%) as white solids. *(R,R*)-**3c**. $[\alpha]_D^{25} +97$ (*c* 0.0015, CH_2Cl_2); ESIMS *m/z* (%): 1131 ([M + Na]⁺, 100); ¹H NMR (CDCl_3 , 200 MHz, 25 °C) δ 8.80 (m, 4H, naphthalene), 8.22 (s, 4H, naphthalene), 8.02 (s, 4H, binaphthyl), 7.94 (d, 4H, binaphthyl), 7.53 (m, 4H, naphthalene), 7.43 (t, 4H, binaphthyl), 7.27 (m, 4H, binaphthyl), 7.16 (d, 4H, binaphthyl), 5.72 (q, 8H, CH_2), 3.34 (s, 12H, OCH₃); ¹³C NMR (CDCl_3 , 75 MHz, 25 °C) δ 167.0 (Cq), 155.8 (Cq), 134.8 (Cq), 133.1 (CH), 131.9 (Cq), 131.2 (Cq), 130.1 (Cq), 128.6 (Cq), 128.3 (CH), 127.9 (Cq), 127.7 (CH), 127.6 (CH), 127.1 (CH), 125.8 (CH), 125.5 (CH), 125.1 (CH), 124.4 (Cq), 64.1 (CH₂), 61.3 (CH₃).

(R,R,R)-**4c**. $[\alpha]_D^{25} +80$ (*c* 0.0015, CH_2Cl_2). ESIMS *m/z* (%): 1687 ([M + Na]⁺, 100); ¹H NMR (CDCl_3 , 200 MHz, 25 °C) δ 8.90 (m, 6H, naphthalene), 8.19 (s, 6H, naphthalene), 8.13 (s, 6H, binaphthyl); 7.90 (d, 6H, binaphthyl), 7.61 (m, 6H, naphthalene), 7.38 (t, 6H, binaphthyl), 7.20 (m, 12H, binaphthyl), 5.79 (s, 12H, CH_2), 3.35 (s, 18H, OCH₃); ¹³C NMR (CDCl_3 , 75 MHz, 25 °C) δ 166.8 (Cq), 155.1 (Cq), 134.4 (Cq), 131.7 (Cq), 131.4 (Cq), 131.0 (CH), 130.2 (Cq), 128.9 (Cq), 128.2 (CH), 127.9 (CH), 127.7 (CH), 126.9 (CH), 125.9 (CH), 125.5 (CH), 125.1 (CH), 124.3 (Cq), 63.6 (CH₂), 61.2 (CH₃).

Macrocycles *(R,R*)-3d** and *(R,R,R*)-**4d**.** From tetrafluoroterephthalic acid (162 mg, 0.68 mmol, 1 equiv), DICD (317 μL , 2.04 mmol, 3 equiv), *(R*)-**1** (255 mg, 0.68 mmol, 1 equiv), PTSA-DMAP (423 mg, 1.36 mmol, 2 equiv). Purified by column chromatography (hexanes/EtOAc 8:2) to yield **3d** (71 mg, 18%), **4d** (10 mg, 4%) and a noticeable quantity of a higher cyclic adduct (8 mg), as white solids. *(R,R*)-**3d**. $[\alpha]_D^{25} +8.3$ (*c* 0.005, CH_2Cl_2); ESIMS *m/z* (%): 1176 ([M + Na]⁺, 100); ¹H NMR (CDCl_3 , 200 MHz, 25 °C) δ 8.15 (s, 4H, binaphthyl), 7.93 (d, 4H, binaphthyl), 7.43 (t, 4H, binaphthyl), 7.27 (s, 4H, binaphthyl), 7.11 (d, 4H, binaphthyl), 5.67 (dd, 8H, CH_2), 3.44 (s, 12H, -OCH₃); ¹³C NMR (CDCl_3 , 75 MHz) δ 158.7 (Cq), 155.4 (Cq), 144.5 (Cq, dm, *J* = 255 Hz), 134.9 (Cq), 133.4 (CH), 130.0 (Cq), 128.3 (CH), 127.4 (CH), 127.3 (Cq), 125.4 (CH), 125.4 (Cq), 125.2 (CH), 118.0 (Cq, m), 65.4 (CH₂), 61.1 (CH₃). *(R,R,R*)-**4d**. $[\alpha]_D^{25} +4.8$ (*c* 0.005, CH_2Cl_2); ESIMS *m/z* (%): 1752 ([M + Na]⁺, 100); ¹H NMR (CDCl_3 , 200 MHz, 25 °C) δ 8.11 (s, 6H, binaphthyl), 7.92 (d, 6H, binaphthyl), 7.43 (t, 6H, binaphthyl), 7.27 (m, 6H, binaphthyl), 7.17 (d, 6H, binaphthyl), 5.71 (s, 12H, CH_2), 3.29 (s, 18H, -OCH₃); ¹³C NMR (CDCl_3 , 75 MHz) δ 158.7 (Cq), 154.9 (Cq), 144.3 (Cq, *J* = 263 Hz), 134.6 (Cq), 131.5 (CH), 130.1 (Cq), 128.3 (CH), 127.6 (CH), 127.2 (Cq), 125.5 (CH), 125.2 (CH), 124.1 (Cq), 117.6 (Cq, m), 64.9 (CH₂), 61.0 (CH₃).

UV-vis titrations. As described in [28], the titration experiments were conducted as follows: to a stock solution of C_{60} (solution A) in toluene were added several aliquots of the host (solution B) in toluene. Solution B is formed by the ligand at a higher concentration dissolved in solution A, so that the guest always remains at the same, constant concentration. In the case of a 1:1 binding isotherm (Figure 4, bottom), by employing a nonlinear fitting curve program, the plot of A against the macrocycle concentration x was fitted by Equation 1, thus affording the value of the association constant K_a and of the molar absorptivity of the complex ϵ_c :

$$A = (\epsilon_c - \epsilon_s) \frac{K_a (C + x) + 1 - [[K_a (C + x) + 1]^2 - 4K_a^2 Cx]^{0.5}}{2K_a} + \epsilon_s C \quad (1)$$

where A is the measured absorbance, x is the total concentration of titrant added, ϵ_c is the molar absorptivity of the complex, ϵ_s is the molar absorbivity of the substrate at the desired wavelength, which could be directly determined, C is the total concentration of the titrate (which is a constant quantity), and K_a is the association constant for the 1:1 complex [28].

The data for titrations of **4b** with C_{60} (Figure 4, top) were fitted to a general form of the Hill equation:

$$\Delta \text{Abs} = \Delta \text{Abs}_{\text{max}} [x]^n K_a / (1 + [x]^n K_a)$$

which can be conveniently rewritten in:

$$\Delta \text{Abs} = \Delta \text{Abs}_{\text{max}} [x]^n / \left[(1/K_a)^n + [x]^n \right] \quad (2)$$

Equation 2 could be fitted employing a nonlinear fitting program according to the general equation: $f(x) = a \cdot x^b / (c^b + x^b)$, obtaining values of $a = \Delta \text{Abs}_{\text{max}}$, $b = n$ (the Hill coefficient), $c = 1/K_a$.

Supporting Information

Supporting Information File 1

UV spectra for selected macrocycles, additional NMR and MS spectra for all newly synthesized macrocycles.
[<http://www.beilstein-journals.org/bjoc/content/supplementary/1860-5397-10-132-S1.pdf>]

Acknowledgements

Support from the University of Pavia, MIUR (Programs of National Relevant Interest PRIN grants 2004-033354 and 2009-A5Y3N9), and, in part, from the CARIPLO Foundation (2007–2009) and INSTM-Regione Lombardia (2010–2012 and 2013–2015), is gratefully acknowledged.

References

1. Grave, C.; Schlüter, A. D. *Eur. J. Org. Chem.* **2002**, 3075–3098. doi:10.1002/1099-0690(200209)2002:18<3075::AID-EJOC3075>3.0.C0;2-3
2. Yamaguchi, Y.; Yoshida, Z.-i. *Chem.–Eur. J.* **2003**, 9, 5430–5440. doi:10.1002/chem.200305099
3. Höger, S. *Chem.–Eur. J.* **2004**, 10, 1320–1329. doi:10.1002/chem.200305496
4. Zhang, W.; Moore, J. S. *Angew. Chem., Int. Ed.* **2006**, 45, 4416–4439. doi:10.1002/anie.200503988
5. Hua, Y.; Ramabhadran, R. O.; Karty, J. A.; Raghavachari, K.; Flood, A. H. *Chem. Commun.* **2011**, 47, 5979–5981. doi:10.1039/c1cc10428d
6. Pasini, D. *Molecules* **2013**, 18, 9512–9530. doi:10.3390/molecules18089512
7. Droz, A. S.; Diederich, F. *J. Chem. Soc., Perkin Trans. 1* **2000**, 4224–4226. doi:10.1039/b007706m
8. Droz, A. S.; Neidlein, U.; Anderson, S.; Seiler, P.; Diederich, F. *Helv. Chim. Acta* **2001**, 84, 2243–2289. doi:10.1002/1522-2675(20010815)84:8<2243::AID-HLCA2243>3.0.CO;2-G
9. Yus, M. Arene-catalyzed lithiation. In *The Chemistry of Organolithium Compounds*; Rappoport, Z.; Marek, I., Eds.; John Wiley and Sons: Chichester, U.K., 2004; pp 647–748.
10. Campbell, K.; Tykwiński, R. R. Chiral Carbon-rich Macrocycles and Cyclophanes. In *Carbon-Rich Compounds: From Molecules to Materials*; Haley, M. M.; Tykwiński, R. R., Eds.; Wiley-VCH: Weinheim, 2006; pp 229–294.
11. Pasini, D.; Ricci, M. *Curr. Org. Synth.* **2007**, 4, 59–80. doi:10.2174/157017907779981606
12. Ghadiri, M. R.; Grana, J. R.; Buehler, L. K. *Nature* **1994**, 369, 301–304. doi:10.1038/369301a0
13. Leclair, S.; Baillargeon, P.; Skouta, R.; Gauthier, D.; Zhao, Y.; Dory, Y. L. *Angew. Chem., Int. Ed.* **2004**, 43, 349–353. doi:10.1002/anie.200352259
14. Fischer, L.; Decossas, M.; Briand, J.-P.; Didierjean, C.; Guichard, G. *Angew. Chem., Int. Ed.* **2009**, 48, 1625–1628. doi:10.1002/anie.200804019
15. Sakamoto, J.; Schlüter, A. D. *Eur. J. Org. Chem.* **2007**, 2700–2712. doi:10.1002/ejoc.200700118
16. Gong, B. *Acc. Chem. Res.* **2008**, 41, 1376–1386. doi:10.1021/ar700266f
17. Xu, Y.; Smith, M. D.; Geer, M. F.; Pellechia, P. J.; Brown, J. C.; Wibowo, A. C.; Shimizu, L. S. *J. Am. Chem. Soc.* **2010**, 132, 5334–5335. doi:10.1021/ja9107066
18. Pérez, E. M.; Martin, N. *Org. Biomol. Chem.* **2012**, 10, 3577–3583. doi:10.1039/c2ob07159b
19. Canevet, D.; Pérez, E. M.; Martin, N. *Angew. Chem., Int. Ed.* **2011**, 50, 9248–9259. doi:10.1002/anie.201101297
20. Xia, J.; Bacon, J. W.; Jasti, R. *Chem. Sci.* **2012**, 3, 3018–3021. doi:10.1039/c2sc20719b
21. Tashiro, K.; Aida, T.; Zheng, J.-Y.; Kinbara, K.; Saigo, K.; Sakamoto, S.; Yamaguchi, K. *J. Am. Chem. Soc.* **1999**, 121, 9477–9478. doi:10.1021/ja992416m
22. Shoji, Y.; Tashiro, K.; Aida, T. *J. Am. Chem. Soc.* **2006**, 128, 10690–10691. doi:10.1021/ja063828f
23. Liu, S.-Q.; Wang, D.-X.; Zheng, Q.-Y.; Wang, M.-X. *Chem. Commun.* **2007**, 3856–3858. doi:10.1039/b705595a
24. Canevet, D.; Gallego, M.; Isla, H.; de Juan, A.; Pérez, E. M.; Martin, N. *J. Am. Chem. Soc.* **2011**, 133, 3184–3190. doi:10.1021/ja111072j
25. Cao, R., Jr.; Isla, H.; Cao, R.; Pérez, E. M.; Martin, N. *Chem. Sci.* **2011**, 2, 1384–1388. doi:10.1039/C1SC00179E
26. Moletti, A.; Coluccini, C.; Pasini, D.; Taglietti, A. *Dalton Trans.* **2007**, 1588–1592. doi:10.1039/b700059f
27. Coluccini, C.; Castelluccio, A.; Pasini, D. *J. Org. Chem.* **2008**, 73, 4237–4240. doi:10.1021/jo800315s
28. Coluccini, C.; Dondi, D.; Caricato, M.; Taglietti, A.; Boiocchi, M.; Pasini, D. *Org. Biomol. Chem.* **2010**, 8, 1640–1649. doi:10.1039/b920867d
29. Coluccini, C.; Mazzanti, A.; Pasini, D. *Org. Biomol. Chem.* **2010**, 8, 1807–1815. doi:10.1039/b924400j
30. Caricato, M.; Coluccini, C.; Dondi, D.; Vander Griend, D. A.; Pasini, D. *Org. Biomol. Chem.* **2010**, 8, 3272–3280. doi:10.1039/c004379f

31. Colombo, S.; Coluccini, C.; Caricato, M.; Gargiulli, C.; Gattuso, G.;
Pasini, D. *Tetrahedron* **2010**, *66*, 4206–4211.
doi:10.1016/j.tet.2010.03.102

32. Caricato, M.; Olmo, A.; Gargiulli, C.; Gattuso, G.; Pasini, D.
Tetrahedron **2012**, *68*, 7861–7866. doi:10.1016/j.tet.2012.07.038

33. Boiocchi, M.; Bonizzoni, M.; Moletti, A.; Pasini, D.; Taglietti, A.
New J. Chem. **2007**, *31*, 352–356. doi:10.1039/b616492g

34. Bencini, A.; Coluccini, C.; Garau, A.; Giorgi, C.; Lippolis, V.;
Messori, L.; Pasini, D.; Puccioni, S. *Chem. Commun.* **2012**, *48*,
10428–10430. doi:10.1039/c2cc35383k

35. Caricato, M.; Leza, N. J.; Gargiulli, C.; Gattuso, G.; Dondi, D.;
Pasini, D. *Beilstein J. Org. Chem.* **2012**, *8*, 967–976.
doi:10.3762/bjoc.8.109

36. Caricato, M.; Coluccini, C.; Vander Griend, D. A.; Forni, A.; Pasini, D.
New J. Chem. **2013**, *37*, 2792–2799. doi:10.1039/C3NJ00466J

37. Caricato, M.; Leza, N. J.; Roy, K.; Dondi, D.; Gattuso, G.;
Shimizu, L. S.; Vander Griend, D. A.; Pasini, D. *Eur. J. Org. Chem.*
2013, 6078–6083. doi:10.1002/ejoc.201300884

38. Caricato, M.; Sharma, A. K.; Coluccini, C.; Pasini, D. *Nanoscale* **2014**,
doi:10.1039/C4NR00801D

39. Asakawa, M.; Ashton, P. R.; Boyd, S. E.; Brown, C. L.; Menzer, S.;
Pasini, D.; Stoddart, J. F.; Tolley, M. S.; White, A. J. P.; Williams, D. J.;
Wyatt, P. G. *Chem.—Eur. J.* **1997**, *3*, 463–481.
doi:10.1002/chem.19970030319

40. Stock, H. T.; Kellogg, R. M. *J. Org. Chem.* **1996**, *61*, 3093–3105.
doi:10.1021/jo952107o

41. Rosini, C.; Superchi, S.; Peerlings, H. W. I.; Meijer, E. W.
Eur. J. Org. Chem. **2000**, 61–71.
doi:10.1002/(SICI)1099-0690(200001)2000:1<61::AID-EJOC61>3.0.C
O;2-I

42. Baudry, Y.; Bollot, G.; Gorteau, V.; Litvinchuk, S.; Mareda, J.;
Nishihara, M.; Pasini, D.; Perret, F.; Ronan, D.; Sakai, N.; Shah, M. R.;
Som, A.; Sordé, N.; Talukdar, P.; Tran, D.-H.; Matile, S.
Adv. Funct. Mater. **2006**, *16*, 169–179. doi:10.1002/adfm.200500198

43. Ercolani, G. *J. Am. Chem. Soc.* **2003**, *125*, 16097–16103.
doi:10.1021/ja038396c

44. Hamacek, J.; Piguet, C. *J. Phys. Chem. B* **2006**, *110*, 7783–7792.
doi:10.1021/jp056932c

45. Moore, S.; Stupp, S. I. *Macromolecules* **1990**, *23*, 65–70.
doi:10.1021/ma00203a013

License and Terms

This is an Open Access article under the terms of the Creative Commons Attribution License (<http://creativecommons.org/licenses/by/2.0>), which permits unrestricted use, distribution, and reproduction in any medium, provided the original work is properly cited.

The license is subject to the *Beilstein Journal of Organic Chemistry* terms and conditions: (<http://www.beilstein-journals.org/bjoc>)

The definitive version of this article is the electronic one which can be found at:
doi:10.3762/bjoc.10.132



Improving the reactivity of phenylacetylene macrocycles toward topochemical polymerization by side chains modification

Simon Rondeau-Gagné[†], Jules Roméo Néabo[†], Maxime Daigle, Katy Cantin and Jean-François Morin^{*}

Full Research Paper

Open Access

Address:

Département de Chimie and Centre de recherche sur les Matériaux Avancés (CERMA), Université Laval, 1045 avenue de la Médecine, G1V 0A6 Québec, Québec, Canada

Email:

Jean-François Morin^{*} - jean-francois.morin@chm.ulaval.ca

* Corresponding author ‡ Equal contributors

Keywords:

carbon nanomaterials; organogels; phenylacetylene macrocycles; polydiacetylenes; topochemical polymerization

Beilstein J. Org. Chem. **2014**, *10*, 1613–1619.

doi:10.3762/bjoc.10.167

Received: 28 January 2014

Accepted: 25 June 2014

Published: 15 July 2014

This article is part of the Thematic Series "Functionalized carbon-nanomaterials".

Guest Editor: A. Krueger

© 2014 Rondeau-Gagné et al; licensee Beilstein-Institut.

License and terms: see end of document.

Abstract

The synthesis and self-assembly of two new phenylacetylene macrocycle (PAM) organogelators were performed. Polar 2-hydroxyethoxy side chains were incorporated in the inner part of the macrocycles to modify the assembly mode in the gel state. With this modification, it was possible to increase the reactivity of the macrocycles in the xerogel state to form polydiacetylenes (PDAs), leading to a significant enhancement of the polymerization yields. The organogels and the PDAs were characterized using Raman spectroscopy, X-ray diffraction (XRD) and scanning electron microscopy (SEM).

Introduction

The self-assembly of molecular building blocks is an increasingly popular method for the preparation of new semiconducting materials. Rational design of building blocks and their assembly using non-covalent interactions can provide control over the size, shape and electronic properties of the resulting nanoarchitectures [1-3]. It is therefore not surprising that supramolecular interactions are regularly used to afford long-range molecular organization for organic and molecular electronics applications in which high-level of organization is required to reach good charge transport properties [4-6]. However, supra-

molecular assemblies often suffer from poor stability, meaning that variation of the storage and device operation conditions can perturb the molecular organization, leading to a decline of the materials efficiency overtime [7]. In this regard, the covalent immobilization of supramolecular assemblies using physical stimuli (heat or light) is an interesting way to obtain stable, organized materials [8-11]. For example, self-assembled butadiyne-containing molecules can be polymerized in a gel or crystalline state to yield polydiacetylenes (PDAs) following a 1,4-addition mechanism, thus fixing the initial molecular orga-

nization through covalent bonds formation [12,13]. In order for this polymerization to proceed, the molecules within the assembly must be oriented relative to each other following critical parameters, namely a distance of ≤ 4.9 Å and a tilt angle of 45° between the monomers [12]. Thus, careful selection of functional groups onto the molecule is needed to reach these requirements [14–20].

Recently, many research groups used this strategy to design several types of π -conjugated monomers capable of hydrogen bonding to create nanowires [21–23], nanoparticles [24–27], nanotubes [28–31] and two-dimensional layered materials [32] from organogels. The key to success was to obtain a good balance between solubility and gelation properties. Moreover, subtle changes in the chemical nature of the building blocks can have a dramatic impact on the self-assembly process. This was exemplified in the case of nanotubes obtained from self-assembled butadiyne-containing macrocycles, which stack on top of each other in columnar fashion to give supramolecular nanotubular structures [33–38]. Among other things, we have shown that inversion of the amide group configuration (acetanilide vs benzamide) at two different positions on phenyl-acetylene macrocycles (PAMs) leads to significant changes of the gelation properties and, consequently, on the critical parameters needed for polymerization through 1,4-addition reaction [38]. In fact, the acetanilide configuration provides macrocycles which can barely self-assemble in organic solvents while

the benzamide configuration yields macrocycles with much greater gelation properties that allow the formation of PDA-based nanorods. Nonetheless, the polymerization of diyne units within PAMs to give covalent nanorods and nanotubes is very slow and gives low yields of polymerization, generally too low to be determined accurately [38,39]. In order to increase the efficiency of polymerization, the incorporation of external diyne chains on the PAMs core have been realized [31]. This design allowed us to increase the yield of polymerization to 15%. However, the addition of external diyne units is synthetically tedious and a more efficient strategy to significantly increase the yield of the topochemical polymerization is necessary.

In order to take a step further toward a better comprehension of the self-assembly of PAMs and to increase the polymerization yield, we decided to introduce substituents on the inside of the macrocycles, more precisely a polar 2-hydroxyethoxy group. Such a polar group proved to be useful to increase the intermolecular interactions between PAMs through hydrogen bonding in the solid state [40,41]. We hypothesized that this structural change could provide better control over the molecular organization of PAMs and, consequently, could lead to higher yield of PDA-walled nanorods through PAMs polymerization. Herein, we report the synthesis, gelation properties and topochemical polymerization of a new series of PAMs (**PAM2** and **PAM3**, Figure 1) with polar side chains pointing inside the macrocyclic scaffold.

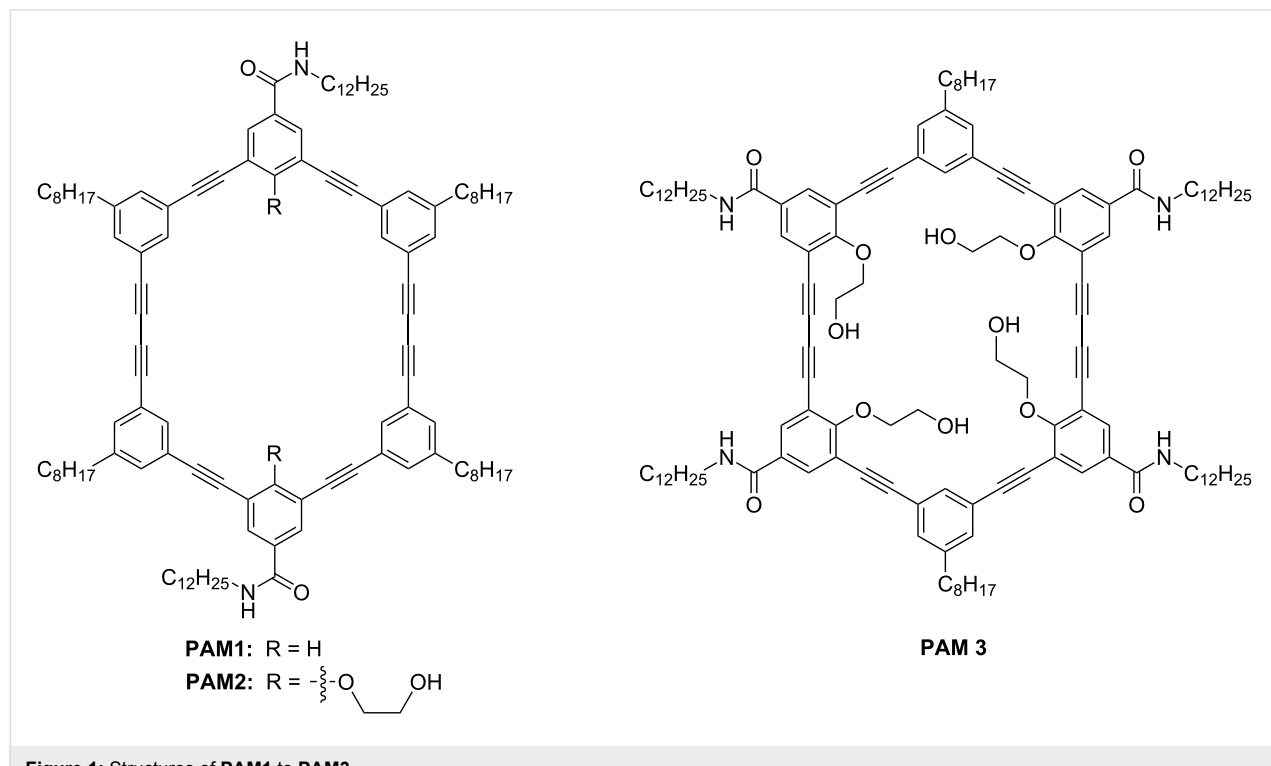


Figure 1: Structures of **PAM1** to **PAM3**.

PAM2 and **PAM3** possess some structural dissimilarity. First, **PAM2** possesses two 2-hydroxyethoxy chains and two amide groups in the benzamide configuration while **PAM3** contains four of each. It is important to mention that the alcohol chains are positioned for synthetic ease. The synthesis and gelation properties of **PAM1** are reported in the literature [39]. **PAM1** was used in this study as a control molecule because of the absence of 2-hydroxyethoxy chains in its structure, providing a reliable comparison.

Results and Discussion

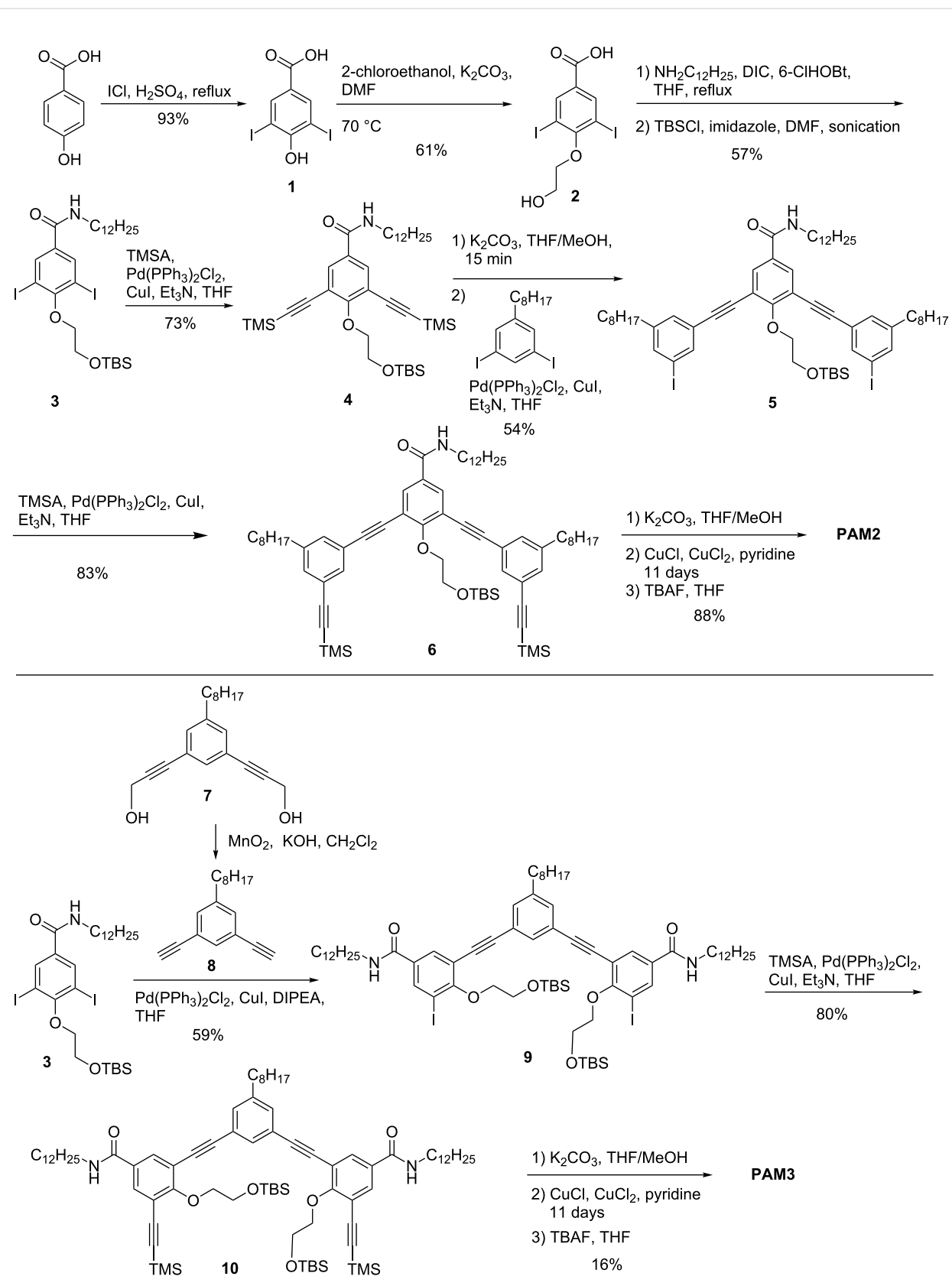
The synthetic pathway toward **PAM2** and **PAM3** is shown in Scheme 1. Starting from commercially available 4-hydroxybenzoic acid, iodination was performed to obtain compound **1** in excellent yield (93%). Then, 2-hydroxyethoxy chains were installed using K_2CO_3 to obtain compound **2** in good yield (61% yield). Amidation using diisopropylcarbodiimide (DIC) and 6-chlorohydroxybenzotriazole (6-ClHOBT) as coupling agents was then performed, followed by protection of the hydroxy moiety with TBS in order to facilitate the further synthetic steps by increasing the solubility of the compound (57% yield over 2 steps). Then, by using a standard Castro–Stephens–Sonogashira coupling, TMS protecting groups were installed (73% yield). After basic removal of the alkyne protective group, the half-macrocycle **5** was obtained by Castro–Stephens–Sonogashira coupling with previously reported 3,5-diiodooctylbenzene [39] in good yields despite of the possible polymerization side reaction (54% yield). TMS-protected alkynes were, then, installed on the half-macrocycle to afford compound **6** which can be deprotected using potassium hydroxide and directly used in modified Eglinton ring closing reaction in pseudo-high dilution to afford hydroxy-protected PAM. Deprotection was directly performed without purification using TBAF to afford **PAM2** in good yields (88% yield). Same approach was used for **PAM3**. Starting from previously synthesized compound **3**, the half-macrocycle **9** was obtained by standard Castro–Stephens–Sonogashira coupling with dialkyne **8** in good yield (59%). It is noteworthy that compound **8** was obtained from oxidative deprotection of compound **7**. After installing TMS-protected alkynes with good yields (compound **10**, 80% yield), selective removal of TMS using potassium hydroxide and ring closing reaction under modified Eglinton conditions were performed to afford a TBS protected PAM. Deprotection of TBS using TBAF was then realized without purification to afford **PAM3** in rather low yield. We hypothesized that this low yield can be due to the increased steric hindrance for compound **10** (2 OTBS groups) compared to compound **6** (1 OTBS group), impairing the macrocyclization reaction and leading to a significant amount of oligomerized product. It is noteworthy that purification of **PAM3** was realized by precipitation in methanol. Standard

column chromatography was not effective due to the low solubility of the macrocycle after deprotection of the hydroxy-containing side chains.

The gelation properties of **PAM2** and **PAM3** have been studied and compared to those of **PAM1**. For each PAM, a precise quantity was mixed with the solvent in a capped glass tube. After sonication to breakdown the aggregates, the mixture was heated until a clear solution was obtained. Then, the solution was allowed to slowly cool at room temperature and the formation of the gel was confirmed in each case by the tube inversion method [39]. The gelation properties of **PAM1**, **PAM2** and **PAM3** in different solvents are summarized in Table S1 (Supporting Information File 1). **PAM2**, containing two amides and two 2-hydroxyethoxy side chains, has exactly the same gelation properties as **PAM1**, demonstrating the absence of the influence of the addition of side chains on the gelation properties. In the case of **PAM3**, however, most of the solvents tested did not lead to gel formation. Thus, only cyclohexane and toluene resulted in a partial gel state. The presence of four amide functions and four 2-hydroxyethoxy groups lead to a significant decrease of solubility, even in hot solvents, limiting the formation of organogels.

In order to investigate the crystallization temperature of solvents within the gel and to compare the influence of the 2-hydroxyethoxy side chains on the thermal stability of the gel, two gel samples were prepared with **PAM1** and **PAM2** in cyclohexane at a 10 mg/mL concentration and subjected to differential scanning calorimetry (DSC). The DSC analysis was carried out at temperatures ranging from 298 to 223 K. In both cases, a very sharp exotherm attributable to the crystallization of supercooled solvent was observed (see Figure S22 and S23 in Supporting Information File 1). For **PAM2**, the exotherm at 279 K is closer to the freezing point of cyclohexane (280 K) than for **PAM1**, which has an exotherm at 267 K. This result suggests that the gel of **PAM2** might be less organized than that of **PAM1**. By heating the gel from 223 to 298 K, an endotherm was observed in both cases, which is closely related to the melting point of free cyclohexane [39].

To explore the morphology of the structures created during the gel formation, scanning electron microscopy (SEM) was performed on **PAM2** only since **PAM3** did not present any gelation properties. For SEM analysis, a gel sample was allowed to dry at room temperature on a metallic substrate to form a xerogel. Then, gold was sputtered on the sample prior to imaging. SEM images of **PAM2** are shown in Figure 2. As previously observed with **PAM1** and other phenylacetylene macrocycles, a dense network of nanofibrils was formed during the gelation process [42–48]. These nanofibrils, commonly

**Scheme 1:** Synthetic pathway to **PAM2** and **PAM3**.

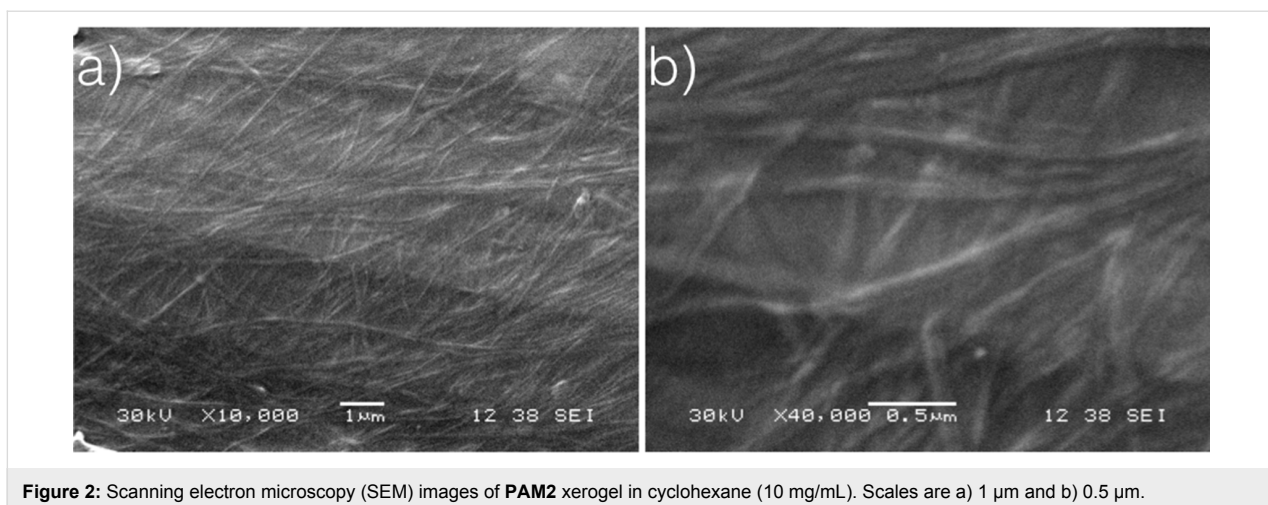


Figure 2: Scanning electron microscopy (SEM) images of **PAM2** xerogel in cyclohexane (10 mg/mL). Scales are a) 1 μm and b) 0.5 μm .

observed in the gel state, resulted from the strong intermolecular interactions that create long-range one-dimensional arrays of molecules [49,50].

In order to gain some insights on the molecular packing within the assembly, X-ray diffraction (XRD) was performed on **PAM2** (see Figure S21 in Supporting Information File 1). Unlike **PAM1**, the presence of a columnar arrangement cannot be established from the diffractogram [31,39]. Instead, only a broad peak at $2\theta = 20^\circ$ was observed, indicating the presence of intramolecular liquid-like order between the alkyl chains [2]. The absence of a well-defined pattern suggests that **PAM2** does not organize as well as **PAM1** in the gel state and that the 2-hydroxyethoxy chains are unfavourable for the long-range supramolecular organization.

Despite this unexpected finding, irradiation of a xerogel sample of **PAM2** in cyclohexane (10 mg/mL) was performed for 24 h under UV light (254 nm). The resulting blue material was purified using size-exclusion chromatography (SEC) (Bio-Beads SX-1) to remove all traces of the starting macrocycle. To our surprise, an increase of the polymerization yields was observed every time a polymerization was achieved with **PAM2**. In several attempts, a maximum yield of 30% (soluble material) was obtained after purification, representing a two-fold increase compared to the best result obtained for the same PAM scaffold ($\approx 15\%$ yield). This result suggests that the diyne units in **PAM2** are in a more suitable orientation than **PAM1** to undergo a topochemical polymerization, although gelation properties and XRD result seem to suggest otherwise. It is also possible that the apparent yield increase comes from a better solubility of the PDA obtained from **PAM2** compared to that obtained from **PAM1**, although quantitative measurements of the solubility have not been conducted because of the small quantity of materials prepared.

Given the observed polymerization of diyne units, UV-vis spectroscopy was performed to confirm the appearance of polydiacetylene. As shown in Figure 3, the UV-vis spectra shows absorption bands at 600 and 650 nm, associated with the red and blue bands of the PDA chain, respectively [51]. To determine whether all the diyne units of **PAM2** reacted during irradiation, Raman spectroscopy was performed on the resulting PDA (Figure 4). As expected, no band associated with the diyne unit (generally around 2200 cm^{-1}) is present. The final PDA presented bands at 1470 and 2100 cm^{-1} , which could be respectively associated to alkene and alkyne moieties of PDA. It should be noted that these two bands are also present in the Raman spectrum of **PAM2** due to partial photo-induced polymerization during spectrum acquisition. This demonstrates the high reactivity of **PAM2** under UV irradiation. Further research on the resulting nanoarchitectures is currently underway to

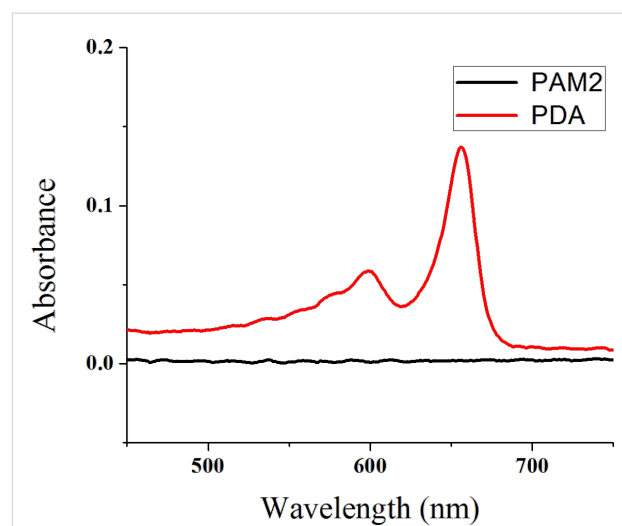


Figure 3: UV-vis spectrum of **PAM2** before (black) and after (red) polymerization (PDA).

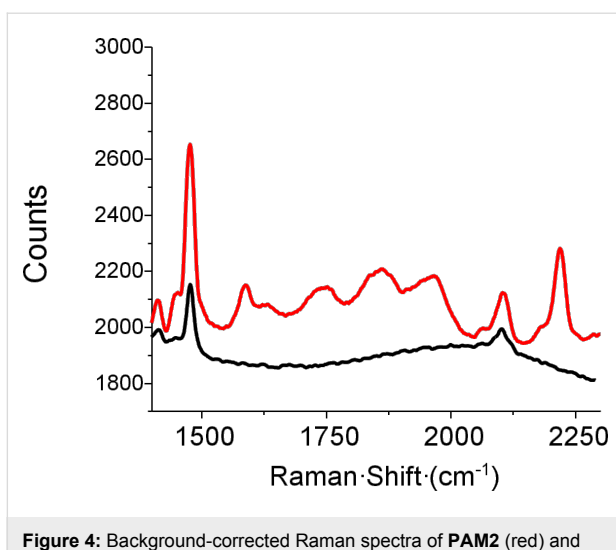


Figure 4: Background-corrected Raman spectra of **PAM2** (red) and the blue material obtained after UV irradiation (black).

establish if covalent nanotubes have been formed and to study their properties.

To assess the presence of nanotubes or nanorods, HRTEM analysis has been performed on the purified blue materials. Although one-dimensional features can be observed at different locations on the grid (see Figure S24 in Supporting Information File 1), the images were not clear enough to confirm whether or not **PAM2** has been transformed exclusively into nanotubes or nanorods and attempts to disperse individual molecules in organic solvents failed. Considering the strict structural parameters needed to undergo a topochemical polymerization and the one-dimensional nature of the starting xerogel of **PAM2**, it is unlikely – but not impossible – that the final blue materials can be made of other nanoarchitectures than the nanotubular or nanorods one. Nonetheless, no conclusive remarks can be made and more analysis will have to be performed in order to gain better insight about the final structure of the PDA obtain from **PAM2**.

Conclusion

In summary, the synthesis and self-assembly of two new phenylacetylene macrocycles were performed. To improve the self-assembly properties in the gel state and further yield to better topochemical polymerization yield, the incorporation of 2-hydroxyethoxy side chains was accomplished. The gelation properties demonstrated that the incorporation of two of these chains (**PAM2**) did not affect the gelation properties while the incorporation of four side chains and four amide groups significantly alter the solubility of the resulting PAM (**PAM3**). Topochemical polymerization on self-assembled **PAM2** to yield PDA-based materials proved to be much more efficient than for the 2-hydroxyethoxy-free analogues (**PAM1**). Characterization

is currently underway to investigate the precise nature of the nanoarchitectures formed.

Supporting Information

Supporting Information File 1

Experimental part.

[<http://www.beilstein-journals.org/bjoc/content/supplementary/1860-5397-10-167-S1.pdf>]

Acknowledgements

This work was supported by NSERC through a Discovery Grant. We thank Rodica Plesu (U. Laval) and Jean-François Rioux (U. Laval) for their help in polymer characterization, and Philippe Dufour (U. Laval) for HRMS experiment. Simon Rondeau-Gagné thanks the NSERC for a PhD scholarship.

References

- Zhao, Y. S.; Fu, H.; Peng, A.; Ma, Y.; Liao, Q.; Yao, J. *Acc. Chem. Res.* **2009**, *43*, 409. doi:10.1021/ar900219n
- Laschat, S.; Baro, A.; Steinke, N.; Giesselmann, F.; Hägele, C.; Scalia, G.; Judele, R.; Kapatsina, E.; Sauer, S.; Schreibvogel, A.; Tosoni, M. *Angew. Chem., Int. Ed.* **2007**, *46*, 4832. doi:10.1002/anie.200604203
- Grimsdale, A. C.; Müllen, K. *Angew. Chem., Int. Ed.* **2005**, *44*, 5592. doi:10.1002/anie.200500805
- Hasegawa, M.; Iyoda, M. *Chem. Soc. Rev.* **2010**, *39*, 2420. doi:10.1039/b909347h
- Babu, S. S.; Prasanthkumar, S.; Ajayaghosh, A. *Angew. Chem., Int. Ed.* **2012**, *51*, 1766. doi:10.1002/anie.201106767
- Stupp, S. I.; Palmer, L. C. *Chem. Mater.* **2014**, *26*, 507. doi:10.1021/cm40328b
- Bushey, M. L.; Nguyen, T.-Q.; Zhang, W.; Horoszewski, D.; Nuckolls, C. *Angew. Chem., Int. Ed.* **2004**, *43*, 5446. doi:10.1002/anie.200301678
- Hoheisel, T. N.; Schrettl, S.; Szillarweit, R.; Frauenrath, H. *Angew. Chem., Int. Ed.* **2010**, *49*, 6496. doi:10.1002/anie.200907180
- Rondeau-Gagné, S.; Morin, J.-F. *Chem. Soc. Rev.* **2014**, *43*, 85. doi:10.1039/c3cs60210a
- Morin, J.-F. *Synlett* **2013**, 2032. doi:10.1055/s-0033-1339680
- Chernick, E. T.; Tykwiński, R. R. *J. Phys. Org. Chem.* **2013**, *26*, 742. doi:10.1002/poc.3160
- Wegner, G. Z. *Naturforsch., B: J. Chem. Sci.* **1969**, *24*, 824.
- Wegner, G. *Makromol. Chem.* **1972**, *154*, 35. doi:10.1002/macp.1972.021540103
- Coates, G. W.; Dunn, A. R.; Henling, L. M.; Dougherty, D. A.; Grubbs, R. H. *Angew. Chem., Int. Ed. Engl.* **1997**, *36*, 248. doi:10.1002/anie.199702481
- Aoki, K.; Kudo, M.; Tamaoki, N. *Org. Lett.* **2004**, *6*, 4009. doi:10.1021/o1048364+
- Nagasawa, J.; Kudo, M.; Hayashi, S.; Tamaoki, N. *Langmuir* **2004**, *20*, 7907. doi:10.1021/la049459n
- Fowler, F. W.; Lauher, J. W. In *Carbon-Rich Compounds*; Haley, M. M.; Tykwiński, R. R., Eds.; Wiley-VCH Verlag GmbH & Co: Weinheim, 2006.

18. Dautel, O. J.; Robitzer, M.; Lère-Porte, J.-P.; Serein-Spirau, F.; Moreau, J. J. E. *J. Am. Chem. Soc.* **2006**, *128*, 16213. doi:10.1021/ja065434u

19. Néabo, J. R.; Tohoudjona, K. I. S.; Morin, J.-F. *Org. Lett.* **2011**, *13*, 1358. doi:10.1021/ol200051m

20. Yarimaga, O.; Jaworski, J.; Yoon, B.; Kim, J.-M. *Chem. Commun.* **2012**, *48*, 2469. doi:10.1039/c2cc17441c

21. Shirakawa, M.; Fujita, N.; Shinkai, S. *J. Am. Chem. Soc.* **2005**, *127*, 4164. doi:10.1021/ja042869d

22. Yip, H.-L.; Zou, J.; Ma, H.; Tian, Y.; Tucker, N. M.; Jen, A. K.-Y. *J. Am. Chem. Soc.* **2006**, *128*, 13042. doi:10.1021/ja064934k

23. Néabo, J. R.; Rondeau-Gagné, S.; Vigier-Carrière, C.; Morin, J.-F. *Langmuir* **2013**, *29*, 3446. doi:10.1021/la305045n

24. Ding, L.; Olesik, S. V. *Chem. Mater.* **2005**, *17*, 2353. doi:10.1021/cm048781g

25. Ding, L.; Olesik, S. V. *Nano Lett.* **2004**, *4*, 2271. doi:10.1021/nl0487931

26. Néabo, J. R.; Vigier-Carrière, C.; Rondeau-Gagné, S.; Morin, J.-F. *Chem. Commun.* **2012**, *48*, 10144. doi:10.1039/c2cc35087d

27. Szilluweit, R.; Hoheisel, T. N.; Fritzsche, M.; Ketterer, B.; Morral, A. F.; Demurtas, D.; Laporte, V.; Verel, R.; Bolisetty, S.; Mezzenga, R.; Frauenrath, H. *Nano Lett.* **2012**, *12*, 2573. doi:10.1021/nl300822f

28. Xu, Y.; Smith, M. D.; Geer, M. F.; Pellechia, P. J.; Brown, J. C.; Wibowo, A. C.; Shimizu, L. S. *J. Am. Chem. Soc.* **2010**, *132*, 5334. doi:10.1021/ja9107066

29. Hsu, T.-J.; Fowler, F. W.; Lauher, L. W. *J. Am. Chem. Soc.* **2012**, *134*, 142. doi:10.1021/ja209792f

30. Rondeau-Gagné, S.; Néabo, J. R.; Desroches, M.; Levesque, I.; Daigle, M.; Cantin, K.; Morin, J.-F. *Chem. Commun.* **2013**, *49*, 9546. doi:10.1039/c3cc43177k

31. Rondeau-Gagné, S.; Néabo, J. R.; Desroches, M.; Larouche, J.; Brisson, J.; Morin, J.-F. *J. Am. Chem. Soc.* **2013**, *135*, 110. doi:10.1021/ja3116422

32. Levesque, I.; Néabo, J. R.; Rondeau-Gagné, S.; Vigier-Carrière, C.; Daigle, M.; Morin, J.-F. *Chem. Sci.* **2014**, *5*, 831. doi:10.1039/c3sc52346b

33. Tobe, Y.; Nagano, A.; Kawabata, K.; Sonoda, M.; Naemura, K. *Org. Lett.* **2000**, *2*, 3265. doi:10.1021/ol006318d

34. Tobe, Y.; Utsumi, N.; Kawabata, K.; Nagano, A.; Adachi, K.; Araki, S.; Sonoda, M.; Hirose, K.; Naemura, K. *J. Am. Chem. Soc.* **2002**, *124*, 5350. doi:10.1021/ja012458m

35. Zhao, T.; Liu, Z.; Song, Y.; Xu, W.; Zhang, D.; Zhu, D. *J. Org. Chem.* **2006**, *71*, 7422. doi:10.1021/jo0611869

36. Zhang, L.; Che, Y.; Moore, J. S. *Acc. Chem. Res.* **2008**, *41*, 1596. doi:10.1021/ar800030w

37. Ide, T.; Takeuchi, D.; Osakada, K. *Chem. Commun.* **2012**, *48*, 278. doi:10.1039/c1cc15311k

38. Rondeau-Gagné, S.; Néabo, J. R.; Desroches, M.; Cantin, K.; Soldera, A.; Morin, J.-F. *J. Mater. Chem. C* **2013**, *1*, 2680. doi:10.1039/c3tc00917c

39. Cantin, K.; Rondeau-Gagné, S.; Néabo, J. R.; Daigle, M.; Morin, J.-F. *Org. Biomol. Chem.* **2011**, *9*, 4440. doi:10.1039/c1ob05441d

40. Vollmeyer, J.; Jester, S.-S.; Eberhagen, F.; Prangenberg, T.; Mader, W.; Höger, S. *Chem. Commun.* **2012**, *48*, 6547. doi:10.1039/c2cc32804f

41. Li, J.; Zhou, W.; Yang, J.; Lang, X.; Huang, P. *J. Colloid Interface Sci.* **2013**, *395*, 99. doi:10.1016/j.jcis.2012.12.053

42. Zang, W.; Moore, J. S. *Angew. Chem., Int. Ed.* **2006**, *45*, 4416. doi:10.1002/anie.200503988

43. Zhao, D.; Moore, J. S. *Chem. Commun.* **2003**, 807. doi:10.1039/b207442g

44. Siemsen, P.; Livingston, R. C.; Diederich, F. *Angew. Chem., Int. Ed.* **2000**, *39*, 2632. doi:10.1002/1521-3773(20000804)39:15<2632::AID-ANIE2632>3.0.CO;2-F

45. Höger, S. *Chem.–Eur. J.* **2004**, *10*, 1320. doi:10.1002/chem.200305496

46. Balakrishnan, K.; Datar, A.; Zhang, W.; Yang, X.; Naddo, T.; Huang, J.; Zuo, J.; Yen, M.; Moore, J. S.; Zang, L. *J. Am. Chem. Soc.* **2006**, *128*, 6576. doi:10.1021/ja0618550

47. Finke, A. D.; Gross, D. E.; Han, A.; Moore, J. S. *J. Am. Chem. Soc.* **2011**, *133*, 14063. doi:10.1021/ja204795q

48. Shigemitsu, H.; Hisaki, I.; Kometani, E.; Yasumiya, D.; Sakamoto, Y.; Osaka, K.; Takur, T. S.; Saeki, A.; Seki, S.; Kimura, F.; Kimura, T.; Tohnai, N.; Miyata, M. *Chem.–Eur. J.* **2013**, *19*, 15366. doi:10.1002/chem.201301967

49. Yu, G.; Yan, X.; Han, C.; Huang, F. *Chem. Soc. Rev.* **2013**, *42*, 6697. doi:10.1039/c3cs60080g

50. Babu, S. S.; Praveen, V. K.; Ajayaghosh, A. *Chem. Rev.* **2014**, *114*, 1973. doi:10.1021/cr400195e

51. Schott, M. *J. Phys. Chem. B* **2006**, *110*, 15864. doi:10.1021/jp0638437

License and Terms

This is an Open Access article under the terms of the Creative Commons Attribution License (<http://creativecommons.org/licenses/by/2.0>), which permits unrestricted use, distribution, and reproduction in any medium, provided the original work is properly cited.

The license is subject to the *Beilstein Journal of Organic Chemistry* terms and conditions: (<http://www.beilstein-journals.org/bjoc>)

The definitive version of this article is the electronic one which can be found at:
doi:10.3762/bjoc.10.167



Aryl substitution of pentacenes

Andreas R. Waterloo¹, Anna-Chiara Sale¹, Dan Lehnher², Frank Hampel¹
and Rik R. Tykwiński^{*1}

Full Research Paper

Open Access

Address:

¹Department of Chemistry and Pharmacy & Interdisciplinary Center for Molecular Materials (ICMM), University of Erlangen-Nürnberg (FAU), Henkestrasse 42, 91054 Erlangen, Germany and ²Department of Chemistry, University of Alberta, Edmonton, AB T6G 2G2, Canada

Beilstein J. Org. Chem. **2014**, *10*, 1692–1705.

doi:10.3762/bjoc.10.178

Received: 06 February 2014

Accepted: 25 June 2014

Published: 28 July 2014

Email:

Rik R. Tykwiński* - rik.tykwiński@fau.de

This article is part of the Thematic Series "Functionalized carbon-nanomaterials".

* Corresponding author

Guest Editor: A. Krueger

Keywords:

carbon-nanomaterials; organic semiconductor; pentacene; π -stacking; polycyclic aromatic hydrocarbon; solid-state structure

© 2014 Waterloo et al; licensee Beilstein-Institut.

License and terms: see end of document.

Abstract

A series of 11 new pentacene derivatives has been synthesized, with unsymmetrical substitution based on a trialkylsilylethynyl group at the 6-position and various aryl groups appended to the 13-position. The electronic and physical properties of the new pentacene chromophores have been analyzed by UV-vis spectroscopy (solution and thin films), thermoanalytical methods (DSC and TGA), cyclic voltammetry, as well as X-ray crystallography (for 8 derivatives). X-ray crystallography has been specifically used to study the influence of unsymmetrical substitution on the solid-state packing of the pentacene derivatives. The obtained results add to our ability to better predict substitution patterns that might be helpful for designing new semiconductors for use in solid-state devices.

Introduction

Conjugated organic molecules are promising candidates for use in optoelectronic applications including OLEDs [1], photovoltaics [2], and OFETs [3]. Even though there is literally an infinite number of possibilities to chemically assemble small organic molecules for such applications, clever design and synthesis have rapidly offered new materials for the nascent era of molecular electronic [4-11]. Prominent p-type organic semiconductors include substituted acenes in general [12-15], and specifically 6,13-(triisopropylsilylethynyl)pentacene (TIPSPc) [13,14]. The latter was synthesized by Anthony over a decade ago [16], but it is still a leading focus of the scientific commu-

nity. Substituted pentacenes can offer several advantages to other small molecule semiconductors, including stability, processability, and semiconductor device performance. Intermolecular π - π -interactions between chromophores can be dramatically improved upon functionalization at the 6- and 13-positions of pentacene, as demonstrated by the two-dimensional (2D) bricklayer-packing motif for TIPSPc [13,14]. A number of well-designed substitution patterns for the pentacene skeleton have been realized to date [17-25], and pentacene derivatives that provide good semiconductor device performance often show similar 6,13-substitution patterns (Figure 1a)

[12,26]. The most reactive positions of the acene core are the 6- and 13-positions [27–29], and these positions can be effectively blocked by different trialkylsilylethynyl units [30]. Inspired by previous studies in which we [18,31], and others [32–34], observed promising solid-state arrangement and properties of aryl-substituted pentacenes, we were interested in the influence of different aryl moieties directly linked to the pentacene core. In this work we present a simple synthetic approach to unsymmetrically substituted pentacenes via stepwise functionalization of pentacenequinone, using a nucleophilic aryl group (Figure 1b). To determine the influence of aryl substitution, the obtained pentacenes have been studied by a variety of spectroscopic characterization methods as well as X-ray crystallography of eight derivatives. The studies reported herein offer an opportunity to interpret various properties of acenes based on their substitution and should contribute toward the use of such derivatives in materials science.

Results and Discussion

Synthesis and Characterization

Synthesis

The synthesis of arylpentacenes was developed based on the known ketone derivatives **4a** and **4b**, formed through the addition of an acetylide to pentacenequinone (Scheme 1) [21,35–38]. With these two ketones in hand, a second nucleophilic addition was initiated. Thus, commercially available aryl halides dissolved in dry THF were subjected to lithium halogen exchange at -78°C using *n*-butyllithium. A stoichiometric amount of *n*-BuLi was used in each case to ensure complete consumption of the *n*-BuLi through Li–halogen exchange and thus avoid the possibility of competitive addition of the nucleophilic *n*-Bu anion to the ketone group of either **4a** or **4b**. After reaction with the appropriate aryl lithium species, the reaction was quenched with a proton source, and the resulting diol intermediates **5a–h** were carried on directly to reductive aromatization

with $\text{SnCl}_2/\text{H}_2\text{SO}_4$ without further purification, ultimately yielding pentacene products **3a–h**. While the isolation and characterization of diol products resulting from nucleophilic additions to pentacenequinone has been possible [17,18,34], previous work has shown that aromatized products were more easily purified by column chromatography and recrystallization following the last step [30,31,36]. Thus, it was deemed procedurally more efficient to eliminate the purification step of the intermediate diols. Once formed, pentacenes **3a–h** were obtained in moderate yield over two steps, as deep-blue solids.

To expand the π -system in a linear fashion along the short molecular axis of the pentacene core, the general procedure described above was changed slightly, and ketone **4a** was treated with a solution of biphenylmagnesium bromide in THF. After work-up and isolation of the intermediate diol **5i**, reductive aromatization gave pentacene **3i** in moderate yield over the two steps. Elaborating on the general idea of lateral functionalization, iodoaryl pentacene **3g** offered an opportunity to vary the pendent substituent through a Pd-catalyzed cross-coupling protocol (Scheme 2). Thus, pentacene **3g** was treated under Suzuki–Miyaura coupling conditions with arylboronic acids, and the desired pentacenes **3j,k** were obtained in yields of 92 and 68%, respectively. Notably, anthracenyl-substituted pentacene **3k** was the least stable of all derivatives synthesized in this study. It slowly decomposed in solution when exposed to ambient laboratory conditions and was unstable toward silica gel chromatography. Compound **3k** could, however, be purified by recrystallization from a mixture of MeOH and acetone.

UV–vis spectroscopy

Aryl pentacenes **3a–k** have been studied by UV–vis absorption spectroscopy in CH_2Cl_2 solutions and as thin films cast from CH_2Cl_2 onto quartz. Solution-state UV–vis spectra show char-

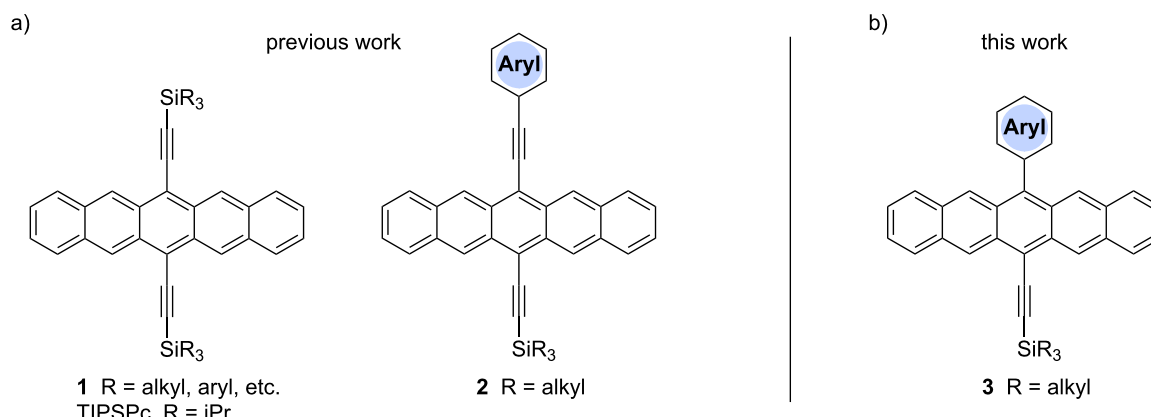
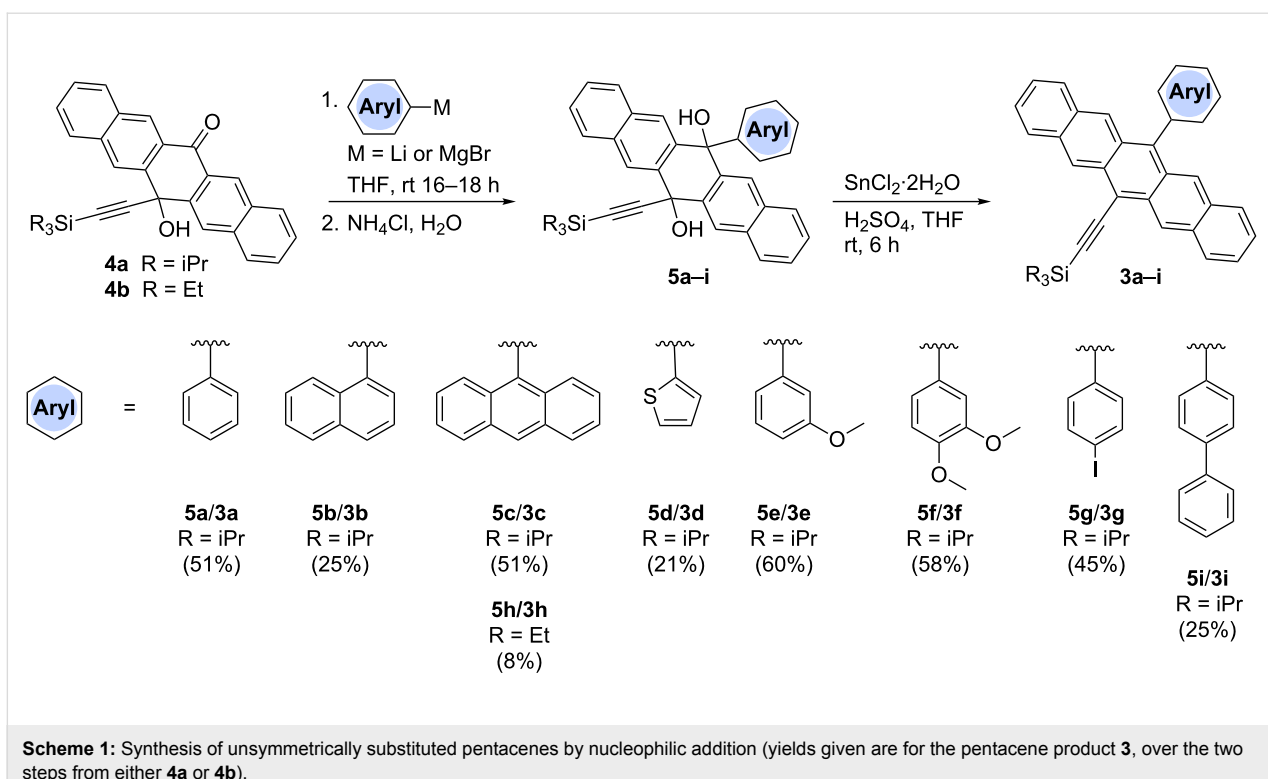
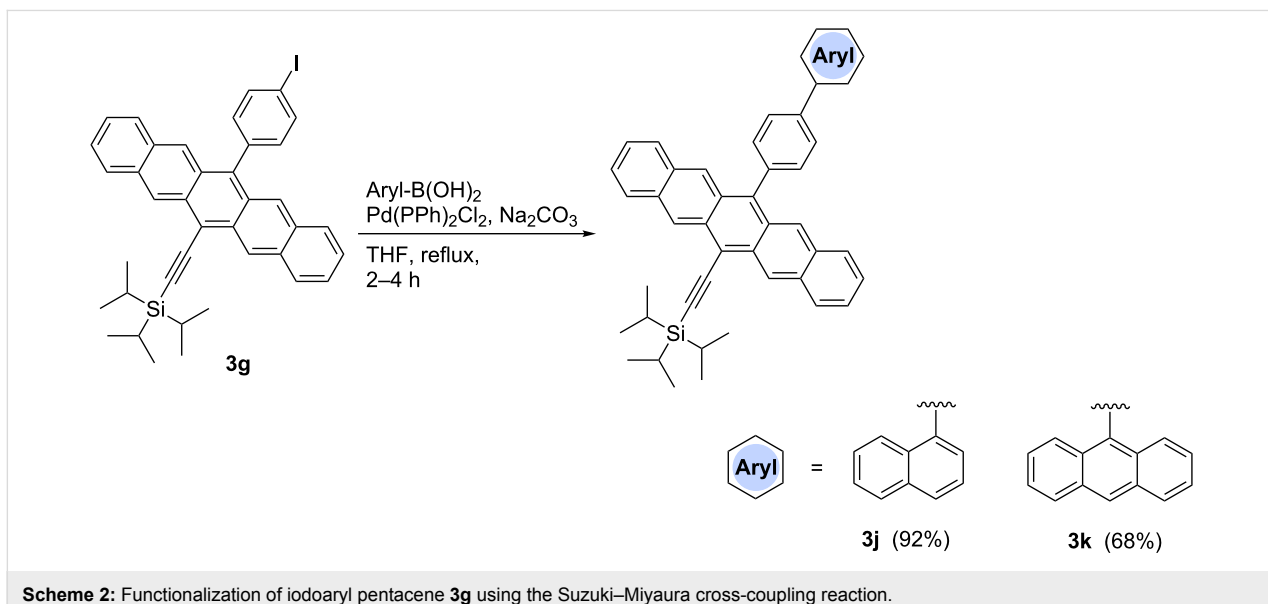


Figure 1: a) Examples of common pentacene functionalization patterns and b) unsymmetrically aryl-substituted pentacenes reported in this work.



Scheme 1: Synthesis of unsymmetrically substituted pentacenes by nucleophilic addition (yields given are for the pentacene product **3**, over the two steps from either **4a** or **4b**).



Scheme 2: Functionalization of iodoaryl pentacene **3g** using the Suzuki–Miyaura cross-coupling reaction.

acteristic absorptions in the high-energy region with a maximum intensity absorption centered at \sim 310 nm, as well as low-energy absorptions at \sim 578 nm and \sim 622 nm. In comparison, unsubstituted pentacene (PEN) shows a $\lambda_{\text{max}} = 576$ nm (measured in benzene) [39], while the symmetrically substituted analogue TIPSPc shows a low-energy absorption at 643 nm (measured in CH₂Cl₂) due to extended conjugation through the two alkyne substituents [11].

As can be seen in the representative spectra in Figure 2, the nature and size of aryl substituents at the 13-position does not alter the basic absorption wavelengths as one progresses, for example, through the series of phenyl (**3a**), naphthyl (**3b**) and anthracenyl (**3c**), although some differences in molar absorptivity are observed. Similar trends are observed within the series of pentacenes **3i**, **3j**, and **3k**. Thus, these UV–vis spectra clearly document the lack of communication between the aryl

substituent and the pentacene unit, as a result of hindered rotation about the aryl–pentacene C–C bond and a preferred conformation in which the π -system of the aryl group is orthogonal to that of the pentacene. The orthogonal orientation of the aryl groups is also well-documented in the solid state by X-ray crystallographic analysis (vide infra). The fluorescence characteristics of **3a–k** are unremarkable, showing only minor variances in emission wavelength ranging from 652–671 nm, as measured in CH_2Cl_2 (see Supporting Information File 1 for details and spectra).

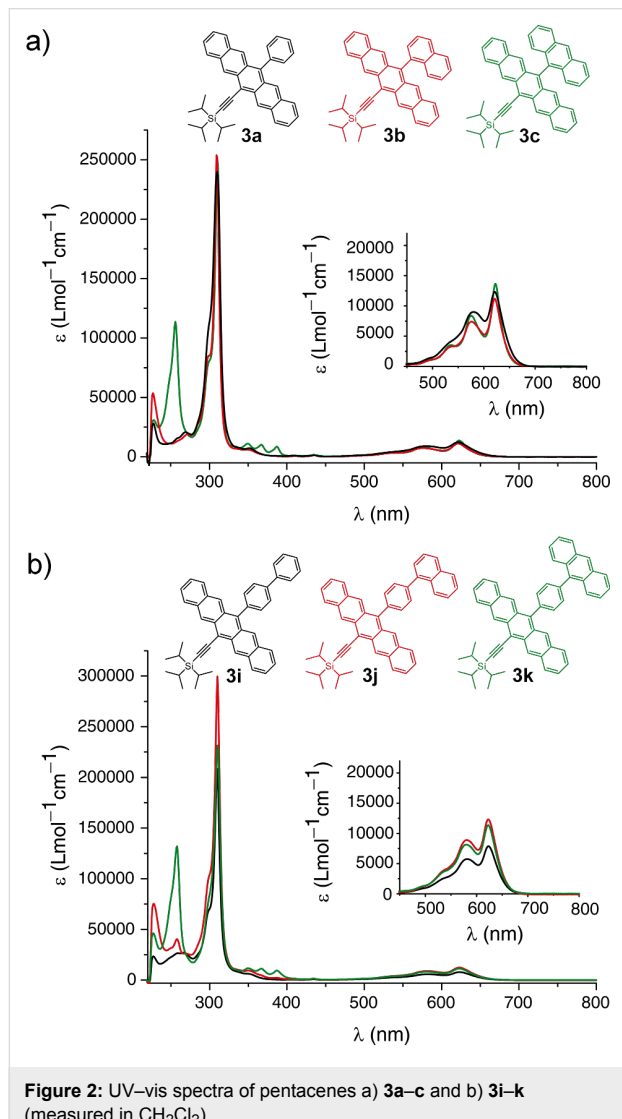


Figure 2: UV–vis spectra of pentacenes a) **3a–c** and b) **3i–k** (measured in CH_2Cl_2).

The major electronic absorptions found in solution are also reproduced to a large extent in spectra obtained from solid-state films. Pentacene samples **3a–k** were drop-cast from a concentrated CH_2Cl_2 solution onto a quartz surface, and after air-drying, the absorption spectra were measured by UV–vis spectroscopy (Figure 3 and Table 1). While this method sometimes

results in rather significant scattering versus the formation of films by spin-casting, only milligram quantities of material are required and the results are qualitatively informative (i.e., absorption wavelengths can be readily discerned, while determination of molar absorptivity is not possible). As can be seen in Figure 3, spectra from thin films show absorption profiles similar to those from solution-state measurements, although signals are broadened and absorptivities vary dramatically due to scattering. In the solid state, there are no observed absorptions at wavelengths beyond ca. 660 nm, and absorptions in the lower energy region show a red shift (7 to 33 nm) in comparison to analogous absorptions in solution. A red shift in the absorption features of samples in the solid state relative to those in solution is typically ascribed to a local electronic interaction

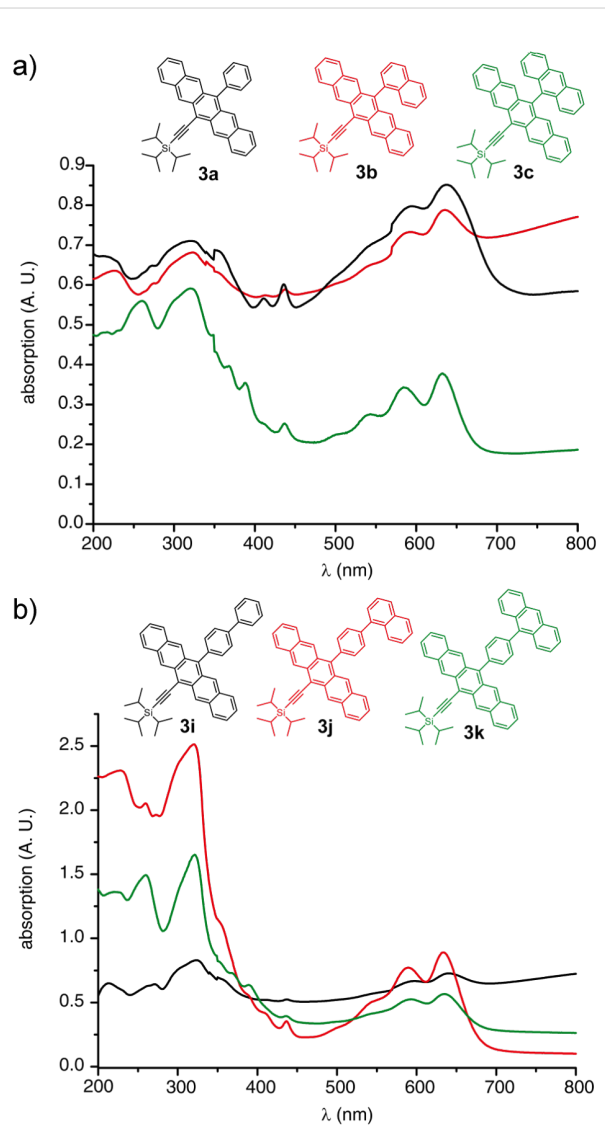


Figure 3: UV–vis spectra of thin films (drop cast on quartz from a CH_2Cl_2 solution) for pentacenes a) **3a–c** and b) **3i–k**.

Table 1: Optical properties of pentacenes **3a–k**, unsubstituted pentacene (PEN), and TIPSPc.

Compound	λ_{max} (in CH_2Cl_2) ^a [nm]	λ_{max} (film) ^b [nm]	red shift [nm] (meV)	$E_{\text{gap, opt}}$ [eV] ^c
3a	621	637	16 (50)	1.89
3b	621	635	14 (44)	1.91
3c	623	637	14 (44)	1.92
3d	623	637	14 (44)	1.91
3e	621	634	13 (41)	1.89
3f	622	655	33 (100)	1.87
3g	621	628	7 (22)	1.90
3h	622	638	16 (50)	1.91
3i	623	641	18 (56)	1.88
3j	623	633	10 (31)	1.89
3k	623	635	12 (38)	1.89
PEN	576 ^d	673 ^e	97 (310)	2.15
TIPSPc	643 ^f	705 ^g	62 (170)	1.84 ^f

^aLowest energy absorption maxima. ^bCast from CH_2Cl_2 onto quartz. ^cDetermined from solution-state spectra, based on a tangent line applied to the lower edge of the longest wavelength absorption peak and the intercept with the x-axis. ^dMeasured in benzene and data taken from [39]. ^eData taken from [41,42]. ^fData taken from [11]. ^gData taken from [35].

between the respective pentacene molecules in the solid state. Of the aryl pentacenes studied here, veratrole derivative **3f** shows the largest red shift (33 nm) as a film compared to its solution-state UV–vis spectrum, although the origin of change in the solid state is not understood. It is worth noting, however, that more significant red-shifted λ_{max} -values are often observed for samples which give solution cast films that result in significant π -stacking between molecules, such as TIPSPc, in which λ_{max} shifts from 643 nm in solution to ca. 705 nm in the solid film [11,35,40]. This same logic also suggests that the minimal difference between the absorption characteristics of **3c** and **3h** results from both a lack of influence from the different silyl

groups, as well as the absence of strong π -stacking for both derivatives in the films, even though X-ray crystallographic analysis suggests that strong interactions might be possible for some derivatives in the solid state (vide infra).

Thermal analysis

The thermal stability of selected aryl pentacenes has been explored by traditional melting point analysis (MPA) in open capillary tubes, thermal gravimetric analysis (TGA), and differential scanning calorimetry (DSC) measurements; the results are summarized in Table 2. TGA shows clearly that significant mass loss occurs in the range of 400 °C, which is also common

Table 2: Thermal properties of a representative selection of pentacenes.

Compound	R	Aryl	TGA T_{d} /°C ^a	MPA mp /°C ^b	DSC mp (DSC dp) /°C ^c
3a	iPr		370	162–165	177 (178/179)
3b	iPr		370	244–246	248

Table 2: Thermal properties of a representative selection of pentacenes. (continued)

3c	iPr		375	306–308 ^d	197 ^e	
3d	iPr		372	316–318 ^d	— (206/247)	
3h	Et		410	291–293	287 (288/290)	
3i	iPr		380	211–214	225	
3j	iPr		380	233–235	220 ^f	

^aMeasured under a nitrogen atmosphere. T_d = decomposition temperature, see Supporting Information File 1 for details. ^bTraditional open capillary melting point analysis (MPA), measured under ambient conditions; uncorrected. ^cMeasured under a nitrogen atmosphere; dp = decomposition point, shown as onset/peak temperatures. ^dDecomposition observed in that temperature range, with no indication of melting or decomposition at lower temperature. ^eEndotherm, although apparently not a true mp based on traditional mp analysis. Exotherm at 286 °C (peak) likely corresponds to dp in DSC. ^fThe strongest of several endotherms.

for ethynylated pentacenes such as **1** and **2** [17,18]. There appears to be little evidence of a trend based on the size of the aryl group versus the temperature of observed mass loss in the TGA. By comparing the TGA data with that of MPA made in open capillary tubes, however, it is clear that all pentacene derivatives undergo either a phase change or decomposition prior to the mass loss observed in the TGA. This premise is also confirmed by DSC analyses, which show a melting point in all cases except for thiophenyl derivative **3d** (which decomposed directly in the solid state). In the case of **3a** and **3h**, melting is followed immediately by decomposition (DSC and TGA scans are provided in Supporting Information File 1).

While no correlation between pendent substituent and stability emerges from this analysis, an important point is nevertheless noted, as exemplified by the examination of **3c** and **3d**. Traditional MPA is often insufficient for characterization of pentacene derivatives, in which subtle changes in the samples can be difficult to discern because of the deep, dark color of the sample, and conflicting results are often observed between MPA and DSC.

Cyclic voltammetry

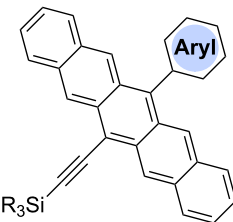
Electrochemical analysis by cyclic voltammetry (CV) was used to investigate the electronic properties of pentacene derivatives **3a–k** in CH_2Cl_2 (ca. 1.5 mM) using tetrabutylammonium hexafluorophosphate as supporting electrolyte and ferrocene as internal standard (all potentials reported are thus given versus

Fc/Fc^+). Aryl-substituted pentacenes **3a–k** each show a one-electron reversible oxidation event in the range between 0.30–0.37 V (Table 3), and a second oxidation process (quasi-reversible) in the range of 0.80–0.99 V. There is, unfortunately, no clear trend observed for the oxidation potentials based on the substitution pattern of the aryl moieties, although both oxidations appear somewhat easier for pentacene **3f** as a result of the two electron-donating methoxy groups attached to the pendent phenyl ring.

Aryl-substituted pentacenes **3a–k** each show one reversible reduction event in a rather narrow range of –1.59 to –1.68 V. Similar to that observed for the oxidation potentials, there is no obvious trend that can be identified in the reduction potentials based on substitution pattern, aside from the observation that the silyl substituent might have a slight impact on reduction (**3h** is slightly harder to reduce than **3c**), and the reduction of thiophenyl derivative **3d** (–1.59 V) stands out as lower than the others.

Substituted pentacenes **3a–k** are slightly easier to oxidize than TIPSPc ($E_{\text{ox}1} = 0.39$ V), and the $E_{\text{ox}1}$ values of **3a–k** fall into a similar range as found for pentacene-based PAH dyads **2a–c** in which the pendant aryl groups are linked by an ethynyl spacer that allows electronic communication between the two arenes [18]. The range of oxidation potentials between TIPSPc, **2a–c**, and **3a–k** is, however, quite narrow, suggesting that the pendent substituent offers little influence on the HOMO level. On the other hand, there is a marked difference in the observed reduc-

Table 3: Electrochemical properties of **3a–k** compared to TIPSPc and **2a–c**.^a



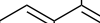
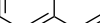
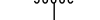
Compound	R	Aryl	E_{ox1} [V]	E_{ox2} [V]	E_{red1} [V]	$E_{\text{gap,el}}$ [eV] ^b
3a	iPr		0.34	0.87	-1.63	1.97
3b	iPr		0.37	0.99	-1.61	1.98
3c	iPr		0.36	0.93	-1.65	2.01
3h	Et		0.32	0.91	-1.68	2.00
3d	iPr		0.35	0.87	-1.59	1.94
3e	iPr		0.32	0.87	-1.68	2.00
3f	iPr		0.30	0.80	-1.67	1.97
3g	iPr		0.34	0.87	-1.65	1.99
3i	iPr		0.32	0.87	-1.66	1.98
3j	iPr		0.32	0.93	-1.67	1.99
3k	iPr		0.35	0.88	-1.67	2.02
2a^c	iPr		0.39	-	-1.44	1.83

Table 3: Electrochemical properties of **3a–k** compared to TIPSPc and **2a–c**.^a (continued)

2b^c	iPr		0.39	–	–1.42	1.81	
2c^c	iPr		0.33	–	–1.38	1.71	
TIPSPc	iPr		0.39	0.99	–1.52	1.91	

^aCyclic voltammetry was performed in CH_2Cl_2 solutions (1.5 mM) containing 0.1 M $n\text{-Bu}_4\text{NPF}_6$ as supporting electrolyte at a scan rate of 150 mV/s. Platinum wire was used as counter electrode, Ag/AgNO_3 as reference electrode, and Pt working electrode. The potential values (E) were calculated using the following equation $E = (E_{\text{pc}} + E_{\text{pa}})/2$, where E_{pc} and E_{pa} correspond to the cathodic and anodic peak potentials, respectively. Potentials are referenced to the ferrocene/ferrocenium (Fc/Fc^+) couple used as an internal standard. All potentials represent a reversible one-electron reduction or oxidation event. ^bElectrochemical HOMO–LUMO gaps determined by $E_{\text{gap,el}} = E_{\text{ox1}} - E_{\text{red1}}$. ^cData taken from [18].

tion potentials. Compounds **2a–c** are most easily reduced while **3a–k** are the most difficult, and the reduction of TIPSPc falls at approximately a midpoint between the two other classes. Thus, the biggest influence of the pendent substituent appears to be related to the energy of the LUMO.

As suggested by the UV–vis analyses (vide infra), the HOMO–LUMO gap estimated for pentacenes **3a–k** by CV (1.94–2.02 eV) is larger than the HOMO–LUMO gap of TIPSPc (1.91 eV), while incorporation of the ethynyl spacer in **2a–c** provides for the lowest HOMO–LUMO gap of the molecules discussed here.

X-ray crystallographic analysis

Typically, three predominant solid-state packing patterns are found by X-ray crystallographic analysis of pentacene and its derivatives [13]: a) a herringbone packing, b) a one-dimensional (1D) slipped-stack, and c) a 2D “bricklayer” packing, as schematically summarized in Figure 4. While several polymorphs have been reported for unsubstituted pentacene [43–46], the arrangement in the solid state is commonly the edge-to-face, herringbone motif [47]. This packing arrangement provides strong electronic coupling in the solid state, and therefore makes this material interesting as the active component for semiconducting devices [48]. It has been shown that functionalization of the pentacene framework, particular by trialkylsilyl-ethynyl groups, drastically alters the solid-state arrangements of the acenes [30]. In certain cases, this leads to a 2D face-to-face “bricklayer” arrangement, which can potentially facilitate charge transport in an electric device by several orders of magnitude [49].

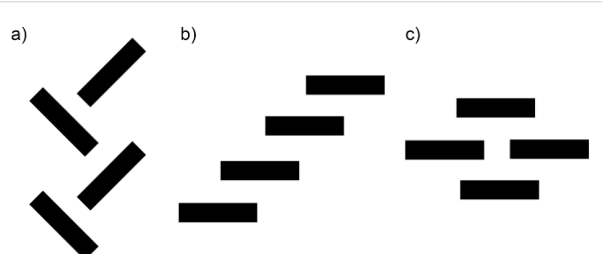


Figure 4: Schematic classification of three common solid-state arrangements of pentacene derivatives a) herringbone packing, b) 1D slipped-stack packing, and c) 2D “bricklayer” packing (as viewed side-on, approximately down the short-molecular axis).

With the understanding that the solid-state packing of acenes can provide vital information about intermolecular interactions, single crystals of pentacenes **3a–d** and **3g–j** were grown and their solid-state arrangements determined by single crystal X-ray diffraction analysis (crystallographic details are provided in Supporting Information File 1). Pentacene **3a** crystallizes in the space group $C2/c$ with eight molecules in the unit cell (Figure 5). Within the solid-state structure, the pendant phenyl ring and the pentacene core are slightly twisted, with a torsion angle of $\sim 71^\circ$. Molecules of pentacene **3a** arrange as dimeric pairs, which then pack into a so-called sandwich herringbone motif (Figure 5c) [50]. Each dimeric pair of pentacenes shows face-to-face π -stacking interactions with an interplanar distance of $\sim 3.40 \text{ \AA}$ and a total overlap of nearly four of the aromatic pentacene rings.

Pentacene **3b** crystallizes in the space group $P-1$ with two molecules in the unit cell (Figure 6). Notably, the naphthyl unit is

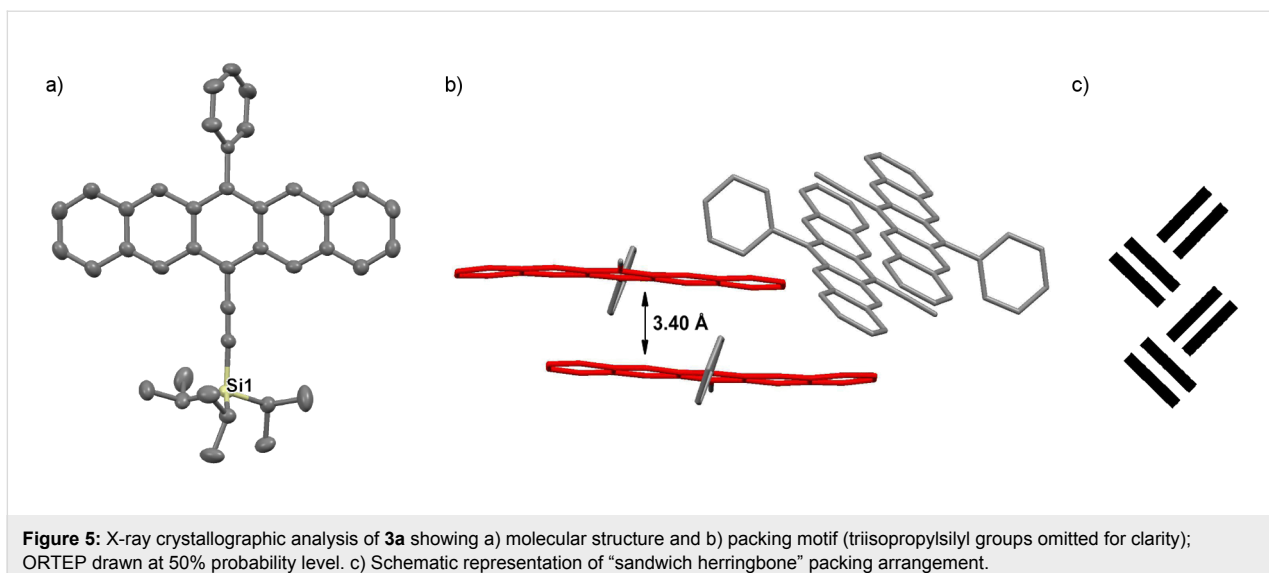


Figure 5: X-ray crystallographic analysis of **3a** showing a) molecular structure and b) packing motif (triisopropylsilyl groups omitted for clarity); ORTEP drawn at 50% probability level. c) Schematic representation of “sandwich herringbone” packing arrangement.

significantly disordered over two unique positions in the solid state but is nearly perpendicular to the pentacene core with a twist angle of $\sim 81^\circ$. Pentacene **3b** assembles in dimeric pairs, which then arrange in a 1D π -slipped stack motif, and the pentacene molecules are separated by interplanar distances of ~ 3.42 Å and ~ 3.52 Å.

Pentacene **3c** crystallizes in the space group $P2_1/c$ with four molecules in the unit cell (Figure 7) [31]. The pentacene skeleton and the anthracenyl substituent are nearly perpendicular to each other with a twist angle of $\sim 90^\circ$. This motif also places the anthracene moieties in a face-to-face packing 1D slipped stack arrangement, although the interplanar distance of ~ 3.61 Å is sizable. The aromatic pentacene cores pack in a face-to-face 2D bricklayer arrangement, with approximately two

pentacene rings overlapping and interplanar distances of ~ 3.52 Å and 3.46 Å.

Pentacene **3d** crystallizes in the space group $P2_1/n$ with four molecules in each unit cell (Figure 8), and the thiaryl and trialkylsilyl groups show disorder in the structure. With a twist angle of $\sim 90^\circ$, the thiaryl unit is essentially perpendicular to the pentacene skeleton. Centrosymmetric dimeric pairs of pentacene **3d** pack with an interplanar distance of 3.52 Å and these pairs then arrange into a sandwich herringbone stacking pattern, similar to phenyl derivative **3a**.

Pentacene **3g** crystallizes in the space group $P2_1/n$ with four molecules in the unit cell (Figure 9). The phenyl substituent is twisted with an angle of $\sim 70^\circ$ relative to the pentacene skeleton.

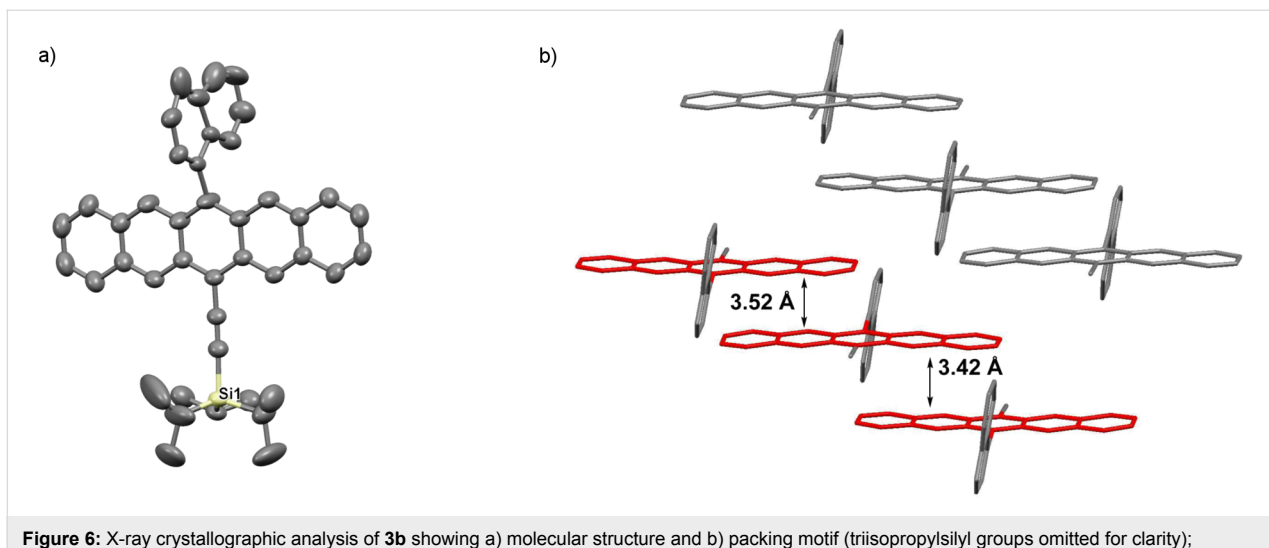


Figure 6: X-ray crystallographic analysis of **3b** showing a) molecular structure and b) packing motif (triisopropylsilyl groups omitted for clarity); ORTEP drawn at 50% probability level.

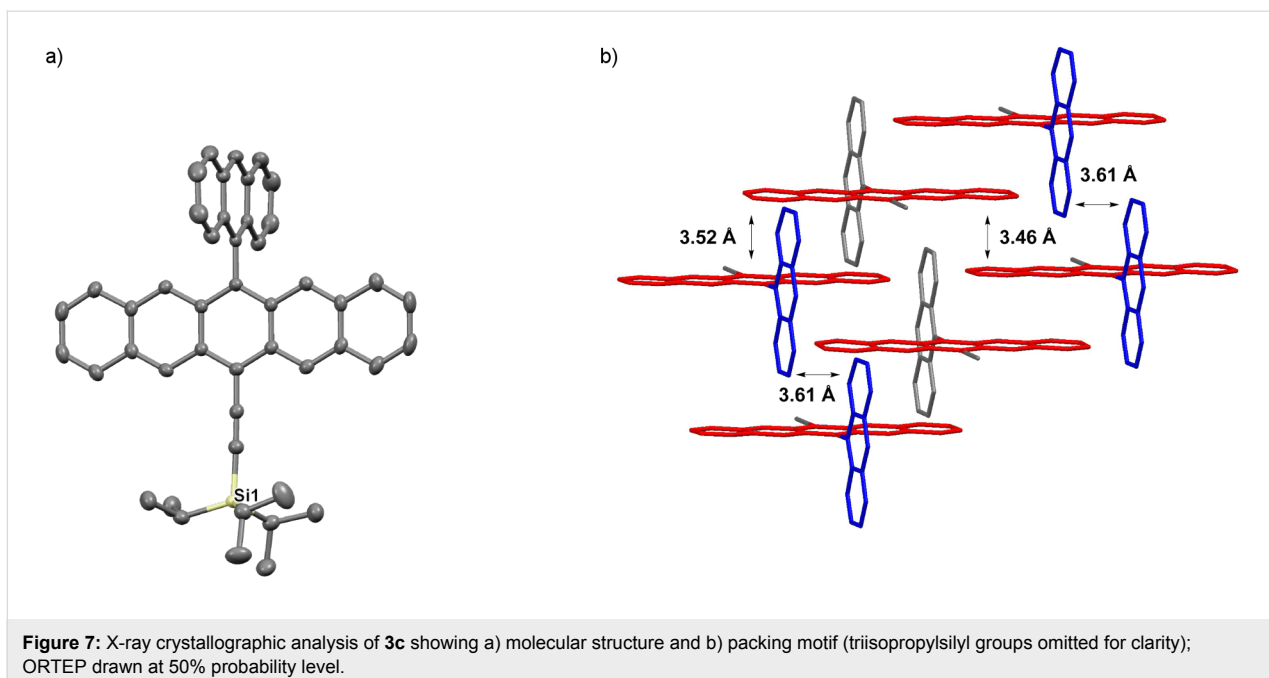


Figure 7: X-ray crystallographic analysis of **3c** showing a) molecular structure and b) packing motif (triisopropylsilyl groups omitted for clarity); ORTEP drawn at 50% probability level.

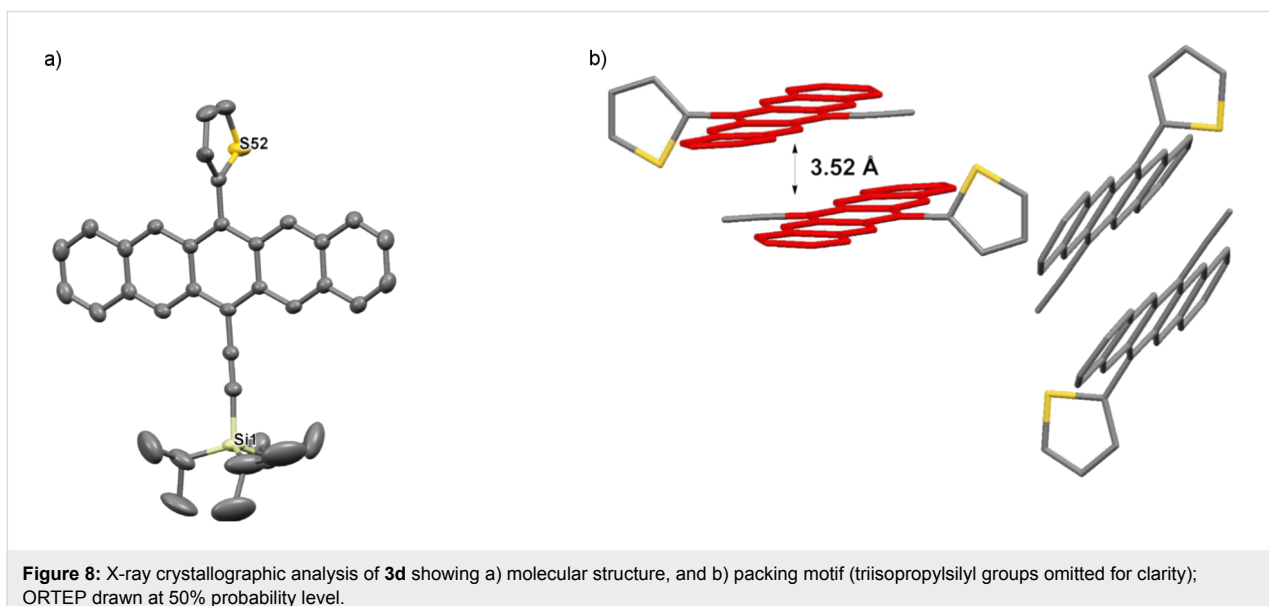


Figure 8: X-ray crystallographic analysis of **3d** showing a) molecular structure, and b) packing motif (triisopropylsilyl groups omitted for clarity); ORTEP drawn at 50% probability level.

Two neighboring molecules of **3g** arrange into a dimeric pair with an interplanar distance of 3.42 Å, and these pairs then pack in a sandwich herringbone arrangement. The overall solid-state arrangement is similar to that observed for **3a** and **3d**.

Pentacene **3h** crystallizes in the space group *P*2₁/c with four molecules in each unit cell (Figure 10). The anthracenyl substituent is twisted relative to the pentacene skeleton with an angle of ~74°, less than that found for **3c** (90°). Interestingly, pentacene **3h** shows an unusual solid-state arrangement not typically observed for pentacene derivatives. Namely, the

pentacene molecules form channels along the crystallographic *a*-axis, which are composed of only two tiers of a brick wall structure. The pentacene molecules within these channels are stacked with an interplanar distance of 3.57 Å. These channels are macroscopically arranged as staircases, dictated by the anthracenyl moieties that are oriented such that CH–π interactions of ~2.90 Å likely play a role in directing the packing (see Supporting Information File 1, Figure S12).

Pentacene **3i** crystallizes in the space group *P*-1 with two molecules in each unit cell (Figure 11). The benzene ring directly at-

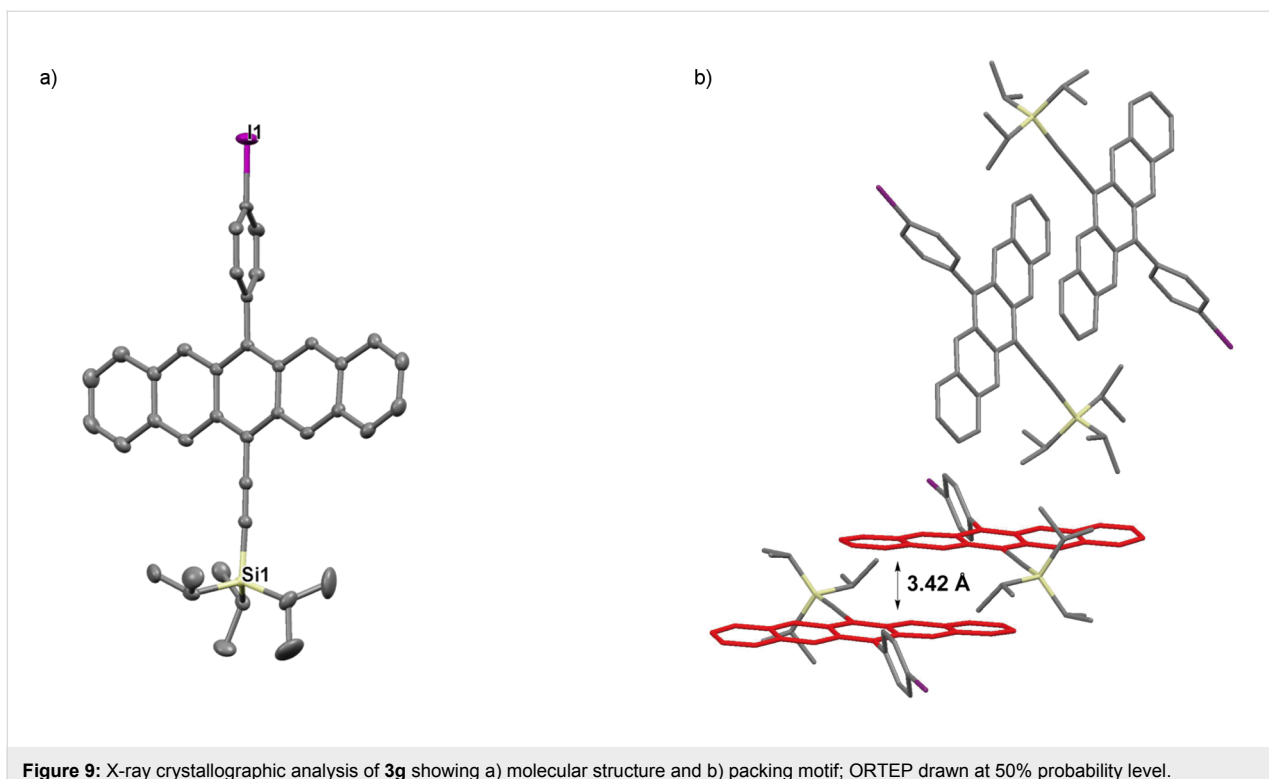


Figure 9: X-ray crystallographic analysis of **3g** showing a) molecular structure and b) packing motif; ORTEP drawn at 50% probability level.

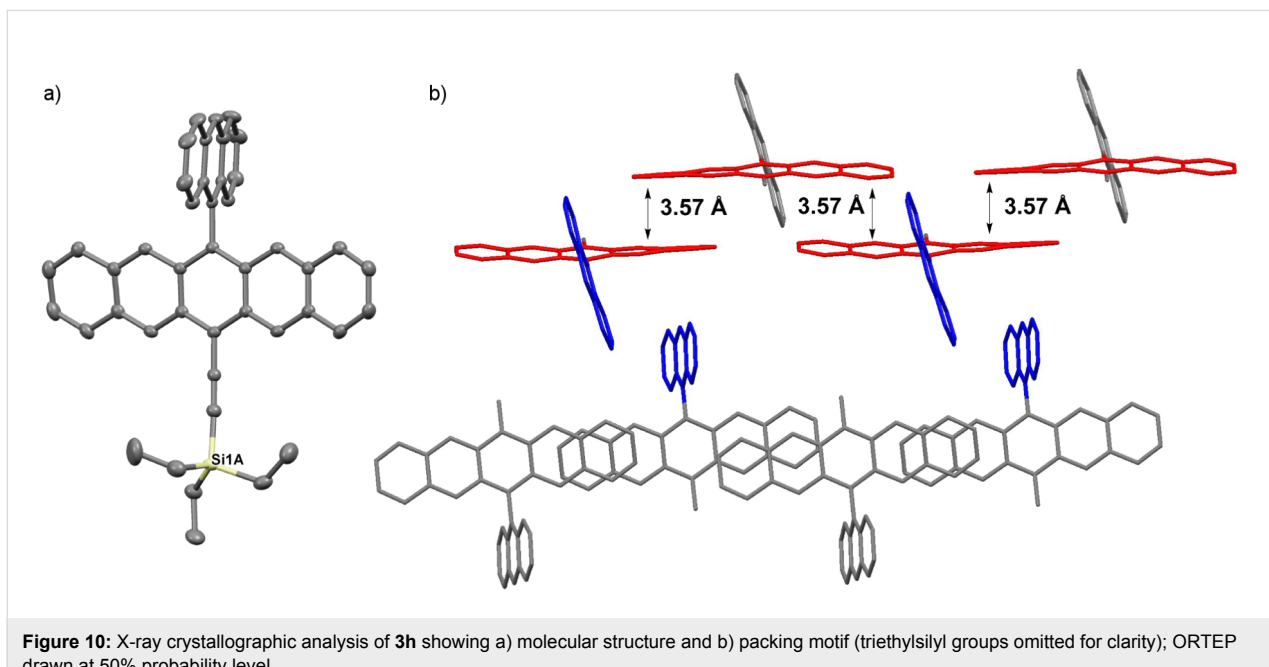


Figure 10: X-ray crystallographic analysis of **3h** showing a) molecular structure and b) packing motif (triethylsilyl groups omitted for clarity); ORTEP drawn at 50% probability level.

tached to the pentacene framework is nearly perpendicular to the pentacene core with an angle of $\sim 81^\circ$, while the torsion angle between the two rings of the biphenyl unit is 32° . The biphenyl substituent is slightly bent from linearity with an angle of $\sim 6^\circ$ (as estimated from the three atoms designated with an asterisk *). Biphenyl-substituted pentacene **3i** arranges in a 1D

slipped stack motif along the crystallographic *c*-axis, with π -stacking distances of 3.28 \AA and 3.35 \AA .

Pentacene derivative **3j** crystallizes in the space group *P*-1 with two molecules in the unit cell (Figure 12). Interestingly, the pentacene core and the naphthyl group are nearly coplanar (4°),

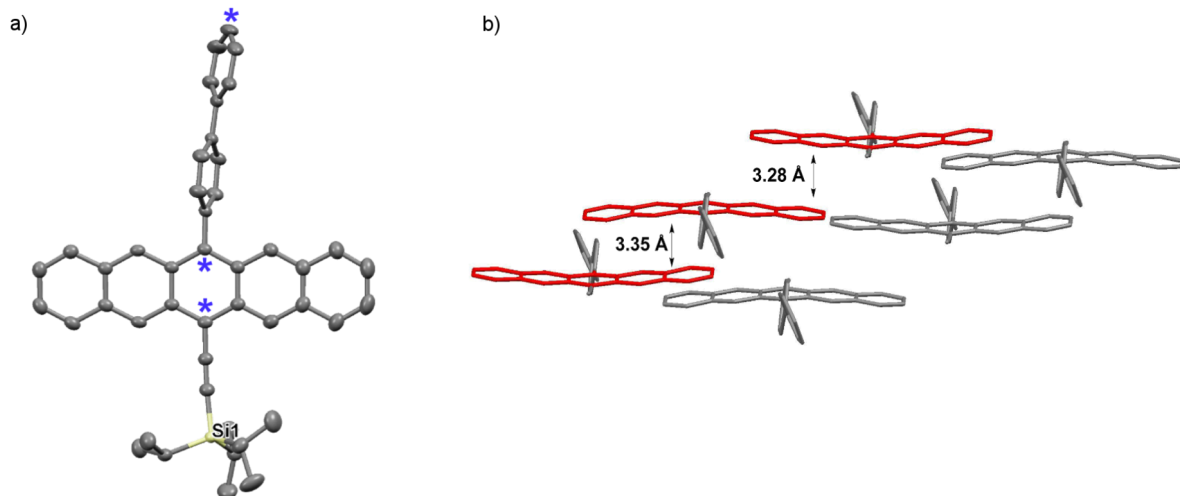


Figure 11: X-ray crystallographic analysis of **3i** showing a) molecular structure and b) packing motif (triisopropylsilyl groups omitted for clarity); ORTEP drawn at 50% probability level.

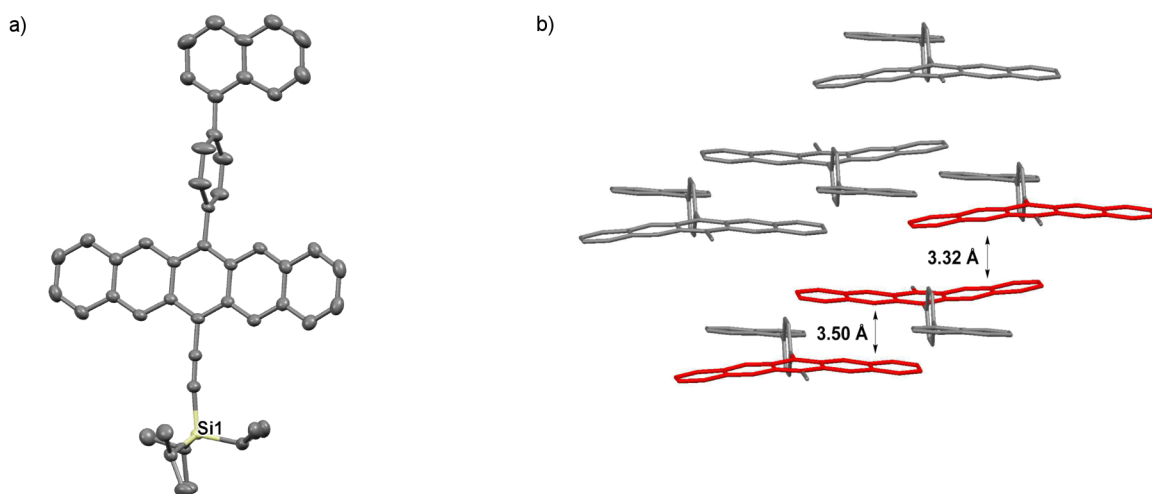


Figure 12: X-ray crystallographic analysis of **3j** showing a) molecular structure and b) packing motif (triisopropylsilyl groups omitted for clarity); ORTEP drawn at 50% probability level.

while the intervening benzene ring is nearly perpendicular to both the pentacene skeleton ($\sim 90^\circ$) and the naphthyl group ($\sim 86^\circ$). Compound **3j** arranges in a 1D slipped stack arrangement along the crystallographic *b*-axis with two different interplanar distances of ~ 3.50 Å and 3.32 Å.

Conclusion

In summary, a library of unsymmetrically substituted pentacenes has been synthesized by a straightforward procedure that requires only one purification step. Optical spectroscopy and cyclic voltammetry reveal that electronic communication between the pentacene core and the different

substituents is limited, as a result of the orthogonal orientation of the pentacene backbone and the pendent aryl moieties. Thus, these results show that the nature of the substituent does not change the electronic properties of the pentacene skeleton itself. Aryl-substitution pattern does however, have a considerable effect on solid-state arrangement of the molecules, and X-ray crystallographic analysis afforded insight on the packing arrangements of the synthesized pentacenes. In spite of the large number of crystallographic analyses that have been examined here, general trends are difficult to establish based on, for example, either the number of π – π and CH– π interactions or the size of the aromatic group appended to the pentacene core. It

does seem, however, that anthracenyl substitution (in **3c** and **3h**) affords the highest degree of π -stacking amongst the derivatives examined.

Supporting Information

Supporting Information File 1

Experimental procedures and characterization data for all new compounds. Copies of ^1H and ^{13}C NMR, UV-vis, and emission spectra; CV, DSC, and TGA scans.

[<http://www.beilstein-journals.org/bjoc/content/supplementary/1860-5397-10-178-S1.pdf>]

Acknowledgements

The authors acknowledge funding for this work from the Energie Campus Nürnberg (EnCN), “Solar Technologies go Hybrid” (an initiative of the Bavarian State Ministry of Science, Research and Art), and the Deutsche Forschungsgemeinschaft (DFG) through the Cluster of Excellence “Engineering of Advanced Materials”. We thank Dr. Michael J. Ferguson for the X-ray crystallographic analysis of ketone **4b**.

References

1. Figueira-Duarte, T. M.; Müllen, K. *Chem. Rev.* **2011**, *111*, 7260–7314. doi:10.1021/cr100428a
2. Hains, A. W.; Liang, Z.; Woodhouse, M. A.; Gregg, B. A. *Chem. Rev.* **2010**, *110*, 6689–6735. doi:10.1021/cr9002984
3. Lucas, B.; Trigaud, T.; Videlot-Ackermann, C. *Polym. Int.* **2012**, *61*, 374–389. doi:10.1002/pi.3213
4. Beaujuge, P. M.; Fréchet, J. M. J. *J. Am. Chem. Soc.* **2011**, *133*, 20009–20029. doi:10.1021/ja2073643
5. Cheng, Y.-J.; Yang, S.-H.; Hsu, C.-S. *Chem. Rev.* **2009**, *109*, 5868–5923. doi:10.1021/cr900182s
6. Martín, N.; Sánchez, L.; Herranz, M. Á.; Illescas, B.; Guldi, D. M. *Acc. Chem. Res.* **2007**, *40*, 1015–1024. doi:10.1021/ar700026t
7. Dang, M. T.; Hirsch, L.; Wantz, G.; Wuest, J. D. *Chem. Rev.* **2013**, *113*, 3734–3765. doi:10.1021/cr300005u
8. Arias, A. C.; MacKenzie, J. D.; McCulloch, I.; Rivnay, J.; Salleo, A. *Chem. Rev.* **2010**, *110*, 3–24. doi:10.1021/cr900150b
9. Hains, A. W.; Liang, Z.; Woodhouse, M. A.; Gregg, B. A. *Chem. Rev.* **2010**, *110*, 6689–6735. doi:10.1021/cr9002984
10. Mei, J.; Diao, Y.; Appleton, A. L.; Fang, L.; Bao, Z. *J. Am. Chem. Soc.* **2013**, *135*, 6724–6746. doi:10.1021/ja400881n
11. Lehnher, D.; Tykwiński, R. R. *Materials* **2010**, *3*, 2772–2800. doi:10.3390/ma3042772
12. Lehnher, D.; Tykwiński, R. R. *Aust. J. Chem.* **2011**, *64*, 919–929. doi:10.1071/CH11169
13. Anthony, J. E. *Chem. Rev.* **2006**, *106*, 5028–5048. doi:10.1021/cr050966z
14. Anthony, J. E. *Angew. Chem., Int. Ed.* **2008**, *47*, 452–483. doi:10.1002/anie.200604045
15. Bendikov, M.; Wudl, F.; Perepichka, D. F. *Chem. Rev.* **2004**, *104*, 4891–4946. doi:10.1021/cr030666m
16. Anthony, J. E.; Brooks, J. S.; Eaton, D. L.; Parkin, S. R. *J. Am. Chem. Soc.* **2001**, *123*, 9482–9483. doi:10.1021/ja0162459
17. Lehnher, D.; Murray, A. H.; McDonald, R.; Tykwiński, R. R. *Angew. Chem., Int. Ed.* **2010**, *49*, 6190–6194. doi:10.1002/anie.201000555
18. Lehnher, D.; Murray, A. H.; McDonald, R.; Ferguson, M. J.; Tykwiński, R. R. *Chem.–Eur. J.* **2009**, *15*, 12580–12584. doi:10.1002/chem.200902179
19. Lehnher, D.; Gao, J.; Hegmann, F. A.; Tykwiński, R. R. *J. Org. Chem.* **2009**, *74*, 5017–5024. doi:10.1021/jo9007089
20. Lehnher, D.; McDonald, R.; Ferguson, M. J.; Tykwiński, R. R. *Tetrahedron* **2008**, *64*, 11449–11461. doi:10.1016/j.tet.2008.09.041
21. Lehnher, D.; Gao, J.; Hegmann, F. A.; Tykwiński, R. R. *Org. Lett.* **2008**, *10*, 4779–4782. doi:10.1021/o1801886h
22. Lehnher, D.; Tykwiński, R. R. *Org. Lett.* **2007**, *9*, 4583–4586. doi:10.1021/o1702094d
23. Kuninobu, Y.; Seiki, T.; Kanamaru, S.; Nishina, Y.; Takai, K. *Org. Lett.* **2010**, *12*, 5287–5289. doi:10.1021/o1102349r
24. Li, Y.; Wu, Y.; Liu, P.; Prostran, Z.; Gardner, S.; Ong, B. S. *Chem. Mater.* **2007**, *19*, 418–423. doi:10.1021/cm062378n
25. Lee, S. H.; Kim, S. H.; Choo, D. J.; Jang, J. *Org. Electron.* **2010**, *11*, 1268–1272. doi:10.1016/j.orgel.2010.03.018
26. Wang, C.; Dong, H.; Hu, W.; Liu, Y.; Zhu, D. *Chem. Rev.* **2012**, *112*, 2208–2267. doi:10.1021/cr100380z
27. Zade, S. S.; Bendikov, M. *J. Phys. Org. Chem.* **2012**, *25*, 452–461. doi:10.1002/poc.1941
28. Biermann, D.; Schmidt, W. *J. Am. Chem. Soc.* **1980**, *102*, 3163–3173. doi:10.1021/ja00529a046
29. Bénard, C. P.; Geng, Z.; Heuft, M. A.; VanCrey, K.; Fallis, A. G. *J. Org. Chem.* **2007**, *72*, 7229–7236. doi:10.1021/jo0709807
30. Anthony, J. E.; Eaton, D. L.; Parkin, S. R. *Org. Lett.* **2002**, *4*, 15–18. doi:10.1021/o10167356
31. Etschel, S. H.; Waterloo, A. R.; Margraf, J. T.; Amin, A. Y.; Hampel, F.; Jäger, C. M.; Clark, T.; Halik, M.; Tykwiński, R. R. *Chem. Commun.* **2013**, *49*, 6725–6727. doi:10.1039/c3cc43270j
32. Zhang, J.; Pawle, R. H.; Haas, T. E.; Thomas, S. W., III. *Chem.–Eur. J.* **2014**, *20*, 5880–5884. doi:10.1002/chem.201402003
33. Kim, Y.-E.; Park, J.-W. *Mol. Cryst. Liq. Cryst.* **2006**, *444*, 137–143. doi:10.1080/15421440500365318
34. Zhang, X.; Jiang, X.; Luo, J.; Chi, C.; Chen, H.; Wu, J. *Chem.–Eur. J.* **2010**, *16*, 464–468. doi:10.1002/chem.200902675
35. Lehnher, D.; McDonald, R.; Tykwiński, R. R. *Org. Lett.* **2008**, *10*, 4163–4166. doi:10.1021/o1801464k
36. Waterloo, A. R.; Kunakom, S.; Hampel, F.; Tykwiński, R. R. *Macromol. Chem. Phys.* **2012**, *213*, 1020–1032. doi:10.1002/macp.201100622
37. Boudebois, A.; Constable, E. C.; Housecroft, C. E.; Neuburger, M.; Schaffner, S. *Acta Crystallogr., Sect. C* **2006**, *62*, o243–o245. doi:10.1107/S0108270106008262
38. Vets, N.; Smet, M.; Dehaen, W. *Synlett* **2005**, 217–222. doi:10.1055/s-2004-836055
39. Maulding, D. R.; Roberts, B. G. *J. Org. Chem.* **1969**, *34*, 1734–1736. doi:10.1021/jo01258a045
40. Platt, A. D.; Day, J.; Subramanian, S.; Anthony, J. E.; Ostroverkhova, O. *J. Phys. Chem. C* **2009**, *113*, 14006–14014. doi:10.1021/jp904021p
41. Ostroverkhova, O.; Shcherbyna, S.; Cooke, D. G.; Egerton, R. F.; Hegmann, F. A.; Tykwiński, R. R.; Parkin, S. R.; Anthony, J. E. *J. Appl. Phys.* **2005**, *98*, 033701. doi:10.1063/1.1949711

42. Lee, K. O.; Gan, T. T. *Chem. Phys. Lett.* **1977**, *51*, 120–124.
doi:10.1016/0009-2614(77)85368-2

43. Mattheus, C. C.; Dros, A. B.; Baas, J.; Oostergetel, G. T.; Meetsma, A.;
de Boer, J. L.; Palstra, T. T. M. *Synth. Met.* **2003**, *138*, 475–481.
doi:10.1016/S0379-6779(02)00467-8

44. Mattheus, C. C.; Dros, A. B.; Baas, J.; Meetsma, A.; de Boer, J. L.;
Palstra, T. T. M. *Acta Crystallogr., Sect. C* **2001**, *57*, 939–941.
doi:10.1107/S010827010100703X

45. Siegrist, T.; Kloc, C.; Schön, J. H.; Batlogg, B.; Haddon, R. C.; Berg, S.;
Thomas, G. A. *Angew. Chem., Int. Ed.* **2001**, *40*, 1732–1736.
doi:10.1002/1521-3773(20010504)40:9<1732::AID-ANIE17320>3.0.CO
;2-7

46. Mattheus, C. C.; de Wijs, G. A.; de Groot, R. A.; Palstra, T. T. M.
J. Am. Chem. Soc. **2003**, *125*, 6323–6330. doi:10.1021/ja0211499

47. Campbell, R. B.; Robertson, J. M.; Trotter, J. *Acta Crystallogr.* **1962**,
15, 289–290. doi:10.1107/S0365110X62000699

48. Anthony, J. E.; Subramanian, S.; Parkin, S. R.; Park, S. K.;
Jackson, T. N. *J. Mater. Chem.* **2009**, *19*, 7984–7989.
doi:10.1039/b911560a

49. Kim, D. H.; Lee, D. Y.; Lee, H. S.; Lee, W. H.; Kim, Y. H.; Han, J. I.;
Cho, K. *Adv. Mater.* **2007**, *19*, 678–682. doi:10.1002/adma.200601259

50. Lim, Y.-F.; Shu, Y.; Parkin, S. R.; Anthony, J. E.; Malliaras, G. G.
J. Mater. Chem. **2009**, *19*, 3049–3056. doi:10.1039/b818693f

License and Terms

This is an Open Access article under the terms of the Creative Commons Attribution License (<http://creativecommons.org/licenses/by/2.0>), which permits unrestricted use, distribution, and reproduction in any medium, provided the original work is properly cited.

The license is subject to the *Beilstein Journal of Organic Chemistry* terms and conditions:
(<http://www.beilstein-journals.org/bjoc>)

The definitive version of this article is the electronic one which can be found at:
doi:10.3762/bjoc.10.178



Synthesis of nanodiamond derivatives carrying amino functions and quantification by a modified Kaiser test

Gerald Jarre¹, Steffen Heyer¹, Elisabeth Memmel¹, Thomas Meinhardt¹
and Anke Krueger^{*1,2}

Full Research Paper

Open Access

Address:

¹Institute for Organic Chemistry, Julius-Maximilians-Universität Würzburg, Am Hubland, 97074 Würzburg, Germany and ²Wilhelm Conrad Röntgen Research Center for Complex Material Systems (RCCM), Julius-Maximilians-Universität Würzburg, Germany

Email:

Anke Krueger* - anke.krueger@uni-wuerzburg.de

* Corresponding author

Keywords:

amino groups; carbon nanomaterials; Diels–Alder reaction; Kaiser test; nanodiamond; pyrazine

Beilstein J. Org. Chem. **2014**, *10*, 2729–2737.

doi:10.3762/bjoc.10.288

Received: 31 July 2014

Accepted: 24 October 2014

Published: 20 November 2014

This article is part of the Thematic Series "Functionalized carbon nanomaterials".

Associate Editor: P. J. Skabara

© 2014 Jarre et al; licensee Beilstein-Institut.

License and terms: see end of document.

Abstract

Nanodiamonds functionalized with different organic moieties carrying terminal amino groups have been synthesized. These include conjugates generated by Diels–Alder reactions of *ortho*-quinodimethanes formed *in situ* from pyrazine and 5,6-dihydro-cyclobuta[*d*]pyrimidine derivatives. For the quantification of primary amino groups a modified photometric assay based on the Kaiser test has been developed and validated for different types of aminated nanodiamond. The results correspond well to values obtained by thermogravimetry. The method represents an alternative wet-chemical quantification method in cases where other techniques like elemental analysis fail due to unfavourable combustion behaviour of the analyte or other impediments.

Introduction

Surface bound amino groups are most versatile for the grafting of larger moieties onto the surface of nanoparticles. Typically, they are used for the formation of amides using protocols from peptide chemistry or in reductive aminations [1,2]. Additionally, amino groups have an influence on the surface polarity and dispersion behaviour due to their protic character and the possibility to protonate the nitrogen.

In the case of diamond the direct amination of the surface has rarely been reported. Sotowa et al. used the photochemical reaction of ammonia with chlorinated diamond [3]. However, the

termination with amino groups is typically not complete and the stability of amino groups directly bound to the diamond surface is limited as they are at least partially replaced by hydroxy groups under ambient conditions [4].

Therefore, in most cases linkers are used in order to establish stable bonding situations on the surface. These include siloxanes (e.g., APTMS) [5], alkyl chains connected to the diamond surface by amide or ester bonds [6], and aminomethyl groups formed by the nucleophilic substitution of tosylated OH groups by cyanide followed by a reduction with LiAlH₄ [7]. Except for

the last case, the linkers are coupled to the diamond surface via heteroatoms. These sites are more easily cleaved compared to carbon–carbon single bonds, e.g., in a physiological environment or other aqueous conditions. It is hence of interest to develop methods that form stable bonds between the diamond surface and the aminated moiety. One commonly used method is the (*in situ*) formation of aromatic diazonium salts and the reaction of the aryl residue with π -bonds, hydrogenated sites or various surface groups (in this case via heteroatoms) on the diamond surface [8–10]. Recently, we have reported an efficient method for the grafting of organic moieties onto diamond carrying sp^2 carbon atoms at its surface using the Diels–Alder reaction of *ortho*-quinodimethanes onto π -bonds on the particle surface. By this reaction two C–C single bonds are formed in one step, thus increasing the stability of the conjugate [11]. We were able to show that the aromatic molecules immobilized by this technique can be further modified using conventional synthetic chemistry [12]. This enables the utilization of such diamond conjugates for biomedical applications as the C–C bound linker between the nanoparticle and the functional moiety is not prone to hydrolytic or enzymatic decay. Stable conjugation is an essential prerequisite for applications such as labelling or targeting.

Here we report on the grafting of nitrogen-containing heterocyclic aromatic compounds using the Diels–Alder reaction of suitable starting materials and diamond carrying sufficient amounts of sp^2 carbon in order to allow the cycloaddition to occur. The aim was to increase the surface loading with aromatic moieties compared to the benzenic moieties due to the modified reactivity of the respective precursors.

Results and Discussion

The functionalization of nanodiamond with aromatic moieties carrying amino groups

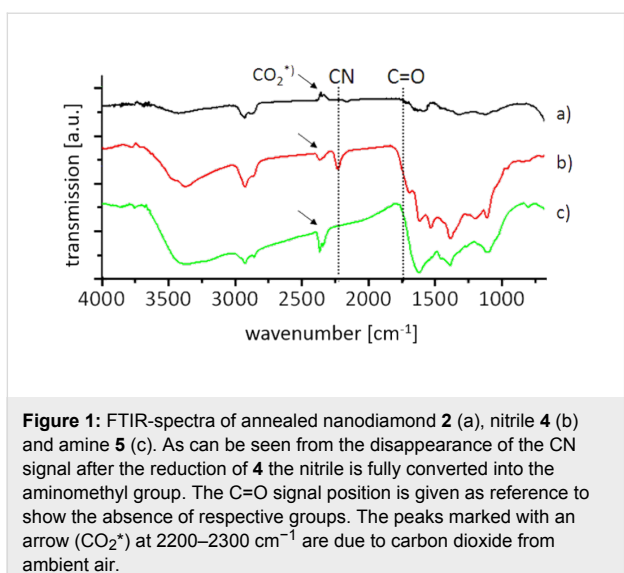
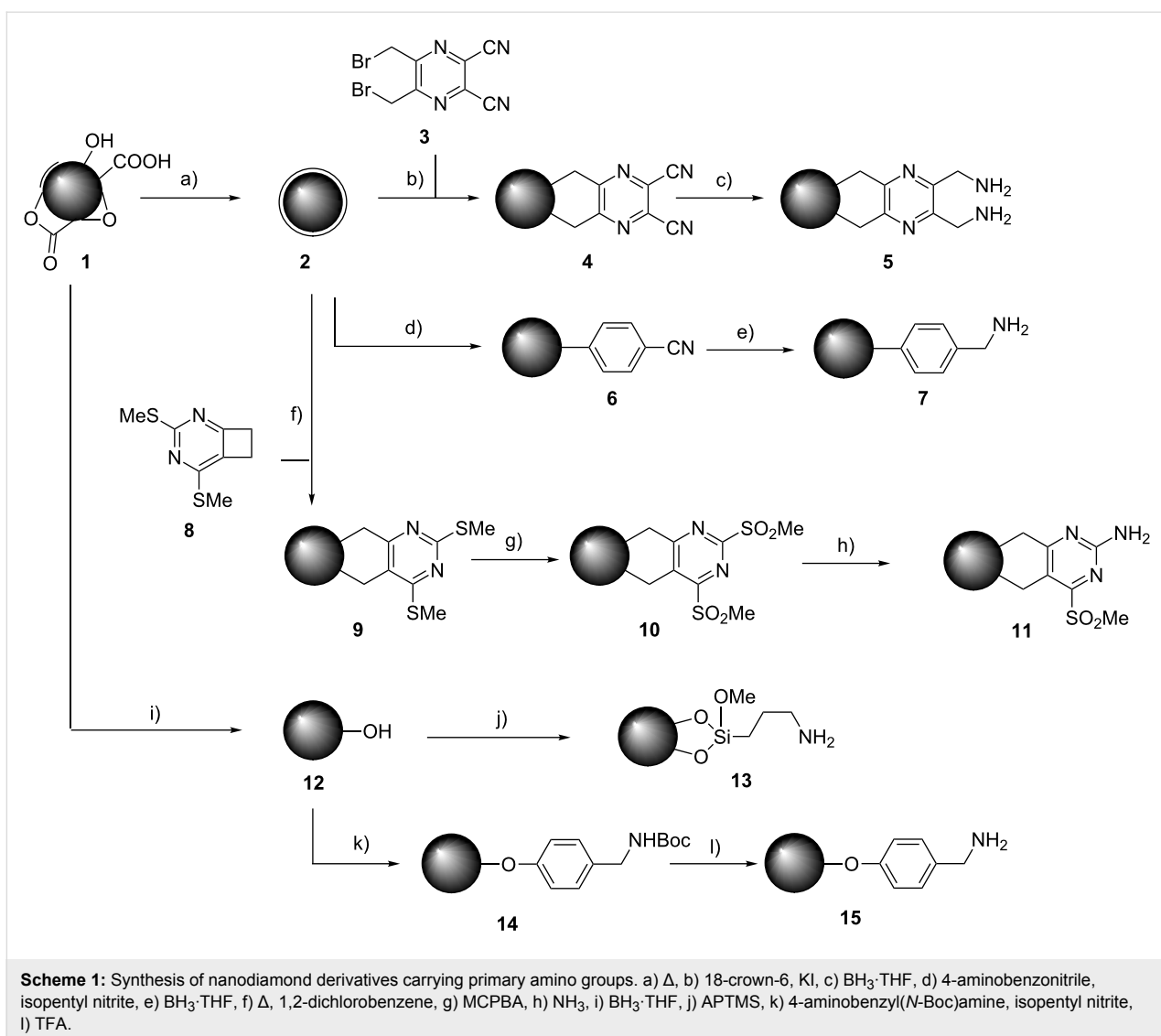
For the synthesis of a broad variety of aminated nanodiamond (ND) derivatives, a series of nanodiamond conjugates with different linker systems was synthesized starting from detonation nanodiamond **1** and thermally annealed nanodiamond **2** as depicted in Scheme 1. Besides the novel functionalization methods using pyrazines and cyclobutenes (see below) several nanodiamond conjugates were prepared for comparison similar to already reported procedures.

It is known that pyrazine derivatives react with fullerenes in a cycloaddition reaction [13]. Pyrazine **3** was synthesized from 1,4-dibromobuta-2,3-dione and diaminomaleonitrile similar to a procedure reported by Fukunishi and coworkers [14]. The resulting 2,3-bis(bromomethyl)-5,6-dicyanopyrazine (**3**) is a precursor for the respective *ortho*-quinodimethane required for the Diels–Alder reaction. The reaction proceeds in analogy to

the one for benzenic starting materials by *in situ* generation of the diene and reaction with surface π -bonds on the nanodiamond acting as dienophiles. The successful grafting can be monitored by the appearance of the distinct signal of nitriles in the IR spectrum at $\sim 2225\text{ cm}^{-1}$ (Figure 1). In addition the aromatic vibration modes of C=N and C=C bonds are observed at 1613 and 1530 cm^{-1} . The removal of solely adsorbed reagent is ensured by a thorough washing procedure and control of the washing solutions using TLC. The functionalized nanodiamond **4** forms very stable colloidal solutions in organic solvents such as acetone or dichloromethane with very low particle sizes close to the size of the pristine primary particles. The determination of the surface loading with the pyrazine moieties, however, leads to contradictory results at first sight. In the elemental analysis by combustion a surprisingly high surface loading of 1.56 mmol g^{-1} is measured whereas the thermogravimetric analysis yields a value of 0.61 mmol g^{-1} . It appears that nanodiamond-carrying nitrogen-rich aromatic moieties have a different combustion behaviour compared to other diamond derivatives. The observed incomplete combustion leads to an underestimation of the carbon content and hence overestimated values for nitrogen and hydrogen (and sulfur, if present). As will be discussed below, the wet-chemical quantification supports the value obtained by thermogravimetry and hence one has to assume that combustion analysis is not suitable for this type of nanodiamond derivatives.

The dicyanopyrazine conjugate **4** can be submitted to a reduction of the nitrile groups using borane solution in THF. This mild yet efficient reaction leads to the complete transformation of the nitriles to amino groups as evidenced by the disappearance of the IR signals of the CN group. Furthermore, no difficult to remove side products are formed. The borate generated by the hydrolysis is easily washed away with water. Again, the value for the surface loading shows a strong discrepancy between TGA and elemental analysis. Both methods show the completely retained surface architecture by comparable values for the dinitrile **4** and the reduction product **5**. However, the incomplete combustion of the nanodiamond samples leads to overestimated values of 1.75 mmol g^{-1} in the case of combustion analysis. The loading determined by TGA (0.60 mmol g^{-1}) is corroborated by the value obtained in the modified Kaiser test (see below). The reduction of the nitrile groups has an important influence on the colloidal stability of the ND conjugate. Whereas the nitrile derivative **4** is soluble in rather nonpolar organic solvents, the amino derivative **5** forms stable aqueous colloids with well dispersed primary particles of nanodiamond.

The use of the pyrazine-derived reagents enables the grafting of $\sim 0.6\text{ mmol g}^{-1}$ of the aromatic moieties onto the particle surface, possessing 1.2 mmol g^{-1} of amino groups. Comparing



this to the typical value of 0.15 mmol g^{-1} for the Diels–Alder reaction of the non-functionalized *ortho*-quinodimethane [11] proves that a significantly increased grafting is observed using the pyrazine derivative.

So far, the reported cycloaddition reactions of *ortho*-quinodimethanes leading to the grafting of aromatic rings by Diels–Alder reaction were based on the 1,4-elimination from suitable precursors. This step requires reagents such as potassium iodide and 18-crown-6 and hence the removal of the resulting side products [11]. Another approach to *ortho*-quinodimethanes makes use of the thermal ring opening of cyclobutenes. This system has been successfully used for the functionalization of fullerenes [15]. The precursor **8** was synthesized according to Martinez et al. starting from cyclobutanone and methyl thiocyanate [16]. The cyclobutene ring opens at temperatures around $190\text{ }^\circ\text{C}$ and the *ortho*-quinodimethane is

formed in situ. The reaction with the nanodiamond surface occurs simultaneously as soon as the diene is formed. The solvent dichlorobenzene was chosen not only for its suitable boiling point but also for the efficient solubilization of the reaction participants.

The ND conjugate **9** shows characteristic signals in the IR spectrum (Figure 2), namely the vibrations at 1590, 1530 and 1430 cm^{-1} are caused by the grafted heteroaromatic moieties. The spectrum corresponds well to the signals observed for 2,4-bis(methylthio)pyrimidine [17]. The surface loading was determined by TGA and elemental analysis based on the nitrogen and sulfur content. All analytical methods yield comparable results around 0.2 mmol g⁻¹.

control experiment using nanodiamond not functionalized with the pyrimidine proved the reactivity of surface groups of the nanodiamond (CH, OH, π -bonds etc. are present on thermally annealed nanodiamond [18]) with MCPBA showing the formation of oxidized surface groups and an increase of the respective IR signals for carbonyl groups (see Supporting Information File 1 for details). When the mass loss related to the groups generated by this side reaction is subtracted from the overall result using the results from the control experiment, the values for the surface loading for compound **10** measured by combustion analysis (using values for N and S and hence only considering the heterocycle) and TGA (where the combined mass loss for the heterocycle and the oxidized groups is measured) are fully comparable.

The generation of the amino functions is carried out using gaseous ammonia and hence the isolation and purification of the reaction product **11** is very simple. As expected the intensity of the sulfone related IR bands decreases upon amination (but does not vanish as only the SO₂Me group in 2-position is exchanged) and new signals corresponding to amino functions (1590 and \sim 3450 cm^{-1}) appear in the spectrum. Furthermore, the sulfur content of the material is reduced to one half of the original value. This shows that the reaction occurs with high efficiency as the remaining sulfur stems from the conserved sulfone group.

From these results it is obvious that the thermal ring opening of suitable cyclobutenes is another valuable addition to the portfolio of cycloaddition related surface reactions of nanodiamond. It allows the efficient immobilization of quite complex organic moieties without the use of auxiliaries or further reagents. No problematic side products or waste are formed and the selective transformation of the different functional groups on the aromatic ring also allows the orthogonal functionalization with different moieties in the subsequent grafting steps.

Analysis of surface amino groups on nanodiamond

Besides spectroscopic techniques, thermogravimetry and combustion (elemental) analysis are typically applied for the quantification of surface groups on nanomaterials. In most cases these methods yield reliable results and the obtained values are comparable for the different methods. However, it turned out that for some nanodiamond derivatives with a high concentration of nitrogen in the surface functionalities the discrepancy between surface loadings determined using elemental analysis and TGA was exceeding the variations brought upon by different measurement methods and experimental deviations. As shown in Table 1 the values obtained by combustion analysis were three times higher than those measured by TGA. Reasons for this difference can be the incomplete combustion

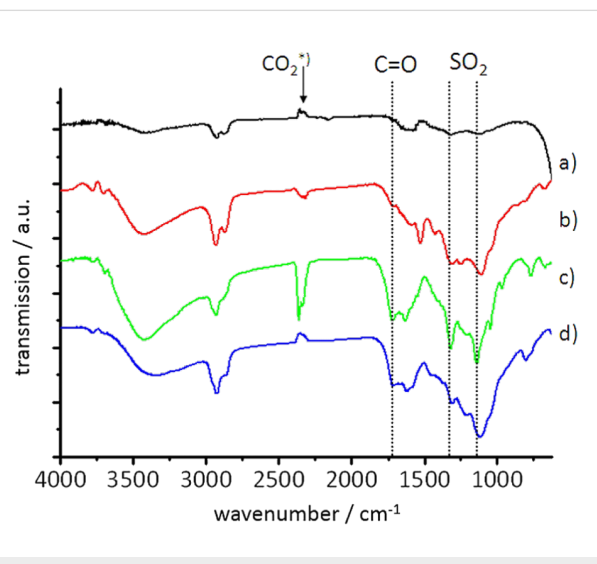


Figure 2: FTIR spectra (left) of compounds **2** (a), **9** (b), **10** (c) and **11** (d). The formation of the sulfone groups in **10** and the reduction of signal intensity for **11** are clearly visible. In the spectrum of **10** and **11** the carbonyl signals generated by the side reaction of MCPBA with surface groups are marked with a dotted line (the CO₂ signal is due to ambient air).

The further reaction depicted in Scheme 1 enables the formation of an aromatic amine at the 2-position of the ring by the oxidation of the thioethers and subsequent substitution of the sulfone by an amino function. Throughout the transformation the surface loading (see TGA data and elemental analysis in the experimental part) with the organic moieties remains the same showing the high stability of the double grafting by covalent C–C bonds. However, during the oxidation of the thioethers to the sulfones a side reaction has been observed. MCPBA reacts not only with the sulfur-containing groups in **9** but also with the annealed diamond surface itself as evidenced by the emergence of IR signals of carbonyl and ether bonds besides the expected signals at 1320 and 1140 cm^{-1} for the symmetric stretching mode of the sulfones (see spectra c) and d) in Figure 2). A

Table 1: Surface loading of nanodiamond-carrying amino groups on different linkers using three independent quantification methods.

sample (sample mass in Kaiser test /mg)	surface loading (mmol g ⁻¹) Kaiser test	surface loading (mmol g ⁻¹) elemental analysis	surface loading (mmol g ⁻¹) TGA ^a
5 (0.8)	0.60	1.75 ^b	0.61
7 (0.7)	0.17	0.22	0.19
11 (–)	– ^c	0.23 (0.20) ^d	0.23
13 (1.2)	1.05	1.07	0.49 ^e
15 (2.0)	0.27	0.29	0.32

^aSurface loading has been calculated from the mass loss step related to the removal of the organic matter. The desorption of water has been ensured by heating to 120 °C where the desorption step ends; ^bthis unexpectedly high value is due to the incomplete combustion of this sample type;

^caromatic amines cannot be quantified using the Kaiser test as no proton in the α -position is available, the qualitative test was negative as expected;

^dvalue based on sulfur (nitrogen) content; ^ethe thermogravimetric analysis of silanized samples often gives less pronounced steps in the thermogram, making the quantification less reliable, furthermore the formation of a stable silica shell reduces the observed mass loss.

and soot formation during elemental analysis. As evidenced by black residues in the crucibles used for the combustion this hypothesis is reasonable. Another aspect to be taken into consideration is the accessibility of functional groups. Using elemental analysis the entire amount of nitrogen in the sample will be determined, including nitrogen in the diamond lattice (which can be segregated of nitrogen content in the pristine material after the measurement) [19] and all amino groups anywhere in the sample. However, this does not mean that all these amino groups are accessible, e.g., for further coupling reactions due to agglomeration or porosity of the material.

Furthermore, the cleavage of strongly bound organic moieties from the surface will occur only at rather elevated temperature. In this case the thermogravimetric step will be less pronounced as it coincides with the early sublimation of carbonaceous material from the diamond surface. The latter sets in at temperatures above 450 °C, where the cleavage and desorption of strongly bound species is not yet completed. Hence, this overlay makes an unambiguous determination of the step temperatures in TGA challenging. It is therefore attractive to find other, independent methods for the quantitative determination of functional groups on the diamond surface, especially those imparting high nitrogen content, such as amino groups.

A very popular technique for the quantification of primary amino groups is the so-called Kaiser test [20]. It makes use of the formation of Ruhemann's Blue by the reaction of ninhydrine with the primary amino groups [21,22]. A major application of this assay is the test on residual amino groups of amino acids in solid-phase supported peptide synthesis. A report on a quantitative variation of the Kaiser test was published by Sarin et al. [23]. As this assay is colorimetric, its execution is very convenient. One limitation of the method, though, is the restriction to primary amines. Secondary amines cannot be detected reliably and aromatic and tertiary amines do not yield positive

test results either [24]. One report on the non-quantitative application of the Kaiser test on ethylene diamine functionalized nanodiamond has been reported recently [25].

For comparison, the monoaminated diamond conjugates **7**, **13** and **15** have been synthesized (see Supporting Information File 1 for details). As it can be seen from the analytical data the surface loading with amino groups for **7** and **15** is about ~0.2 mmol g⁻¹, a very typical value for this type of reaction. The observed surface loading for **13** is higher due to secondary reactions of already grafted alkoxy silanes [5].

In a first series of experiments the assay was carried out on nanodiamond samples **5** and **15** using the protocol reported by Troll et al. [22]. Surprisingly, very low values for the amino group loading were obtained for these samples in the first attempts of wet-chemical analysis (see Supporting Information File 1 for details). However, as **15** did not show a discrepancy between combustion and thermogravimetric analysis the Kaiser test was apparently yielding false results. To elucidate the origin of the deviation a deeper look into the mechanism of the formation of Ruhemann's Blue is required. An important intermediate is hydrindantin, which is formed upon reduction using KCN (see Supporting Information File 1 for a complete reaction mechanism). Its role in the process is still under discussion, and the rate constant of the reaction depends on the hydrindantin concentration in a complex manner – emphasizing its role as an important intermediate [26,27]. Moore and coworkers reported that in the event of insufficient amounts of reducing agent the formation of the coloured species is too low and variable [28]. Although the amount of KCN in the standard protocol is taking this finding into account we suspected that nanodiamond itself could be adsorbing the intermediate species and thus hampering the further proceeding of the reaction. It is well known, that hydrophilic nanodiamond (and samples carrying amino groups count among these) is prone to unspecific adsorption of organic

molecules via hydrogen bonding and other interactions [29]. Therefore it seems reasonable to assume that the rather low amounts of hydrindantin formed upon the addition of KCN can be adsorbed on the diamond surface and hence withdrawn from the reaction mixture. By forming higher amounts of hydrindantin using increased amounts of the reducing agents and thus increasing the concentration of the free intermediate in the solution we hoped to overcome this issue. By tripling the amount of KCN it was indeed possible to obtain reproducible values for the surface loading with NH_2 groups that correspond to the values obtained by other methods. Due to the increased KCN concentration and the increased formation of the intermediate hydrindantin the reaction mixture shows a characteristic red colouring at elevated temperatures as already reported by Sarin et al. [23]. Upon cooling, this colour vanishes almost completely (only a weak residual absorption at 570 nm is observed in the UV–vis spectrum, which has to be taken into account during the quantification). It has to be mentioned that the addition of 60% ethanol solution should be executed only after the disappearance of the red colour. The back oxidation is otherwise hindered and a quantitative determination is rendered impossible (Figure 3).

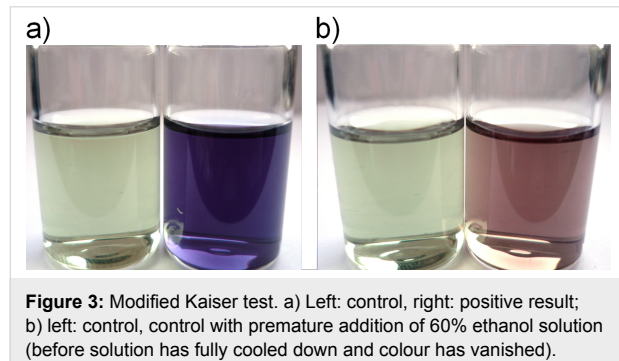


Figure 3: Modified Kaiser test. a) Left: control, right: positive result; b) left: control, right: control with premature addition of 60% ethanol solution (before solution has fully cooled down and colour has vanished).

In order to calibrate the measurement a reference sample for the colorimetric assay was used. Using benzylamine at different concentrations in water a standard graph was established for the new test protocol (with triple amount of KCN and delay before the addition of the ethanol) measuring the extinction of the Ruhemann's Blue in the absorption spectra. Additionally, the required reaction time was determined using nanodiamond **5** with the same protocol and taking samples of 1 mL at time intervals. After work-up these samples were submitted to the colorimetric assay and a minimum duration until complete transformation was found to be in the range of 10 min. Using this optimized assay protocol a series of aminated nanodiamond samples have been examined (Table 1). Furthermore, the dicyano derivative **4** and the Boc-protected derivative **14** were tested and showed a negative test result as expected. The results of the Kaiser test for compounds **5**, **7**, **13** and **15** show a high

reproducibility and correspond well within the error limits to the values obtained by thermogravimetry in all cases except **13** and with elemental analysis when complete combustion of the nanodiamond derivative is achieved. The deviation of the TGA results in the case of **13** is most likely due to the incomplete removal of the siloxane shell, which can crosslink and form a glassy layer around the nanodiamond core upon heating. This reduces the apparent surface loading as complete removal is assumed in the calculation. As can be seen from the results, the modified Kaiser test is a valuable tool for the quantification of amino groups on nanoparticle surfaces, namely when only low amounts of sample are available, e.g., when using fluorescent nanodiamond as the starting material or when the material shows unfavourable properties in other analytical methods. However, care should be taken in the event of strong agglomeration of the nanoparticles. Only the surface groups accessible by the reagents will be measured using this wet-chemical method.

Conclusion

In summary, we have established two new functionalization methods for the covalent grafting of organic moieties onto nanodiamond using pyrazine and cyclobutene precursors for the *in situ* formation of *ortho*-quinonodimethanes. These can be used as dienes in Diels–Alder reactions with π -bonds on the surface of nanodiamond. The use of pyrazine **3** results in a significantly increased grafting rate compared to other aromatic moieties linked by carbon–carbon bonds. Furthermore, a modified Kaiser test for the quantitative analysis of primary amino groups on nanodiamond has been developed and tested with a broad variety of aminated diamond samples. The modified conditions ensure the formation of sufficient amounts of the required hydrindantin intermediate and deliver reproducible and comparable results. The method can be used for other nanoparticles with similar adsorption properties as well and represents a useful addition to the wet-chemical analysis of functional groups on nanomaterials.

Experimental

General chemicals and methods

Detonation diamond has been purchased from Gansu Lingyun Corp. (Lanzhou, China). All other chemicals have been purchased from Aldrich and Fluka and have been used without further purification. Solvents have been dried according to standard procedures.

The following apparatus have been used for the experimental work:

Sonication: Ultrasound bath: Bandelin Sonorex Digitec Type DT52 (max. 80 W, 35 kHz), centrifuges: Hettich EBA 21 Type 1004, FTIR: Perkin-Elmer 1600 Series with ATR equipment

and home-made vacuum cell (KBr pellet). Samples for measurements using the vacuum cell were heated at 100–120 °C for 2 h in vacuo in order to remove most of the water adsorbed on the diamond surface; UV-vis: Kontron Instruments Uvikon 943, Thermogravimetry (TGA): Perkin Elmer STA 6000, measurements were performed in high purity nitrogen with a heating rate of 10 °C min⁻¹ (ca. 20 mg of sample were used for each analysis); elemental analysis: Euro Vector Euro EA 3000 Series; NMR: Bruker AC 250, tube furnace: Thermolyne Type 21100.

Reagents for Kaiser test

- 1.) Buffer pH 5.5: 36 g of sodium acetate was dissolved in 6.9 mL of conc. acetic acid and distilled water was added until a volume of 100 mL was reached.
- 2.) 5% ninhydrin solution: 5 g of ninhydrin were dissolved in 100 mL of ethanol.
- 3.) KCN pyridine reagent: 2 mL of 0.03 M KCN solution were diluted to a volume of 100 mL with pyridine.
- 4.) Phenol solution: 80 g of phenol were dissolved in 20 mL of ethanol while being gently heated.
- 5.) Ethanol solution: 60 mL of ethanol was diluted with 40 mL of deionized water.

Procedure for the quantification of amino groups on nanodiamond

The nanodiamond carrying amino groups (typically 0.5–2 mg of the powder) was suspended in 1 mL of dist. water. To this suspension 1 mL of the buffer solution (no. 1, see above) was added and the mixture was sonicated in an ultrasonic bath for 15 min. After that, 1 mL of the KCN solution (no. 3) and 1 mL phenol solution (no. 4) were added and the suspension was heated at 120 °C (oil bath temperature) for 10 min, 1 mL of ninhydrin solution (no. 2, see above) was added and heated for another 10 min. The solution was cooled to room temperature within 30 min and 5 mL of the ethanol solution was added. The solid was separated by centrifugation and from the supernatant a UV-spectrum was recorded.

The following equation was used for the quantification:

$$\text{surface loading [mmol g}^{-1}\text{]} = \frac{[(A - 0.36697) \cdot 0.50741]}{X} \Big/ N$$

with

A = absorption; X = weight of diamond sample [g]; N = number of amino groups per molecule. The absolute values are obtained from the calibration curve measured with benzylamine. For the

calibration curve and the reaction time optimization see Supporting Information File 1.

Synthesis of aminated nanodiamond samples

Synthesis of 4: A suspension of 250 mg of annealed detonation diamond **2** (2 h, 750 °C, vacuum), 1.16 g (6.96 mmol) potassium iodide, 520 mg (1.81 mmol) 2,3-bis(bromomethyl)-5,6-dicyanopyrazine (**3**) and 660 mg (2.50 mmol) 18-crown-6 in 10 mL of abs. toluene was heated for 72 h under reflux and nitrogen atmosphere. After cooling the diamond particles were isolated by centrifugation (15000 min⁻¹, 10 min). The precipitate was washed eight times with acetone, three times with water, three times with acetone and three times with dichloromethane in consecutive dispersion/centrifugation cycles. 150 mg (60% yield) of a black solid was obtained as the product. Elemental analysis: N: 10.4%, C: 74.1%, H: 1.7%; FTIR (vacuum cell) $\tilde{\nu}$: 3370, 2923 (CH), 2227 (CN), 1635, 1614, 1529, 1384, 1197, 1110, 842, 696 cm⁻¹; TGA (% weight loss): 120–460 °C: 9.6% (fragment: C₈H₄N₄; 156 g mol⁻¹); Surface loading: 1.56 mmol g⁻¹ (calculated from EA), 0.61 mmol g⁻¹ (calculated from TGA), Kaiser-Test: negative, zetapotential: not measured as no stable colloidal solution in water was obtained. Particle size: 15 nm (acetone).

Synthesis of 5: 65 mg of **4** was suspended in 5 mL BH₃·THF (1 M) and heated for 20 h under nitrogen atmosphere at 50 °C. Excess borane was decomposed by adding 2 N HCl. The diamond particles were isolated by centrifugation (15000 min⁻¹, 10 min). The precipitate was washed six times with a mixture of dioxane/water (9:1), three times with acetone and three times with dichloromethane in consecutive dispersion/centrifugation cycles. 49 mg (75% yield) of a black solid was obtained as the product. Elemental analysis: N: 11.2%, C: 68.4%, H: 3.9%; FTIR (vacuum cell) $\tilde{\nu}$: 3359, 3215, 2924 (CH), 2854 (CH), 1620 (NH), 1384, 1261, 1108, 799, 673, 614 cm⁻¹; TGA (% weight loss): 140–300 °C: 10.0% (fragment: C₈H₁₂N₄; 164 g mol⁻¹); Quantitative Kaiser test: UV: $A = 2.2501$ (568 nm); Surface loading: 1.75 mmol g⁻¹ (calculated from EA), 0.61 mmol g⁻¹ (calculated from TGA), 0.60 mmol g⁻¹ (Kaiser-Test); zetapotential: 19.9 mV, particle size: 13 nm (water).

Synthesis of 9: 120 mg of annealed nanodiamond **2** was suspended in a solution of 120 mg (0.61 mmol) of **8** in 10 mL 1,2-dichlorobenzene and heated to reflux for 20 h under nitrogen atmosphere. The solid was recovered by centrifugation and the supernatant was discarded. The solid was washed six times with acetone, five times with water and five times with dichloromethane in consecutive dispersion/centrifugation cycles. After drying at 70 °C for 24 h the product was obtained

as a dark grey solid. Yield: 101 mg (84%). Elemental analysis: C: 88.9%, H: 1.3%, N: 2.9%, S: 1.4%; FTIR (vacuum cell) $\tilde{\nu}$: 3430 (br), 2934 (s, v(C-H)), 2871 (s, v(C-H)), 1589 (w, v(C=C_{arom.})), 1528 (m, v(C=C_{arom.})), 1425 (m, v(C=C_{arom.})), 1312 (w), 1252 (w), 1110 (m), 860 (w), 810 (w), 677 (m) cm^{-1} ; TGA (% weight loss): 150–540 °C: 4.2% ($\text{C}_8\text{H}_{10}\text{N}_2\text{S}_2$); surface loading: 0.23 mmol g^{-1} (calculated from sulfur content in EA), 0.21 mmol g^{-1} (calculated from nitrogen content in EA), 0.21 mmol g^{-1} (calculated from TGA); zetapotential: +34.2 mV (measured in aqueous dispersion).

Synthesis of 10: 50 mg of functionalized nanodiamond **9** were suspended in a solution of 170 mg (0.99 mmol) *meta*-chloroperoxybenzoic acid (MCPBA) in 10 mL dry dichloromethane and stirred for 20 h at room temperature under nitrogen atmosphere. The solid was separated by centrifugation and the supernatant was discarded. The solid was washed six times with dichloromethane, six times with acetone and six times with water in consecutive dispersion/centrifugation cycles. After drying at 70 °C for 24 h the product was obtained as a grey solid. Yield: 40 mg (80%). Elemental analysis: C: 85.9%, H: 1.2%, N: 3.0%, S: 1.3%; FTIR (vacuum cell) $\tilde{\nu}$: 3433 (br), 2931 (m, v(C-H)), 1722 (m, v(C=O)), 1630 (m), 1550 (w), 1405 (w), 1320 (s, v(C₂SO₂)), 1211 (w), 1140 (s, v(C₂SO₂)), 1046 (m), 968 (m), 770 (m), 670 (m) cm^{-1} ; TGA: (% weight loss): 130–520 °C: 7.0% ($\text{C}_8\text{H}_{10}\text{N}_2\text{O}_4\text{S}_2$) (including 1.4% direct surface oxidation by MCPBA as demonstrated in a control experiment); surface loading: 0.21 mmol g^{-1} (calculated from sulfur content in EA), 0.23 mmol g^{-1} (calculated from nitrogen content in EA), 0.21 mmol g^{-1} (calculated from corrected TGA data); zetapotential: +19.8 mV (measured in aqueous dispersion).

Synthesis of 11: 20 mg of the functionalized nanodiamond **10** were suspended in 5 mL dichloromethane and stirred at room temperature while gaseous ammonia was bubbled through the solution for 6 h. The solid was separated by centrifugation and the supernatant was discarded. The solid was washed six times with acetone and six times with water in consecutive dispersion/centrifugation cycles. After drying at 70 °C for 24 h the product was obtained as grey solid. Yield: 17 mg (85%); Elemental analysis: C: 82.0%, H: 1.3%, N: 3.0%, S: 0.7%; FTIR (vacuum cell) $\tilde{\nu}$: 3342 (br), 2925 (s, v(C-H)), 2869 (m, v(C-H)), 1716 (m, v(C=O)), 1622 (m), 1585 (m, $\delta(\text{NH})$), 1312 (s, v(C₂SO₂)), 1207 (w), 1120 (s, v(C₂SO₂)), 800 (m) cm^{-1} ; TGA (% weight loss): 140–510 °C: 5.9% (including 1.4% mass loss from direct surface oxidation (see above)); surface loading: 0.23 mmol g^{-1} (calculated from sulfur content in EA), 0.20 mmol g^{-1} (calculated from nitrogen content in EA), 0.23 mmol g^{-1} (calculated from corrected TGA); zetapotential: +12.2 mV (measured in aqueous dispersion).

Supporting Information

Supporting Information File 1

Details for calibration of the Kaiser test, test robustness and optimization of the reaction time, reaction mechanism for colorimetric assay; synthesis of organic precursor compounds and further nanodiamond derivatives.
[<http://www.beilstein-journals.org/bjoc/content/supplementary/1860-5397-10-288-S1.pdf>]

Acknowledgements

We gratefully acknowledge the financial support by the Deutsche Forschungsgemeinschaft (DFG) under projects KR3316/1-2 and FOR1493 (KR3316/6-1), by the European Commission (project DINAMO, contract number: 245122) and the Fonds der Chemischen Industrie.

References

- Nicolas, J.; Mura, S.; Brambilla, D.; Mackiewicz, N.; Couvreur, P. *Chem. Soc. Rev.* **2013**, *42*, 1147–1235. doi:10.1039/c2cs35265f
- Sun, G.; Berezin, M. Y.; Fan, J.; Lee, H.; Ma, J.; Zhang, K.; Wooley, K. L.; Achilefu, S. *Nanoscale* **2010**, *2*, 548–558. doi:10.1039/b9nr00304e
- Sotowa, K.-I.; Amamoto, T.; Sobana, A.; Kusakabe, K.; Imato, T. *Diamond Relat. Mater.* **2004**, *13*, 145–150. doi:10.1016/j.diamond.2003.10.029
- Charrier, G.; Aureau, D.; Gonçalves, A.-M.; Collet, G.; Bouttemy, M.; Etcheberry, A.; Simon, N. *Diamond Relat. Mater.* **2013**, *32*, 36–42. doi:10.1016/j.diamond.2012.11.014
- Krüger, A.; Liang, Y.; Jarre, G.; Stegk, J. *J. Mater. Chem.* **2006**, *16*, 2322–2328. doi:10.1039/b601325b
- Mochalin, V. N.; Neitzel, I.; Etzold, B. J. M.; Peterson, A.; Palmese, G.; Gogotsi, Y. *ACS Nano* **2011**, *5*, 7494–7502. doi:10.1021/nn2024539
- Ciftan Hens, S.; Cunningham, G.; Tyler, T.; Moseenkov, S.; Kuznetsov, V.; Shenderova, O. *Diamond Relat. Mater.* **2008**, *17*, 1858–1866. doi:10.1016/j.diamond.2008.03.020
- Yeap, W. S.; Chen, S.; Loh, K. P. *Langmuir* **2009**, *25*, 185–191. doi:10.1021/la8029787
- Girard, H. A.; Arnault, J. C.; Perruchas, S.; Saada, S.; Gacoin, T.; Boilot, J.-P.; Bergonzo, P. *Diamond Relat. Mater.* **2010**, *19*, 1117–1123. doi:10.1016/j.diamond.2010.03.019
- Liang, Y.; Meinhardt, T.; Jarre, G.; Ozawa, M.; Vrdoljak, P.; Schöll, A.; Reinert, F.; Krueger, A. *J. Colloid Interface Sci.* **2011**, *354*, 23–30. doi:10.1016/j.jcis.2010.10.044
- Jarre, G.; Liang, Y.; Betz, P.; Lang, D.; Krueger, A. *Chem. Commun.* **2011**, *47*, 544–546. doi:10.1039/c0cc02931a
- Hartmann, M.; Betz, P.; Sun, Y.; Gorb, S. N.; Lindhorst, T. K.; Krueger, A. *Chem. – Eur. J.* **2012**, *18*, 6485–6492. doi:10.1002/chem.201104069
- Fernández-Paniagua, U. M.; Illescas, B.; Martín, N.; Seoane, C. *J. Org. Chem.* **1997**, *62*, 3705–3710. doi:10.1021/jo9701344
- Jaung, J.-y.; Matsuoka, M.; Fukunishi, K. *Dyes Pigm.* **1997**, *34*, 255–266. doi:10.1016/S0143-7208(96)00086-1

15. González, B.; Herrera, A.; Illescas, B.; Martín, N.; Martínez, R.; Moreno, F.; Sanchez, L.; Sanchez, A. *J. Org. Chem.* **1998**, *63*, 6807–6813. doi:10.1021/jo9801891
16. García Martínez, A.; Herrera Fernández, A.; Moreno-Jiménez, F.; Luengo Fraile, M. J.; Subramanian, L. R. *Synlett* **1994**, 559–560. doi:10.1055/s-1994-22929
17. Mosrin, M.; Boudet, N.; Knochel, P. *Org. Biomol. Chem.* **2008**, *6*, 3237–3239. doi:10.1039/b812528g
18. Cui, J.-F.; Fang, X.-W.; Schmidt-Rohr, K. *J. Phys. Chem. C* **2014**, *118*, 9621–9627. doi:10.1021/jp503053r
19. Shenderova, O. A.; Zhirnov, V. V.; Brenner, D. W. *Crit. Rev. Solid State Mater. Sci.* **2002**, *27*, 227–356. doi:10.1080/10408430208500497
20. Kaiser, E.; Colescott, R. L.; Bossinger, C. D.; Cook, P. I. *Anal. Biochem.* **1970**, *34*, 595–598. doi:10.1016/0003-2697(70)90146-6
21. Ruhemann, S. *J. Chem. Soc., Trans.* **1910**, *97*, 457–461. doi:10.1039/CT9109700457
22. Troll, W.; Cannan, R. K. *J. Biol. Chem.* **1953**, *200*, 803–811.
23. Sarin, V. K.; Kent, S. B. H.; Tam, J. P.; Merrifield, R. B. *Anal. Biochem.* **1981**, *117*, 147–157. doi:10.1016/0003-2697(81)90704-1
24. McCaldin, D. J. *Chem. Rev.* **1960**, *60*, 39–51. doi:10.1021/cr60203a004
25. Gaillard, C.; Girard, H. A.; Falck, C.; Paget, C.; Simic, V.; Ugolin, N.; Bergonzo, P.; Chevillard, S.; Arnault, J. C. *RSC Adv.* **2014**, *4*, 3566–3572. doi:10.1039/c3ra45158e
26. Lamotte, P. J.; McCormick, P. G. *Anal. Chem.* **1972**, *44*, 821–825. doi:10.1021/ac60312a003
27. MacFadyen, D. A.; Fowler, N. *J. Biol. Chem.* **1950**, *186*, 13–22.
28. Moore, S.; Stein, W. H. *J. Biol. Chem.* **1948**, *176*, 367–388.
29. Mona, J.; Kuo, C.-J.; Perevedentseva, E.; Priezzhev, A. V.; Cheng, C.-L. *Diamond Relat. Mater.* **2013**, *39*, 73–77. doi:10.1016/j.diamond.2013.08.001

License and Terms

This is an Open Access article under the terms of the Creative Commons Attribution License (<http://creativecommons.org/licenses/by/2.0>), which permits unrestricted use, distribution, and reproduction in any medium, provided the original work is properly cited.

The license is subject to the *Beilstein Journal of Organic Chemistry* terms and conditions: (<http://www.beilstein-journals.org/bjoc>)

The definitive version of this article is the electronic one which can be found at:
doi:10.3762/bjoc.10.288



Detonation nanodiamonds biofunctionalization and immobilization to titanium alloy surfaces as first steps towards medical application

Juliana P. L. Gonçalves^{‡1}, Afnan Q. Shaikh^{‡1,2}, Manuela Reitzig¹, Daria A. Kovalenko^{1,2}, Jan Michael^{1,3}, René Beutner², Gianaurelio Cuniberti², Dieter Scharnweber² and Jörg Opitz^{*1,2}

Full Research Paper

Open Access

Address:

¹Inspection and Diagnosis Methods, Fraunhofer Institute for Ceramic Technologies and Systems –Materials Diagnostics, Maria-Reiche-Str. 2, 01109 Dresden, Germany, ²Max Bergmann Center of Biomaterials MBC, Technische Universität Dresden, Budapest Str. 27, 01069 Dresden, Germany and ³Chair of General Biochemistry, Technische Universität Dresden, Bergstr. 66, 01069 Dresden, Germany

Email:

Jörg Opitz* - joerg.opitz@ikts-md.fraunhofer.de

* Corresponding author ‡ Equal contributors

Keywords:

biofunctionalization; carbon-nanomaterials; detonation nanodiamond; electrochemical immobilization; surface modification; titanium alloy

Beilstein J. Org. Chem. **2014**, *10*, 2765–2773.

doi:10.3762/bjoc.10.293

Received: 29 January 2014

Accepted: 14 November 2014

Published: 26 November 2014

This article is part of the Thematic Series "Functionalized carbon nanomaterials".

Guest Editor: A. Krueger

© 2014 Gonçalves et al; licensee Beilstein-Institut.

License and terms: see end of document.

Abstract

Due to their outstanding properties nanodiamonds are a promising nanoscale material in various applications such as microelectronics, polishing, optical monitoring, medicine and biotechnology. Beyond the typical diamond characteristics like extreme hardness or high thermal conductivity, they have additional benefits as intrinsic fluorescence due to lattice defects without photo-bleaching, obtained during the high pressure high temperature process. Further the carbon surface and its various functional groups in consequence of the synthesis, facilitate additional chemical and biological modification. In this work we present our recent results on chemical modification of the nanodiamond surface with phosphate groups and their electrochemically assisted immobilization on titanium-based materials to increase adhesion at biomaterial surfaces. The starting material is detonation nanodiamond, which exhibits a heterogeneous surface due to the functional groups resulting from the nitrogen-rich explosives and the subsequent purification steps after detonation synthesis. Nanodiamond surfaces are chemically homogenized before proceeding with further functionalization. Suspensions of resulting surface-modified nanodiamonds are applied to the titanium alloy surfaces and the nanodiamonds subsequently fixed by electrochemical immobilization. Titanium and its alloys have been widely used in bone and dental implants for being a metal that is biocompatible with body tissues and able to bind with adjacent bone during healing. In order to improve titanium material properties towards biomedical applications the authors aim to increase adhesion to bone material by incorporating nanodiamonds into the implant surface, namely the anodically grown titanium dioxide layer. Differ-

ently functionalized nanodiamonds are characterized by infrared spectroscopy and the modified titanium alloys surfaces by scanning and transmission electron microscopy. The process described shows an adsorption and immobilization of modified nanodiamonds on titanium; where aminosilanized nanodiamonds coupled with *O*-phosphorylethanolamine show a homogeneous interaction with the titanium substrate.

Introduction

Detonation nanodiamonds (DND) are a promising carbon-derived nanoscale material, which has been investigated since some decades due to its outstanding properties, like extreme hardness and high thermal conductivity [1-3]. Beyond this, lattice defects, predominantly originating from nitrogen vacancy centers [4,5], enable fluorescence without photo-bleaching. Nanodiamonds can thus be used as markers for optical monitoring [6,7]. Toxicity has not been observed so far, so it has gained particular interest in biological and medical applications [8,9]. A number of publications on single cell labeling with nanodiamond particles [10-12] and use in therapeutic delivery were reported [13-15]. In such way, the low or non-existent toxicity and improved biocompatibility, in comparison to the unmodified DND, extends the applications of this carbon material from microelectronics, polishing and optical monitoring to biomedicine.

Titanium and titanium-based alloys have been used as bone implant material for a long time, because of their excellent corrosion properties, good mechanical strength and osteointegration, due to naturally occurring oxide layer at their surface [16]. Based on the surface oxide properties, various methods of surface modification of titanium and its alloys have been realized in the past decades to achieve improved surface properties with enhanced wear behavior, corrosion resistance, and biocompatibility.

Scharnweber et al. worked on biofunctionalization of titanium implant materials by immobilizing collagen type I and studied conformational changes caused by adsorptive immobilization [17,18]. Others worked on collagenous matrix coatings on titanium implants modified with decorin and chondroitin sulfate that enhanced osteoblast adhesion and increased expression of osteopontin (a bone-specific marker) [19]. Immobilization of biologically active molecules, by using tripartite molecules (linker, spacer and bioactive ligand), enables an easier process control and operability under nearly physiological conditions [20]. Scharnweber, Schwenzer and co-workers contributed to the development of implant materials based on titanium by demonstrating a new modular method of immobilization via regioselective partial incorporation of biofunctional molecules into anodically grown oxide layers. The authors electrochemically immobilized nucleic acids on titanium alloys for its surface modification with bioactive molecules [21-25], as, e.g.,

oligonucleotides and RGD peptide conjugates, for osteoblasts adhesion [26].

A successful incorporation of DND has already been achieved in a related research of our group in Dresden on nanodiamonds for corrosion protection and devising a nondestructive surveillance tool for corrosion monitoring in light metals such as aluminum and its alloys for aircraft industry [27].

Recently, the properties of nanodiamonds have been investigated in the field of bone tissue engineering [28-33]. For the presented study, a new hybrid implant material based on titanium alloy with functionalized nanodiamonds on anodic oxide layers is being conceived, to improve material properties. The motivation of our research was to perform first steps towards immobilization of functionalized DND to reinforce the surface of the material and to improve the exquisite properties of titanium to shape an improved material for medical uses.

DND exhibit several functional groups around the carbon core as shown in Figure 1, originating from the purification after the detonation process [28]. This enables task-oriented chemical or biological functionalization. For binding substances to titanium surfaces, phosphate groups are favored as anchors, because they

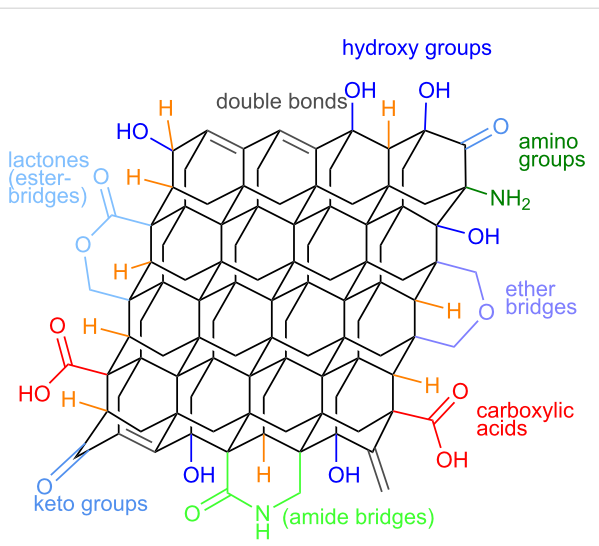


Figure 1: Proposed functional groups on purified DND surface.

possess a hydrolytically stable structure and support the formation of monolayers on metal oxide surfaces. [34–36] Especially in the case of titanium mono-, bi- or even tridentate phosphate coordination leads to exceptional strong binding that could not be achieved by mere electrostatic interaction or hydrogen bridging.

In this work we studied various functionalization methods for the attachment of the phosphate moieties to DND particles. We investigated further the binding of the modified nanodiamond particles to the surface of titanium alloys in combination with the formation of anodic oxide layers.

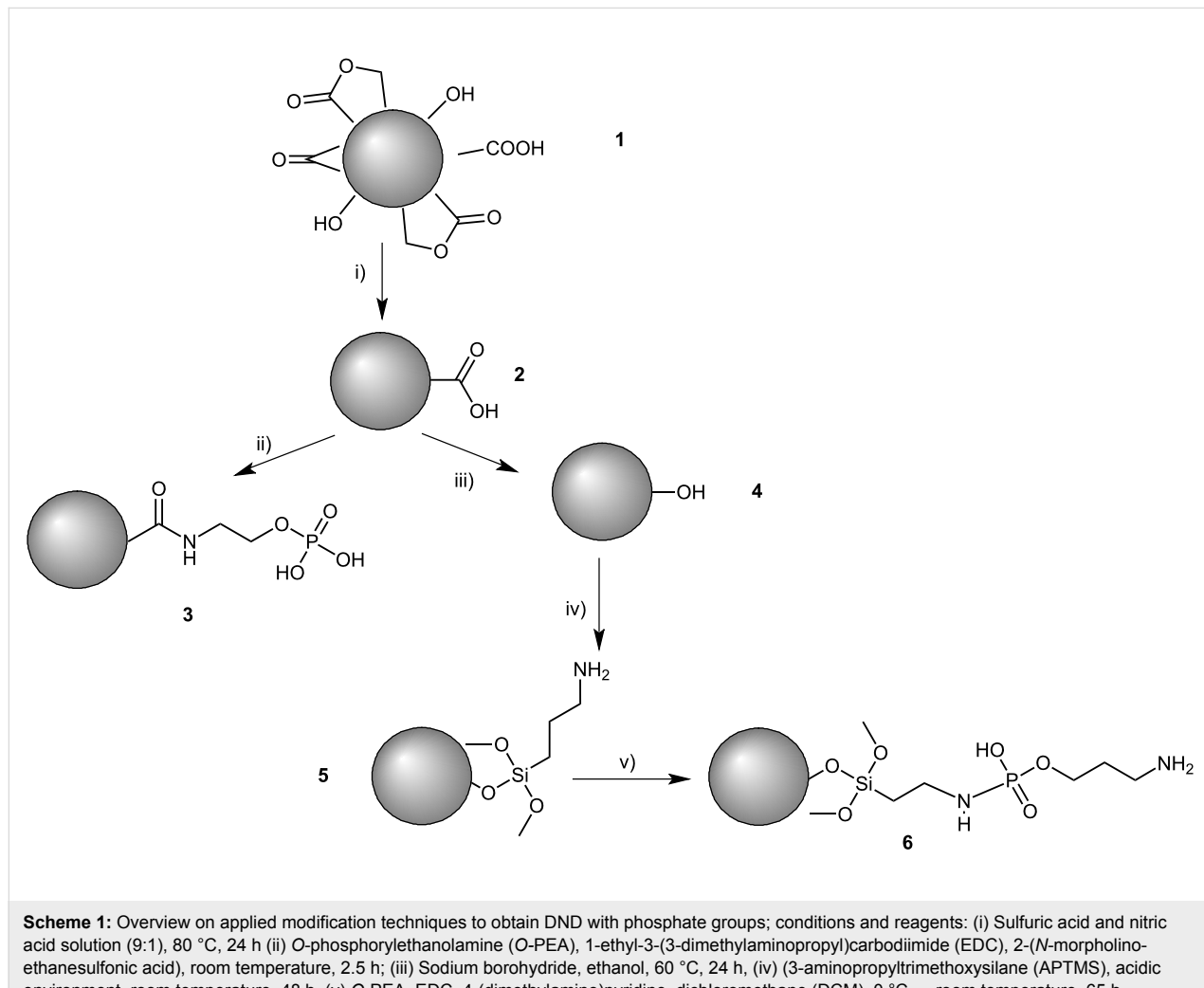
Results and Discussion

Covalent surface modification of DND

The functionalization of nanodiamonds with phosphate groups was carried out considering protocols available in literature [37–39]. Those protocols were adapted and are summarized in Scheme 1.

Reaction step (ii) was performed to directly graft the phosphate group on the surface of the DND, whereas reactions (iii) and (iv) were performed to provide an amino group in the end of the functionalization, allowing the integration of further species, as shown in reaction (v). Even though product **5** does not contain a phosphate group, it was included as control to verify the interaction of amino groups and the titanium based alloy. Furthermore, products **3** and **6** can be seen as ‘inversely modified’ DND with a terminal phosphate and a secondary amide **3** or with a primary amine and a secondary phosphoroamidate **6**. This might help to assess the character of binding of amino and phosphate groups. The obtained products were characterized by infrared spectroscopy.

Figure 2 depicts the IR spectra of samples with phosphate groups coupled to the surface of the nanodiamond which use *O*-phosphorylethanolamine as main reagent. Figure 3 shows the infrared qualitative analysis of the efficiency of the synthesis achieved on the surface of DND, represented in Scheme 1.



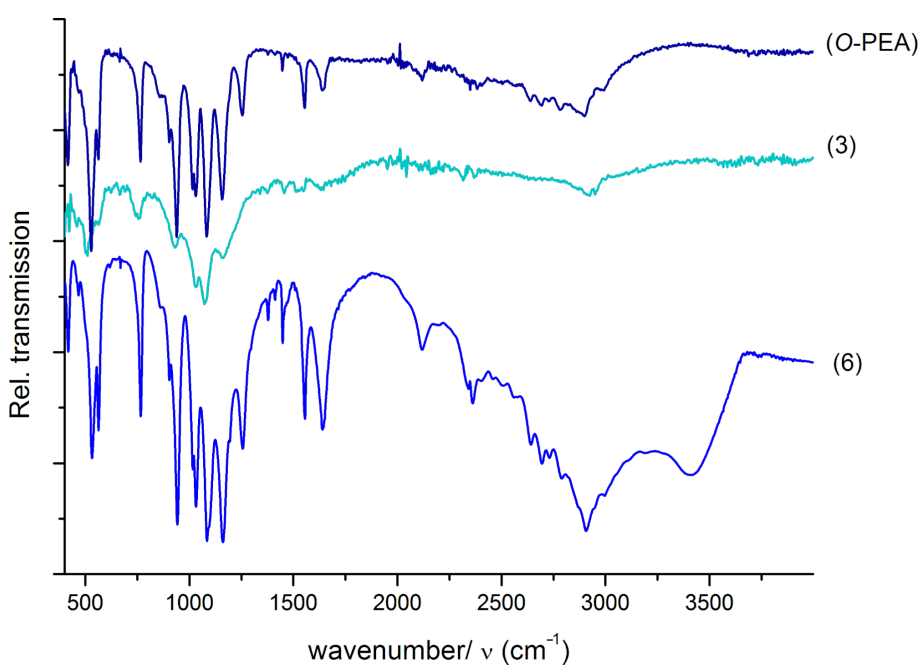


Figure 2: ATR-FTIR spectra of species **3** and **6** from Scheme 1 in comparison to O-phosphorylethanolamine (O-PEA).

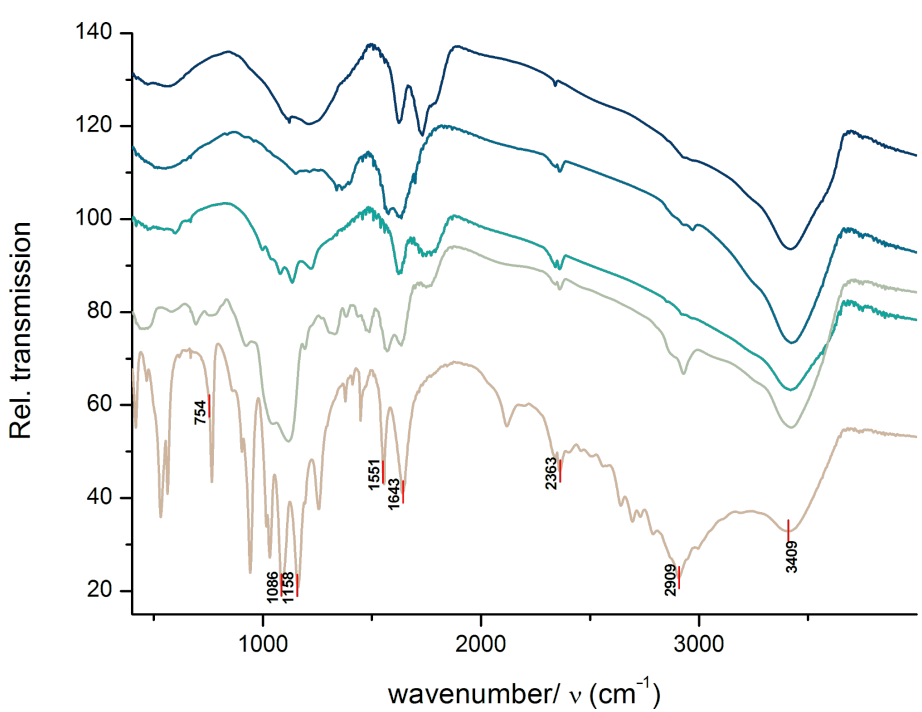


Figure 3: ATR-FTIR spectra of species involved in the synthesis process, from Scheme 1.

Table S1 (please see the Supporting Information File 1) summarizes the characteristic absorption bands of the qualitative analysis from the synthesized species by IR spectroscopy [40,41]. The evaluation of the surface functionalization of DND

can be proved by a qualitative analysis from the Figure 2 and Figure 3. The characteristic absorptions of some functional groups is directly related with the success of the synthesis, which are particularly observed on the assignments of the silane

groups (1000 cm^{-1}) in **4** and **5** and amino groups around 950 cm^{-1} and 1560 cm^{-1} in **4**, **5** and **6**. It is still possible to see some carboxylic groups on **4**, which may result from an incomplete oxidation process.

A positive signal of the integration of the phosphate group can be seen in **3** and **6**, at the wavenumber of 1090 cm^{-1} that is also present in the *O*-PEA.

In order to prove the covalent character of the formed bonds, physisorption tests were performed (see Supporting Information File 1). The tests demonstrated that no physical loading occurred on the surface of the nanodiamonds by the functionalizing agent, *O*-PEA.

Immobilization of DND

Scanning electron microscopy (SEM) was used to characterize the surface morphology of titanium samples coated with previously functionalized nanodiamonds. DND before and after functionalization were used to evaluate the improvement on the interaction of DND with the titanium alloy surface.

Figure 4 shows the topological information of all nanodiamond entities immobilized onto Ti6Al7Nb surfaces either by adsorption to preformed anodic oxide layers (adDND), or by adsorption to air formed oxide layers followed by growth of the oxide layer by anodic polarization (anodDND). Image g and h in which silanized DND functionalized with *O*-phosphorylethanolamine depicts more homogeneous distribution indicating better interaction with titanium alloy surface when compared to other entities. Moreover, the particle size and agglomeration are also effectively reduced after the functionalization with *O*-PEA (image h), compared to the unmodified DND (image b).

STEM (scanning transmission electron microscopy) investigation of a FIB (focused ion beam) cut reveals a well-defined layer system as shown in Figure 5, for the immobilized aminosilanized DND **6** adsorbed to air formed oxide layer of Ti6Al7Nb followed by anodic polarization. The titanium based alloy substrate at the bottom is covered on top with an anodic oxide layer (thickness approx. 120 nm). An immobilization of **6** on titanium anodic oxide layer can clearly be seen, which was already indicated in the SEM images in Figure 4 for **6**. At this point, successful immobilization of **6** on the anodic oxide layer can be confirmed but with no signs of incorporation so far within the anodically grown oxide layer of the sample.

The initial interaction between all used entities (functionalized and unfunctionalized) of DND with the oxide layers on the titanium alloy surface is regulated by the pH of the electrolyte.

Since the isoelectric point of these oxide layers lies between pH 4 and 4.5, the titanium dioxide surface will be negatively charged at the physiological pH of 7.4 [21].

Interactions between unmodified DND, and substrate are caused by hydrogen bridging and electrostatic affinity to positively charged amino groups. SEM results Figure 4 from unfunctionalized DND demonstrate a better interaction with the titanium oxide layer than carboxylated DND with *O*-PEA **3** and silanized DND **5**. This may be explained by the presence of several functional groups around the carbon core of the DND, as shown in Figure 1. These functional groups are originated in the purification treatment after the detonation process [28]. When in solution, the polarity of those functional groups may facilitate the formation of an aqueous suspension that was longer stable and translucent than the other suspensions prepared, although no longer stable than sample **6**. This functionalized sample also performed a homogenous suspension and was stable for 12 h. This fact establishes a strong correlation between the suspension stability and a well distributed surface adhesion of the related DND on the titanium oxide layer.

As an explanation for the homogenous immobilization of **6**, the authors believe the ability to form a stable suspension with **6** and the presence of phosphate anchor groups facilitates binding of finer nanodiamonds to the titanium oxide surface as seen in Figure 4, images g and h. Especially in the field of nanoparticles, entropic and surface effects, play a meaningful role that supports the electrostatic forces and possible covalent interaction, therefore the immobilization leads to binding of more and finer nanodiamonds (Figure 4g) and the incorporation increases the binding stability, leading to a meliorated surface distribution (Figure 4 h) of the small agglomerates of the functionalized nanodiamonds with *O*-PEA **6**, when compared to the all other tested samples. During the preparation of the nanodiamond suspension, silanized DND functionalized with *O*-phosphorylethanolamine revealed to be stable for 12 h. The strong phosphate attraction to titanium, even at neutral or weak basic pH, results in a firm adhesion of samples with phosphate moieties to the titanium dioxide layer [20,41]. Sample **6** possesses amino groups that build hydrogen bridges with the surface of the titanium alloy. The stable interaction observed is also achieved by coordinative binding of the oxygen in the phosphate group, which support the formation of monolayers on the titanium [42,43].

Conclusion

Covalent functionalization of DND was carried out by different paths, with the main aim to couple phosphate groups. Successful DND functionalization was confirmed by infrared spectroscopy, depicting the presence of the attached functional

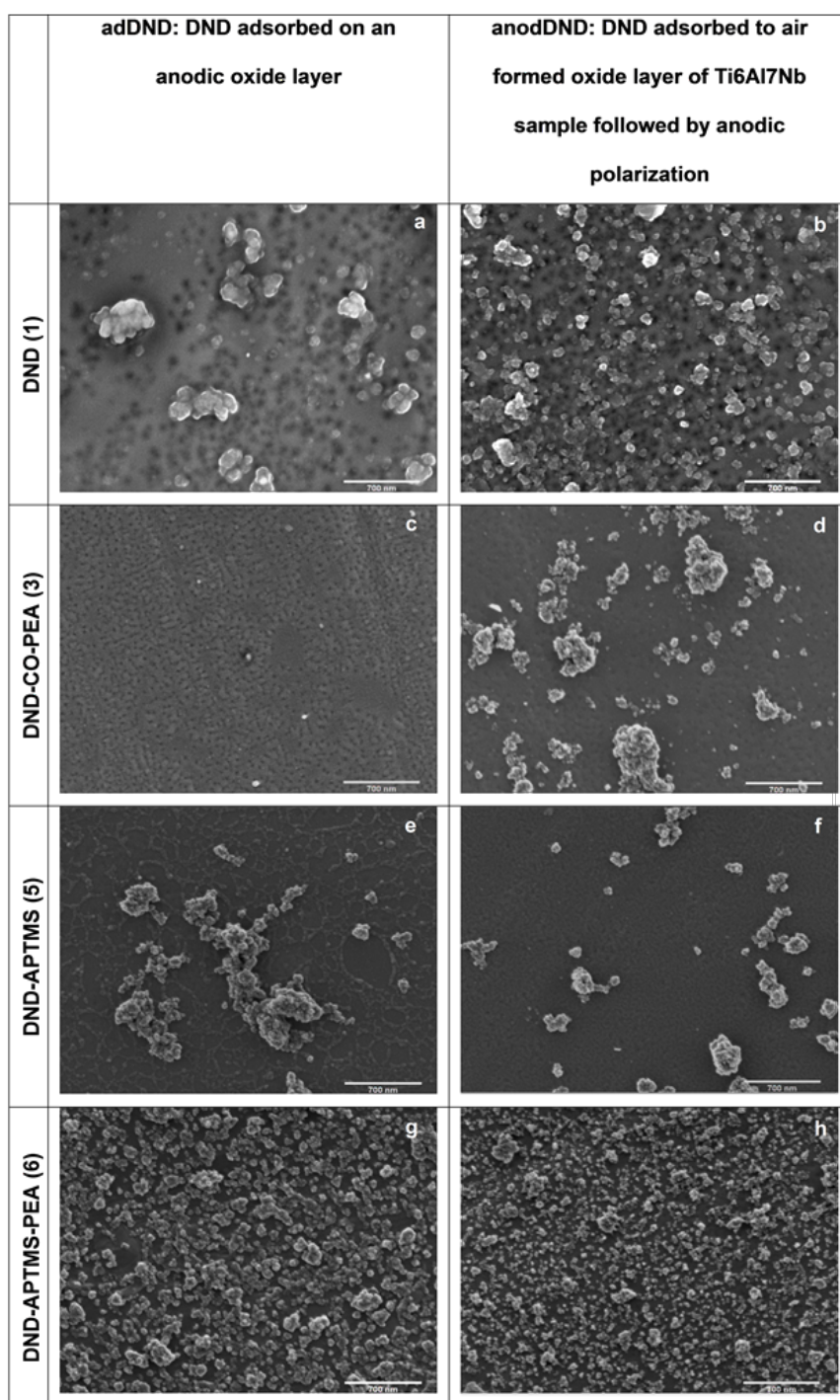


Figure 4: SEM images of titanium anodic oxide surface with: (a,b) unmodified DND; (c,d) DND-COOH functionalized with O-PEA (3); (e,f) silanized nanodiamonds with APTMS 5 and (g,h) silanized nanodiamonds functionalized with O-PEA 6. Left column – adDND. DND adsorbed on an anodic oxide layer and right column – anodDND with adsorption of DND on air formed oxide layer of Ti sample followed by anodic polarization. Anodic polarization was consistently carried out at 60 V and 50 mA/cm².

groups at the DND surface. SEM results show better adhesion and homogeneous immobilization on the titanium alloy for the nanodiamonds functionalized with the phosphate group after the silanization process. These results indicate that the surface func-

tionalization of DND is one important parameter for successful adsorption and immobilization on titanium alloy substrate. Another crucial parameter is to achieve a stable suspension of nanodiamonds. Sedimentation and agglomeration of several

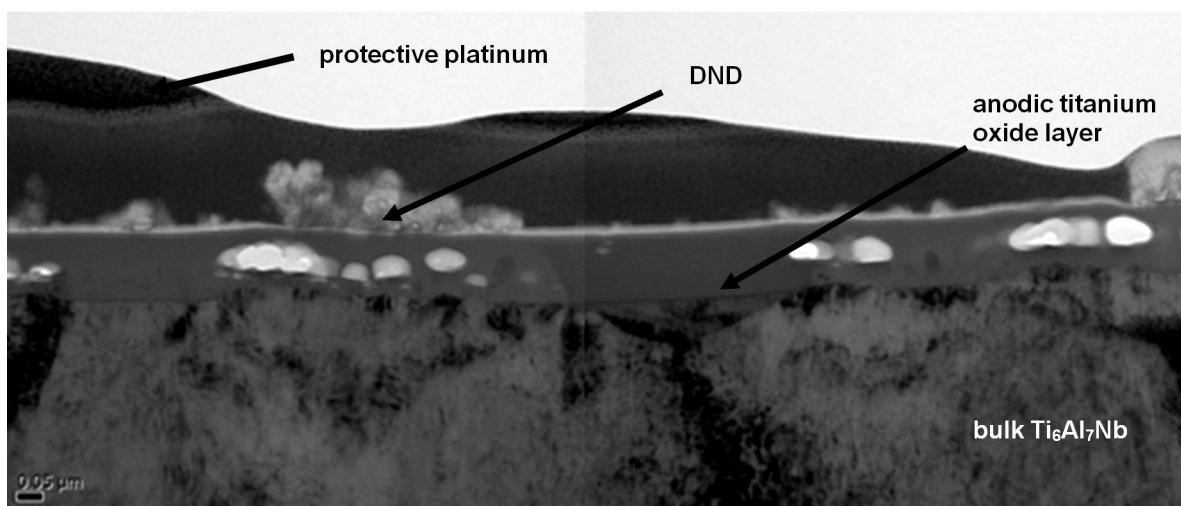


Figure 5: STEM image of immobilized aminosilanized DND **6** adsorbed to the air-formed passive layer of $\text{Ti}_6\text{Al}_7\text{Nb}$ sample followed by anodic polarization (60 V, 50 mA/cm^2).

modified DND appeared to have a substantial influence on the success of the electrochemical immobilization. Silanized DND modified with *O*-phosphorylethanolamine **6** showed better dispersion in buffer compared to other samples and hence resulted in more homogeneous deposition during the electrochemical immobilization. We applied an electrochemical technique of anodic oxidation to get a stable immobilization of the particles during anodic oxide layer growth. A FIB-STEM tool was used to characterize the topology and layer system of titanium based alloy after immobilization of **6**.

In order to produce a stable suspension with the functionalized DND in different solvents and different acidic conditions, to optimize the electrochemical process, further experiments need to be performed. Further work is needed to describe in detail the adhesion mechanism of **6** on an anodic oxide layer. Stability and biocompatibility investigations of the achieved coatings will then follow.

Experimental Chemicals

DND were purchased from Plasmachem GmbH (purity degree: 95%). All buffers were made from p.a. grade chemicals supplied by Merck KGaA and autoclaved before use. All other chemicals have been purchased with p.a. quality from Roth, Sigma-Aldrich and Fluka and were used without further purification.

Carboxylated DND functionalized with *O*-phosphorylethanolamine

200 mg of carboxylated DND **2** were washed with 0.1 M 2-(*N*-morpholinoethanesulfonic acid) (MES) and resuspended in

4 mL of MES containing 6 mg of 1-ethyl-3-(3-dimethylaminopropyl)carbodiimide (EDC). The mixture was stirred for 20 min at room temperature. Afterwards, 25 mL of *O*-phosphorylethanolamine (8% aqueous) solution was added to the activated particles and the suspension was stirred for 2.5 h at room temperature. The sample **3** was rinsed with phosphate-buffered saline (PBS, pH 7.2) and dried under vacuum.

Silanization of DND

1 g of hydroxylated DND **4** was mixed in a round bottom flask with 200 mg of 3-aminopropyltrimethoxsilane (APTMS) for 48 h at room temperature, while stirring. Afterwards, the solution was centrifuged to prepare the washing step with 40 mL of acetone for 24 h at 40 °C. The sample **5** was then dried under vacuum.

Silanized DND functionalized with *O*-phosphorylethanolamine

200 mg of silanized DND **5**, 80 mg of *O*-phosphorylethanolamine, 35 mg of DMAP, 50 mg of EDC and 20 mL of dichloromethane (DCM), reacted under ice cooling for one hour; afterwards the slurry was stirred at room temperature for 65 h. At the end, the sample **6** was washed twice with acetone and twice with water and dried under vacuum.

Preparation of titanium alloy samples

Sample disks of $\text{Ti}_6\text{Al}_7\text{Nb}$ with a diameter of 15 mm × 2 mm height were used and were ground down to a grain size of P500. Sample etching in a mixed solution of 1 M nitric acid (HNO_3) and 0.4 M hydrofluoric acid at room temperature was carried out for 2 min. This was followed by ultrasonic cleaning in sterile deionized water for 30 min.

Suspension of functionalized DND

Dried powder of functionalized DND was used to form slurry or suspensions. For this purpose, 0.1 g of functionalized DND were mixed in 100 mL deionized water and ultrasonicated for 60 min.

Electrolytic solution

A borate buffer of pH 7.12 prepared from 0.2 M boric acid, 0.05 M borax and 0.1 M Na_2SO_4 was used as an electrolyte. The pH of an equal mixture of buffer and nanodiamond suspension is set to be 7.42 with an electrical conductivity of 8.70 mS/cm.

Immobilization of modified ND

For immobilization and incorporation experiments, a setup developed by Michael et al. [22] is used. It consists of a specially designed conical cell, made from acrylic glass, which mounts a titanium based alloy sample inside. Only 1.8 cm^2 circular surface of sample is exposed to the electrolyte solution. A platinum wire is used as a counter electrode. Potential is measured against a saturated Ag/AgCl electrode inside a 3 M KCl solution connected to a conical glass cell via salt bridge. The salt bridge is formed by filling a capillary plastic tube with agarose gel (2 % w/v in 2 mol/L borate buffer, pH 7.4).

The experimental conical cell has a capacity of 3 mL. 1.5 mL of an aqueous slurry of modified DND is poured inside the cell, followed by an adsorption time of 20 min. After adsorption, 1.5 mL of borate buffer was added to the cell and anodic polarization was carried under galvanostatic mode of operation with 60 V as target potential and a current density of 50 mA/cm^2 . With 60 V of target potential, an anodic oxide layer of approximately 120 nm is expected to be formed. A potentiostat/galvanostat (Votlab 4.0 Radiometer Analytical) was used for polarization.

Adsorption on titanium anodic oxide layer

For adsorption experiments, anodic polarization was carried out initially forming an anodic oxide layer on the titanium alloy sample by adding borate buffer. Once an anodic oxide layer is formed, the buffer is removed and the sample is washed with deionized water for three times. This is followed by pouring 1.5 mL of aqueous DND slurry on anodically oxidized sample surface. After 20 min of adsorption time, samples are rinsed in deionized water.

Characterization

The FTIR measurements were carried out with ALPHA's Platinum ATR from Bruker. The samples were measured in solid state, without previous preparation. Parameters were: 32 scans, 4 cm^{-1} resolution; wavelength range 4000–400 cm^{-1} .

SEM measurements for topological characterization were performed with a Carl Zeiss 1500STES Gemini SEM. All titanium alloy samples with and without immobilized DND were first sputtered with carbon before observation under microscope.

For STEM investigation a Carl Zeiss LIBRA® 200 was used. Focused ion beam lamella was cut every time to observe the layer structure of the titanium alloy. Sample preparation includes carbon coating followed by platinum deposition for sample protection.

Supporting Information

Supporting Information File 1

Physisorption test.

[<http://www.beilstein-journals.org/bjoc/content/supplementary/1860-5397-10-293-S1.pdf>]

Acknowledgements

The authors thank Yvonne Standke for help with the SEM measurements and Dr. Uwe Mühle for assistance with the STEM measurements. This project has been funded with support from the European Commission and a DAAD/HEC scholarship A/11/92671. This publication reflects the views only of the authors, and the Commission cannot be held responsible for any use which may be made of the information contained therein.

References

1. Harlow, G. E.; Davies, R. M. *Elements* **2005**, *1*, 67–70. doi:10.2113/gselements.1.2.67
2. Krueger, A. *Chem. – Eur. J.* **2008**, *14*, 1382–1390. doi:10.1002/chem.200700987
3. Mochalin, V. N.; Shenderova, O.; Ho, D.; Gogotsi, Y. *Nat. Nanotechnol.* **2012**, *7*, 11–23. doi:10.1038/nnano.2011.209
4. Mita, Y. *Phys. Rev. B* **1996**, *53*, 11360. doi:10.1103/PhysRevB.53.11360
5. Davies, G.; Lawson, S. C.; Collins, A. T.; Mainwood, A.; Sharp, S. J. *Phys. Rev. B* **1992**, *46*, 13157. doi:10.1103/PhysRevB.46.13157
6. Schietinger, S.; Schröder, T.; Benson, O. *Nano Lett.* **2008**, *8*, 3911–3915. doi:10.1021/nl8023627
7. Hannstein, I.; Adler, A.-K.; Lapina, V.; Osipov, V.; Opitz, J.; Schreiber, J.; Meyendorf, N. Smart Sensor Phenomena, Technology, Networks, and Systems. In *Proceedings of SPIE*, March 8, 2009; Meyendorf, N. G.; Peters, K. J.; Ecke, W., Eds.; San Diego, California, USA; 72930O.
8. Schrand, A. M.; Huang, H.; Carlson, C.; Schlager, J. J.; Ohsawa, E.; Hussain, S. M.; Dai, L. *J. Phys. Chem. B* **2007**, *111*, 2–7. doi:10.1021/jp066387v
9. Yu, S.-J.; Kang, M.-W.; Chang, H.-C.; Chen, K.-M.; Yu, Y.-C. *J. Am. Chem. Soc.* **2005**, *127*, 17604–17605. doi:10.1021/ja0567081

10. Fu, C.-C.; Lee, H.-Y.; Chen, K.; Lim, T.-S.; Wu, H.-Y.; Lin, P.-K.; Wei, P.-K.; Tsao, P.-H.; Chang, H.-C.; Fann, W. *Proc. Natl. Acad. Sci. U. S. A.* **2007**, *104*, 727–732. doi:10.1073/pnas.0605409104

11. Mkandawire, M.; Pohl, A.; Gubarevich, T.; Lapina, V.; Appelhans, D.; Rödel, G.; Pompe, W.; Schreiber, J.; Opitz, J. *J. Biophotonics* **2009**, *2*, 596–606. doi:10.1002/jbio.200910002

12. Faklaris, O.; Joshi, V.; Irinopoulou, T.; Tauc, P.; Sennour, M.; Girard, H.; Gesset, C.; Arnault, J.-C.; Thorel, A.; Boudou, J.-P.; Curmi, P. A.; Treussart, F. *ACS Nano* **2009**, *3*, 3955–3962. doi:10.1021/nn901014j

13. Liu, K.-K.; Zheng, W.-W.; Wang, C.-C.; Chiu, Y.-C.; Cheng, C.-L.; Lo, Y.-S.; Chen, C.; Chao, J.-I. *Nanotechnology* **2010**, *21*, 315106. doi:10.1088/0957-4484/21/31/315106

14. Zhang, X.-Q.; Lam, R.; Xu, X.; Chow, E. K.; Kim, H.-J.; Ho, D. *Adv. Mater.* **2011**, *23*, 4770–4775. doi:10.1002/adma.201102263

15. Huang, H.; Pierstorff, E.; Osawa, E.; Ho, D. *Nano Lett.* **2007**, *7*, 3305–3314. doi:10.1021/nl071521o

16. Baughman, R. H.; Zakhidov, A. A.; de Heer, A. W. *Science* **2002**, *297*, 787–792. doi:10.1126/science.1060928

17. Scharnweber, D.; Born, R.; Flade, K.; Roessler, S.; Stoelzel, M.; Worch, H. *Biomaterials* **2004**, *25*, 2371–2380. doi:10.1016/j.biomaterials.2003.09.025

18. Scharnweber, D.; Flössel, F.; Born, R.; Worch, H. *J. Mater. Sci.: Mater. Med.* **2007**, *18*, 391–397. doi:10.1007/s10856-006-0704-7

19. Bierbaum, S.; Douglas, T.; Hanke, H.; Scharnweber, D.; Tippelt, S.; Monsees, T. K.; Funk, R. H. W.; Worch, H. *J. Biomed. Mater. Res., Part A* **2006**, *77*, 551–562. doi:10.1002/jbm.a.30572

20. Beutner, R.; Sewing, A. *Biomaterialen* **2007**, *8*, 25–31. doi:10.1515/BIOMAT.2007.8.1.25

21. Beutner, R.; Michael, J.; Förster, A.; Schwenzer, B.; Scharnweber, D. *Biomaterials* **2009**, *30*, 2774–2781. doi:10.1016/j.biomaterials.2009.01.047

22. Michael, J.; Beutner, R.; Hempel, U.; Scharnweber, D.; Worch, H.; Schwenzer, B. *J. Biomed. Mater. Res., Part B* **2007**, *80*, 146–155. doi:10.1002/jbm.b.30579

23. Beutner, R.; Michael, J.; Schwenzer, B.; Scharnweber, D. *J. R. Soc., Interface* **2010**, *7* (Suppl. 1), S93–S105. doi:10.1098/rsif.2009.0418.focus

24. Schliephake, H.; Strecker, N.; Förster, A.; Schwenzer, B.; Reichert, J.; Scharnweber, D. *Eur. Cells Mater.* **2012**, *23*, 161–169.

25. Schliephake, H.; Bötel, C.; Förster, A.; Schwenzer, B.; Reichert, J.; Scharnweber, D. *Biomaterials* **2012**, *33*, 1315–1322. doi:10.1016/j.biomaterials.2011.10.027

26. Michael, J.; Schönzart, L.; Israel, I.; Beutner, R.; Scharnweber, D.; Worch, H.; Hempel, U.; Schwenzer, B. *Bioconjugate Chem.* **2009**, *20*, 710–718. doi:10.1021/bc800372e

27. Hannstein, I.; Mkandawire, M.; Rödel, G.; Opitz, J.; Lapina, V.; Schreiber, J. *Mater. Test.* **2009**, *51*, 659–663. doi:10.3139/120.110054

28. Xing, Z.; Pedersen, T. O.; Wu, X.; Xue, Y.; Sun, Y.; Finne-Wistrand, A.; Kloss, F. R.; Waag, T.; Krueger, A.; Steinmüller-Nethl, D.; Mustafa, K. *Tissue Eng., Part A* **2013**, *19*, 1783–1791. doi:10.1089/ten.tea.2012.0336

29. Fox, K.; Palamara, J.; Judge, R.; Greentree, A. D. *J. Mater. Sci.: Mater. Med.* **2013**, *24*, 849–861. doi:10.1007/s10856-013-4860-2

30. Yu, M.; George, C.; Cao, Y.; Wootton, D.; Zhou, J. *J. Mater. Sci.* **2014**, *49*, 3629–3641. doi:10.1007/s10853-014-8066-x

31. Zhang, Q.; Mochalin, V. N.; Neitzel, I.; Hazeli, K.; Niu, J.; Kortsos, A.; Zhou, J. G.; Leikes, P. I.; Gogotsi, Y. *Biomaterials* **2012**, *33*, 5067–5075. doi:10.1016/j.biomaterials.2012.03.063

32. Kloss, F. R.; Gassner, R.; Preiner, J.; Ebner, A.; Larsson, K.; Hächl, O.; Tuli, T.; Rasse, M.; Moser, D.; Laimer, K.; Nickel, E. A.; Laschober, G.; Brunauer, R.; Klima, G.; Hinterdorfer, P.; Steinmüller-Nethl, D.; Lepperdinger, G. *Biomaterials* **2008**, *29*, 2433–2442. doi:10.1016/j.biomaterials.2008.01.036

33. Bacakova, L.; Kopova, I.; Stankova, L.; Liskova, J.; Vacik, J.; Lavrentiev, V.; Kromka, A.; Potocky, S.; Stranska, D. *Phys. Status Solidi A* **2014**. doi:10.1002/pssa.201431402

34. Shenderova, O. A.; Zhirnov, V. V.; Brenner, D. W. *Crit. Rev. Solid State Mater. Sci.* **2002**, *27*, 227–356. doi:10.1080/10408430208500497

35. Michelmore, A.; Gong, W.; Jenkins, P.; Ralston, J. *Phys. Chem. Chem. Phys.* **2000**, *2*, 2985–2992. doi:10.1039/B001213K

36. Mutin, P. H.; Lafond, V.; Popa, A. F.; Granier, M.; Markey, L.; Dereux, A. *Chem. Mater.* **2004**, *16*, 5670–5675. doi:10.1021/cm035367s

37. Krueger, A.; Stegk, J.; Liang, Y.; Lu, L.; Jarre, G. *Langmuir* **2008**, *24*, 4200–4204. doi:10.1021/la703482v

38. Kaur, R.; Chitanda, J. M.; Michel, D.; Maley, J.; Borondics, F.; Yang, P.; Verrall, R. E.; Badea, I. *Int. J. Nanomed.* **2012**, *7*, 3851–3866. doi:10.2147/IJN.S32877

39. Krueger, A.; Lang, D. *Adv. Funct. Mater.* **2012**, *22*, 890–906. doi:10.1002/adfm.201102670

40. Coates, J. Interpretation of Infrared Spectra, A Practical Approach. *Encyclopedia of Analytical Chemistry*; John Wiley & So: Chichester, 2000.

41. Gong, W. *Int. J. Miner. Process.* **2001**, *63*, 147–165. doi:10.1016/S0301-7516(01)00045-X

42. Viorney, C.; Chevrolot, Y.; Léonard, D.; Aronsson, B.; Péchy, P.; Mathieu, H. J.; Descouts, P.; Grätzel, M. *Langmuir* **2002**, *18*, 2582–2589. doi:10.1021/la010908i

43. Gao, W.; Dickinson, L.; Grozinger, C.; Morin, F. G.; Reven, L. *Langmuir* **1996**, *12*, 6429–6435. doi:10.1021/la9607621

License and Terms

This is an Open Access article under the terms of the Creative Commons Attribution License (<http://creativecommons.org/licenses/by/2.0/>), which permits unrestricted use, distribution, and reproduction in any medium, provided the original work is properly cited.

The license is subject to the *Beilstein Journal of Organic Chemistry* terms and conditions: (<http://www.beilstein-journals.org/bjoc>)

The definitive version of this article is the electronic one which can be found at: doi:10.3762/bjoc.10.293